

# **Biofunctional Upconversion Nanoparticles for Cancer Theranostics**

By

**Liuen Liang**

A thesis submitted to Macquarie University

For the degree of Doctor of Philosophy

Department of Biomedical Sciences

September 2016



**MACQUARIE**  
University  
SYDNEY • AUSTRALIA



Except where acknowledged in the customary manner, the material presented in this thesis is, to the best of my knowledge, original and has not been submitted in whole or part for a degree in any university. This thesis has obtained the approval of the Ethics Committee at Macquarie University for the research on animal and the reference number of the approval is ARA2013/007-4.



\_\_\_\_\_  
Luen Liang





# Acknowledgements

I would like to express my sincere gratitude to my supervisor Professor Yi Qian, for having me as his student, and providing with the opportunity to strengthen my research in Macquarie University. I am very thankful for his constant support and enormous patience, and allowing me to have the freedom to carry out the research in my own way.

I am deeply grateful to my supervisor A/Professor Andrei Zvyagin, who has offered me the greatest supervision and support throughout my entire doctoral project. This thesis would not have come to fruition without his help. He has always been the most positive, supportive, and inspiring supervisor to me. I feel very fortunate and blessed to work with him for the past few years.

I am also thankful to my co-supervisor Dr. Run Zhang, for his valuable inputs to my project. Much of the success in laboratory work is attributed to his insights and experimental experiences. I appreciate the research skills and project management he taught me, and the advice and encouragement he provided. I have learned a great deal from him, and because of that, I become a better researcher.

I would like to thank my collaborators, Professor Sergey Deyev, Professor Nicki Packer, Professor Helen Pask, Andrew, Lu, Annie, Anna, Arun, Anwar, Tiago, for lending me their expert hands. Their helpful ideas and constructive comments have contributed a lot to improve the quality of my papers.

I would also like to extend my gratitude to my colleagues, Wan, Zahra, Varun, Katya, Kaavya, David, Xianlin, and Jie Lu, who have given their assistance and suggestion, shared the knowledge and thoughts with me. It was a great pleasure to work by the side of these talented researchers.

I am also thankful to the admirable staff from the Department of Biomedical Sciences, the Department of Physics and Astronomy, the Department of Chemistry and Biomolecular Sciences, and Macquarie University Microscope Unit, for their kind help in solving many technical or laboratory problems.

## ACKNOWLEDGEMENTS

---

I would also like to thank my wonderful friends, Ru, Yameng, Liqin, Chuanping, and Yunqi, for lending me their ears, putting up with my moods, offering me their advice, and supporting me through the PhD process. The good times we had, the workout, cardboard games, bushwalking, traveling, and pillow talk were all greatly appreciated.

My deepest gratitude also goes to my families, my parents and my brothers, whose unconditional love and belief in my capabilities has kept me strong enough to overcome many hurdles that I confronted. Special thanks to my beloved husband, Dr. Zibin Chen, for his endless love, understanding, and support through this challenging and rewarding journey. Thank you for bearing with me through the hard times and sharing with me the happiest moments in life.

Finally, I wish to acknowledge Macquarie University for awarding me the Macquarie University Research Excellence Scholarship (MQRES), and providing the financial support for me to attend the national and international conferences during this project.

# List of Publications

## Papers

- [1] **L. Liang**, Y. Lu, R. Zhang, A. Care, T.A. Ortega, S.M. Deyev, Y. Qian, and A.V. Zvyagin, “Deep-penetrating Photodynamic Therapy with KillerRed Mediated by Upconversion Nanoparticles”, *Acta Biomaterialia*, in press.
- [2] **L. Liang**, A. Care, R. Zhang, Y. Lu, N.H. Packer, A. Sunna, Y. Qian, and A.V. Zvyagin, “Facile Assembly of Functional Upconversion Nanoparticles for Targeted Cancer Imaging and Photodynamic Therapy”, *ACS Applied Materials & Interfaces*, **2016**, 8, 11945-11935.
- [3] **L. Liang**, A.V. Everest-Dass, R. Zhang, Y. Qian, N.H. Packer, and A.V. Zvyagin, “The Effect of Surface Characteristics of Upconversion Nanoparticle on Corona Formation and Cell Interaction”, prepared for submission to *RSC Advances*.
- [4] A. Nadort, **L. Liang**, E. Grebenik, A. Guller, Y. Lu, Y. Qian, E.M. Goldys, and A.V. Zvyagin, “Systematic Assessment of Blood Circulation Time of Functionalized Upconversion Nanoparticles in the Chick Embryo”, *SPIE Micro+Nano Materials, Devices, and Applications*, International Society for Optics and Photonics, **2015**, 96683Y-96683Y-7.

## Conference Proceedings

- [1] **L. Liang**, A. Nadort, E. Grebenik, Y. Lu, R. Zhang, V.K.A. Sreenivasan, A. Guller, and A.V. Zvyagin, “Functional Luminescent Nanoparticles for Imaging Tumours on Chick Embryo Choriallantoic Membrane”, the 5<sup>th</sup> International NanoMedicine Conference, **2014**.

## LIST OF PUBLICATIONS

---

- [2] **L. Liang**, R. Zhang, V.K.A. Sreenivasan, A. Nadort, S.M. Deyev, Y. Qian, and A.V. Zvyagin, “KillerRed Conjugated Upconversion Nanoparticles for Tumour Imaging and Photodynamic Therapy”, MQ BioFocus Research Conference, **2014**.
- [3] **L. Liang**, A. Care, R. Zhang, Y. Lu, N.H. Packer, A. Sunna, Y. Qian, and A.V. Zvyagin, “Smart Peptide Linker Conjugated Upconversion Nanoparticles for Targeted Cancer Imaging and Photodynamic Therapy”, the 9<sup>th</sup> International Mesostructured Material Symposium, **2015**.
- [4] **L. Liang**, A. Care, R. Zhang, Y. Lu, N.H. Packer, A. Sunna, Y. Qian, and A.V. Zvyagin, “Imaging-Guided Photodynamic Therapy for Cancer Using Smart Peptide-Conjugated Upconversion Nanoparticles”, Materials Research Society Fall Meeting and Exhibit, **2015**.
- [5] **L. Liang**, R. Zhang, A. Care, Y. Lu, A. Sunna, S.M. Deyev, N.H. Packer, Y. Qian, and A.V. Zvyagin, “Biofunctionalized Upconversion Nanoparticles for Cancer Imaging and Near-infrared Triggered Photodynamic Therapy”, the 7<sup>th</sup> International NanoMedicine Conference, **2016**.

# Abstract

Development of new approaches for diagnosis and therapy of tumours, termed theranostics, is one of the most dynamic areas of the life sciences, where new nanomaterials afford new opportunities. The nanomaterial merits include programmability of their physical and chemical properties; abundance of reactive functional groups on their surface; large effective surface area and optimal size, which determines preferential accumulation of nanoparticles (NPs) in tumour tissue. Photoluminescent nanomaterials add to the list of merits their high optical contrast achievable on the crowded background of biological cells, tissues and whole organisms. In order to fully harness the potential of photoluminescent NPs, they need to be coupled with functional biological molecules, accomplished by procedures of NP surface redressing and bioconjugation, to enable controlled targeting and therapeutic action in the delicate environment of a biological system. Interactions of these biofunctional hybrid assemblies with live cells and organisms, however, are overly complex, poorly understood and controlled. It is increasingly being accepted that NPs encountering biological medium are swiftly coated by a biomolecular adsorption layer called “protein corona”. Consequently, the molecular machinery of a living cell or organism will interact with the corona rather than biofunctional hybrid assemblies, making it a key determinant of the biological response of NP exposure. In this PhD thesis, the design and characterisation of photoluminescent biofunctional nanoparticles and their applications for targeted delivery and photodynamic therapy of cancer cells are addressed, in addition to the systematic investigation of protein corona formation on polymer-coated nanoparticles.

My thesis research was centred at a new-generation biofunctional photoluminescent nanoparticles with unique optical properties termed upconversion nanoparticles (UCNPs). UCNPs are photoexcited by near-infrared light (NIR) at 980 nm capable for deep penetration (up to 1 cm) in biological tissue. This excitation confers another key advantage of background-free imaging in cells and tissues due to very little excitation of autofluorescence. UCNP emission is tuneable by design from ultraviolet to visible or even

## ABSTRACT

---

NIR spectral bands, which enabled my colleagues and me to address the main limitation of photodynamic therapy (PDT), shallow treatment depths. Indeed, the conversion of deeply-penetrating near-infrared to visible light allows photosensitisation of such potent PDT agents, as fluorescent protein KillerRed and Rose Bengal.

In the first paper, we have demonstrated the PDT therapeutic efficacy of a water-soluble photosensitiser protein KillerRed coupled to UCNPs covalently. The spectral overlap between the UCNPs emission and KillerRed absorption ensured the efficient energy transfer, leading to reactive oxygen species (ROS) generation upon the excitation at 980 nm, which exerted toxicity to MDA-MB-231 breast cancer cells. Cross-comparison between the conventional KillerRed and UCNPs-mediated KillerRed PDT treatment of cancer cells buried under 1-cm muscle tissue clearly demonstrated superiority of KillerRed-UCNPs photosensitisation by the NIR light, with no detectable PDT effect in the case of KillerRed photosensitised by a yellow laser.

In the second paper, we have reported a facile strategy to assemble PDT nanocomposites functionalised for cancer targeting, based on the coating of UCNPs with a silica layer encapsulating the Rose Bengal photosensitiser and bioconjugation to antibodies through a bifunctional fusion protein consisting of a solid-binding peptide linker (L) genetically fused to Streptococcus Protein G' (PG). The fusion protein (Linker-Protein G, LPG) mediates the functionalisation of silica-coated UCNPs with cancer cell antibodies allowing for specific target recognition and delivery. The resulting nanocomposites were shown to target cancer cells specifically, generate intracellular reactive oxygen species under 980-nm excitation, and induce NIR-triggered phototoxicity to suppress cancer cell growth *in vitro*.

In the third paper, the effect of protein corona formation on UCNPs coated with positively- (polyethylenimine), negatively- (polyacrylic acid) charged and nearly neutral (polyethylene glycol) polymers was investigated. Our protein assaying study corroborated the TEM observation, showing profound effect of the UCNPs-polymer surface charge: UCNPs-polyethylenimine acquired four-fold of protein content as compared to the other coatings. The composition of protein binding to UCNPs is notably influenced by the surface charges of the UCNPs-polymer. We also found that the protein corona inhibited the cell binding and cellular uptake of UCNPs coated with positive and

neutral polymers, whereas enhanced that of UCNP-polyethylenimine. Moreover, the presence of protein corona slightly mitigated the mild cytotoxic effects of nanoparticles. These results provide valuable guidance into rational design of UCNP-based biofunctional agents.

In a separated published work carried out with my colleagues, we investigated effect of the surface functionalisation of UCNPs on the blood circulation lifetime using *in vivo* early-stage developed animal model (chicken embryo). The preference of NP coating with polyethylene glycol was expected and confirmed. This study was critical for purpose-design of NPs evading rapid filtration from the blood circulation, therefore maximising nanoparticle accumulation in the tumour *in vivo*.

# Contents

Acknowledgements.....	V
List of Publications .....	VII
Abstract .....	IX
CHAPTER 1: Thesis Outline.....	1
CHAPTER 2: Photoluminescent Nanoparticles for Cancer Theranostics .....	3
2.1 Nanotechnology in Cancer Diagnosis and Treatment.....	3
2.2 Photoluminescent Nanoparticles for Cancer Theranostics.....	4
2.2.1 Silica Nanoparticles .....	5
2.2.2 Quantum Dots.....	7
2.2.3 Carbon Nanomaterials .....	10
2.2.4 Gold Nanoparticles .....	13
2.3 Limitations of the Existing Photoluminescent Nanoparticles in Current Theranostics.....	15
2.4 Upconversion Nanoparticles (UCNPs) .....	17
2.4.1 Composition and Structure .....	17
2.4.2 Upconversion Photoluminescence.....	19
2.4.3 Optical Properties .....	20
2.4.4 Cytotoxicity .....	25
2.5 References .....	27
CHAPTER 3: Synthesis, Design and Applications of UCNPs in Theranostics .....	34
3.1 Synthesis Strategy .....	34
3.1.1 Thermal Decomposition .....	35
3.1.2 Hydro(solvo)thermal Synthesis .....	36



3.1.3 Coprecipitation.....	37
3.2 Surface Passivation.....	37
3.3 Surface Modification and Bioconjugation .....	39
3.3.1 Ligand Exchange .....	40
3.3.2 Ligand Oxidization .....	41
3.3.3 Ligand Removal.....	42
3.3.4 Ligand Attraction.....	42
3.3.5 Layer-by-layer Assembly .....	43
3.3.6 Surface Silanization .....	44
3.3.7 Bioconjugation.....	46
3.4 Integration with Therapeutic Agents .....	48
3.4.1 Physical Adsorption.....	49
3.4.2 Covalent Conjugation .....	51
3.4.3 Silica Encapsulation.....	52
3.5 Applications in Cancer Imaging and Treatment.....	55
3.5.1 High-Contrast Bioimaging Using UCNP.....	55
3.5.2 Applications of UCNP for Drug Delivery.....	62
3.5.3 Applications of UCNP in Photodynamic Therapy.....	67
3.6 References .....	73
CHAPTER 4: Deep-Penetrating Photodynamic Therapy with KillerRed Mediated by Upconversion Nanoparticles .....	81
4.1 Introduction .....	81
4.2 Author's Contribution to The Paper .....	82
4.3 Full Paper .....	83
CHAPTER 5: Facile Assembly of Functional Upconversion Nanoparticles for Targeted Cancer Imaging and Photodynamic Therapy .....	113

## CONTENTS

---

5.1 Introduction .....	113
5.2 Author's Contribution to The Paper .....	114
5.3 Full Paper .....	115
CHAPTER 6: The Effect of Surface Characteristics of Upconversion Nanoparticle on Corona Formation and Cell Interaction .....	135
6.1 Introduction .....	135
6.2 Author's Contribution to The Paper .....	136
6.3 Full Paper .....	137
CHAPTER 7: Systematic Assessment of Blood Circulation Time of Functionalized Upconversion Nanoparticles in the Chick Embryo.....	165
7.1 Introduction .....	166
7.2 Author's Contribution to The Paper .....	166
7.3 Full Paper .....	167
CHAPTER 8: Summary and Future Scope.....	174
8.1 Summary .....	174
8.2 Future Scope.....	176
APPENDICES .....	179
List of Abbreviations.....	179
Ethics Approval.....	182

# 1

## Thesis Outline

Nowadays, photoluminescent (PL) nanomaterials emerge as a promising platform, which combines therapeutic and diagnostic capabilities in a single system, leading to more specific and efficient tools for disease diagnosis and treatment. Despite the progress, the state-of-the-art PL nanoparticles possess several shortcomings, such as rapid photobleaching, low optical imaging contrast, and shallow imaging depth. These limit their application scope towards high-sensitivity cancer detection and centimetre-deep-tumour treatment. Aiming to address these problems, this thesis explores the use of upconversion nanoparticles (UCNPs), as an alternative PL nanomaterial for the design of theranostics nanocomposites. UCNPs are exceptionally photostable and photoexcited by deep-penetrating near-infrared light to emit ultraviolet, visible or near-infrared radiation via the process of photon energy upconversion. Therefore, theranostics nanoplateforms introduced and demonstrated in this work offer a lucrative approach to delivering ultraviolet and visible light at the centimetre-depth in highly scattering and absorbing biological tissue. This offers several possibilities to trigger photochemical and photobiological reactions in depth. In this work, in collaboration with my colleagues, I have demonstrated photodynamic therapy of cancer at the extended depth of sub-centimetres to centimetre, which was mediated by rationally designed UCNP complexes.

The secondary focus of this work relates to the process of target delivery of UCNP complexes, which is accompanied by the complex interaction with plasma proteins. As a result of this interaction, nanoparticles and UCNPs in particular, acquire a protein layer on their surface termed “protein corona”, which can change UCNP nanocomposite targeting and therapeutic properties. Systematic investigation of the protein corona

## CHAPTER 1

---

formation on the surface of three most representative surface-functionalised types of UCNPs is also addressed in this thesis.

This thesis is comprised of eight chapters and organized, as follows.

An introductory Chapter 2 provides an overview of the most widespread PL nanoparticles employed in cancer theranostics research. The limitations of these nanoparticles in the context of biological imaging are discussed, providing a backdrop for introduction of UCNPs. The composition and structure, upconversion photon energy transfer process, unique optical properties, and cytotoxicity of UCNPs are presented. Chapter 3 is a comprehensive review that covers main aspects of the development of a UCNPs-based theranostics nanocomposite, including the nanoparticle synthesis methods, surface design and bioconjugation, approaches to coupling with biological molecules and drugs, and examples of applications in cancer research. Chapter 4 (paper 1, accepted by *Acta Biomaterialia*) is designed to investigate the feasibility of using UCNPs to achieve effective treatment of deep-seating cancers. The PDT efficiency of NIR photoexcited KillerRed-UCNP was evaluated under a sub-centimetre-thick tissue and compared with that of unbound KillerRed, using a yellow laser as the excitation light source. Chapter 5 (paper 2, published in *ACS Applied Materials and Interfaces*) presents a facile assembly strategy of the design of UCNPs nanocomposites for cancer targeted PDT. The developed method outperformed the conventional bioconjugation strategies in ensuring the functional display of immobilized antibodies and providing versatility in antibodies selection. Chapter 6 (paper 3, prepared for submission to *RSC Advances*) investigates the surface charge effect of UCNPs on the protein corona formation, affecting the interaction of UCNPs with cells. This chapter demonstrates the critical understanding of the protein absorption on UCNPs, aimed at providing useful information for improved design of UCNPs for biomedical applications. Chapter 7 (paper 4, published in *Proceedings of 2015 SPIE Micro+Nano Materials, Devices, and Systems*) describes investigation of the surface chemistry (carboxyl, amine, and polyethylene glycol) impact on the blood circulation lifetime of UCNPs in a chick embryo, thus providing assessment of UCNPs properties in *in vivo* scenarios. Chapter 8 summarizes the key research outcomes of the thesis and provides information on possible future research in this direction.

# 2

## **Photoluminescent Nanoparticles for Cancer Theranostics**

In this chapter, applications of nanotechnology in cancer diagnosis and treatment are overviewed, followed by a brief review of photoluminescent nanoparticles used in theranostics. Both merits and limitations of these nanoparticles in the context of biomedical imaging will be discussed. Lastly, upconversion nanoparticles will be introduced as an emerging photoluminescent nanomaterial, which holds promise due to its unique optical properties. Fundamental knowledge of upconversion nanoparticles, including their composition and structure, photoluminescence mechanisms and aspects of this material interaction with biological matter will be presented.

### **2.1 Nanotechnology in Cancer Diagnosis and Treatment**

Cancer is the second leading cause of death worldwide following cardiovascular diseases. The crucial prevention of the cancer mortality is early detection and treatment of the malignant cancer cells. While new medicines and imaging techniques are evolving to improve the cure and survival odds, application of nanotechnology has brought about exciting breakthroughs in devising innovative diagnostic and therapeutic tools for fighting cancers. The development, exploration, and deployment of nanomaterials in the field of cancer research have undergone significant expansion over the last decades. One of the compelling reason is the nanometer size of the materials that enables their preferential accumulation in tumours via the enhanced permeability and retention effect (EPR). This process can be harnessed to largely enhance the delivery efficiency of anticancer drugs to tumour sites. Because of the small dimensions at the nanoscale, nanoparticles exhibit many unique optical, electronic, magnetic properties, which are not observed in their bulk origin materials. These properties can be fine-tuned by controlling size, shape, composition of the nanoparticles, resulting in particles with customized

properties for different applications. Nanoparticles can be endowed with different surface chemistry by coating or surface modifications to facilitate their chemical or physical interaction with biofunctional compounds. Another key hallmark of nanomaterials is their large surface area-to-volume ratio, which allows them to absorb, bind, and carry a variety of therapeutic agents and biological molecules with high loading efficiency. Effective and safer drugs delivery is of great importance in cancer treatment. To this aim, multifunctional nanoparticles can be designed with controlled surface properties to increase their circulation time in the bloodstream, attachment to cell-specific ligands to enable cancer-targeting therapy, integration with stimulus-responsive elements to regulate the drug release, and loading with synergistic drugs to enhance the therapeutic efficacy. It has also been shown that diagnosis and therapy can be combined within a single nanoplatform, known as theranostic nanoparticles. These particles with multiple capabilities aim to serve as excellent imaging probes to locate tumour sites, and as carriers for selective targeting and delivery of therapeutic payloads to cancer cells, thereby minimizing the side effect on the neighbouring healthy tissues. Moreover, such an ideal nanosystem is capable of elucidating the pharmacokinetics and pharmacodynamics of therapeutics during the evolving course of the treatment, thus providing a rational and informative basis for improvement on formulation of individual nanotheranostics. Therefore, nanotheranostics is envisioned to provide a wealth of new opportunities to modernizing the diagnosis and treatment strategies for cancer and taking a step further towards a future of personalized medicine.

### **2.2 Photoluminescent Nanoparticles for Cancer Theranostics**

Photoluminescence (PL) imaging is a useful technique in biomedical research, especially in the diagnosis of disease at the early stage, cancer screening, imaging-guided therapy, and monitoring therapeutic response. In contrast to other imaging techniques such as magnetic resonance imaging (MRI), computed tomography (CT), and positron emission tomography (PET), PL imaging offers many core advantages, including low cost, rapid imaging for *in situ* diagnosis and intraoperative decision, and no radiation side effects [1]. As a matter of fact, PL imaging is now being applied in clinics and in operations for locating malignant tumours, as well as breast cancer pre-screening [2]. The PL bioimaging was accomplished by the use of photoluminescent agents and fluorescent imaging systems. With rapid advances in nanotechnology research, efforts in the PL

imaging technique have been geared towards the development of photoluminescent nanoparticles that allow for high-sensitivity detection and high-contrast imaging. Furthermore, PL nanoparticles are also a prominent platform for the design of multifunctional nanohybrid complexes that embrace various functionalities, such as targeting, sensing, and therapeutic modalities. PL nanomaterials that are well developed and widely used in current cancer research include silica nanoparticles [3], quantum dots (QDs) [4], carbon-based nanoparticles [5], and gold nanoparticles [6]. In this section, a brief description of these PL nanoparticles will be presented.

### **2.2.1 Silica Nanoparticles**

Silica nanoparticles is a long-standing bio-safe nanomaterial that has been extensively explored as a delivery vehicle in the life science studies. Silica nanoparticles can be divided into two types: solid and mesoporous nanoparticles. These particles cannot function as an imaging probe on their own, being optically non-absorbing in the usable spectral range. However, they can be rendered fluorescent by incorporation of organic dyes into the silica matrix (Figure 2.1a) [7-9]. Depending on dyes used for the doping, silica nanoparticles can be engineered to emit fluorescence in the range of 300–1000 nm (Figure 2.1b) [9, 10]. Alternatively, high-optical-contrast nanoparticles, such as QDs and gold nanoparticles can be encapsulated in a silica shell to yield photoluminescent silica nanocomposites [11, 12].

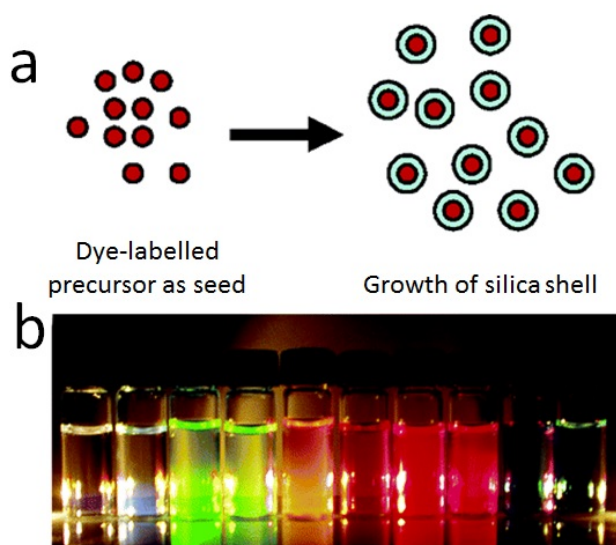


**Figure 2. 1** (a) Introduction of fluorescent dyes to solid silica nanoparticles during the particle formation. (b) The emission wavelength of fluorescent silica nanoparticles can be tuned from UV to near infrared range by doping different organic dyes. The organic dyes that are incorporated in silica nanoparticles from left to right are Alexa 350, N-(7-(dimethylamino)-4-methylcoumarin-3-yl), Alexa 488, fluorescein isothiocyanate, tetramethylrhodamine isothiocyanate, Alexa 555, Alexa 568, Texas Red, Alexa 680, and Alexa 750. Reproduced from Ref. [9].

Solid silica nanoparticles are prepared by a well-established Stöber method via the ammonia catalysed hydrolysis and condensation of tetraethyl orthosilicate (TEOS) in a mixture of water and alcohol [13]. The size of the obtained silica nanoparticles can be controlled in the range of 50–2000 nm by simply adjusting the concentrations of the reactants in the synthesis [13]. To bring functionalities to the particles, silane with active groups can be readily coupled to the surface of as-synthesized silica nanoparticles by simple mixing. Mesoporous silica nanoparticles are generally synthesized by a sol-gel process in which amphiphilic templates, such as cetyltrimethylammonium bromide (CTAB) are embedded into the nanoparticles, followed by the template removal through solvent extraction or calcination [14]. In following steps, organic dyes and therapeutic drugs are incorporated into the mesoporous silica nanoparticles to yield theranostic nanocomposites. The porous structure in mesoporous silica nanoparticles is advantageous for downloading a substantial payload to the particles.

The utility of silica in conjugation with organic dyes and therapeutic agents for cancer theranostics has been demonstrated in a wide range of studies [15]. For example, Wang and co-workers have reported the preparation of a silica-based theranostic nanocomposite



by entrapping a water-soluble photosensitiser, methylene blue, in the dense silica nanoparticle for simultaneous *in vivo* imaging and photodynamic therapy [16]. Liu *et al.* developed a multifunctional silica nanoparticle by co-loading the particle with a photosensitizer protoporphyrin IX and an NIR fluorophore IR-820 [17]. The prepared nanoparticles demonstrated a feasible application in the killing cancer cells via photodynamic therapy and in various types of *in vivo* animal imaging (Figure 2.2) [17].

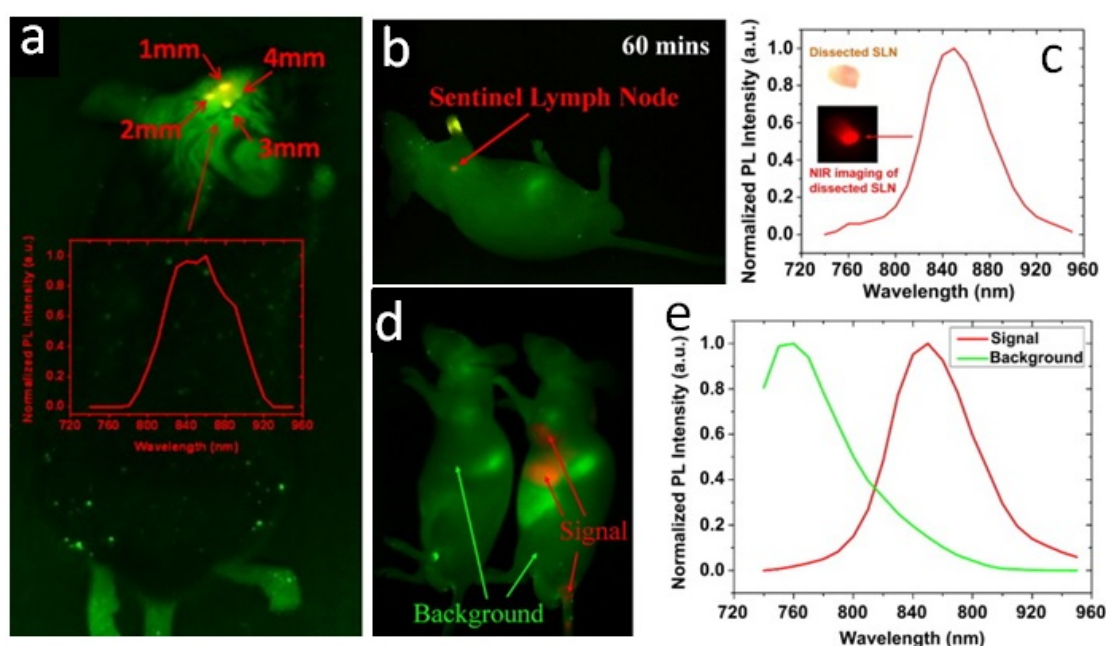


**Figure 2. 2** (a) NIR imaging of a mouse after the injection of PEG-modified IR-820 doped silica nanoparticle into the different depths of the brain. The nanoparticles were excited at 704 nm, and coloured in red in the image and the background autofluorescence was coloured in green. The inset is the fluorescence spectrum of IR-820. (b) Imaging the sentinel lymph node (SLN) of a nude mouse after the intradermal injection of PEG modified IR-820 doped silica nanoparticles for 60 mins. (c) NIR imaging and fluorescence spectrum of the dissected SLN from (b). (d) NIR fluorescence images of a control mouse (left) and a tumour-bearing mouse after treatment with nanoparticles (right). Red colour represents accumulation of nanoparticles in the liver and tumour post-intravenous injection 5 h. (e) Fluorescence spectra of the particle signal and background autofluorescence from a mouse under the excitation at 704 nm, with its image shown in (d) Reproduced from Ref. [17].

### 2.2.2 Quantum Dots

QDs are an important class of light-emitting nanomaterial that offers excellent optical properties for bioimaging applications. QDs are composed of semiconductor bandgap materials and typically made up from nanocrystals of CdSe, CdTe, PbS, InAs, InP, ZnSe. In order to enhance the quantum efficiency of QDs, an inorganic shell that possesses the

higher band gap (*e.g.* ZnS, CdS) than that of the core structure is usually coated on the core QD to provide the exciton confinement and minimize surface defects [18]. The unique optical properties of QDs stem from the fact that their physical dimensions (typically 2–10 nm) are smaller than the exciton Bohr radius [19]. Upon excitation, QDs display size-dependent narrow-bandwidth emission spectra. The emission wavelength can be precisely adjusted from UV to infrared by increasing the core particle size to provide a redshift of the spectrum (Figure 2.3) [20].

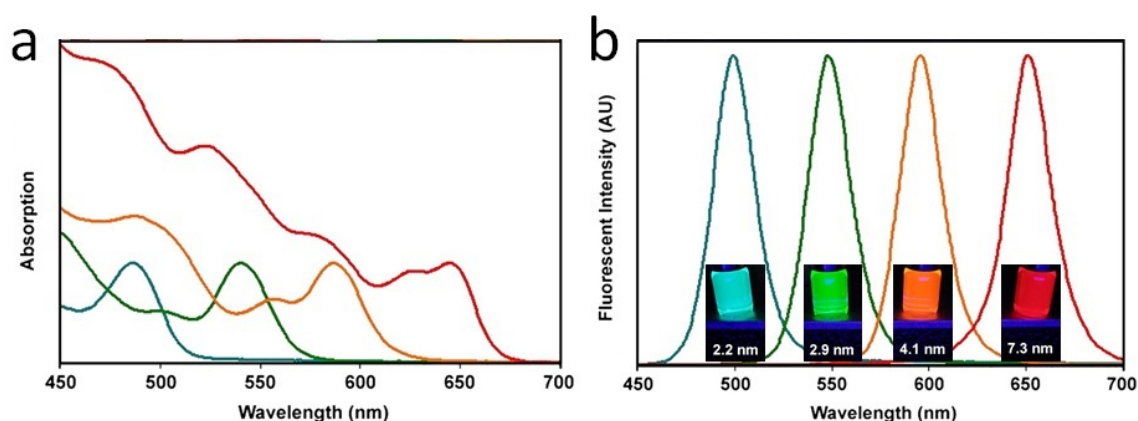


**Figure 2. 3** (a) Absorption spectra of CdSe QDs with sizes of 2.2 nm, 2.9 nm, 4.1 nm, and 7.3 nm. (b) Fluorescence spectra of the same CdSe QD samples. Insets are the UV-excited fluorescence images of four different CdSe QDs in vials. Reproduced from Ref. [20].

The most popular synthesis of QDs is based on the high-temperature decomposition of organometallic precursors in the presence of surfactants and organic solvents with high boiling points [21]. The size of the resulting QDs is controllable by the alteration of precursor concentration and crystal growth time [22]. QDs manufactured by this method typically possess good crystallinity and narrow size distribution. However, due to the presence of alkyl surface ligands, as-produced QDs are not water dispersible. In order to make QDs compatible with biological fluids, several surface modification methods have been introduced to render QDs hydrophilic. These include a thiol ligand exchange method to replace as-synthesised surface moieties, additional surface coating with amphiphilic compounds (polymers), and silica-coating [23].

There are a number of distinctive optical properties that make QDs potent fluorescent nanomaterial, such as a high quantum yield, narrow fluorescence band, broad excitation spectrum, excellent photostability, long fluorescence lifetime, and large Stokes shift [24].

These remarkable photophysical parameters of QDs led to their broad recognition in the life sciences. The examples of these applications include monitoring discrete biological events, tracking cell migrations, detection of pathogens and whole-animal imaging [19]. For example, Gao and co-workers have developed cancer-targeting theranostic QDs by coating core-shell CdSe-ZnS QDs with amphiphilic polymer and attaching a tumour-binding ligand to the nanocomposite [25]. The designed multifunctional QDs demonstrated successful recognition of *in vivo* tumour by the passive labelling via EPR effect and by the active targeting to the cancer-specific biomarkers (Figure 2.4a) [25]. Bioconjugated QDs in their study also allowed excellent detection sensitivity and multicolour imaging in living animals (Figure 2.4b-d), demonstrating a potential of QDs in the multiplexed and high-sensitivity cancer imaging [25]. When coated with surface species such as polymer, liposome or silica, QDs can also be applied as drug vehicle to carry therapeutic contents for cancer treatment [26-29]. Nonetheless, due to the innate toxicity of QDs, reports on QD-based drug delivery vehicles are scarce.

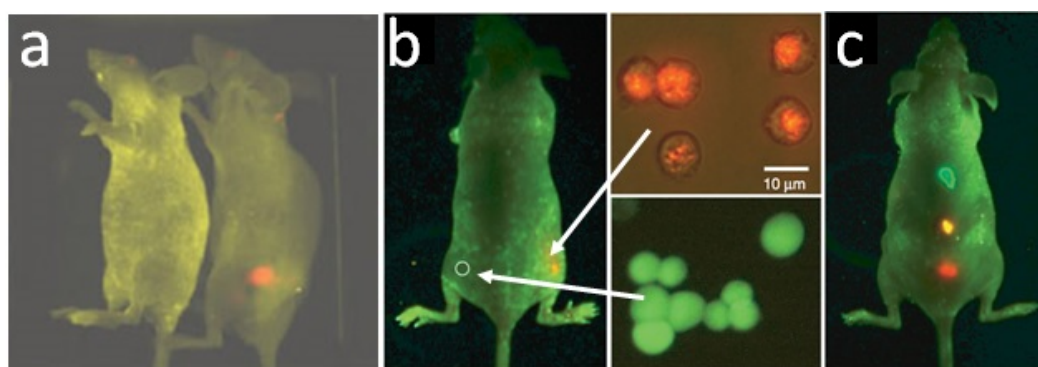


**Figure 2. 4** (a) *In vivo* imaging of antibody conjugated QDs accumulating in the prostate tumour. (b) Comparison of the imaging sensitivity of QDs and green fluorescence proteins. QD-tagged cancer cells (orange coloured) and GFP-transfected cancer cells (green coloured) were subcutaneously implanted into the same mouse. (c) Imaging of QD-encoded microbeads injected into three sites of a mouse. [25]

The potential toxic effect of quantum QDs presents a key shortfall that limits their applications in theranostics. The toxicity of QDs majorly originates from the leakage of component ions (*e.g.* Cd, Se, and Te) in cells [30]. On the cellular level, these ions can be leached out from degraded QDs, and induce the formation of reactive oxygen species that will cause cell death by affecting mitochondria, inducing apoptosis, and damaging DNA [31]. The cytotoxicity of QDs depends on several factors [32], (i) the physicochemical properties of QDs including QD size, particle charge, stability, and

surface coatings; (ii) QD dosage and exposure concentration; (iii) routes of exposures. In order to reduce the cytotoxicity of QDs, strategies have been employed to coat the toxic core with a protective ZnS layer [33], cap QD with bio-safe PEG polymers [34], or replace the toxic elements with no-toxic components [35]. Nonetheless, the metabolism and degradation of QDs within the body is still largely unknown and the associated toxic hazard remains a problem for the usage of QDs in biomedical applications.

### 2.2.3 Carbon Nanomaterials

Carbon nanomaterials, including fluorescent carbon nanoparticles, carbon nanotubes (CNTs), fullerenes, graphenes, graphene oxides, nanodiamonds, carbon nanohorns, and carbon nanocaps are intrinsic photoluminescent materials that have gained significant research attention due to outstanding physical properties. Because of the  $\pi$ -electron cloud and associated unique electronic configurations of a carbon, carbon nanomaterials exhibit fascinating physiochemical properties that offer substantial benefits in a wide range of applications. These materials are typically characterised by a broad bandgap, which can enable photoluminescence properties rendering optical contrast for biological imaging. For example, polymer-functionalized multiple-wall (MWNT) and single-wall (SWNT) carbon nanotubes are strongly photoluminescent in both organic and aqueous solutions, exhibiting broad photoluminescence emission bands spanning from visible to NIR region (Figure 2.5) [36]. In addition, carbon nanomaterials have generally very well developed surface area and some of them are hollow structure materials, which entails considerable loading capacity for therapeutic cargo delivery in cancer therapy applications.

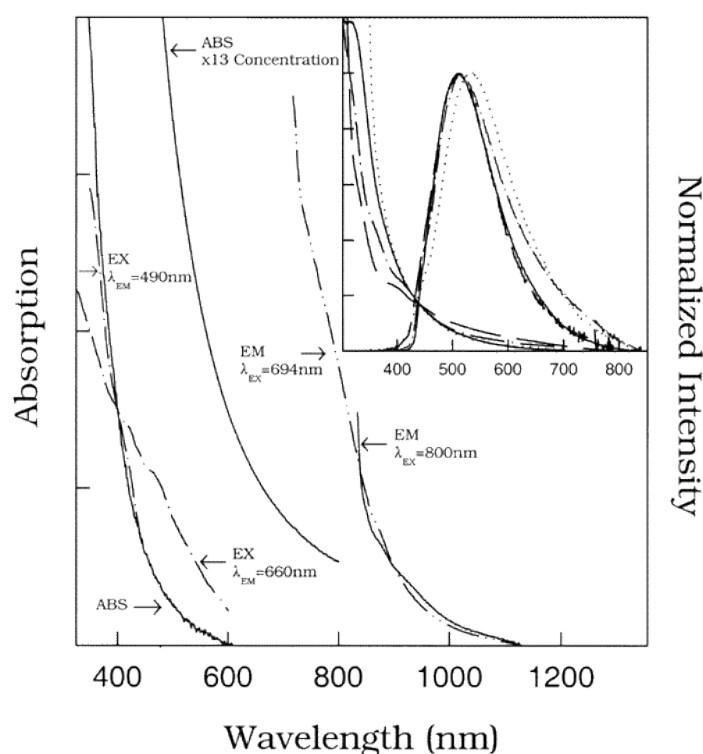


**Figure 2. 5** Absorption (ABS), photoluminescence (EM), and photoluminescence excitation (EX) spectra of the poly(propionylethylenimine-co-ethylenimine) (PPEI-EI) coated MWNT and SWNT in chloroform at room temperature. Inset: a comparison of the absorption and photoluminescence (excitation, 440 nm) spectra of PPEI-EI-MWNT (solid line) and PPEI-EI-SWNT (dashed line) suspended in chloroform at room temperature. [36]

Carbon nanomaterials can be synthesized by chemical vapour deposition, laser ablation, ball milling, and carbonisation of carbohydrates [37-40]. As-produced carbon nanoparticles are mostly hydrophobic and not amenable for bioconjugation. Further chemical and physical processes are employed to endow carbon nanomaterials with improved water dispersibility and biology-friendly surface functional groups. Among these approaches, reacting the surface hydrophobic moieties with amphiphilic molecules, or chemical functionalization like oxidation and cycloaddition lead to hydrophilization of carbon nanomaterials. At the same time, the  $\pi$ -electron-rich surface of carbon nanomaterials can be used to carry hydrophobic drugs via  $\pi$ - $\pi$  stacking. For example, an anti-tumour drug doxorubicin was reported to load on the surface of graphene oxide by the noncovalent  $\pi$ - $\pi$  interaction [41].

Besides their drug delivery applications in cancer therapy, carbon nanomaterials, such as carbon nanotubes, graphenes, graphene oxides, fullerenes, and carbon nanohorns have

demonstrated exceptional photothermal responsivity and photosensitized production of oxidative stress in cancer cells. These types of nanomaterials are promising therapeutic agents in photodynamic and photothermal therapy of cancer. For instance, Dai *et al.* have reported high performance of SWNTs to *in vivo* suppression of a tumour by the photothermal pathway using low-intensity NIR laser irradiation ( $0.6 \text{ W/cm}^2$ ) [42]. Zhang and co-workers explored the production of reactive oxygen species (ROS) by SWNTs and their potential application for *in vivo* cancer photodynamic therapy [43]. As-produced SWNTs were converted to the hydrophilic phase by covalent conjugation with polyethyleneimine (PEI) and non-covalent coating with polyvinylpyrrolidone k30 (PVPk30) (Figure 2.6a and b) [43]. Their study has shown that, when irradiated with a halogen lamp, cell-internalized CNTs (coated with polymers) were capable of inhibiting the tumour growth by effective generation of ROS (Figure 2.6c) [43]. In addition, histological analysis of the tumour tissues confirmed that no damage was observed in the tumour tissues of all control groups but marked apoptotic and necrotic tumour cells were found in the SWNT-PEI plus illumination treatment group [43].

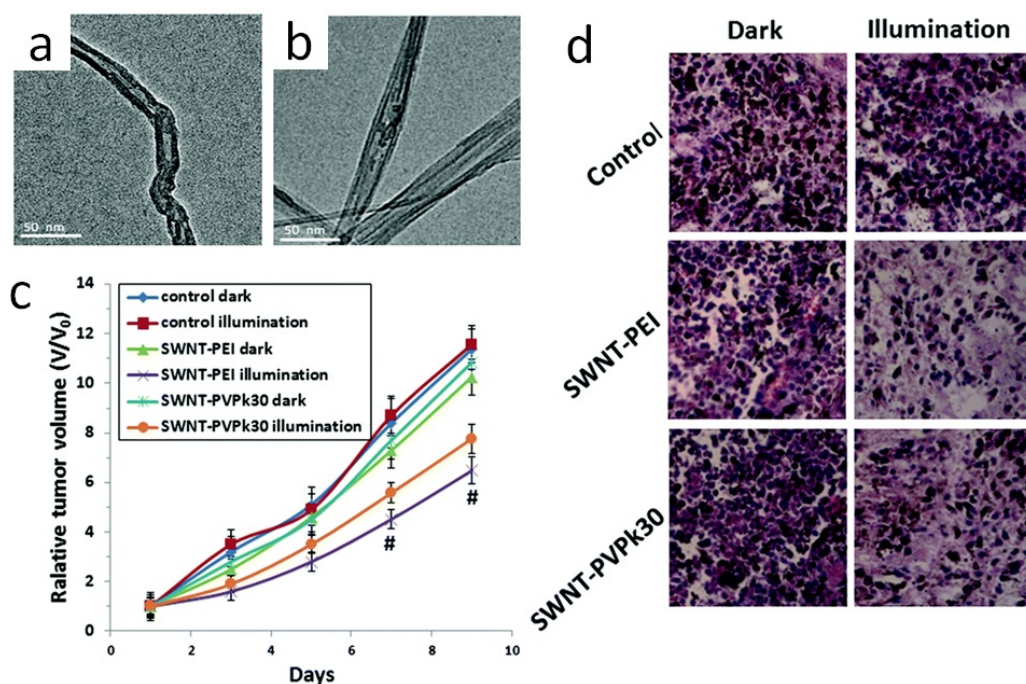


**Figure 2. 6** TEM images of (a) SWNT-PEI and (b) SWNT-PVPk30. (c) Tumour volume measurement of laboratory mice in several groups for a time interval of 10 days, following the intratumoral injection of the nanoparticles. (d) Images of hematoxylin and eosin-stained tumour tissues harvested from the mice after the treatments. [43]



### 2.2.4 Gold Nanoparticles

A number of unique physiochemical properties of gold nanoparticles, such as water-solubility, chemical stability, biological inertness, strong surface plasmon absorption, tuneable colour, and ease of modification, have made them appealing nanomaterials for biomedical applications. Gold nanoparticles exhibit size- and shape-dependent optical properties [44]. Gold nanospheres have characteristic absorption at 500–600 nm [45, 46], whereas gold nanorods exhibit maximum absorption in the spectral range of 600–1100 nm, as a function of the aspect ratio (Figure 2.7 a-b) [47]. Increasing the nanosphere size or elongating the nanorods will lead to a red-shift of the surface plasmon absorption peak (Figure 2.7 a-b) [44, 48-50]. On the other hand, gold nanoparticles exhibit size-dependent resonance absorption, when exposed to light of a specific wavelength – termed plasmonic resonance. This anomalously high plasmonic absorption renders gold nanoparticles optically bright due to the enhanced scattering of light. At the same time, the energy of the absorbed photons produce heat in virtue of the phonon relaxation, which can be used for photothermal therapy [51, 52]. In this regard, NIR-absorbing gold nanorods, nanocages and nanoshells have been developed and applied in non-invasive photothermal cancer therapies by converting the innocuous NIR light into thermal energy [53].

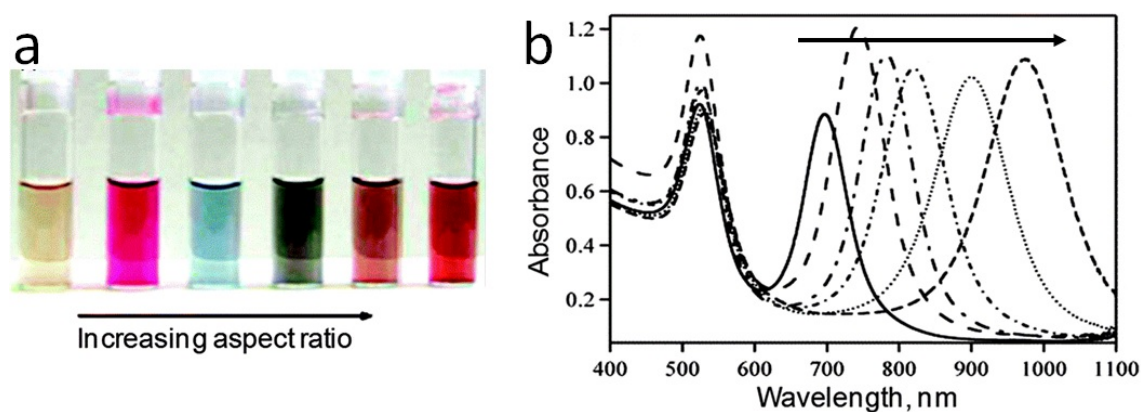


**Figure 2. 7** (a) Photographs of gold nanoparticle colloidal suspensions. The first sample on the left is 4-nm gold nanospheres, with the nanoparticle aspect ratio progressively increased from left to right [48]. (b) UV-visible absorption spectra of gold nanorods of the following lengths: (1)  $108 \pm 7$  nm, (2)  $89 \pm 7$  nm, (3)  $75 \pm 6$  nm, (4)  $73 \pm 4$  nm, (5)  $61 \pm 5$  nm, and (6)  $46 \pm 6$  nm [49].

Since the uptake rate of gold nanoparticles is so high in various applications of the life sciences, a number of synthetic approaches have been developed for preparation of high-quality gold nanoparticles [54, 55]. The fabrication is generally conducted in an aqueous

phase, where gold salt (chloroauric acid) is reduced into gold atoms and form different shapes of nanoparticles, using reducing agents, such as sodium borohydride, citrate acid, and ascorbic acid [54, 56, 57]. Surfactants are employed, as the capping agents in the synthesis to control the nanocrystal growth and stabilize nanoparticles in the colloidal suspensions [58]. Since gold is characterised by strong interaction with thiol, the surface of gold nanoparticles can be readily modified with thiol derivatives to couple the particles with biological molecules. Thiolated species (like thiol-labelled oligonucleotide) can also be directly tethered to gold nanoparticle surface [59].

Although gold nanoparticles have shown tremendous promise, as the contrast agents in MRI and CT, fluorescence of gold nanoparticles is relatively weak, limiting their application scope in optical imaging of cancers. Impact factors, such as the particle size and surface capping ligands have been investigated and optimized to enhance gold nanoparticle fluorescence [60, 61], yet the imaging contrast is not sufficient for high-sensitivity biomedical imaging. Two-photon excitation implemented by means of ultrashort-pulse femtosecond laser excitation was used to counter the low fluorescence quantum yield of gold nanoparticles [62]. For example, Xia and co-workers used the two-photon microscopy to examine the targeting efficiency of anti-EGFR (epidermal growth factor receptors) conjugated gold nanocages to EGFR-overexpressing cancer cells [63]. The developed nanocages exhibited a broad photoluminescence emission band from 450 nm to 650 nm under the two-photon excitation at 800 nm (Figure 2.8a) [63] and were clearly visualized under two-photon optical imaging [63]. At the same time, reports on the applications of gold nanoparticles, as photothermal agents in cancer treatment, are more numerous in scientific literature. As an example, Choi and co-workers prepared targeted gold nanorods by conjugating as-synthesised particles with cetuximab (CET) for image-guided photothermal therapy of cancer [64]. Since these gold nanorods had strong absorption at 800 nm, their targeting ability could be confirmed by using NIR absorption imaging technique (Figure 2.8b) [64]. Additionally, the nanocomposites demonstrated excellent potential of photothermal destroying tumours in an animal model, evidenced by the tissue damage in comparison with the control group, without the photothermal treatment (Figure 2.8c) [64].



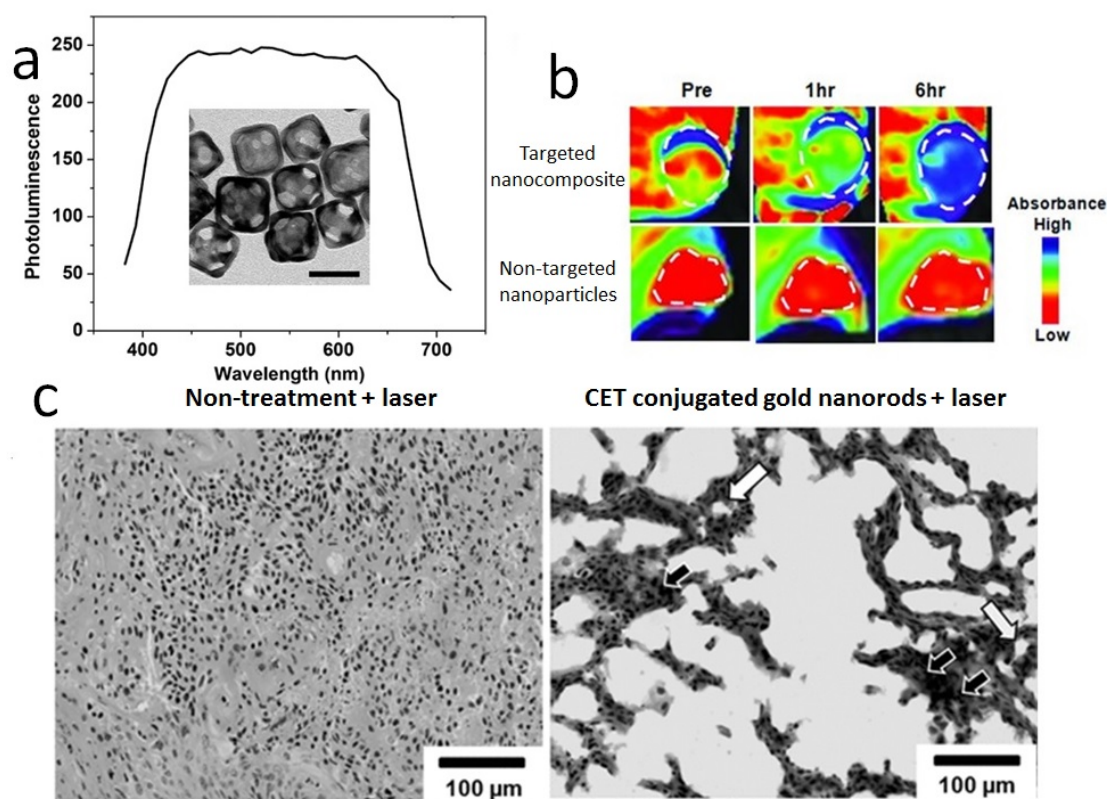


**Figure 2. 8** (a) A photoluminescence spectrum of Au nanocages (~50 nm). Inset shows an TEM image of the gold nanocages. Scale bar, 50 nm. [63] (b) *In vivo* NIR absorption pseudo-colour images of tumour tissues after an intravenous injection of CET conjugated gold nanorods and non-targeted gold nanorods. White dashed circles demarcate the tumour regions. [64] (c) Silver staining eosin of tumour tissues with and without photothermal treatment. [64]

### 2.3 Limitations of the Existing Photoluminescent Nanoparticles in Current Theranostics

PL nanoparticles discussed above provide a lucrative platform for design and testing of theranostic agents for cancer detection and treatment. They allow convenient and versatile integration of therapeutic and targeting capabilities. Studies have demonstrated their promise in biological imaging and targeted drug delivery. At the same time, most of the existing photoluminescent nanomaterials are not ideal for biomedical imaging and therapy. Photostability is one the limitations typical to several important classes of PL nanoparticles. For example, fluorescent dyes encapsulated in silica nanoparticles suffer from rapid photobleaching and low photostability, which preclude time-lapse microscopy, imaging of molecular trafficking and whole-animal imaging for prolonged time intervals [65, 66]. Secondly, the optical contrast of the state-of-the-art PL nanoparticles

overviewed here is limited. This limitation stems from the short-wavelength excitation of PL nanoparticles using UV or visible light, which results in the concomitant excitation of the biological tissues, resulting into unwanted autofluorescence. In addition to the back-scattered excitation light bleeding through the detection path optical filters, this elicited autofluorescence generates a hefty background, which oftentimes lowers the detection sensitivity from the PL probes. Thirdly, UV/visible excitation and/or emission light exhibit low penetration depth (*e.g.* 60  $\mu\text{m}$  at 365 nm increasing up to several mm for far-red light at 650 nm) in biological samples due to the considerable tissue absorption and scattering. These preclude the use of PL nanoparticles for *in vivo* whole animal imaging and most of the clinical imaging applications. Additionally, in case of light-induced therapeutic nanosystems where high-intensity activation is required, the prolonged exposure of UV and visible excitation light causes severe photodamage to nucleic acids, cells, and tissues in living organisms [67, 68]. Potential phototoxicity, especially in the UV range poses a challenge for the realization of nanotheranostics in practical applications.

The use of near infrared (NIR) excitation light to elicit photoluminescence in nanoparticles provides a lucrative opportunity to overcome the shortcomings, as outlined in the previous paragraph. It is well-known that biological tissues have an optical transparency window in the spectral range of 700–1300 nm, where light is minimally absorbed and scattered by biological tissue [69]. Since NIR light falls into the biological transparency window, it penetrates deeper (measured in centimetres) and excites considerably less autofluorescence and exerts less phototoxicity compared to UV and visible light. It is noted that NIR-assisted multiphoton excitation has been applied in the optical imaging of dyes, QDs, carbon nanomaterials, and gold nanoparticles to achieve increased resolution and higher imaging depth [70-73]. Nonetheless, NIR two-photon absorption cross-sections of these nanoparticles is sufficient only at the very large values of the excitation intensity measured in  $\text{mW}/\text{cm}^2$ , and widespread applications of the two-photon microscopy is thus largely hampered.

The limitations of the existing PL nanoparticles prompted the development of a new type of NIR excitable PL nanoparticles, which can be illuminated with a relatively low-cost continuous-wave NIR laser, generating bright photoluminescence and exhibit good

photostability. These critical requirements have pointed to the adoption of upconversion nanoparticles, which are emerging as the next-generation of photoluminescent nanomaterials for bioimaging. In the following section, the composition and structure, upconversion photoluminescence, optical properties, and cytotoxicity of upconversion nanoparticles will be briefly described.

## 2.4 Upconversion Nanoparticles (UCNPs)

Upconversion nanoparticles represent an inorganic nanocrystal host co-doped with trivalent lanthanide ions. The upconversion refers to a non-linear optical process in which the nanoparticle sequentially absorbs two or more low-energy NIR photons and emits a high-energy photon of the shorter wavelength (UV, visible, or NIR). In contrast with the multiphoton process used to excite organic fluorescent dyes or other PL nanoparticles [74], the absorption of photons in UCNPs occurs via a real energy level, not a virtual level as in the case of the multiphoton excitation [75]. In comparison with the virtual energy level mediated photon absorption, the upconversion process is several orders of magnitude more efficient, thus allowing the nanoparticles to be excited by low-cost continuous-wave lasers at a low excitation intensities (typically, 1-1000 W/cm<sup>2</sup>) [76]. This upconversion process provides UCNPs with unique optical properties that are unattainable in conventional optical probes, making them particularly well-suited for applications in theranostics.

### 2.4.1 Composition and Structure

Lanthanide-doped UCNPs are comprised of three key components, a host matrix to embed the lanthanide dopants in; a sensitizers or absorbers to harvest NIR light; and activators or emitters to produce upconversion photoluminescence. Figure 2.9a illustrates the composition of a typical UCNP. The selection of the host matrix is critical as it determines the doping level and the network of lanthanide ions, hence largely influences the spectral properties and emission efficiency of UCNPs. In order to reduce the lattice stress and achieve high doping levels, the lattice of the host should match that of the dopant ions. To this aim, inorganic compounds of lanthanide ions such as oxides, phosphates and fluorides are good choices, since the lanthanide ions have similar ionic sizes as that of the dopants. Additionally, the host materials are generally required to have low phonon energies to ensure the high conversion of NIR to upconversion emission,

since such a host induces a minimal non-radiative energy loss during the upconversion process. Compared to the other hosts, fluoride-based matrix, such as sodium yttrium fluoride ( $\text{NaYF}_4$ ), possesses relatively lower phonon energy ( $\sim 350\text{ cm}^{-1}$ ), and is therefore regarded as an optimal host material for the design of upconversion nanoparticles.

The popular hosts  $\text{NaREF}_4$  ( $\text{RE} = \text{Y}$  or  $\text{Gd}$ ) are known to be crystallized in either cubic or hexagonal phases during UCNP synthesis, whereas the hexagonal phase is regarded more stable thermodynamically (Figure 2.9b and c) [77]. A transition from the cubic to hexagonal phases can be achieved via heating treatment (such as annealing). The cubic and hexagonal phase UCNPs possess different photoluminescent properties, as attributed to the different interaction of lanthanide ions in these two crystal structures. For example,  $\text{Er}^{3+}$ -doped UCNPs of the cubic phase exhibited relatively more intense red emission, while the particles of the hexagonal phase displayed dominant green emission [78]. Additionally, the emission intensity of lanthanide ions in the hexagonal phase has been reported to be at least one order of magnitude greater than that in the cubic phase [79]. In fact, hexagonal-phase  $\text{NaYF}_4$  ( $\beta\text{-NaYF}_4$ ) is the most efficient up-to-date host materials for green- and blue-emitting upconversion nanoparticles [80]. Therefore, upconversion nanoparticles produced for this thesis study is based on  $\beta\text{-NaYF}_4$ .

The upconversion emission originates from the energy absorption and transfer process among lanthanide dopants. As such, the wavelength and emission intensity of UCNPs are essentially determined by the selection of dopants and their doping concentrations. Among many lanthanide ions,  $\text{Yb}^{3+}$  ion is often used as the sensitizer/absorber due to its large absorption cross-section in the NIR spectral region. 20-30% doping ratios of  $\text{Yb}^{3+}$  is an optimal choice in UCNP production protocols.  $\text{Er}^{3+}$ ,  $\text{Tm}^{3+}$ ,  $\text{Ho}^{3+}$  ions are typically co-doped with  $\text{Yb}^{3+}$  and used as the efficient activators/emitters to generate discrete emission bands in the overall photoluminescent spectrum (Figure 2.9d) [81]. These activating ions feature discrete ladder-like energy level structure that facilitates the photon absorption and energy transfer process for generating the upconversion emission. The doping level of the activators is usually kept as low as  $\sim 2\%$ , and precisely controlled to avoid the excitation energy loss due to the concentration-associated quenching (cross-relaxation) effects [82]. In the study reported here,  $\text{NaYF}_4\text{:}18\%\text{Yb}, 2\%\text{Er}$  UCNPs were prepared and explored.

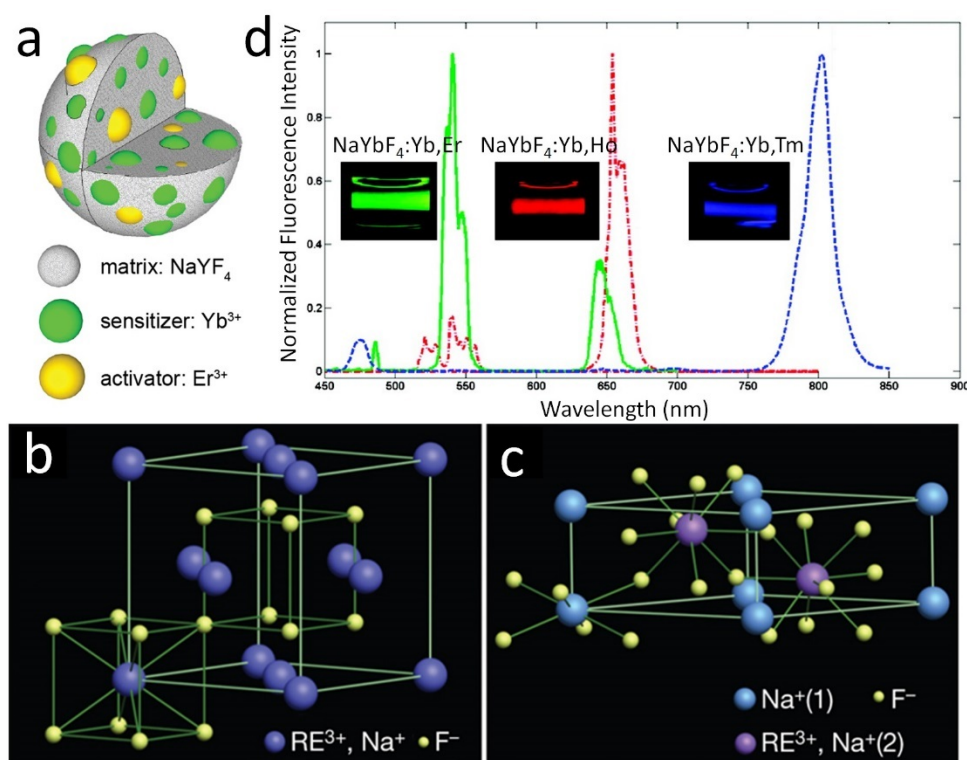


**Figure 2. 9** (a) Schematic illustration of a UCNP composed of a NaYF<sub>4</sub> host, Yb<sup>3+</sup> ions as the sensitizers and Er<sup>3+</sup> ions as the activators [83]. (b) Cubic and (c) hexagonal phase of NaYF<sub>4</sub> crystal structures [77]. (d) NIR-excited photoluminescent spectra of NaYbF<sub>4</sub>:Yb,Er, NaYbF<sub>4</sub>:Yb,Ho, NaYbF<sub>4</sub>:Yb,Tm UCNP in colloidal suspensions [81].

### 2.4.2 Upconversion Photoluminescence

The upconversion photoluminescence process takes place via a combination of several complex optical pathways, such as ground state absorption, excited state absorption, and energy transfer. In a simplified upconversion process, an incoming NIR photon pumps the sensitizer ion from its ground state to an excited state from which a non-radiative energy transfer to the neighbouring activator ion takes place, and promotes it to an intermediate excited state. Another incoming NIR photon stimulates the sequential process of the non-radiative energy transfer, resulting in the same activator ion being transferred to the higher excited state. Following the energy transfer, the sensitizer ions relax to their ground state, while the activator ion at its higher excited state undergoes non-radiative relaxation to the lower energy states, followed by radiative decays with characteristic upconversion emission and eventually returning to its ground state. The upconversion process for NaYF<sub>4</sub>:Yb,Er UCNP and its optical spectrum are shown in Figure 2.10. The energy level <sup>2</sup>F<sub>5/2</sub> of the Yb<sup>3+</sup> dopants is resonant with the <sup>4</sup>I<sub>11/2</sub> level of

$\text{Er}^{3+}$ , enabling efficient energy transfer between these two ions. In addition,  $\text{Er}^{3+}$  ions have multiple excited states with exceptionally long lifetime (hundreds of microseconds to milliseconds), allowing sequential absorption of multiple photons. Eventually,  $\text{Er}^{3+}$  ions emit strong upconversion photoluminescence centring in green and red colour bands of the spectrum (522, 541, and 658 nm) attributed to the  $^2\text{H}_{11/2}$ ,  $^4\text{S}_{3/2} \rightarrow ^4\text{I}_{15/2}$  and  $^4\text{F}_{9/2} \rightarrow ^4\text{I}_{15/2}$  transitions, respectively. The intense upconversion visible emission from  $\text{NaYF}_4:\text{Yb},\text{Er}$  renders it a valuable PL nanomaterial for biomedical imaging, as well as a prominent energy donor in energy transfer-based applications.

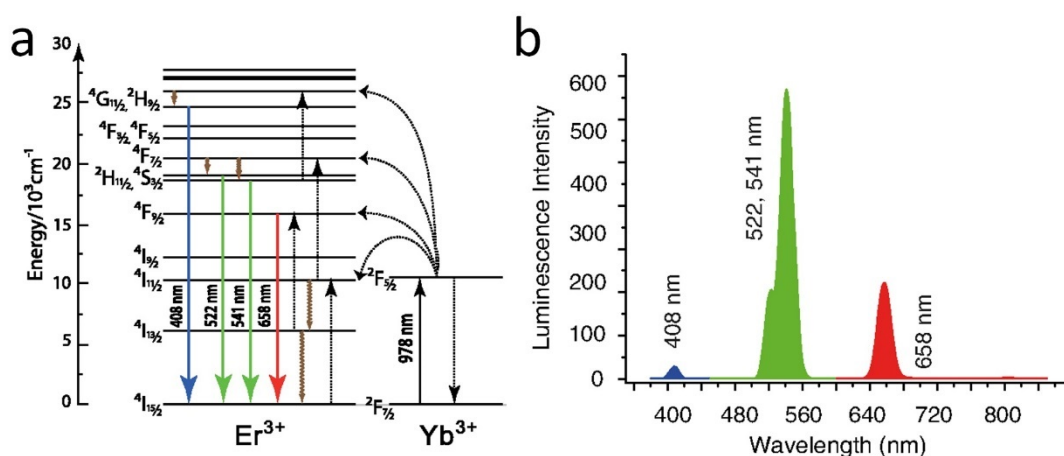


**Figure 2. 10** (a) Detailed energy level diagram of  $\text{NaYF}_4:\text{Yb},\text{Er}$ . (b) Photoluminescence spectrum of  $\text{NaYF}_4:\text{Yb},\text{Er}$  UCNPs. Reproduced from Ref. [84].

## 2.4.3 Optical Properties

### 2.4.3.1 Large Anti-Stokes Shift and Narrow Multicolour Emission

In general, fluorescence emitters rely on a single photon excitation occurring in UV or visible spectral range to produce emission with the lower photon energies, the process known as Stokes emission. In contrast, upconversion nanoparticles sequentially absorb two or more low-energy photons at the higher wavelength (*e.g.* 980 nm) producing anti-Stokes emission at the shorter wavelength (UV, visible, and NIR emission). This multiphoton process results in the large anti-Stokes shift (up to 500 nm) between the excitation and emission wavelengths, allowing more efficient and easy separation of the photoluminescence and excitation light. Additionally, the emission peaks of UCNPs are narrow-band in comparison with the conventional photoluminescent nanoparticles, with the emission bandwidths being typically  $\sim 20$  nm. The narrow emission of lanthanide ions

is attributed to their unique electronic configurations  $4f^n 5s^2 5p^6$  ( $n = 0-14$ ), in which 5s and 5p electrons in the subshells provide strong shielding on the inner 4f electrons from the surrounding host lattice [85]. As a consequence, the influence of the host lattice on optical transitions occurring within the 4f-shell is insignificant, leading to the generation of narrow emission peaks [85]. Meanwhile, UCNPs are characterized by a unique set of distinguishable emission peaks. These multicolour peaks are narrow and featured, usually excited simultaneously using a single NIR continuous-wave excitation source. Hence, the multicolour property of UCNPs is particularly useful in multiplexed encoding and biological labelling. This property is harnessed by means of engineering UCNPs with more pronounced spectral features of choice, culminating in monochromatic UCNP. Labelling biological structures with such narrow-band quasi-monochromatic UCNP allows simultaneous acquisition of several molecular species, potentially leading to the greater multiplexing/demultiplexing imaging.

#### ***2.4.3.2 Tuneable Upconversion Luminesce***

The capability of manipulating the output colour is another fascinating property of UCNPs, especially when the nanoparticles are used as a donor in the energy transfer-mediated application or in multicolour imaging. To date, various approaches have been developed to control the emission colour and spectroscopic profiles of UCNPs, such as varying the host lattices [86], controlling the doping composition [87] and concentration [88], and exploiting the core-shell structure [89]. For example, Liu and co-workers have reported a versatile method to elaborately tune the output colour of  $\text{NaYF}_4:\text{Yb,Er}$  by varying the doping concentrations of  $\text{Yb}^{3+}$  and  $\text{Er}^{3+}$  (Figure 2.11a and c7-8) and controlling the combination of  $\text{Tm}^{3+}$  and  $\text{Er}^{3+}$  (Figure 2.11b and c1-6) [87]. The  $\text{NaYF}_4:\text{Yb,Er}$  system exhibited an overall yellow colour due to the integration of blue, red, and blue emissions. By increasing the concentration of  $\text{Yb}^{3+}$ , the energy transferred from  $\text{Er}^{3+}$  back to  $\text{Yb}^{3+}$  was increased, resulted in the decrease of blue and green emission, thus the colour display of UCNPs can be tailored from yellow to red (Figure 2.11c7-10) [87]. Moreover, adding the second emitter with variable concentrations to the nanoparticles enabled the generation of an additional set of characteristic emissions with different relative intensities. Based on the colour balance of the dual emissions from the two emitters, a tuneable colour output was demonstrated [87] [90].



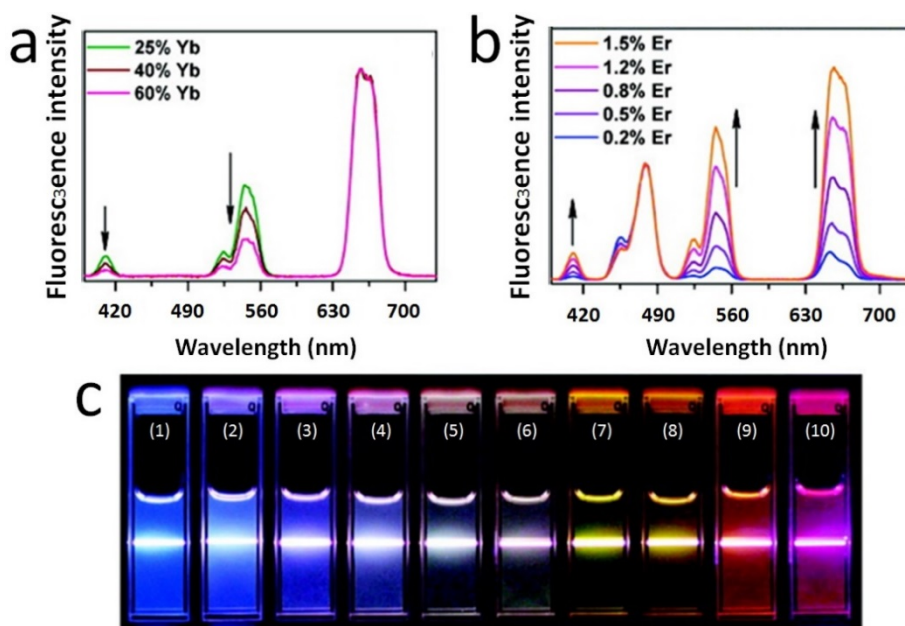


**Figure 2. 11** (a) NIR-excited photoluminescence spectra of NaYF<sub>4</sub>:Yb,Er UCNPs doped with different concentrations of Yb<sup>3+</sup> (25–60 mol%). (b) NIR-excited photoluminescence spectra of NaYF<sub>4</sub>:Yb,Tm,Er doped with different concentrations of Er<sup>3+</sup>. (0.2–1.5 mol %) (c) Photographs of (1) NaYF<sub>4</sub>:20%Yb,0.2%Tm, (2-6) NaYF<sub>4</sub>:20%Yb,0.2%Tm co-doped with different concentrations of Er<sup>3+</sup> (0.2–1.5 mol %), and (7-10) NaYF<sub>4</sub>:2%Er co-doped with different concentrations of Yb<sup>3+</sup> (18–60 mol %). The samples were excited with a 980-nm NIR laser. Reproduced from Ref. [87].

#### 2.4.3.3 Background-free Deep Tissue Imaging

Capabilities for the background-free and deep tissue imaging are the most compelling reasons for development of UCNP in photoluminescence-assisted optical imaging. In optical imaging, light travelling through biological tissues undergoes multiple events of absorption and scattering that will contribute to the attenuation of the light. The absorption is mainly caused by molecules such as haemoglobin (Hb), oxyhaemoglobin (HbO<sub>2</sub>) in the blood (Figure 2.12) – in UV/visible part of the spectrum; and water – in the NIR. The scattering process takes place on the boundaries between optical interfaces, being more efficient on high refractive-index structures, including lipids, melanin, etc. This attenuation effect is minimal when using light at the wavelength range from 700 nm to 1300 nm, hence this region is identified, as a biological tissue transparency window. The characteristic excitation of a particular type of UCNP, Tm-doped UCNP at 980 nm and its NIR emission at ~800 nm fall into this window, thus minimising the effects of absorption and scattering. Therefore, NIR-emitting UCNP are considered advantageous for deep-tissue imaging. Additionally, the autofluorescence from biological samples is



greatly eliminated due to the NIR excitation. As a result, a high contrast of UCNP can be detected in small animal imaging.

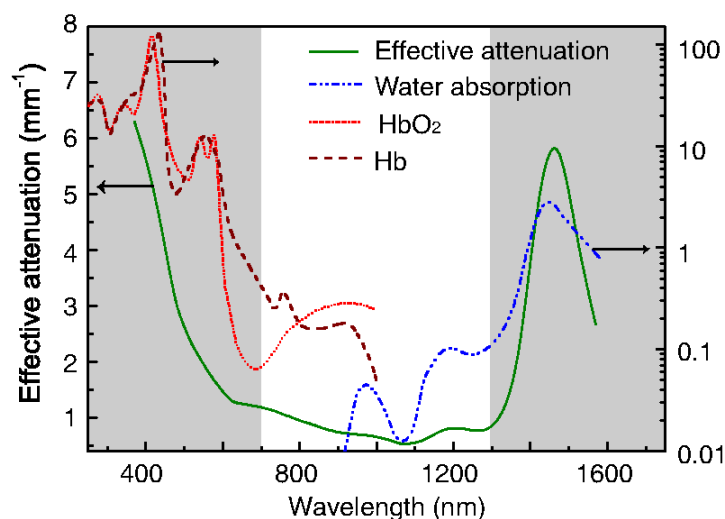


**Figure 2. 12** Effective attenuation spectra of skin tissue (green solid line) originated from the absorption and scattering effect of water (blue dashed line), Hb (brown dashed line), HbO<sub>2</sub> (red solid line). A biological transparency window ranging from 700 to 1300 nm is boundary marked against the grey-shaded area. Reproduced from [84].

#### 2.4.3.4 Superb Photostability

UCNP emission under continuous-wave excitation appeared to be extremely photostable, exhibiting nor photobleaching (typical for organic dyes), nor photoblinking (typical for QDs) is another feature that makes this PL material attractive as high optical contrast probes in biological imaging. Photostability refers to the ability of an emitter to reside in the excited state for repeated cycles of the excitation and emission. The cessation of the emission, also termed photobleaching, is resulted from the photochemical alteration of the fluorescent molecules. For example, a single fluorescent dye molecule (*e.g.* Rhodamine 6G) typically survives about 1 million excitation-emission cycles, followed by transition to a triplet metastable state from where it reacts with neighbouring molecules. As a result, the fluorescent molecule undergoes an irreversible transition to the dark state manifested by the cessation of the fluorescence. In ensemble, this is manifested by gradual decrease of the fluorescence signal upon cw excitation. Fluorescence intermittency or blinking is another imaging problem observed with fluorescent dyes and quantum dots that limits their application at the single molecule label. Alternatively, studies on the photostability of a single UCNPs have shown virtually no photobleaching of the particle

during the 1-h of continuous illumination with a 10-mW 980-nm laser (Figure 2.13a and b), suggesting the feasibility of UCNPs for repetitive and long-term imaging. In addition, UCNPs displayed no blinking behaviour at timescales down to 1 ms (Figure 2.13c and d), rendering them attractive tools for *in vitro* and *in vivo* single-molecule tracking.

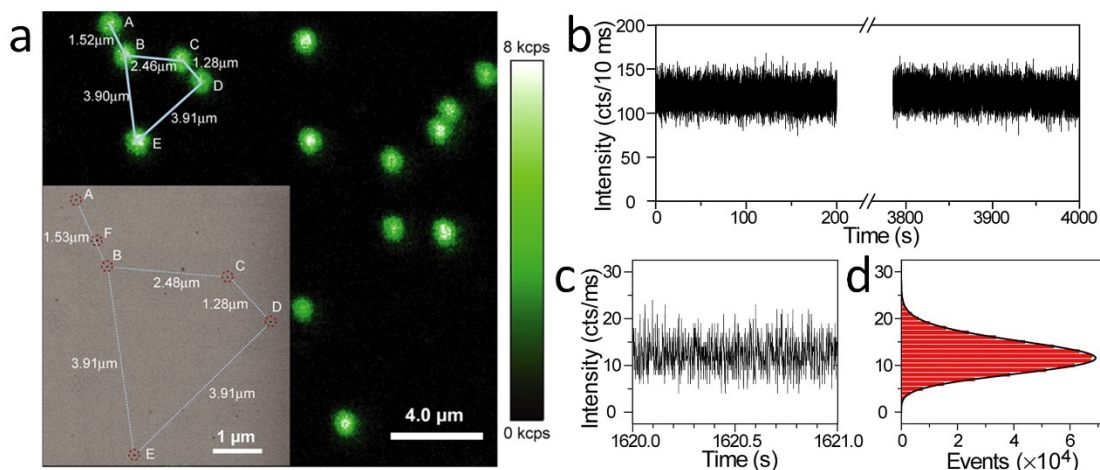


**Figure 2.13** (a) Confocal microscopy image of individual UCNPs on a silicon nitride membrane. (b) The time trace of emission intensity from a single UCNP under continuous laser illumination for more than 1 h. (c) The zoom-in time trace of emission intensity, showing no blinking behaviour. (d) The histogram of emission intensity of (c). Reproduced from [91].

#### 2.4.3.5 Long Photoluminescence Lifetime

Driving towards ultrahigh-sensitivity optical imaging is met by introduction of alternative strategies in addition of the conventional spectral filtration of the spectrally-separated emission light. A promising strategy to discriminate the excitation and emission light makes use time-gated detection approach. This technique makes use the difference between the photoluminescence lifetimes ( $\tau$ ) of fluorescent probes and fluorescent organic compounds. The time-gating is implemented by setting a time delay (microsecond-scale) between the trailing edge of an excitation pulse illuminating a biological specimen labelled with long- $\tau$  PL nanoparticles and a start of the photodetection. The time delay is chosen to allow the short-lived autofluorescence and excitation light to fade away, so that only the persistent PL light is photo-detected. Due to the unique electronic configuration of lanthanide ions, UCNPs are usually characterized by long photoluminescent lifetimes (tens to hundreds of microseconds), which are greatly longer than that of the background autofluorescence (nanoseconds). This optical property allows the feasibility of implementing UCNPs in time-gated

fluorescence imaging to eliminate the background noises and visualize UCNPs with the improved contrast ratios. The principle of using UCNPs in the time-gated technique is illustrated in Figure 2.14 [92]. *In vitro* and *in vivo* studies of the time-gated imaging of UCNPs have demonstrated a significant enhancement in the contrast, as compared to the conventional photoluminescence detection employing the spectral filtration [93-96]. Taken together, in-depth background-free UCNP-aided optical imaging has paved new paths for high-sensitivity optical imaging of superficial pathology lesions, as well as single molecule trafficking on obscuring biological background.

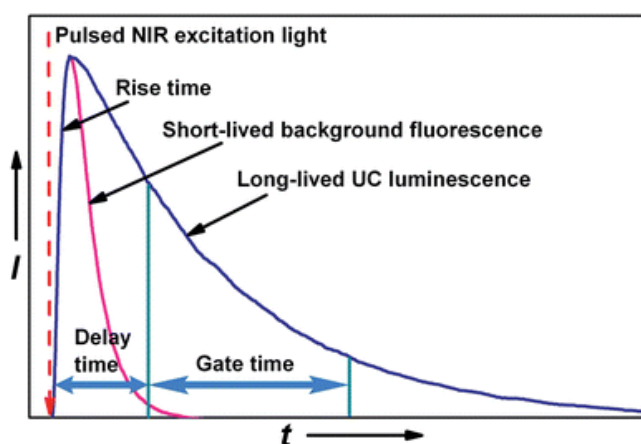


**Figure 2. 14** The time-resolved photoluminescence lifetime of NIR excitation light, short-lived background autofluorescence, and long-lived upconversion (UC) luminescence. Reproduced from Ref. [92].

#### 2.4.4 Cytotoxicity

Toxic and cytotoxic properties of nanoparticles measured by their potential effects on cells and biological tissues/organisms are essential considerations for their applications in biomedicine. Accordingly, prior to the biological applications of UCNPs, systematic studies have been performed to evaluate the biocompatibility and long-term toxicity of nanoparticles *in vitro* and *in vivo*. The most common *in vitro* evaluation of UCNP cytotoxicity is viability assays, which assess the overall dosage-dependent toxicity of nanoparticles on cells, evaluating an impact of nanoparticles exerted on the cell phenotype, survival rate, and proliferation, following the nanoparticle treatment. These standard assays involve the use of thiazolyl blue tetrazolium bromide (MTT), 3-(4,5-dimethylthiazol-2-yl)-5-(3-carboxymethoxyphenyl)-2-(4-sulfophenyl)-2H-tetrazolium (MTS), and cell counting CCK-8 to observe changes in the mitochondrial functions of cells. Cytotoxicity assessment is carried out using several types of human cancer and

normal cell lines. It is generally held that the cytotoxicity of UCNPs is negligible, especially at the dosage below 400  $\mu\text{g/mL}$  [97], the concentration of which is much higher than the dosing regimen for a typical cellular experiment. It is also noted that the surface chemistry of UCNPs has a significant effect on the particle cytotoxicity, even to the extent that they predominantly determine the cytotoxicity of UCNP. The correlation of the nanoparticle uptake and cytotoxicity level is another worthwhile aspect of this study. For example, the positively charged UCNPs are generally more toxic than negatively and neutrally charged UCNPs on cells (Figure 2.15a) [98]. *In vivo* toxicity studies of UCNPs are based on observation of the animal behaviour, measurement of the animal weight, histological and haematological examination on the animal organs, and analysis of the serum biochemistry. Up to now, no noticeable *in vivo* toxicity has been observed regardless the surface coatings of UCNPs [97]. *In vivo* toxicity evaluation in zebrafish embryos demonstrated that UCNPs exhibited ten times lower toxicity than QDs [99], evidencing the safer option of using UCNPs, as PL probes. Li and co-workers investigated toxic effects of the UCNPs injection (15 mg/kg) *in vivo* in mice for 115 days and reported no adverse influence of UCNPs on the tested animals (Figure 2.15b-c) [100]. As seen from Figure 2.15c, the tissue structures of organs from the treated mice were hardly different from the control groups without nanoparticle injection, suggesting no toxic effect was observed. Overall, the current *in vitro* and *in vivo* toxicology studies have indicated good biocompatibility and low toxicity of UCNPs, which is encouraging for the exploration of their applications in biomedicine.

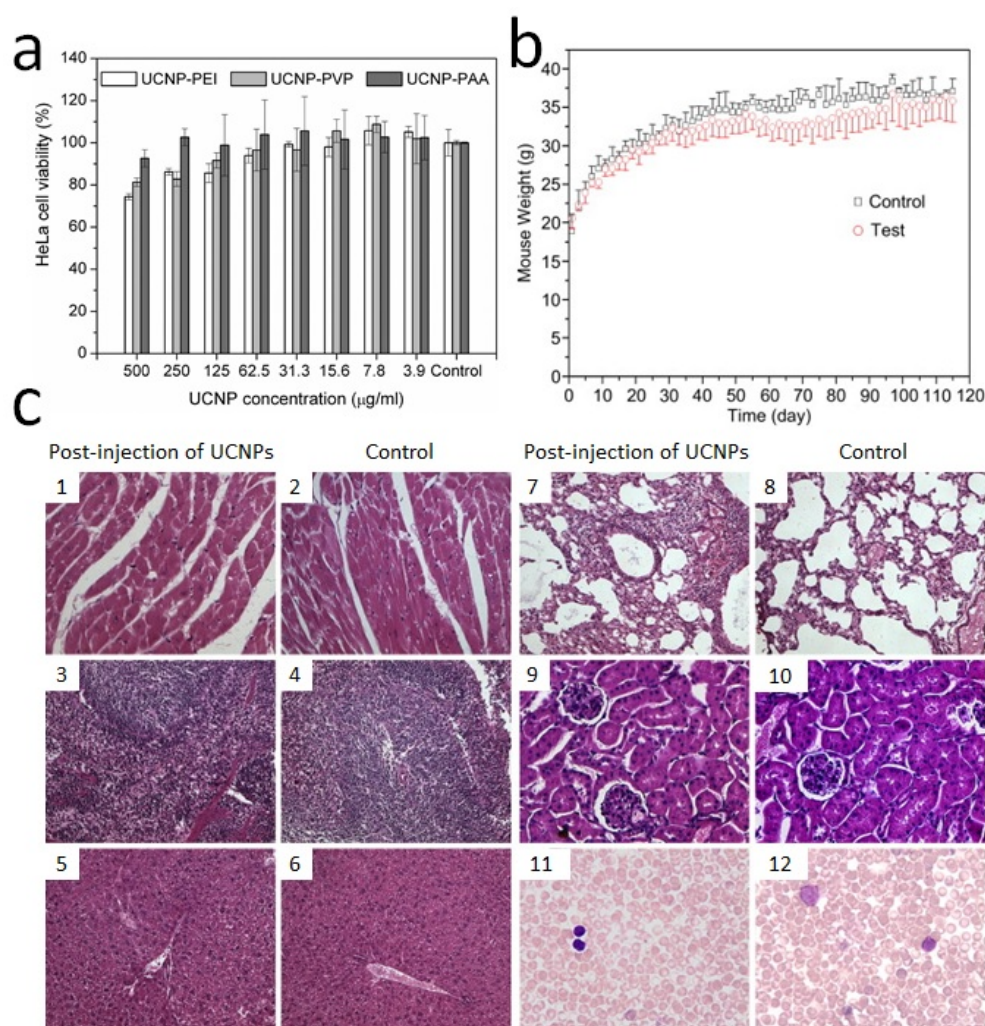


**Figure 2.15** (a) Cell viability of HeLa cells after treating with positively charged PEI coated UCNPs (PEI-UCNPs), negatively charged polyacrylic acid coated UCNPs (PAA-UCNPs) and neutrally charged polyvinylpyrrolidone coated UCNPs (PVP-UCNPs) for 24 h. The concentration of the nanoparticles ranged from 3.9 to 500 µg/mL. [98] (b) Measurement of mice body weight after intravenous injection of PAA-UCNPs (15 mg/kg) (test) and without injection (control). [100] (c) H&E stained tissue sections from mice after intravenous injection of PAA-UCNPs for 115 days and control without particles injection. The organ tissues were harvested from heart (1, 2), spleen (3, 4), liver (5, 6), lung (7, 8), kidney (9, 10) and blood smear (11, 12). [100]

## 2.5 References

1. Herranz, M. and A. Ruibal, *Optical imaging in breast cancer diagnosis: the next evolution*. Journal of oncology, 2012. **2012**.
2. Hadjipanayis, C.G., H. Jiang, D.W. Roberts, and L. Yang. *Current and future clinical applications for optical imaging of cancer: from intraoperative surgical guidance to cancer screening*. in *Seminars in oncology*. 2011. Elsevier.

3. Lu, J., M. Liong, Z. Li, J.I. Zink, and F. Tamanoi, *Biocompatibility, biodistribution, and drug - delivery efficiency of mesoporous silica nanoparticles for cancer therapy in animals*. Small, 2010. **6**(16): p. 1794-1805.
4. Zhang, H., D. Yee, and C. Wang, *Quantum dots for cancer diagnosis and therapy: biological and clinical perspectives*. Nanomedicine, 2008. **3**(1): p. 83-91.
5. Liu, Z. and X.-J. Liang, *Nano-carbons as theranostics*. Theranostics, 2012. **2**(3): p. 235-237.
6. Conde, J., G. Doria, and P. Baptista, *Noble metal nanoparticles applications in cancer*. Journal of drug delivery, 2011. **2012**.
7. Ha, S.-W., C.E. Camalier, G.R. Beck Jr, and J.-K. Lee, *New method to prepare very stable and biocompatible fluorescent silica nanoparticles*. Chemical Communications, 2009(20): p. 2881-2883.
8. Mader, H., X. Li, S. Saleh, M. Link, P. Kele, and O.S. Wolfbeis, *Fluorescent silica nanoparticles*. Annals of the New York Academy of Sciences, 2008. **1130**(1): p. 218-223.
9. Ow, H., D.R. Larson, M. Srivastava, B.A. Baird, W.W. Webb, and U. Wiesner, *Bright and stable core-shell fluorescent silica nanoparticles*. Nano letters, 2005. **5**(1): p. 113-117.
10. Wolfbeis, O.S., *An overview of nanoparticles commonly used in fluorescent bioimaging*. Chemical Society Reviews, 2015. **44**(14): p. 4743-4768.
11. Jana, N.R., C. Earhart, and J.Y. Ying, *Synthesis of water-soluble and functionalized nanoparticles by silica coating*. Chemistry of Materials, 2007. **19**(21): p. 5074-5082.
12. Farrer, R.A., F.L. Butterfield, V.W. Chen, and J.T. Fourkas, *Highly efficient multiphoton-absorption-induced luminescence from gold nanoparticles*. Nano Letters, 2005. **5**(6): p. 1139-1142.
13. Stöber, W., A. Fink, and E. Bohn, *Controlled growth of monodisperse silica spheres in the micron size range*. Journal of colloid and interface science, 1968. **26**(1): p. 62-69.
14. Trewyn, B.G., I.I. Slowing, S. Giri, H.-T. Chen, and V.S.-Y. Lin, *Synthesis and functionalization of a mesoporous silica nanoparticle based on the sol-gel process and applications in controlled release*. Accounts of Chemical Research, 2007. **40**(9): p. 846-853.
15. Vivero-Escoto, J.L., R.C. Huxford-Phillips, and W. Lin, *Silica-based nanoprobes for biomedical imaging and theranostic applications*. Chemical Society Reviews, 2012. **41**(7): p. 2673-2685.
16. He, X., X. Wu, K. Wang, B. Shi, and L. Hai, *Methylene blue-encapsulated phosphonate-terminated silica nanoparticles for simultaneous in vivo imaging and photodynamic therapy*. Biomaterials, 2009. **30**(29): p. 5601-5609.
17. Qian, J., D. Wang, F. Cai, Q. Zhan, Y. Wang, and S. He, *Photosensitizer encapsulated organically modified silica nanoparticles for direct two-photon photodynamic therapy and in vivo functional imaging*. Biomaterials, 2012. **33**(19): p. 4851-4860.
18. Kim, S., B. Fisher, H.-J. Eisler, and M. Bawendi, *Type-II quantum dots: CdTe/CdSe (core/shell) and CdSe/ZnTe (core/shell) heterostructures*. Journal of the American Chemical Society, 2003. **125**(38): p. 11466-11467.
19. Jamieson, T., R. Bakhshi, D. Petrova, R. Pocock, M. Imani, and A.M. Seifalian, *Biological applications of quantum dots*. Biomaterials, 2007. **28**(31): p. 4717-4732.
20. Smith, A.M., H. Duan, A.M. Mohs, and S. Nie, *Bioconjugated quantum dots for in vivo molecular and cellular imaging*. Advanced drug delivery reviews, 2008. **60**(11): p. 1226-1240.
21. Murray, C., D.J. Norris, and M.G. Bawendi, *Synthesis and characterization of nearly monodisperse CdE (E= sulfur, selenium, tellurium) semiconductor nanocrystallites*. Journal of the American Chemical Society, 1993. **115**(19): p. 8706-8715.



22. Michalet, X., F. Pinaud, T.D. Lacoste, M. Dahan, M.P. Bruchez, A.P. Alivisatos, and S. Weiss, *Properties of fluorescent semiconductor nanocrystals and their application to biological labeling*. *Single Molecules*, 2001. **2**(4): p. 261-276.
23. Wang, J., S. Han, D. Ke, and R. Wang, *Semiconductor quantum dots surface modification for potential cancer diagnostic and therapeutic applications*. *Journal of Nanomaterials*, 2012. **2012**: p. 1.
24. Bruchez, M., M. Moronne, P. Gin, S. Weiss, and A.P. Alivisatos, *Semiconductor nanocrystals as fluorescent biological labels*. *science*, 1998. **281**(5385): p. 2013-2016.
25. Gao, X., Y. Cui, R.M. Levenson, L.W. Chung, and S. Nie, *In vivo cancer targeting and imaging with semiconductor quantum dots*. *Nature biotechnology*, 2004. **22**(8): p. 969-976.
26. Pan, J., Y. Liu, and S.-S. Feng, *Multifunctional nanoparticles of biodegradable copolymer blend for cancer diagnosis and treatment*. *Nanomedicine*, 2010. **5**(3): p. 347-360.
27. Bagalkot, V., L. Zhang, E. Levy-Nissenbaum, S. Jon, P.W. Kantoff, R. Langer, and O.C. Farokhzad, *Quantum dot-aptamer conjugates for synchronous cancer imaging, therapy, and sensing of drug delivery based on bi-fluorescence resonance energy transfer*. *Nano letters*, 2007. **7**(10): p. 3065-3070.
28. Qi, L. and X. Gao, *Quantum dot- amphipol nanocomplex for intracellular delivery and real-time imaging of siRNA*. *ACS nano*, 2008. **2**(7): p. 1403-1410.
29. Zrazhevskiy, P., M. Sena, and X. Gao, *Designing multifunctional quantum dots for bioimaging, detection, and drug delivery*. *Chemical Society Reviews*, 2010. **39**(11): p. 4326-4354.
30. Rzigalinski, B.A. and J.S. Strobl, *Cadmium-containing nanoparticles: perspectives on pharmacology and toxicology of quantum dots*. *Toxicology and applied pharmacology*, 2009. **238**(3): p. 280-288.
31. Winnik, F.M. and D. Maysinger, *Quantum dot cytotoxicity and ways to reduce it*. *Accounts of chemical research*, 2012. **46**(3): p. 672-680.
32. Hardman, R., *A toxicologic review of quantum dots: toxicity depends on physicochemical and environmental factors*. *Environmental health perspectives*, 2006: p. 165-172.
33. Kirchner, C., T. Liedl, S. Kudera, T. Pellegrino, A. Muñoz Javier, H.E. Gaub, S. Stölzle, N. Fertig, and W.J. Parak, *Cytotoxicity of colloidal CdSe and CdSe/ZnS nanoparticles*. *Nano letters*, 2005. **5**(2): p. 331-338.
34. Ballou, B., B.C. Lagerholm, L.A. Ernst, M.P. Bruchez, and A.S. Waggoner, *Noninvasive imaging of quantum dots in mice*. *Bioconjugate chemistry*, 2004. **15**(1): p. 79-86.
35. Winkler, J., P. Martin-Killias, A. Plückthun, and U. Zangemeister-Wittke, *EpCAM-targeted delivery of nanocomplexed siRNA to tumour cells with designed ankyrin repeat proteins*. *Molecular Cancer Therapeutics*, 2009. **8**(9): p. 2674-2683.
36. Riggs, J.E., Z. Guo, D.L. Carroll, and Y.-P. Sun, *Strong luminescence of solubilized carbon nanotubes*. *Journal of the American Chemical Society*, 2000. **122**(24): p. 5879-5880.
37. Journet, C., M. Picher, and V. Jourdain, *Carbon nanotube synthesis: from large-scale production to atom-by-atom growth*. *Nanotechnology*, 2012. **23**(14): p. 142001.
38. Yudasaka, M., S. Iijima, and V.H. Crespi, *Single-wall carbon nanohorns and nanocones*, in *Carbon nanotubes*. 2007, Springer. p. 605-629.
39. Mochalin, V.N., O. Shenderova, D. Ho, and Y. Gogotsi, *The properties and applications of nanodiamonds*. *Nature nanotechnology*, 2012. **7**(1): p. 11-23.
40. Kumar, M. and Y. Ando, *Chemical vapor deposition of carbon nanotubes: a review on growth mechanism and mass production*. *Journal of nanoscience and nanotechnology*, 2010. **10**(6): p. 3739-3758.

41. Yang, X., X. Zhang, Z. Liu, Y. Ma, Y. Huang, and Y. Chen, *High-efficiency loading and controlled release of doxorubicin hydrochloride on graphene oxide*. The Journal of Physical Chemistry C, 2008. **112**(45): p. 17554-17558.
42. Robinson, J.T., K. Welsher, S.M. Tabakman, S.P. Sherlock, H. Wang, R. Luong, and H. Dai, *High performance in vivo near-IR ( $> 1 \mu\text{m}$ ) imaging and photothermal cancer therapy with carbon nanotubes*. Nano research, 2010. **3**(11): p. 779-793.
43. Wang, L., J. Shi, R. Liu, Y. Liu, J. Zhang, X. Yu, J. Gao, C. Zhang, and Z. Zhang, *Photodynamic effect of functionalized single-walled carbon nanotubes: a potential sensitizer for photodynamic therapy*. Nanoscale, 2014. **6**(9): p. 4642-4651.
44. Zheng, J., C. Zhang, and R.M. Dickson, *Highly fluorescent, water-soluble, size-tunable gold quantum dots*. Physical Review Letters, 2004. **93**(7): p. 077402.
45. Henglein, A., *Radiolytic preparation of ultrafine colloidal gold particles in aqueous solution: optical spectrum, controlled growth, and some chemical reactions*. Langmuir, 1999. **15**(20): p. 6738-6744.
46. Pastoriza-Santos, I. and L.M. Liz-Marzán, *Formation of PVP-protected metal nanoparticles in DMF*. Langmuir, 2002. **18**(7): p. 2888-2894.
47. Zhu, J., K.-T. Yong, I. Roy, R. Hu, H. Ding, L. Zhao, M.T. Swihart, G.S. He, Y. Cui, and P.N. Prasad, *Additive controlled synthesis of gold nanorods (GNRs) for two-photon luminescence imaging of cancer cells*. Nanotechnology, 2010. **21**(28): p. 285106.
48. Murphy, C.J., A.M. Gole, S.E. Hunyadi, J.W. Stone, P.N. Sisco, A. Alkilany, B.E. Kinard, and P. Hankins, *Chemical sensing and imaging with metallic nanorods*. Chemical Communications, 2008(5): p. 544-557.
49. Hu, M., X. Wang, G.V. Hartland, P. Mulvaney, J.P. Juste, and J.E. Sader, *Vibrational response of nanorods to ultrafast laser induced heating: theoretical and experimental analysis*. Journal of the American Chemical Society, 2003. **125**(48): p. 14925-14933.
50. Palmal, S. and N.R. Jana, *Gold nanoclusters with enhanced tunable fluorescence as bioimaging probes*. Wiley Interdisciplinary Reviews: Nanomedicine and Nanobiotechnology, 2014. **6**(1): p. 102-110.
51. Hutter, E. and J.H. Fendler, *Exploitation of localized surface plasmon resonance*. Advanced Materials, 2004. **16**(19): p. 1685-1706.
52. Pissuwan, D., S.M. Valenzuela, and M.B. Cortie, *Therapeutic possibilities of plasmonically heated gold nanoparticles*. TRENDS in Biotechnology, 2006. **24**(2): p. 62-67.
53. Choi, J., J. Yang, E. Jang, J.-S. Suh, Y.-M. Huh, K. Lee, and S. Haam, *Gold nanostructures as photothermal therapy agent for cancer*. Anti-Cancer Agents in Medicinal Chemistry (Formerly Current Medicinal Chemistry-Anti-Cancer Agents), 2011. **11**(10): p. 953-964.
54. Sun, Y. and Y. Xia, *Shape-controlled synthesis of gold and silver nanoparticles*. Science, 2002. **298**(5601): p. 2176-2179.
55. Grzelczak, M., J. Pérez-Juste, P. Mulvaney, and L.M. Liz-Marzán, *Shape control in gold nanoparticle synthesis*. Chemical Society Reviews, 2008. **37**(9): p. 1783-1791.
56. Kimling, J., M. Maier, B. Okenve, V. Kotaidis, H. Ballot, and A. Plech, *Turkevich method for gold nanoparticle synthesis revisited*. The Journal of Physical Chemistry B, 2006. **110**(32): p. 15700-15707.
57. Jana, N.R., L. Gearheart, and C.J. Murphy, *Seed-mediated growth approach for shape-controlled synthesis of spheroidal and rod-like gold nanoparticles using a surfactant template*. Advanced Materials, 2001. **13**(18): p. 1389.
58. Xiao, J. and L. Qi, *Surfactant-assisted, shape-controlled synthesis of gold nanocrystals*. Nanoscale, 2011. **3**(4): p. 1383-1396.
59. Maxwell, D.J., J.R. Taylor, and S. Nie, *Self-assembled nanoparticle probes for recognition and detection of biomolecules*. Journal of the American Chemical Society, 2002. **124**(32): p. 9606-9612.



60. Wu, Z. and R. Jin, *On the ligand's role in the fluorescence of gold nanoclusters*. Nano letters, 2010. **10**(7): p. 2568-2573.
61. Shang, L., S. Dong, and G.U. Nienhaus, *Ultra-small fluorescent metal nanoclusters: synthesis and biological applications*. Nano Today, 2011. **6**(4): p. 401-418.
62. Tcherniak, A., S. Dominguez-Medina, W.-S. Chang, P. Swanglap, L.S. Slaughter, C.F. Landes, and S. Link, *One-photon plasmon luminescence and its application to correlation spectroscopy as a probe for rotational and translational dynamics of gold nanorods*. The Journal of Physical Chemistry C, 2011. **115**(32): p. 15938-15949.
63. Au, L., Q. Zhang, C.M. Cobley, M. Gidding, A.G. Schwartz, J. Chen, and Y. Xia, *Quantifying the cellular uptake of antibody-conjugated Au nanocages by two-photon microscopy and inductively coupled plasma mass spectrometry*. ACS nano, 2009. **4**(1): p. 35-42.
64. Choi, J., J. Yang, D. Bang, J. Park, J.S. Suh, Y.M. Huh, and S. Haam, *Targetable gold nanorods for epithelial cancer therapy guided by near - IR absorption imaging*. Small, 2012. **8**(5): p. 746-753.
65. Resch-Genger, U., M. Grabolle, S. Cavaliere-Jaricot, R. Nitschke, and T. Nann, *Quantum dots versus organic dyes as fluorescent labels*. Nature methods, 2008. **5**(9): p. 763-775.
66. Eggeling, C., J. Widengren, R. Rigler, and C. Seidel, *Photobleaching of fluorescent dyes under conditions used for single-molecule detection: Evidence of two-step photolysis*. Analytical Chemistry, 1998. **70**(13): p. 2651-2659.
67. Sortino, S., *Photoactivated nanomaterials for biomedical release applications*. Journal of Materials Chemistry, 2012. **22**(2): p. 301-318.
68. Min, Y., J. Li, F. Liu, E.K. Yeow, and B. Xing, *Near - Infrared Light - Mediated Photoactivation of a Platinum Antitumor Prodrug and Simultaneous Cellular Apoptosis Imaging by Upconversion - Luminescent Nanoparticles*. Angewandte Chemie, 2014. **126**(4): p. 1030-1034.
69. Prasad, P.N., *Introduction to biophotonics*. 2004: John Wiley & Sons.
70. Durr, N.J., T. Larson, D.K. Smith, B.A. Korgel, K. Sokolov, and A. Ben-Yakar, *Two-photon luminescence imaging of cancer cells using molecularly targeted gold nanorods*. Nano letters, 2007. **7**(4): p. 941-945.
71. Ohulchanskyy, T.Y., I. Roy, K.T. Yong, H.E. Pudavar, and P.N. Prasad, *High - resolution light microscopy using luminescent nanoparticles*. Wiley Interdisciplinary Reviews: Nanomedicine and Nanobiotechnology, 2010. **2**(2): p. 162-175.
72. Yong, K.-T., J. Qian, I. Roy, H.H. Lee, E.J. Bergey, K.M. Tramposch, S. He, M.T. Swihart, A. Maitra, and P.N. Prasad, *Quantum rod bioconjugates as targeted probes for confocal and two-photon fluorescence imaging of cancer cells*. Nano letters, 2007. **7**(3): p. 761-765.
73. Li, J.L., H.C. Bao, X.L. Hou, L. Sun, X.G. Wang, and M. Gu, *Graphene Oxide Nanoparticles as a Nonbleaching Optical Probe for Two - Photon Luminescence Imaging and Cell Therapy*. Angewandte Chemie International Edition, 2012. **51**(8): p. 1830-1834.
74. He, G.S., P.P. Markowicz, T.-C. Lin, and P.N. Prasad, *Observation of stimulated emission by direct three-photon excitation*. Nature, 2002. **415**(6873): p. 767-770.
75. Auzel, F., *Upconversion and anti-stokes processes with f and d ions in solids*. Chemical reviews, 2004. **104**(1): p. 139-174.
76. Heer, S., K. Kömpe, H.U. Güdel, and M. Haase, *Highly Efficient Multicolour Upconversion Emission in Transparent Colloids of Lanthanide - Doped NaYF<sub>4</sub> Nanocrystals*. Advanced Materials, 2004. **16**(23 - 24): p. 2102-2105.
77. Wang, F., Y. Han, C.S. Lim, Y. Lu, J. Wang, J. Xu, H. Chen, C. Zhang, M. Hong, and X. Liu, *Simultaneous phase and size control of upconversion nanocrystals through lanthanide doping*. Nature, 2010. **463**(7284): p. 1061-1065.

78. Park, Y.I., S.H. Nam, J.H. Kim, Y.M. Bae, B. Yoo, H.M. Kim, K.-S. Jeon, H.S. Park, J.S. Choi, and K.T. Lee, *Comparative study of upconverting nanoparticles with various crystal structures, core/shell structures, and surface characteristics*. The Journal of Physical Chemistry C, 2013. **117**(5): p. 2239-2244.
79. Krämer, K.W., D. Biner, G. Frei, H.U. Güdel, M.P. Hehlen, and S.R. Lüthi, *Hexagonal sodium yttrium fluoride based green and blue emitting upconversion phosphors*. Chemistry of Materials, 2004. **16**(7): p. 1244-1251.
80. Haase, M. and H. Schäfer, *Upconverting nanoparticles*. Angewandte Chemie International Edition, 2011. **50**(26): p. 5808-5829.
81. Zhan, Q., J. Qian, H. Liang, G. Somesfalean, D. Wang, S. He, Z. Zhang, and S. Andersson-Engels, *Using 915 nm laser excited Tm<sup>3+</sup>/Er<sup>3+</sup>/Ho<sup>3+</sup>-doped NaYbF<sub>4</sub> upconversion nanoparticles for in vitro and deeper in vivo bioimaging without overheating irradiation*. ACS nano, 2011. **5**(5): p. 3744-3757.
82. Vetrone, F., J.-C. Boyer, J.A. Capobianco, A. Speghini, and M. Bettinelli, *Significance of Yb<sup>3+</sup> concentration on the upconversion mechanisms in codoped Y<sub>2</sub>O<sub>3</sub>: Er<sup>3+</sup>, Yb<sup>3+</sup> nanocrystals*. Journal of Applied Physics, 2004. **96**: p. 661-667.
83. Nadort, A., V.K. Sreenivasan, Z. Song, E.A. Grebenik, A.V. Nechaev, V.A. Semchishen, V.Y. Panchenko, and A.V. Zvyagin, *Quantitative imaging of single upconversion nanoparticles in biological tissue*. PLoS One, 2013. **8**(5): p. 1-13.
84. Song, Z., Y.G. Anissimov, J. Zhao, A.V. Nechaev, A. Nadort, D. Jin, T.W. Prow, M.S. Roberts, and A.V. Zvyagin, *Background free imaging of upconversion nanoparticle distribution in human skin*. Journal of Biomedical Optics, 2013. **18**(6): p. 061215.
85. Werts, M.H., *Making sense of lanthanide luminescence*. Science progress, 2005. **88**(2): p. 101-131.
86. Zhao, J., Z. Lu, Y. Yin, C. McRae, J.A. Piper, J.M. Dawes, D. Jin, and E.M. Goldys, *Upconversion luminescence with tunable lifetime in NaYF<sub>4</sub>: Yb, Er nanocrystals: role of nanocrystal size*. Nanoscale, 2013. **5**(3): p. 944-952.
87. Wang, F. and X. Liu, *Upconversion multicolor fine-tuning: visible to near-infrared emission from lanthanide-doped NaYF<sub>4</sub> nanoparticles*. Journal of the American Chemical Society, 2008. **130**(17): p. 5642-5643.
88. Lu, Y., J. Zhao, R. Zhang, Y. Liu, D. Liu, E.M. Goldys, X. Yang, P. Xi, A. Sunna, and J. Lu, *Tunable lifetime multiplexing using luminescent nanocrystals*. Nature Photonics, 2014. **8**(1): p. 32-36.
89. Wang, F., R. Deng, J. Wang, Q. Wang, Y. Han, H. Zhu, X. Chen, and X. Liu, *Tuning upconversion through energy migration in core-shell nanoparticles*. Nature Materials, 2011. **10**(12): p. 968-973.
90. Zhang, F., Q. Shi, Y. Zhang, Y. Shi, K. Ding, D. Zhao, and G.D. Stucky, *Fluorescence upconversion microbarcodes for multiplexed biological detection: nucleic acid encoding*. Advanced Materials, 2011. **23**(33): p. 3775-3779.
91. Wu, S., G. Han, D.J. Milliron, S. Aloni, V. Altoe, D.V. Talapin, B.E. Cohen, and P.J. Schuck, *Non-blinking and photostable upconverted luminescence from single lanthanide-doped nanocrystals*. Proceedings of the National Academy of Sciences, 2009. **106**(27): p. 10917-10921.
92. Wang, F., D. Banerjee, Y. Liu, X. Chen, and X. Liu, *Upconversion nanoparticles in biological labeling, imaging, and therapy*. Analyst, 2010. **135**(8): p. 1839-1854.
93. Zheng, X., X. Zhu, Y. Lu, J. Zhao, W. Feng, G. Jia, F. Wang, F. Li, and D. Jin, *High-contrast visualization of upconversion luminescence in mice using time-gating approach*. Analytical chemistry, 2016. **88**(7): p. 3449-3454.
94. Zhang, L., X. Zheng, W. Deng, Y. Lu, S. Lechevallier, Z. Ye, E.M. Goldys, J.M. Dawes, J.A. Piper, and J. Yuan, *Practical implementation, characterization and applications of a multi-colour time-gated luminescence microscope*. Scientific reports, 2014. **4**: p. 6597.

95. Ju, Q., Y. Liu, D. Tu, H. Zhu, R. Li, and X. Chen, *Lanthanide - Doped Multicolor GdF<sub>3</sub> Nanocrystals for Time - Resolved Photoluminescent Biodetection*. Chemistry–A European Journal, 2011. **17**(31): p. 8549-8554.
96. Tu, D., L. Liu, Q. Ju, Y. Liu, H. Zhu, R. Li, and X. Chen, *Time - Resolved FRET Biosensor Based on Amine - Functionalized Lanthanide - Doped NaYF<sub>4</sub> Nanocrystals*. Angewandte Chemie International Edition, 2011. **50**(28): p. 6306-6310.
97. Gnach, A., T. Lipinski, A. Bednarkiewicz, J. Rybka, and J.A. Capobianco, *Upconverting nanoparticles: assessing the toxicity*. Chemical Society Reviews, 2015. **44**(6): p. 1561-1584.
98. Jin, J., Y.-J. Gu, C.W.-Y. Man, J. Cheng, Z. Xu, Y. Zhang, H. Wang, V.H.-Y. Lee, S.H. Cheng, and W.-T. Wong, *Polymer-coated NaYF<sub>4</sub>: Yb<sup>3+</sup>, Er<sup>3+</sup> upconversion nanoparticles for charge-dependent cellular imaging*. ACS nano, 2011. **5**(10): p. 7838-7847.
99. Jang, G.H., M.P. Hwang, S.Y. Kim, H.S. Jang, and K.H. Lee, *A systematic in-vivo toxicity evaluation of nanophosphor particles via zebrafish models*. Biomaterials, 2014. **35**(1): p. 440-449.
100. Xiong, L., T. Yang, Y. Yang, C. Xu, and F. Li, *Long-term in vivo biodistribution imaging and toxicity of polyacrylic acid-coated upconversion nanophosphors*. Biomaterials, 2010. **31**(27): p. 7078-7085.

# 3

## **Synthesis, Design and Applications of UCNPs in Theranostics**

In this chapter, the synthesis and design of UCNP-based biofunctional nanocomposites, and their applications in cancer theranostics are reviewed. The chapter includes the following sections: Section 1 describes currently developed strategies for preparing UCNPs; Section 2 addresses methods of the surface passivation for enhancing the upconversion emission of UCNPs; Section 3 summarizes surface engineering techniques in converting hydrophobic UCNPs into hydrophilic and bioconjugation of UCNPs with biomolecules. In particular, such surface modification approaches, as ligand exchange, surface silanization, and biomolecular cross-linking methods are more relevant to this work and hence covered in more details in this thesis. Section 4 discusses methods of coupling UCNPs with therapeutic agents. Section 5 provides an overview of the advanced studies in applications of UCNPs in cancer imaging and treatment.

### **3.1 Synthesis Strategy**

Among various types of host materials, lanthanide fluorides, such as  $\text{LnF}_3$ ,  $\text{LnOF}$ , and  $\text{MLnF}_n$  ( $M = \text{Li, Na, K or Ba}$ ;  $n = 4 \text{ or } 5$ ) are regarded as ideal host matrices to produce efficient upconversion nanocrystals, because of the high chemical stability and low phonon energy. Considering that, a number of synthesis methods have been developed to prepare lanthanide fluoride-based UCNPs with controlled size, shape, crystalline phase, and composition that presents desirable physiochemical properties for their potential applications. The most common synthesis methods are divided into three major groups and described below.

### 3.1.1 Thermal Decomposition

Thermal decomposition is a well-established method for the synthesis of monodispersed UCNPs with uniformed shape, tailored size and single crystal structure. This strategy is based on the decomposition of organometallic precursors in the presence of organic solvents (*e.g.* 1-octadecane, ODE) and surfactants (*e.g.* oleic acid, OA, and oleylamine, OM). The commonly used precursors include metallic or lanthanide trifluoroacetate, lanthanide oleates, lanthanide acetates, and lanthanide chlorides. The surfactants usually contain a functional group to cap the surface of UCNPs for controlling their growth and a long hydrocarbon chain to assist their dispersion in organic solvents. In general, the synthetic process is conducted at elevated temperature (250–330 °C) in an oxygen-free and anhydrous environment, wherein the precursors decompose to form the nucleus for a particle to grow on. This method was introduced by Yan and co-workers on the preparation of triangular LaF<sub>3</sub> nanoplates (Figure 3.1a) [1], and was later improved as a broadly applicable route to produce UCNPs of high quality and narrow size distribution (Figure 3.1b-f). Various sizes and shapes of UCNPs have been produced by tailoring the experimental parameters, including the reaction temperature, reaction time, nature and concentration of solvents, and the concentration of reagents. Another refined approach was reported by Li and co-worker for the preparation of  $\beta$ -NaYF<sub>4</sub>:Yb,Er/Tm UCNPs [2]. Their method was demonstrated to be user-friendly in minimizing the use of fluoride reactions and decreasing the amount of toxic by-products generated at high temperature [2]. Their method was adopted to prepare UCNPs for studies reported in this thesis. Although the thermal decomposition has been proven to be an effective strategy, UCNPs fabricated using this method exhibit certain defects and hence a relatively lower upconversion quantum yield.

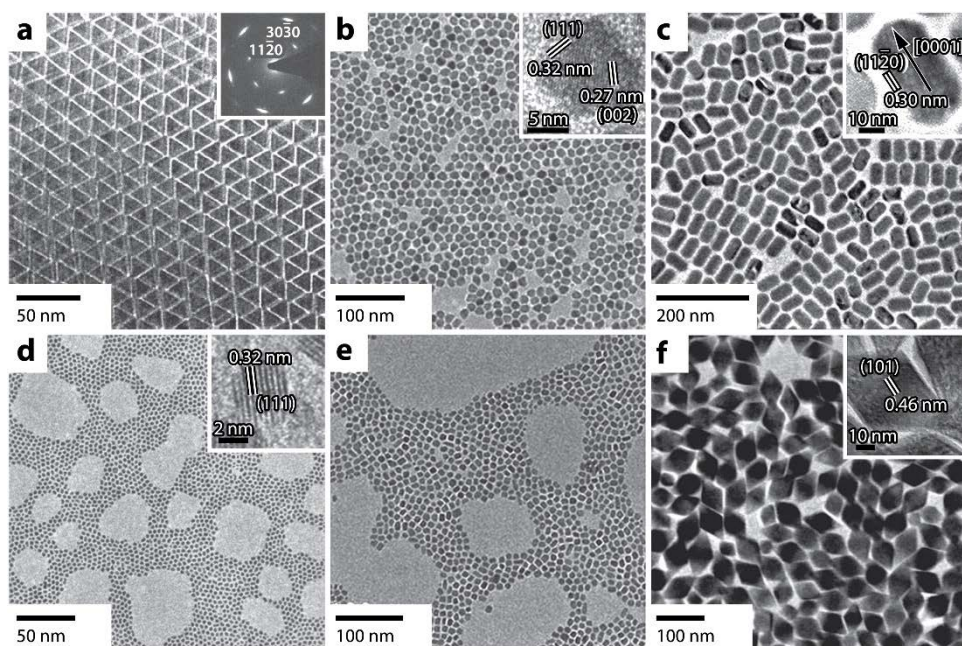


**Figure 3. 1** TEM images of UCNPs (a)  $\text{LaF}_3$ , (b)  $\alpha\text{-NaF}_4$ , (c)  $\beta\text{-NaYF}_4$ , (d)  $\text{LaOF}$ , (e)  $\text{BaGdF}_5$  and (f)  $\text{LiErF}_4$  prepared by the thermal decomposition strategy. Reproduced from Ref. [3].

### 3.1.2 Hydro(solvo)thermal Synthesis

Hydro(solvo)thermal method is performed with the assistance of high temperature and pressure to dissolve solid reactants as well as to speed up the reaction. The possible advantages of this technique are the relatively lower reaction temperature, high-quality crystalline phase of the obtained nanoparticles, and excellent control over the particle size and shape. The main disadvantages are the adoption of specialized reaction vessels (Teflon-lined autoclave) and inability to monitor the particle growth. In a typical process, lanthanide precursors (such as lanthanide nitrites, chlorides, and oxides) and fluoride precursors (such as  $\text{HF}$ ,  $\text{NH}_4\text{F}$ ,  $\text{NH}_4\text{HF}_2$ ,  $\text{NaF}$ , and  $\text{KF}$ ) and surfactants are mixed in aqueous solution and placed in an autoclave, then sealed and heated at a temperature between  $160\text{ }^\circ\text{C}$  and  $220\text{ }^\circ\text{C}$ . Morphologies of the UCNP product can easily be tuned by varying the reactant concentration, reaction temperature, reaction time, and pH of the solution. This method was firstly reported by Li's group on the synthesis of  $\text{NaYF}_4$ ,  $\text{YF}_3$ ,  $\text{LaF}_3$  and  $\text{YbF}_3$  nanocrystals [4]. Another example of the hydro(solvo)thermal synthesis was reported by Zhao and co-workers to generate monodispersed  $\beta\text{-NaYF}_4$  with various morphologies, such as nanorods (Figure 3.2a), nanotubes (Figure 3.2b), and flower-patterned nanodisks (Figure 3.2c) [5].

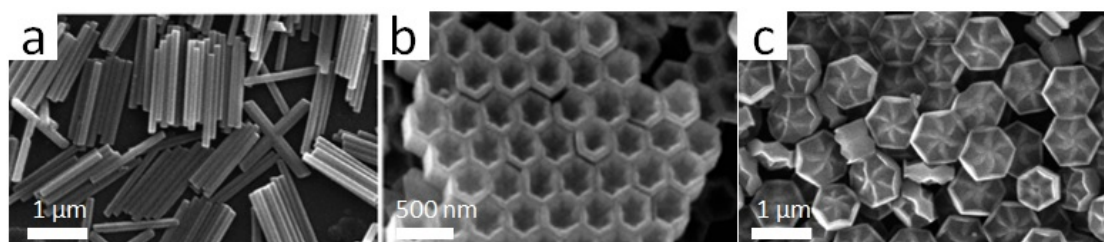


**Figure 3. 2** SEM images of  $\beta$ -NaYF<sub>4</sub> (a) nanorods, (b) nanotubes, and (c) nanodisks prepared with the hydro(solvo)thermal method. Reproduced from Ref. [6].

### 3.1.3 Coprecipitation

Coprecipitation approach is the most convenient and simplest way to prepare NaYF<sub>4</sub> UCNPs, since no costly equipment, complex procedures, and stringent reaction conditions are required for this synthesis. In a typical example, ethylenediaminetetraacetic acid (EDTA) was used as a chelate agent to form a lanthanide-EDTA complex, followed by a rapid injection of this complex to a vigorously stirred NaF solution [7]. This process was helpful in forming a homogenous nucleus for subsequent growth of nanoparticles. The particle size can be effectively controlled between 37 nm and 166 nm by adjusting the molar ratio of EDTA to lanthanide salts [7]. Normally,  $\alpha$ -NaYF<sub>4</sub> UCNPs obtained using this method suffer from the low photoluminescent yield. In view of that, a post-treatment by annealing is required to drive transition of the particles from cubic to hexagonal phase, which results in the brighter UCNPs [7]. Haase and co-workers have demonstrated successful production of water-dispersible  $\beta$ -NaYF<sub>4</sub> UCNPs without the need of the calcination step [8]. Besides, the use of EDTA, the other alternative surface ligands, such as polyethylenimine (PEI) [5] and polyvinylpyrrolidone (PVP) [9] were also employed to control the nanoparticle growth and yielded nanoparticles capped with these polymers.

## 3.2 Surface Passivation

Lanthanide-doped upconversion nanocrystals normally have a considerable number of dopant ions close to the particle surface. Photoluminescence of these lanthanide dopants is therefore more susceptible for quenching by the surface ligands or neighbouring solvent molecules characterised by high vibrational and phonon energy. As a result, the lanthanide dopants are quenched and the upconversion emission of the particles is

decreased, which is detrimental for UCNPs in the context of biological optical imaging and bioanalytical applications. The application of core-shell structures provides an effective solution to minimize the surface quenching effect in which a shell is designed to encompass the core UCNP to protect the surface dopant ions from capping ligands and surrounding molecules, as well as suppress the energy loss on the particle surface. Materials such as NaYF<sub>4</sub>, NaGdF<sub>4</sub>, LaF<sub>3</sub> are frequently employed to construct the shell due to their low lattice mismatch with the core composition. Currently, two main approaches are widely used to form a shell on the pre-produced UCNP surface (Figure 3.3). Both strategies are able to yield uniform and monodispersed core-shell nanoparticles.

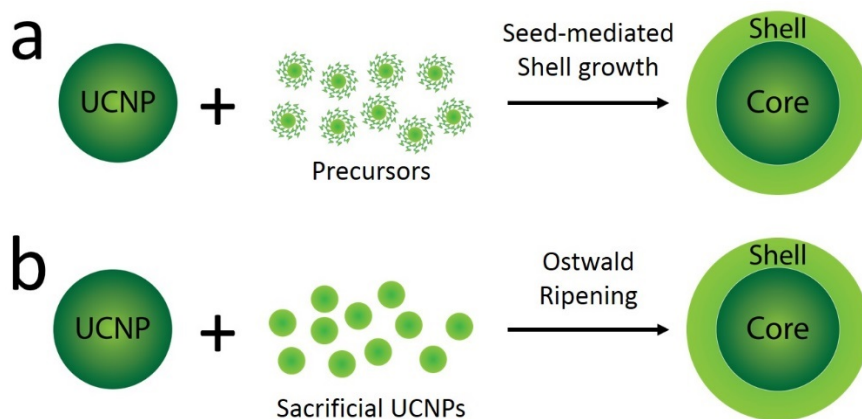


**Figure 3. 3** Two approaches to produce core-shell UCNPs with reduced surface quenching of the photoluminescence.

The first method is seed-mediated shell growth by mixing precursors with core nanoparticles in mixed solvents of ODE and OA. Using the thermal decomposition technique, monomers are formed by the precursors and gradually deposited on the surface of the core particles, leading to the formation of a uniform shell layer. Based on this method, Yi *et al.* have demonstrated coating of NaYF<sub>4</sub>:Yb,Er/Tm UCNP with a ~2 nm layer of inert NaYF<sub>4</sub> and observed 7.4 times and 29.6 times upconversion emission increase for NaYF<sub>4</sub>:Yb,Er, and NaYF<sub>4</sub>:Yb,Tm particles, respectively [10]. An increase in the photoluminescence efficiency of UCNPs was also demonstrated by Chen and co-workers, who reported coating of NaYF<sub>4</sub>:Yb,Tm with NaGdF<sub>4</sub> to bring in 3-times photoluminescence enhancement [11]. Notably, the introduction of paramagnetic Gd<sup>3+</sup> ions in a shell also endows magnetic resonance imaging (MRI) properties to nanoparticles [11].



The second method involves the use of small one-digit nanometre-scale sacrificial nanoparticles (such as  $\alpha$ -NaYF<sub>4</sub>) in which the sacrificial nanoparticles rapidly dissolve into monomers, deposit on the core nanoparticles and thereby form a shell through an Ostwald ripening process. Typically, the core particles are dispersed in a mixed solution of OA, ODE, and OM and heated up to a high temperature, and the sacrificial nanoparticles are then injected into the core particle suspension. In this way, the thickness of the shell can be precisely controlled by a number of the sacrificial particles that are successively injected into the reaction. The shell composition can also be easily adjusted via layer-by-layer shell-growth using the sacrificial particles with selected materials. This method was firstly developed by van Veggel and co-workers who monitored the growth process of seed-mediated core-shell UCNPs and verified the presence of cubic nanoparticle as the intermediate product during the heating up process [12]. They employed the more flexible concept of dissolving unstable cubic UCNPs to yield a ripened shell on the core UCNPs [12]. Using this method, a variety of core-shell UCNPs have been prepared, including NaYF<sub>4</sub>@NaYF<sub>4</sub>, NaYF<sub>4</sub>@NaGdF<sub>4</sub>, CaF<sub>2</sub>@CaF<sub>2</sub>, and GdF<sub>3</sub>@LnF<sub>3</sub>.

### 3.3 Surface Modification and Bioconjugation

The hydrophilicity and stable dispersity in biological buffers is the prerequisite for nanoparticles to be used in most biomedical applications. However, UCNPs prepared by the methods described above are generally hydrophobic owing to the hydrophobic nature of the capping reagents (*e.g.* OA or OM), which greatly limits their application in theranostics. In order to transfer these hydrophobic nanoparticles into water, a number of surface modification methods have been developed encompassing ligand exchange, ligand oxidation, ligand removal, ligand attraction, layer-by-layer assembly, and surface silanization (Figure 3.4) [13]. These surface engineering methods not only render UCNPs water soluble by also provide reactive groups for subsequent conjugation to biomolecules. A summary of the current surface modification and bioconjugation methods is presented in this section.

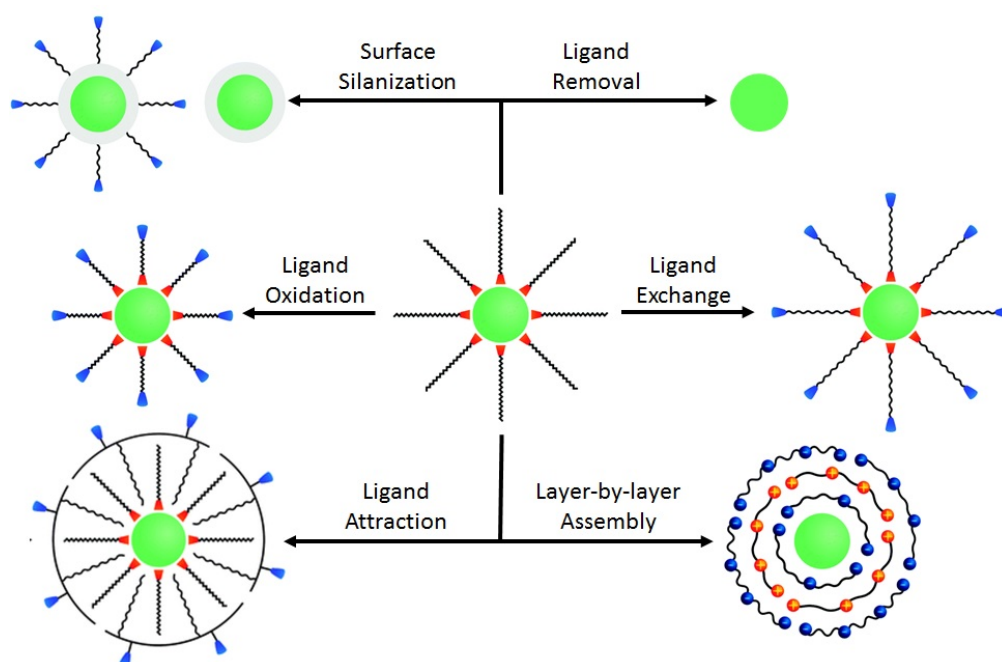


**Figure 3. 4** A diagram of surface modification methods used to alter the surface chemistry of UCNPs. Reproduced from Ref. [13].

### 3.3.1 Ligand Exchange

Ligand exchange is a physical process in which original hydrophobic capping ligands on UCNPs are replaced with new binding molecules. Usually, the new binding molecules should have functional groups that allow them to firmly anchor on the NP surface along with hydrophilic end tails to impart water dispersity and functionality to the NP. A variety of molecules that meet such structure requirements have been used to decorate UCNPs with hydrophilic moieties including polyacrylic acid (PAA) [14], poly(ethylene glycol) (PEG)-phosphate [15], PEG-diacid [16], 2-aminoethyl dihydrogen phosphate [17], poly(amidoamine) (PAMAM) [18], PEI [19], hexanedioic acid [20], 6-aminohexanedioic acid [21], 3-mercaptopropionic acid [22], citrate [23], and tetramethylammonium hydroxide (TMAH) [24]. Zhang *et al.* have reported the prior work using the ligand exchange method to replace OA on UCNPs with PAA under elevated temperature (240 °C) [14]. A more versatile strategy was recently developed by Marray and co-workers, who reported the use of nitrosonium tetrafluoroborate ( $\text{NOBF}_4$ ) to replace the original surface ligands (OA or OM) at room temperature, thereby stabilizing NPs in aqueous solutions [25]. More importantly, the intermediate NPs ( $\text{NOBF}_4$ -UCNP) can be subject to further

surface manipulation by replacing the capping ligand  $\text{NOBF}_4$  with desired surface molecules for subsequent bioconjugation (Figure 3.5) [25].

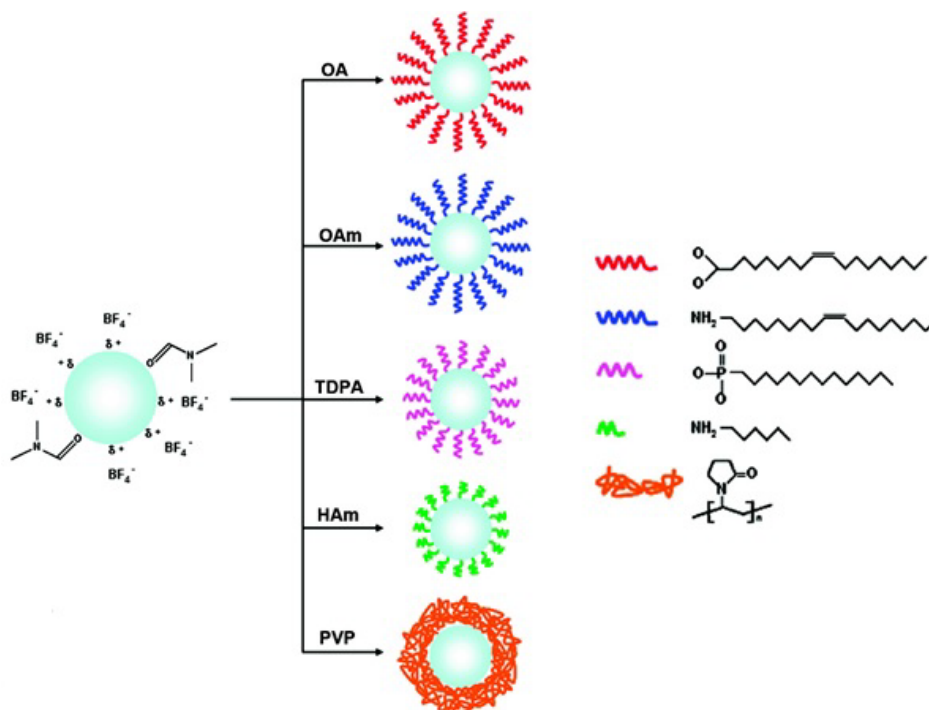


**Figure 3. 5** A diagram of the subsequent ligand exchange of  $\text{NOBF}_4$ -UCNPs with OA, OM, tetradecylphosphonic acid (TDPA), hexylamine (HAm), or PVP, respectively. Reproduced from Ref. [25].

### 3.3.2 Ligand Oxidization

Ligand oxidization refers to the direct oxidation of the unsaturated carbon-carbon double bond ( $-\text{C}=\text{C}-$ ) of OA to carboxylic acid groups, thereby converting the hydrophobic UCNPs into a water-soluble phase. This strategy was reported by Li and co-workers, who used the Lemieux-von Rudloff reagent ( $\text{MnO}_4^-/\text{IO}_4^-$ ) to oxidize the surface ligands OA on UCNPs into azelaic acids [26]. The carboxylic groups of the resulting azelaic acid not only provided high solubility to the NPs but also enabled them to conjugate to biomolecules (Figure 3.6) [26]. In analogy, Yan and co-workers used ozone to oxidize OA into azelaic acid ligands and/or azelaic aldehyde [27]. Their study showed that the oxidation strategy had no adverse influence on the morphology, crystalline phase, composition and optical properties of UCNPs [27]. This ligand oxidation method is very

easy to implement, nonetheless, it is only applicable to limited types of hydrophobic surface ligands that contain unsaturated carbon-carbon double bonds.

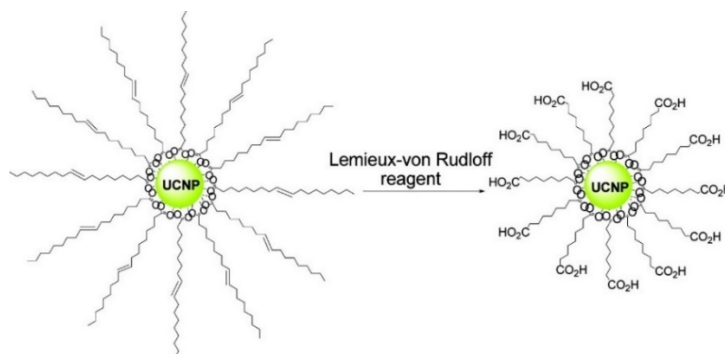


**Figure 3. 6** A diagram of oxidation of OA on UCNP with Lemieux-von Rudloff reagent. Reproduced from Ref.[26].

### 3.3.3 Ligand Removal

Ligand removal is another straightforward strategy to acquire water-soluble UCNPs by removing oleate ligands coated on UCNPs. The removal process can be implemented by treating UCNPs with excess ethanol under sonication or simply with strong acid. As an example of the first case, Xu and co-workers have demonstrated the removal of oleic acid by washing particles with substantial amount of ethanol assisted by ultrasonication [28]. Alternatively, Capobianco and co-workers dispersed OA-capped UCNPs with HCl at pH 4 to remove OA and yield hydrophilic UCNPs [29]. At such low pH, OA is gradually protonated and dissociates from the particle, leaving the UCNP naked with lanthanide ions being exposed on their surfaces [29]. Because of the high surface charge of these positive lanthanides, the obtained UCNPs can form a stable dispersion in aqueous solutions for a long time. Furthermore, the surface lanthanide ions enable the ligand-free UCNPs to coordinate with biomolecules that contain functional groups such as  $-\text{COOH}$ ,  $-\text{OH}$ ,  $-\text{NH}_2$ .

### 3.3.4 Ligand Attraction

The ligand attraction method is based on the hydrophobic-hydrophobic interaction between amphiphilic molecules and hydrophobic capping ligands on UCNP to add a second layer of amphiphilic molecules on the particle. In a typical ligand-attracted UCNP

(Figure 3.7), hydrophobic units of the amphiphilic compounds interact with the organic capping molecules on the UCNP surface to form an inner layer, while the hydrophilic units facing outwards form the external layer and facilitate dispersion of NPs in aqueous solution as well as provide functional groups for the subsequent bioconjugation. Amphiphilic molecules used in this approach can be modified amphiphilic polymers, block copolymers or surfactants. So far, poly(maleic anhydride-*alt*-1-octadecene) (PMAO) [30], PMAO-PEG [31], octylamine-poly(acrylic acid)-poly(ethylene glycol) (OA-PAA-PEG) [32], poly(ethylene glycol)-*block*-poly(caprolactone) (PEG-*b*-PCL) [33], poly((ethylene glycol)-*block*-lactic acid) (PEG-*b*-PLA) [33], poly(ethylene glycol)-*block*-poly(lactic-co-glycolic acid) (PEG-*b*-PLGA) [33], sodium dodecyl sulphate (SDS) [34], cetyltrimethylammonium bromide (CTAB) [34], polyethylene glycol *tert*-octylphenyl ether (C<sub>8</sub>PhE<sub>10</sub>) [34], and phospholipids [35] have been reported to be successfully attracted by UCNPs and render the particles hydrophilic.

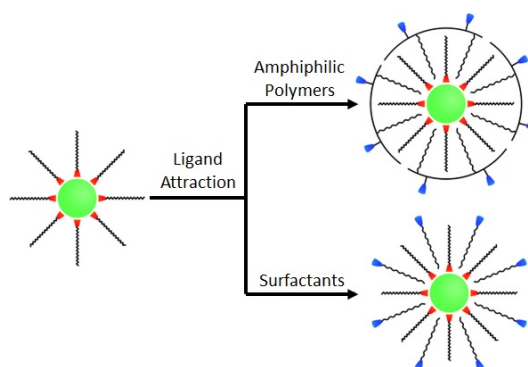


**Figure 3. 7** A diagram of modification of hydrophobic UCNPs via the ligand attraction using amphiphilic polymers or surfactants. Reproduced from Ref.[13].

### 3.3.5 Layer-by-layer Assembly

Layer-by-layer assembly makes use of the electrostatic interaction between species with opposite charge to coat polymers on a charged surface of UCNP. Polyions and polycations are normally used in this method for alternate deposition on UCNPs surface in a layer-by-layer manner [36, 37]. The deposition process is mainly performed in a solution by repeated incubation and washing. Hence, this method is simple and versatile in controlling the hydrodynamic size and surface charge of the obtained UCNPs. Also, desired functional groups can be incorporated to the UCNP surface and act as attachment

sites for biomolecules to immobilize on. In a typical study, Li and co-workers have reported the modification of UCNPs by depositing positively-charged polymer, poly(allylamine hydrochloride) (PAH), and negatively charged polymer, poly(styrene sulfonate) (PSS), sequentially on the negatively charged UCNPs to generate PAH/PSS/PAH UCNP nanocomposites [36]. The outmost layer of PAH provided abundant amine groups that enabled coupling with biotin for bioanalytical applications [36].

### **3.3.6 Surface Silanization**

Silica-coating with further surface silanization is another popular method to modify UCNPs. Silica is a water-soluble material with many known merits, such as biocompatibility, optical transparency, and chemical stability. The surface chemistry of silica can be easily tuned by organofunctional alkoxysilane molecules via self-assembly. As a result, the coating of a silica shell on UCNPs is able to stabilize the particles in various buffers and provide an amenable surface for easy add-on of functionalities (-NH<sub>2</sub>, -COOH, or -SN). Silica-coating is applicable to both hydrophobic and hydrophilic UCNPs. Hydrophobic UCNPs can be coated with silica by using a well-developed reverse microemulsion method (Figure 3.8a). In a typical process, detergent (such as Igepal CO-520) is employed to form reverse micelles in a nonpolar solvent (such as cyclohexane), wherein tetraethyl orthosilicate (TEOS) undergo hydrolysis in the presence of ammonia to grow a silica layer on UCNPs. On the other hand, Stöber method can be applied to coat silica on hydrophilic UCNPs (Figure 3.8b). Instead of using nonpolar solvent, hydrophilic UCNPs are dispersed in ethanol or a mixture of water and ethanol in which a similar hydrolysis reaction of TEOS occurs to form a silica shell on UCNPs. The thickness of the silica shell can be feasibly controlled by varying the amount of TEOS. Based on these two approaches, uniform silica shells of different thickness have been successfully coated on UCNPs to generate core-shell nanocomposites with excellent water solubility and biocompatibility. For example, Shi and co-workers have reported the coating of silica on NaYF<sub>4</sub>:Yb,Er,Tm,Gd UCNPs with a controllable shell thickness of 5 nm, 10 nm, 15 nm and 20 nm [38]. Zhang and Li used Stöber method to form a thin layer of silica (1-3 nm) on PVP-stabilized NaYF<sub>4</sub> [9].

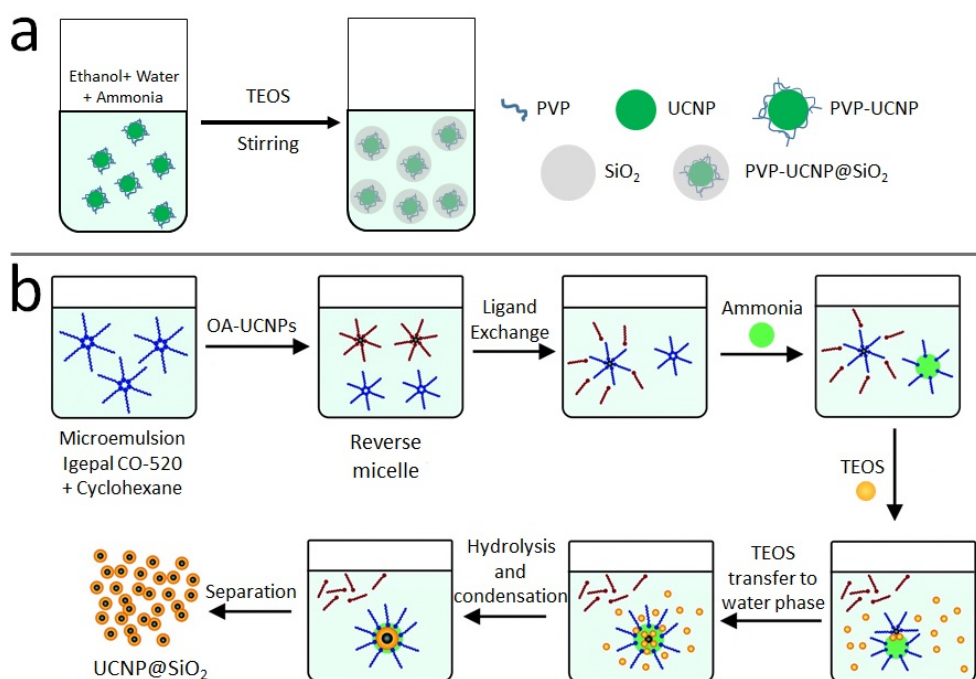


**Figure 3. 8** A diagram of the coating a silica shell on (a) hydrophilic PVP-UCNP via Stöber method, and (b) hydrophobic OA-UCNP surface via the reverse microemulsion method.

Besides coating of a dense silica layer (dSiO<sub>2</sub>), many groups have also devoted efforts to grow a mesoporous silica (mSiO<sub>2</sub>) shell or hollow mesoporous silica (hmSiO<sub>2</sub>) on UCNP in an attempt to use the nanocomposite as drug delivery vehicles (Figure 3.9) [39]. The unique porous or rattle structure of mSiO<sub>2</sub> and hmSiO<sub>2</sub> is particularly useful in nano-theranostics, when high loading of therapeutic materials is required. The mesoporous structure can be achieved by adding a micelle-forming reagent (such as CTAB) during the formation of a silica shell. The micelles are then removed by washing the colloid with a solvent of suitable pH or by refluxing particles [40, 41]. Compared with mSiO<sub>2</sub>, the hmSiO<sub>2</sub> coating provides the larger accommodation volume for drugs due to the presence of voids between the UCNP core and mesoporous shell. The hmSiO<sub>2</sub> coating method was recently developed by Shi and co-workers in which they coated two layers of dSiO<sub>2</sub> on a hydrophobic UCNP followed by etching the first dSiO<sub>2</sub> shell along with generating mesopores in the second silica shell, yielding a rattle structure [42].



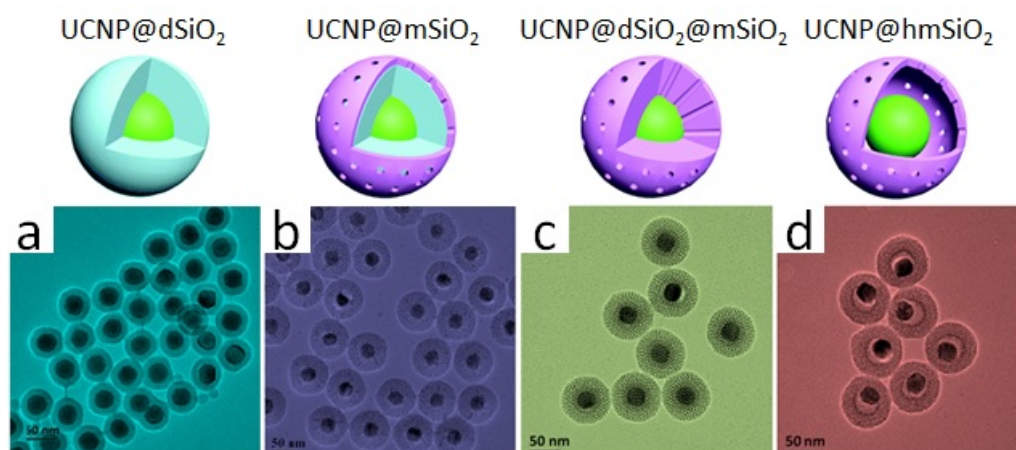


**Figure 3. 9** Schematic illustration and TEM images of (a) UCNP@dSiO<sub>2</sub>, (b) UCNP@mSiO<sub>2</sub>, (c) UCNP@dSiO<sub>2</sub>@mSiO<sub>2</sub>, and (d) UCNP@hmSiO<sub>2</sub>. Reproduced from Ref.[39, 43].

### 3.3.7 Bioconjugation

In order to implement UCNPs in theranostic applications, a crucial step is to couple the particles with molecules that possess biological functions, such as antibodies, peptides, and nucleic acid ligands. This biofunctionalization step, also referred as bioconjugation, can be realized by attachment of biomolecules to the UCNP surface via physical binding or chemical conjugation. The physical process relies on simple electrostatic and hydrophobic interactions. For example, a negatively-charged protein streptavidin was demonstrated to adhere to the surfaces of positive UCNPs by means of electrostatic interaction [44]. In the same way, folic acid (FA), a widely used targeting ligand, can coordinate to the surface of positive UCNPs through its carboxylic groups [45]. However, physically adsorbed proteins might detach from the UCNP surface when the nanocomposites are used in complicated *in vivo*/body system. In contrast, the covalent linkage that formed between the reactive group on UCNP and the other group in biomolecules is stronger and more robust, providing a better alternative for bioconjugation of UCNPs. To this aim, functional groups such as -COOH, -NH<sub>2</sub> and maleimide are generally introduced to the surface of UCNPs and used for binding of biomolecules. Figure 3.10 illustrates the bioconjugation chemistry that is frequently utilized in UCNPs.

For carboxyl-terminated UCNPs, biological molecules that contain -NH<sub>2</sub> groups can react with the surface -COOH groups to create stable amide bonds (Figure 3.10a). In a



typical procedure, the -COOH groups are firstly activated with 1-ethyl-3-(3-dimethylaminopropyl) carbodiimide hydrochloride (EDC) and the N-hydroxysulfosuccinimide sodium salt (sulfo-NHS) in buffers to form *O*-acylisourea intermediate product, which can subsequently react with -NH<sub>2</sub> group to complete the chemical bonding. Carboxylic groups can be provided by a variety of surface ligands, such as azelaic acid [46, 47], hexanedioic acid [20], citrate [45, 48], thioglycolic acid [49, 50], 3-mercaptopropionic acid [51, 52], 5-mercaptosuccinic acid [53], dimecaptosuccinic acid [54], 1,10-decanedicarboxylic acid [55], 11-mercaptoundecanoic acid [55], 3-mercaptopropionic [22], diacid PEG [56], PAA [11, 57].

On the other hand, -NH<sub>2</sub> groups on UCNPs are able to covalently bind to -COOH, -CHO (aldehyde), and S=C=N (thiocyanate) groups contained in many biomolecules (Figure 3.10b). The -NH<sub>2</sub> groups can be provided by surface modifications with aminoundecanoic acid [56], PEI [5, 19, 58], diamino-PEG [59, 60], PAH [61], PAMAM [18], 2-aminoethyl dihydrogen phosphate (AEP) [62], and (3-aminopropyl) triethoxysilane (APTES) [63, 64]. For example, Xiong and co-workers have reported the preparation of 6-aminohexanoic acid modified UCNPs to provide sufficient amine content for the conjugation to FA [65]. The resulting nanocomposites were demonstrated to be effective in targeting HeLa cells that overexpress folate receptors [65].

A number of the other biomolecules (such as cysteines and thiolated peptides) are also known to have active -SH (thiol) groups that preferentially react with maleimide groups on UCNPs. In this case, the double carbon bond in a maleimide group can link to the thiol group and form a strong carbon-sulphur bond. To this aim, the maleimide groups can be introduced to UCNP using maleimide PEG or via the reaction between *N*-hydroxysuccinimide (NHS) ester and amine-terminated UCNPs.

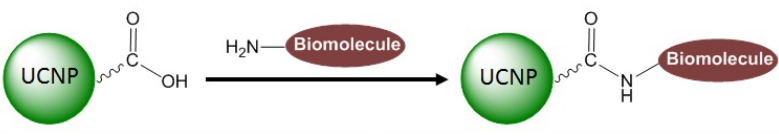
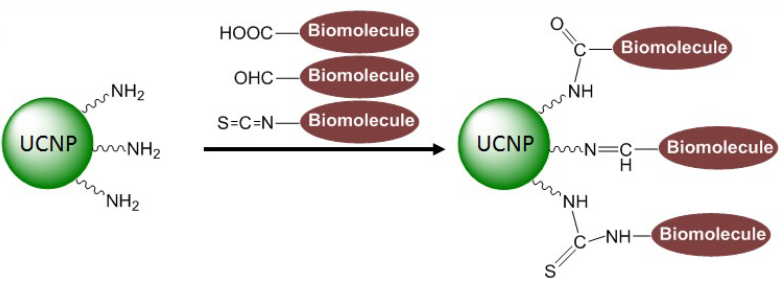
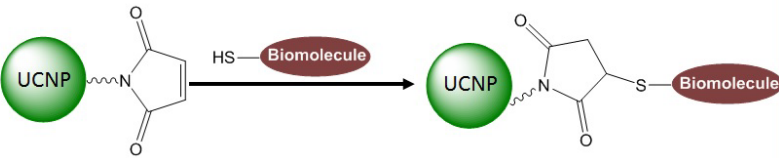
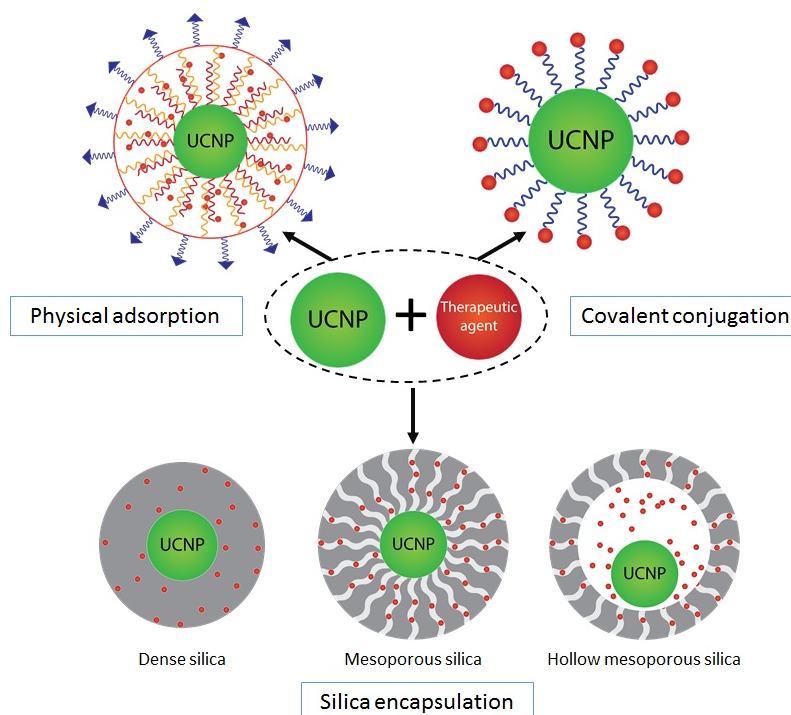
Bioconjugation scheme	Biomolecules
<p><b>a</b></p> 	diamino-PEG [46] antibodies [22] streptavidin [57] FA-chitosan [54] Concanavalin A [66] DNA [67] Peptide [68]
<p><b>b</b></p> 	Chlorotoxin [69] Biotin [36] Streptavidin [70] FA [65] Peptide [71] Antibodies [19] DNA [61] Mannose [18]
<p><b>c</b></p> 	Thiolated-peptide [72] Ni-nitrilotriacetate [73]

Figure 3. 10 A table diagram of the bioconjugation chemistry commonly used for coupling UCNPs with biomolecules.

### 3.4 Integration with Therapeutic Agents

The potential of using biofunctional UCNPs combined with anticancer drugs, photosensitizing agents, or therapeutic genes for cancer treatment have been extensively investigated in the last ten years. A successful anticancer effect of such UCNP theranostic hybrids depends on treatment attributes of the integrated therapeutic molecules. Therefore, optimal loading of therapeutic agents on UCNPs is crucial to ensure therapeutic efficiency and adequate drug release after delivering to the diseased site. The established methods for integrating UCNPs with therapeutic agents include physical adsorption between UCNPs and therapeutic molecules (hydrophobic interaction or electrostatic attraction),

covalent conjugation between functional groups on UCNP and drug molecules (chemical reaction through active groups), and silica encapsulation (silica layer entrapping drugs) (Figure 3.11).



**Figure 3. 11** Schematic illustrations of the three strategies for integrating UCNP with therapeutic agents.

### 3.4.1 Physical Adsorption

Many of the currently used anticancer drugs (*e.g.* porphyrin, doxorubicin, paclitaxel, and vincristine) are hydrophobic and poorly soluble in physiological buffers. As a result, the pharmaceutical effect of these useful drugs is largely diminished and their administration via conventional delivery methods proves to be challenging. Fortunately, these hydrophobic drugs can be easily loaded into the hydrophobic layer of amphiphilic polymer that is often used in UCNP surface modification. The hydrophobic arms of the amphiphilic polymers are normally attached to UCNP surface via hydrophobic interaction with UCNP surface ligands (*e.g.* OA), creating a hydrophobic network for storage of the drugs. The hydrophobic drug is firstly dispersed in an organic solvent (*e.g.* dimethylsulfoxide and dimethyl formamide) to which as-produced polymer-UCNPs are added to allow slow diffusion of the drug to the hydrophobic network. The nanocomposites are then collected and washed to remove unabsorbed or loosely absorbed

drug to yield the final product. Once delivered to the diseased site, adsorbed hydrophobic drugs can be released by stimuli. For example, Wang and co-workers have described the loading of Chlorin e6 (Ce6), a photosensitizing molecule, to octylamine-grafted-PAA modified UCNPs, wherein Ce6 was accommodated in a hydrophobic layer created by octylamine and oleic acid interaction (Figure 3.12a) [74]. Moreover, they functionalized PAA-UCNPs with PEI via layer-by-layer assembly to generate a positive surface for the subsequent adsorption of small interfering RNA (siRNA) (Figure 3.12a) [74]. In a report by Liu and co-workers, doxorubicin (DOX) was physically loaded onto the polymer layer of PMAO-PEG-coated UCNPs (Figure 3.12b) [59]. In this study, the release of DOX was achieved by adjusting pH of the solution, with the higher drug dissociation rate observed under the acidic condition (pH = 5) [59].

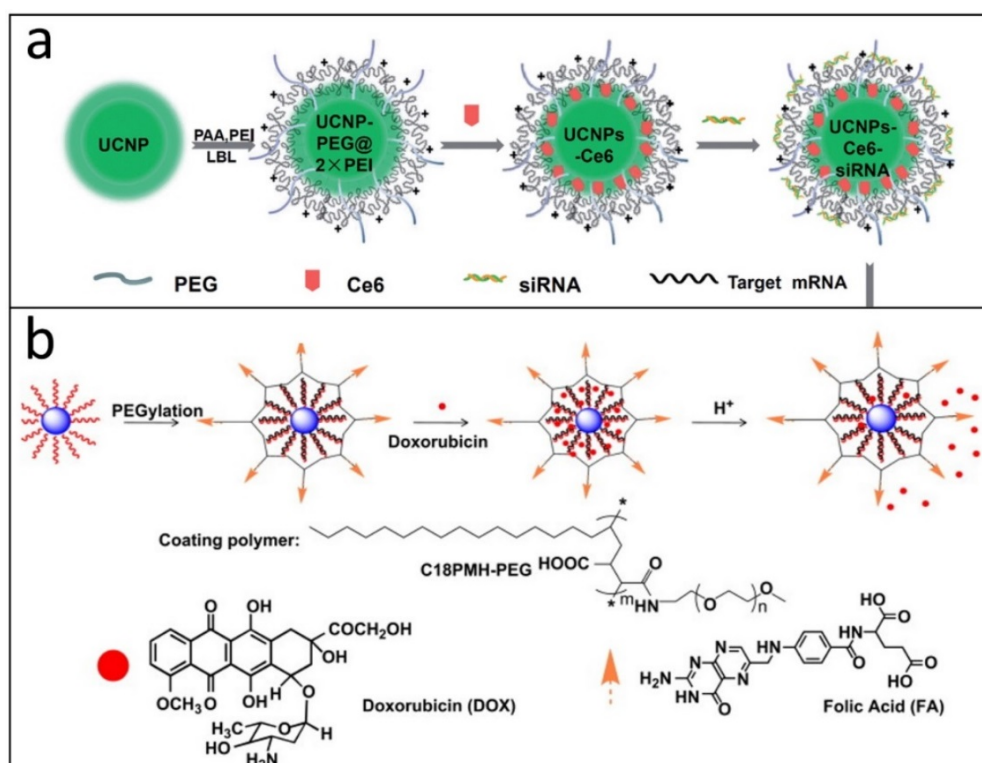


**Figure 3. 12** (a) Schematic illustrations showing the functionalization of UCNPs with octylamine-grafted-PAA and PEI, and the co-loading with Ce6 and siRNA [74]. (b) The development of UCNPs-based drug delivery system by surface modification with amphiphilic PMAO-PEG polymers and loading with DOX [59].

### 3.4.2 Covalent Conjugation

Compared to the physical methods, the covalent conjugation between drug molecules and UCNPs is sufficiently strong to secure drug remaining in the nanocarriers during *in vivo* delivery. Also, such robust binding is important in UCNP-mediated photodynamic therapy, when leakage of photosensitizing drugs is undesirable and will result in a loss of the therapeutic efficacy. On the other hand, the release of payload drugs that are covalently conjugated to UCNPs is essentially difficult. Therefore, covalent conjugation method is less favoured by delivery therapy, when drug release is required for the therapeutic action.

In this method, the attachment of drugs to UCNPs is generally achieved by cross-linking between amine groups on UCNPs and carboxylic groups on the therapeutic molecules, or *vice versa*. For instance, Zhang and co-workers managed to bind a photosensitizing molecule, Rose Bengal (RB), onto AEP-UCNPs by conjugating carboxyl groups of hyaluronic acid modified RB to amino groups of AEP-UCNP to form amide bonds (Figure 3.13a). By comparing with the RB loading via physical adsorption, they confirmed the significant improvement in drug loading rate using the covalent method to conjugate RB to UCNPs [62]. Dai and co-workers described the introduction of cisplatin (IV) anticancer prodrug to UCNPs by modifying the cisplatin (IV) prodrug (DSP) with axial carboxylic acid to allow for its covalently binding to PEI coatings on UCNPs [75].

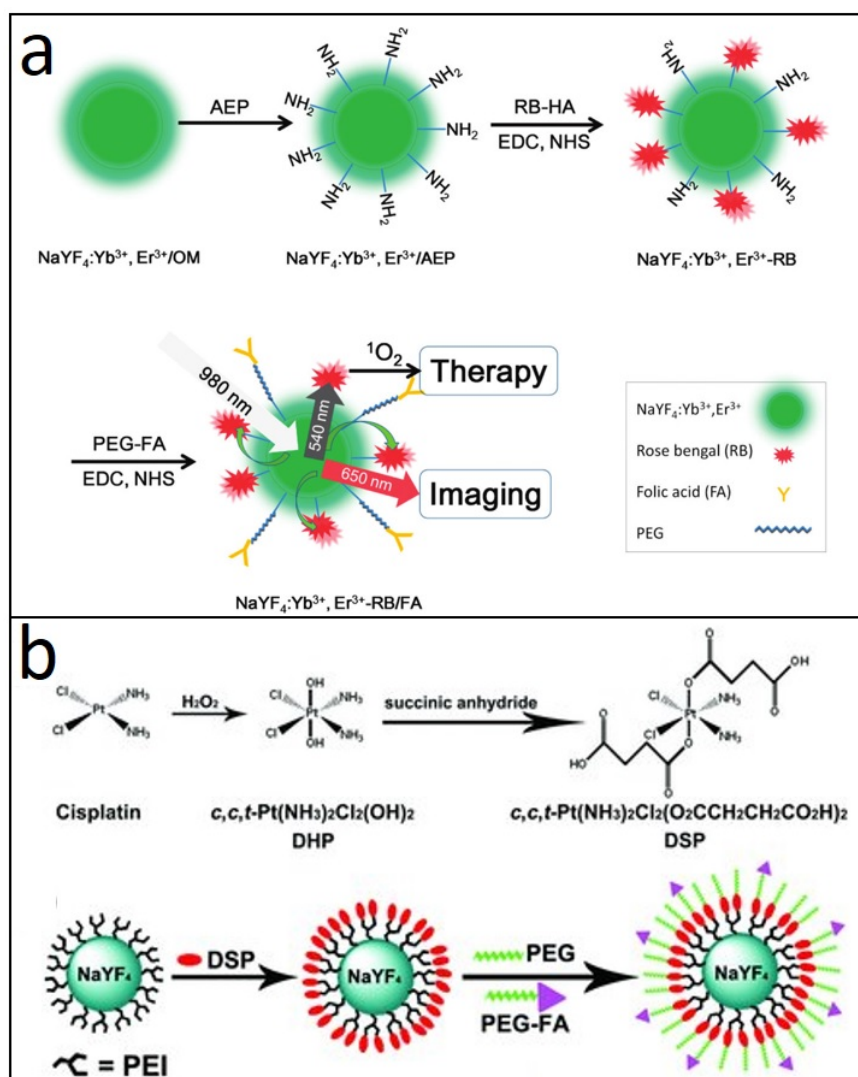


**Figure 3. 13** Schematic illustration showing the covalent conjugation between photosensitizing molecule RB and AEP-UCNPs [62]. (b) Attachment of the cisplatin (IV) prodrug (DSP) to UCNP by chemically conjugating DSP to PEI coating of UCNP [75].

### 3.4.3 Silica Encapsulation

In silica-coated UCNPs, a dense or mesoporous silica shell on the outer layer of the particle can serve as a drug storage vehicle for loading therapeutic materials. For dense silica layer to encapsulate drugs, water-soluble therapeutic molecules (such as methylene blue, MB) are generally loaded during the formation of the silica layer on UCNP (Figure 3.14a) [76]. In a typical procedure using the reverse microemulsion method, oleate- or oleylamine-capped UCNPs are firstly mixed with the Igepal CO-520 formed reverse micelles in an organic solvent (such as cyclohexane). An aqueous solution of drugs is

then added to the reaction followed by ammonia addition and the controlled injection of TEOS. The hydrolysed TEOS is hydrophilic by virtue of silanol groups, therefore can transfer to hydrophilic interior of the reverse micelles, where hydrophilic drugs are present. The hydrolysis and condensation of TEOS then occur, leading to the formation of a silica layer accompanied with the entrapment of drugs. Although the dense silica loading method is simple, the drug loading capacity is limited precluding this method application in therapies that require drug release on demand.

Alternatively, the mesoporous silica ( $mSiO_2$ ) coating can offer much larger internal drug storage space and allow drug release through mesoporous channels. Depending on the size of therapeutic agents, the diameter of pores in the mesoporous layer can be easily tuned by selecting an appropriate synthetic method. Taking advantage of the unique porous structure, Zhang and co-worker deposited zinc phthalocyanine (ZnPc) on  $UCNP@mSiO_2$ , wherein ZnPc molecules were stable, without being released from the silica layer either in PBS or in cell culture medium [40]. To obtain the higher therapeutic efficacy, they co-loaded two photosensitizers, ZnPc and merocyanine 540 (MC540), in the mesoporous silica shell and demonstrated much higher photodynamic efficacy than the single photosensitizing counterpart [77]. A mesoporous silica shell is also widely used in the design of UCNP-based drug delivery and release systems. Wu and co-workers have developed an NIR light-triggered DOX release device by loading  $UCNP@mSiO_2$  with DOX and grafting the particle surface with ruthenium (Ru) complexes as photoactive molecular valves (Figure 3.14b) [78]. Under NIR irradiation, the UV emission from UCNP was able to trigger photocleavage of the Ru complexes to open the valves, which can consequently induce the release of DOX in a controlled manner (Figure 3.14b) [78].

Owing to a cavity between the UCNP and mesoporous silica shell,  $UCNP@hmSiO_2$  enables much higher loading level of therapeutic agents, as compared with the other two silica structures. The preparation of such hollow silica coating UCNP has been described in Section 3.3.6. Li and co-worker have demonstrated the construction of a photo-controlled drug release system based on the impregnation of a photo-responsive therapeutic compound into the hollow cavity of  $UCNP@hmSiO_2$  (Figure 3.14c) [79]. The therapeutic compound was synthesized by a reaction between amino-acoumarin derivative and chlorambucile (amino-coumarin as the phototrigger and chlorambucile as



the caged drug, denoted as ACCh). In comparison with the use of mesoporous silica, the mhSiO<sub>2</sub> coating demonstrated 6-fold higher drug loading rate [79]. Under physiological conditions, no premature release of drugs was detected from this fabricated nanocomposite. Upon NIR irradiation, upconversion UV emission from UCNPs can effectively prompt the cleavage of phototrigger moieties, enabling a precise control over the releasing of chlorambucil drugs from the nanocarriers (Figure 3.14c) [79].

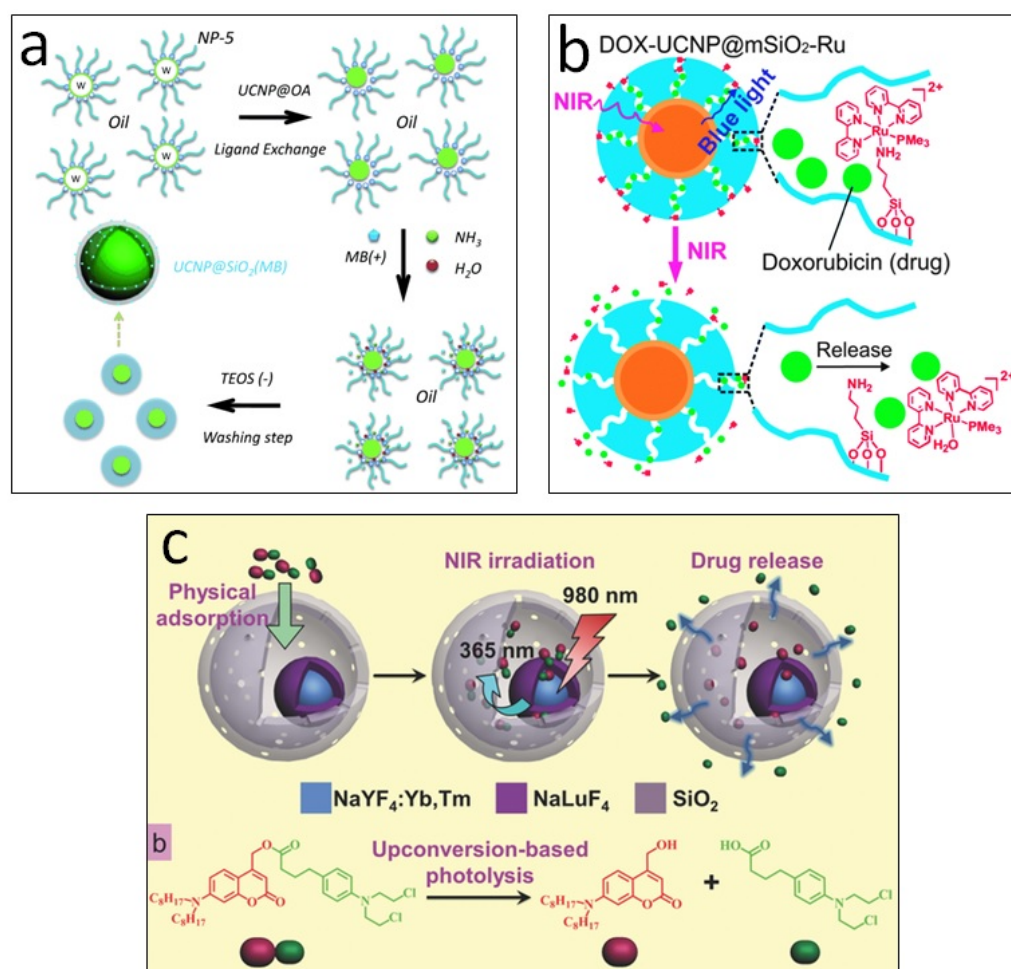


**Figure 3. 14** (a) Schematic diagrams of the loading of a photosensitizing molecule, MB on UCNPs via the dense silica encapsulation using the water-in-oil reverse microemulsion technique [76]. (b) Schematic illustration of loading DOX into the mesopores of UCNPs@mSiO<sub>2</sub>, and triggering the cleavage of the Ru complexes and the release of DOX from the nanocomposite [78]. (c) Illustration of loading anticancer drugs (ACCh) into the cavity of UCNPs@hmSiO<sub>2</sub> and the photolysis of the therapeutic compound to release caged drugs under upconversion emission from UCNPs [79].



### 3.5 Applications in Cancer Imaging and Treatment

In recent years, design of multifunctional nanoparticles for biomedical applications has attracted intensive interest, especially in the field of cancer nanomedicine. One of the major aims of theranostics is to combine diagnosis and therapy into one a single nanoplatform and achieve image-guided treatment or imaging-monitored evaluation of therapy. Since UCNPs can be used as promising imaging contrast agents, various UCNP-based nanocomposites have been explored for delivering anticancer drugs, mediating photodynamic therapies, visualizing *in vivo* tumours and reporting delivery process. The following section summarizes recent efforts in applications of UCNPs in cancer imaging and treatment.

#### 3.5.1 High-Contrast Bioimaging Using UCNPs

##### 3.5.1.1 Photoluminescent Imaging

Photoluminescent imaging is an exceptionally versatile tool in cancer diagnosis. However, conventional fluorophores (organic dyes, fluorescent proteins, and quantum dots) experience many limitations, when exploited in the photoluminescent imaging, such as high background noise from biotissue autofluorescence, photobleaching, and photodamage to biological samples. These drawbacks associated with *in vivo* fluorescence imaging can be lifted by using UCNPs.

A particularly useful type of UCNPs is co-doped with  $\text{Yb}^{3+}$  and  $\text{Tm}^{3+}$ , which emits NIR photoluminescence in the range of 750–850 nm under 980-nm excitation. The excitation and emission wavelengths of these NIR-to-NIR UCNPs lie in the optical transparency window of the biological tissue. Therefore, the use of these UCNPs can allow for minimal autofluorescence and light scattering from the biotissue, leading to an ultrahigh imaging contrast. For example, Li have reported the high-contrast targeted imaging of a nude mouse bearing human glioblastoma U87MG tumours by linking the surface of  $\text{NaYF}_4:\text{Yb,Tm}$  nanoparticles with RGD peptide [46]. RGD peptide is known to have high affinity towards  $\alpha_v\beta_3$  integrin that overexpressed by U87MG cells and less expressed by human breast cancer cells MCF-7. *In vivo* fluorescence imaging of the animal showed clear targeted capability of the assembly nanocomposite towards U87MG tumour whereas no particle accumulation was observed in the MCF-7 tumour in the same mouse

(Figure 3.15a) [46]. More importantly, the signal-to-noise ratio between the labelled tumour and background was determined to be  $\sim 24$  [46], the level of which cannot be easily obtained in single-photon or two-photon fluorescence imaging. Another high-contrast imaging results were obtained by Xiong and co-workers, who employed FA-functionalized NIR-to-NIR UCNP for targeted labelling HeLa tumours *in vivo* (Figure 3.15b) [65].

Another fascinating feature of NIR-to-NIR UCNP is their capability of deep tissue imaging. Recently, Prasad and co-workers have reported the development of an NIR-to-NIR core-shell  $\text{NaYbF}_4\text{:Tm@CaF}_2$  UCNP for the whole body photoluminescent imaging of a mouse [80]. They obtained an extraordinarily high signal-to-noise ratio of 310 when using this novel kind of core-shell UCNP for imaging (Figure 3.15c) [80]. Remarkably, the fluorescence signal from UCNP can still be detected and imaged under 3.2-cm thick pork tissues (Figure 3.15d-e) [80]. This imaging depth will be of great use for *in vivo* and clinical imaging.

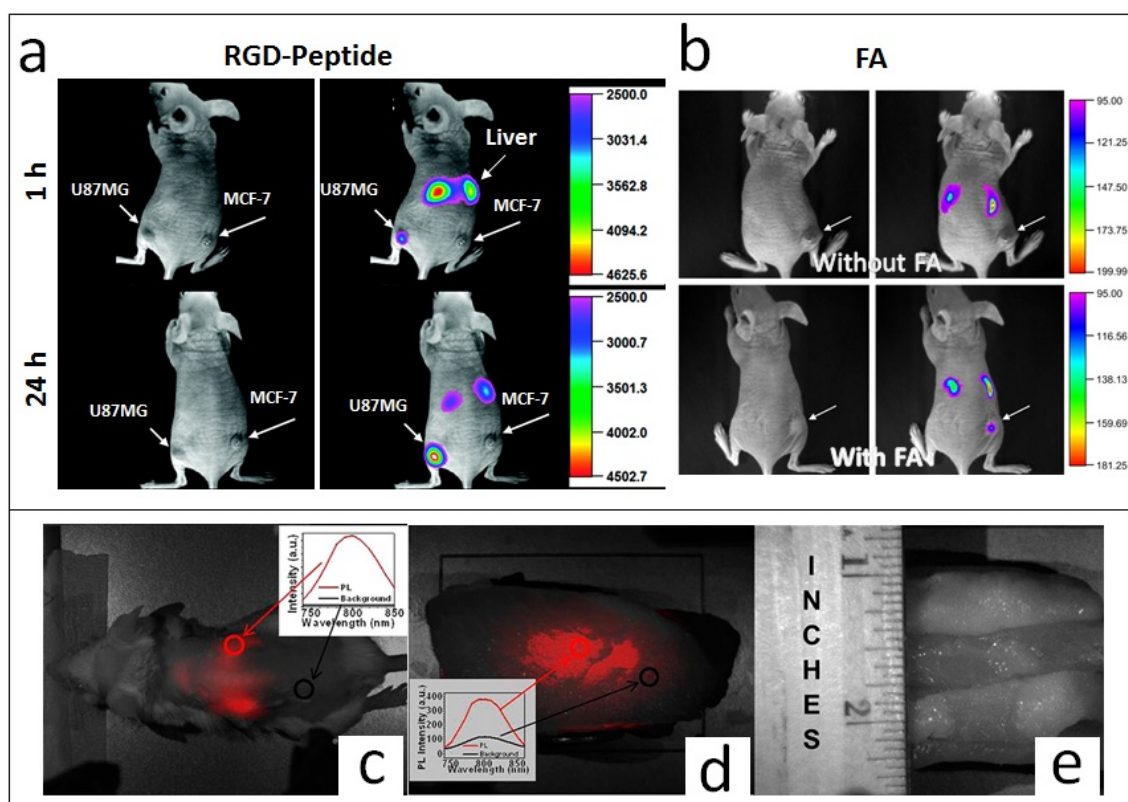


**Figure 3. 15** (a) *In vivo* photoluminescent imaging of the U87MG tumour and MCF-7 tumour bearing mice after intravenous injection with RGD-conjugated NaYF<sub>4</sub>:Yb,Tm for 1 h and 24 h [46]. (b) *In vivo* photoluminescence imaging of HeLa tumour-bearing athymic nude mice after intravenous injection of UCNPs conjugated without or with FA [65]. (c) Imaging of a BALB/c mouse injected with the hyaluronic acid modified core-shell NaYbF<sub>4</sub>:Tm@CaF<sub>2</sub> through tail vein [80]. (d) Photoluminescent image of the cuvette containing NaYbF<sub>4</sub>:Tm@CaF<sub>2</sub> and covered with pork tissue [80]. (e) Bright-field image of the pork tissues (side view), showing the imaging depth [80]. The insets in (c) and (d) were the spectra of the NIR-excited photoluminescence and background taken from the indicated circles [80].

### 3.5.1.2 Multimodal Imaging

In addition to the photoluminescent imaging, there are other imaging modalities that are clinically popular in diagnostics of tumours, including magnetic resonance imaging (MRI), computed tomography (CT), positron emission tomography (PET), and single-photon emission computed tomography (SPECT). These imaging modalities vary in many aspects, and each of them has its own unique benefits and intrinsic limitations. The use of dual- or multi- modalities is highly desirable for accurate diagnostic imaging in providing complementary information from each imaging modality. In this context, contrast agents for MRI, CT, PET and SPECT can be introduced into UCNPs for the development of UCNP-based multimodal imaging probes.

$\text{Gd}^{3+}$  has four unpaired 4f-electrons and has been used as a useful  $T_1$ -weighted MRI agent in imaging blood vessels.  $\text{Gd}^{3+}$ -based UCNPs are considered as promising probes for optical and MRI dual-imaging.  $\text{Gd}^{3+}$  can be co-doped in the UCNP host matrix used as a host matrix material or shell material in the core-shell UCNPs. Park and co-workers have reported the development of a  $\text{Gd}^{3+}$ -based multifunctional UCNPs by generating shell  $\text{NaGdF}_4$  on the core nanocrystal  $\text{NaYF}_4:\text{Yb,Er}$  (Figure 3.16a) [81]. The tumour in their study was clearly observed not only in the photoluminescent imaging *in vivo* (Figure 3.16b), but also in the magnetic resonance imaging (Figure 3.16c) [81]. Another effective approach to introducing MR modality to UCNPs is by combining superparamagnetic iron oxide ( $\text{Fe}_3\text{O}_4$ ) with lanthanide-doped UCNPs for  $T_2$ -enhanced MR imaging. For example, Li and co-workers coated a  $\sim 5\text{-nm}$   $\text{Fe}_x\text{O}_y$  shell on the as-synthesized  $\text{NaYF}_4:\text{Yb,Tm}$  to integrate NIR-to-NIR photoluminescent and magnetic functions in a single UCNPs (Figure 3.16d) [82]. The obtained core-shell UCNPs nanocomposite demonstrated great promise in *in vivo* dual-modality  $T_2$ -enhanced MRI and optical imaging of the lymphatic system (Figure 3.16e-f) [82].

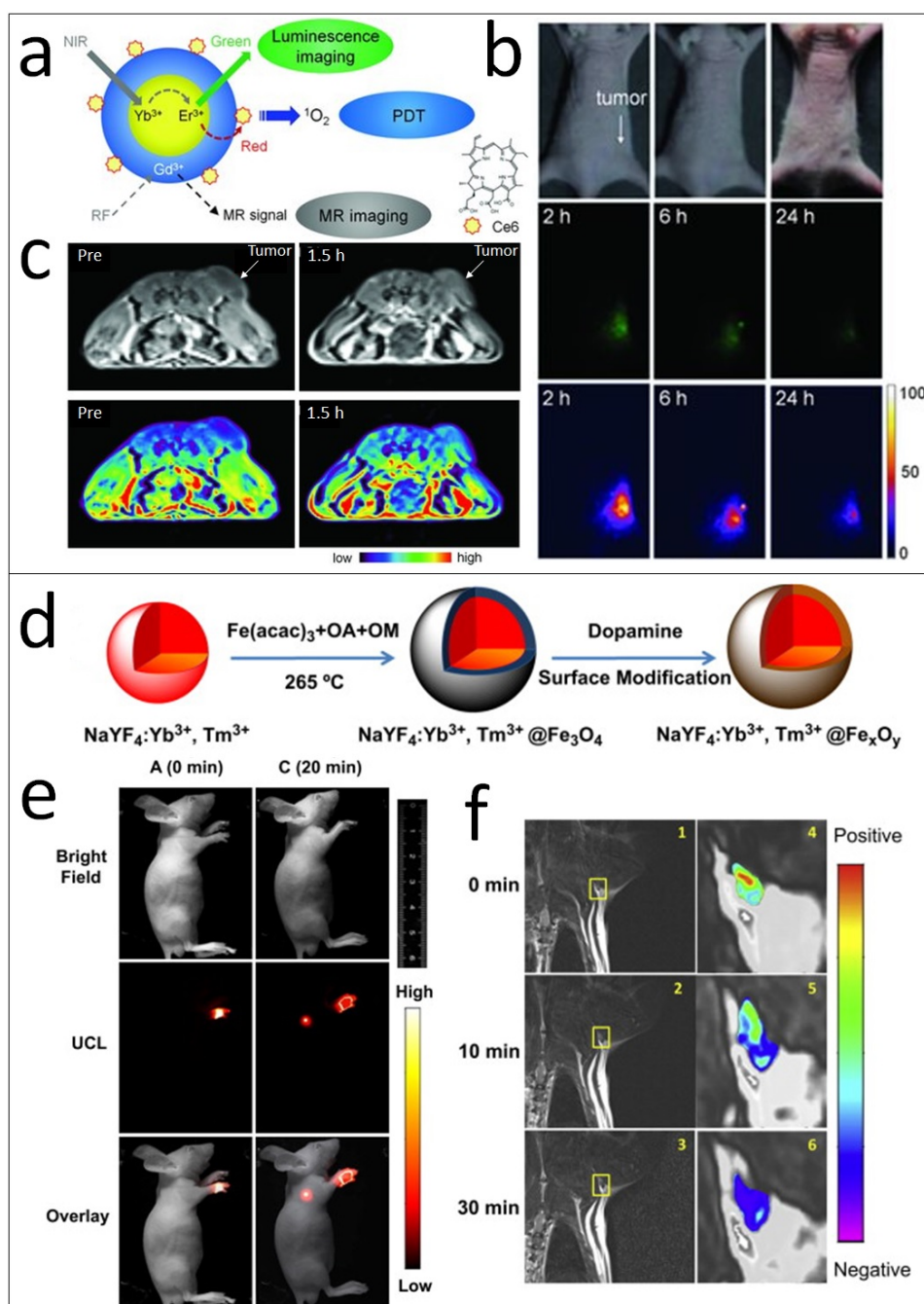


**Figure 3. 16** (a) Schematic illustration of dual-modality imaging and photodynamic therapy using Ce6 loaded  $\text{NaYF}_4:\text{Yb},\text{Er}@\text{NaGdF}_4$  (UCNP-Ce6) [81]. (b) Upconversion luminescence images of nude mice bearing tumour after intravenous injection of the as-produced UCNPs-Ce6 [81]. (c) *In vivo* MR images of tumour-bearing mice after intravenous injection of UCNPs-Ce6. The upper row is T1 images of before and after 1.5 h of injection. The lower row is colour-mapped images of the upper row. [81] (d) Schematic illustration of coating  $\text{NaYF}_4:\text{Yb},\text{Tm}$  with a thin layer of  $\text{Fe}_x\text{O}_y$ . [82] (e) *In vivo* photoluminescent imaging of lymphatic system after injection of  $\text{NaYF}_4:\text{Yb},\text{Tm}@\text{Fe}_x\text{O}_y$  into the nude mouse for 0 min and 20 min. [82] (f) MR images of the armpit region after injection with  $\text{NaYF}_4:\text{Yb},\text{Tm}@\text{Fe}_x\text{O}_y$  for various time points and the corresponding colour-mapped coronal images of the lymph node.[82]

Because of the high X-ray shielding ability, the lanthanide elements that compose UCNPs can also be used as CT contrast agents. For example,  $\text{Yb}^{3+}$ -based UCNPs ( $\text{NaYbF}_4\text{:Er}$ ) and  $\text{Gd}^{3+}$ -based UCNPs ( $\text{NaGdF}_4\text{:Yb,Er}$ ) have been developed as dual-imaging probes for the optical and CT imaging [83, 84].  $\text{Lu}^{3+}$  ions, having the highest atomic number among the lanthanide elements, are recently considered as the new matrix material ions in developing UCNPs ( $\text{NaLuF}_4$ ) for CT imaging. These  $\text{Lu}^{3+}$ -based UCNPs demonstrated much higher contrast effects than that of the commercial iodinated agents, emerging as a highly promising substitute for the traditional CT agents [85]. Li and co-workers synthesized  $\text{Lu}^{3+}$ -based UCNP ( $\text{NaLuF}_4\text{:Yb,Er/Tm}$ ) coated with  $\text{Fe}_3\text{O}_4$  [85]. The resulting core-shell UCNPs exhibited the obvious enhancement of the CT effect in the tumour site after intratumoral injection of the particles (Figure 3.17 I b-d) [85]. Since the  $\text{Fe}_3\text{O}_4$  can be used for MRI, the fabricated nanocomposite can be as a trimodal imaging probe for *in vivo* optical imaging, MRI, and CT (Figure 3.17I a-d) applications [85]. PET radioactive ions such as  $^{18}\text{F}^-$  can be incorporated into a  $\text{NaYF}_4$  matrix via the cation-assisted ligand assembly, resulting in  $^{18}\text{F}$ -labeled UCNPs [45]. These nanoparticles are able to visualize the liver and spleen under both photoluminescent and PET imaging (Figure 3.17 II a-b) [45]. SPECT probe can also be added to UCNPs to functionalize the particles with an additional imaging modality. As such, the clinically SPECT imaging probe,  $^{153}\text{Sm}^{3+}$ , has been added to UCNP and enable the nanoparticles with SPECT imaging capability [86]. Sun and co-workers prepared a multimodal probe that has a  $\text{NaLuF}_4\text{:Yb,Tm}$  core that can be used for CT and optical imaging and a  $\text{NaGdF}_4$  shell doped with  $^{153}\text{Sm}^{3+}$  ions that can be used for MR and SPECT imaging (Figure 3.17 III a-d) [86]. These nanomaterials were demonstrated to be an effective and applicable probe for quadruple-modal imaging *in vivo* [86].

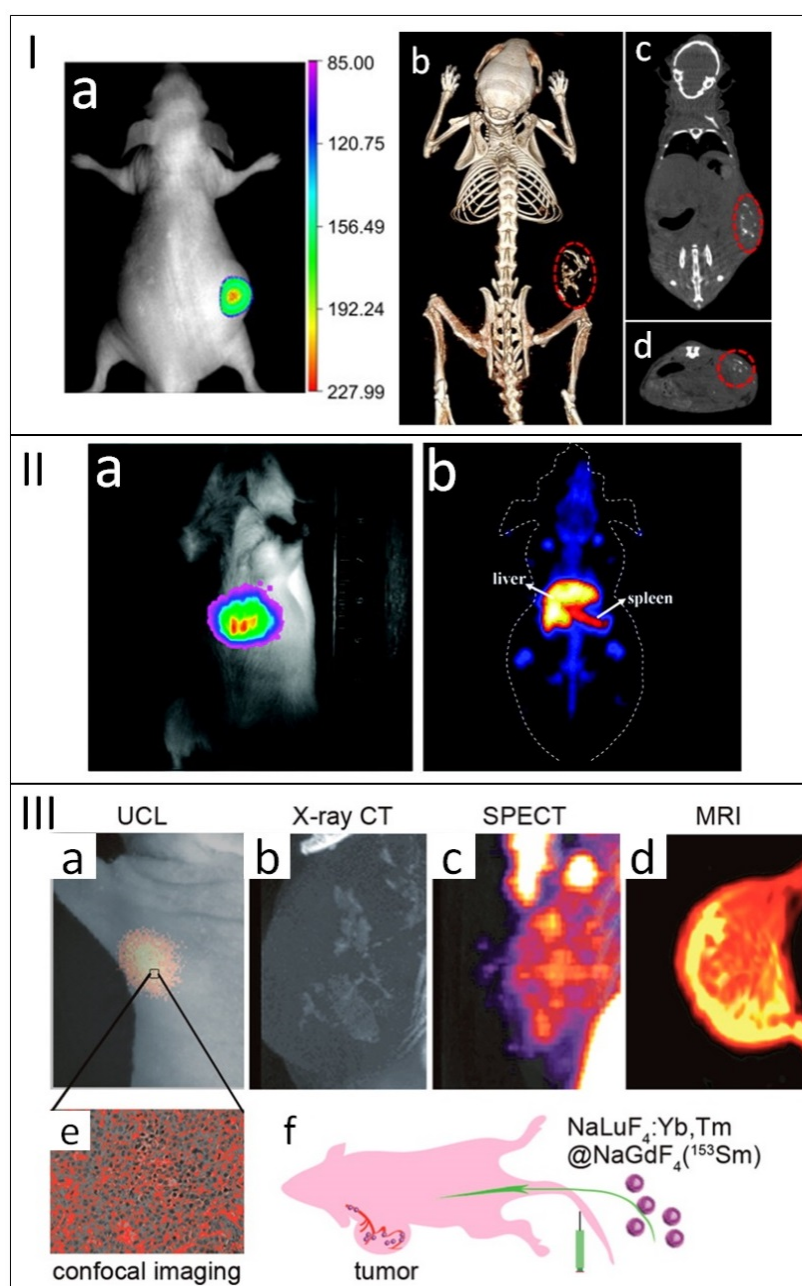


**Figure 3. 17** (I) (a) *In vivo* photoluminescent image of the tumour-bearing nude mouse after intratumoral injection with  $\text{NaLuF}_4:\text{Yb,Er/Tm}@Fe_3O_4$ . *In vivo* CT volume-rendered (b), maximum intensity projection of coronal (c), and transversal (d) images of the tumour-bearing mouse after intratumoral injection with  $\text{NaLuF}_4:\text{Yb,Er/Tm}@Fe_3O_4$ . The position of the tumour was marked with red circles. [85] (II) *In vivo* upconversion luminescence imaging (a) and PET imaging (b) of Kunming mice after injection of  $^{18}\text{F}$ -labeled UCNPs through the tail vein. [45] (III) Four-modal imaging of the tumour-bearing nude mouse 1 h after intravenous injection of  $\text{NaLuF}_4:\text{Yb,Tm}@NaGdF_4(^{153}\text{Sm})$ , focusing on the tumour region. (a) *In vivo* upconversion luminescence image, (b) X-ray CT image, (c) SPECT image, (d) MR image of the tumour. (e) Upconversion luminescence confocal image of the sectioned tissue of tumour. (f) Illustration of imaging tumour angiogenesis using  $\text{NaLuF}_4:\text{Yb,Tm}@NaGdF_4(^{153}\text{Sm})$ . [86]

### 3.5.2 Application of UCNPs for Drug Delivery

Chemotherapy is a cancer treatment method that has achieved great success in clinics. The treatment relies on the use of anticancer drugs to selectively kill cancerous cells by damaging their DNA or halting the cell division. In order to enhance the therapeutic efficacy, reduce adverse side-effects, and minimize the drug dosage, efforts have been dedicated to developing stimuli-responsive nanoparticle delivery systems, with an emphasis on the focussed drug delivery and controlled release. Among various external/internal stimuli, light is a popular means due to its focussed positioning and easy manipulation in regulating the drug release from the nanoparticle delivery system. Compared to the conventional drug release systems using UV or visible lights, UCNP-based delivery device can be activated by NIR irradiation and therefore does not have the drawbacks, as the limited tissue-penetration depth and photodamage to the biological tissues. As such, functional UCNPs are regarded as highly attractive drug carriers in cancer chemotherapy.

NIR-controlled drug delivery based on UCNPs are generally designed to regulate the release of drugs via NIR irradiation or to activate the toxicity of anticancer prodrugs within the tumour [43]. In the first case, UCNPs are generally integrated anticancer reagents and photolabile protecting molecules or photoswitchable molecules that cage drugs inside the nanocarrier. Upon irradiation with the appropriate wavelength, the caged drugs are liberated after photolysis of the protecting molecules or through the mouth opened by photoswitchable molecules. In the UCNP delivery system, UCNPs serve as a powerful NIR light converter to transform NIR irradiation into UV or visible upconversion emission that drives the photoreaction of these protecting compounds. The control of the drug release can be achieved by tuning the power intensity and irradiation time of the excitation light. In a typical example, Ford and co-workers prepared silica-coated  $\text{NaYF}_4:\text{Yb,Er}@ \text{NaYF}_4$  UCNPs and functionalized the surface with Roussin's black salt anion  $\text{Fe}_4\text{S}_3(\text{NO})_7^-$  (RBS) via electrostatic interaction [87]. When exposed to NIR irradiation, the visible emission from UCNPs at 550 nm was able to trigger the uncaging of nitric oxide from RBS to impose suppression effect on tumours [87]. Another example is reported by Shi and co-worker, who developed a novel NIR-triggered photosensitive carrier by loading the azobenzene (azo) groups and DOX inside the mesopores of the silica layer on  $\text{NaYF}_4:\text{Yb,Tm}@ \text{NaYF}_4@m\text{SiO}_2$  (Figure 3.18 a-b) [88].



In their fabricated nanocomposites, *trans* isomer of the azo molecules will transform into the *cis* isomer by UV upconversion emission, whereas the *cis* isomer will reverse to the *trans* isomer again when excited with visible upconversion emission [88]. This back-and-forth wagging motion of the azo molecules is responsible for impelling the release of DOX (Figure 3.18a) [88]. The release amount of DOX can be readily controlled by the NIR power density and irradiation duration (Figure 3.18c). The longer exposure time of NIR light will result in the higher release amount of DOX that will end up in the cell nuclei (Figure 3.18d) [88].

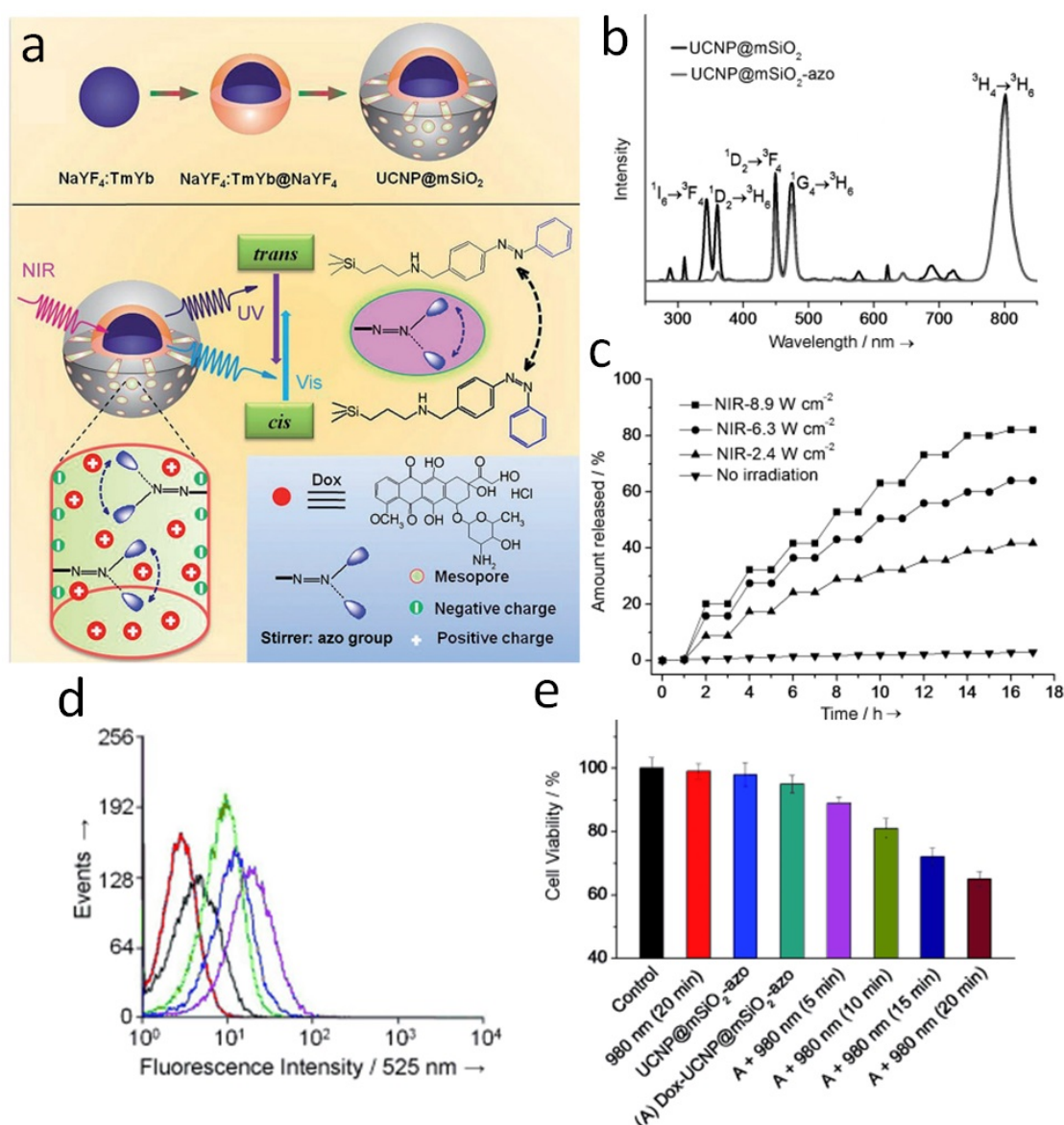


**Figure 3. 18** (a) Synthetic illustration of DOX-loaded UCNP@mSiO<sub>2</sub> and the mechanism of NIR-triggered DOX release. (b) Emission spectra of UCNP@mSiO<sub>2</sub> and UCNP@mSiO<sub>2</sub>-azo under NIR irradiation, demonstrating the absorption of UV light by azo molecules. (c) DOX release in PBS under NIR light irradiation with different power densities (0, 2.4, 6.3 and 8.9 W/cm<sup>2</sup>). (d) Flow cytometry results showing the DOX fluorescent intensity in HeLa cell nuclei. The red curve represents the results of negative control without NIR irradiation. The black, green, blue and purple lines are the results of samples treated with NIR light for 5, 10, 15, and 20 minutes, respectively (e) Cell viability of HeLa cell after different treatment conditions. Reproduced from Ref. [88].

In the second case, nontoxic cancer prodrug can be formulated with UCNP and stimulated by light for transformation into toxic drugs within the tumours. Platinum (Pt)-based drugs are one of this type of anticancer molecules. Pt (IV) complexes generally exhibit less toxicity than the Pt (II) drug, the conversion of which can be activated by using UV light.

Accordingly, the upconverted UV emission from UCNPs can be used as an effective trigger to turn the Pt (IV) prodrugs into cytotoxic Pt (II) inside the tumours without causing an adverse effect to the surrounding healthy tissues. For example, Lin *et al.* have developed an NIR-controlled drug delivery system by conjugating the prodrug, *trans,trans,trans*-[Pt(N<sub>3</sub>)<sub>2</sub>(NH<sub>3</sub>)(py)(O<sub>2</sub>CCH<sub>2</sub>CH<sub>2</sub>COOH)<sub>2</sub>] (denoted as DPP), onto the surface of core-shell NaYF<sub>4</sub>:Yb,Tm@NaGdF<sub>4</sub>:Yb [89]. The NIR-to-UV conversion of the UCNPs is able to selectively trigger the localized activation of the DPP into highly toxic Pt (II) complexes (Figure 3.19a,b), accompanied by the bleaching of DPP at 289 nm (Figure 3.19c) [89]. The prodrug conjugated UCNPs demonstrated much higher antitumor efficacy using NIR irradiation than with UV light activation *in vivo* (Figure 3.19d) [89]. Since the Gd<sup>3+</sup> ions can be used as MRI contrast agent and the Yb<sup>3+</sup> and Gd<sup>3+</sup> ion can be used for CT imaging, the multifunctional nanoparticles in their studies also represent a trimodal imaging probe for photoluminescence, MR and CT imaging (Figure 3.19e) [89].

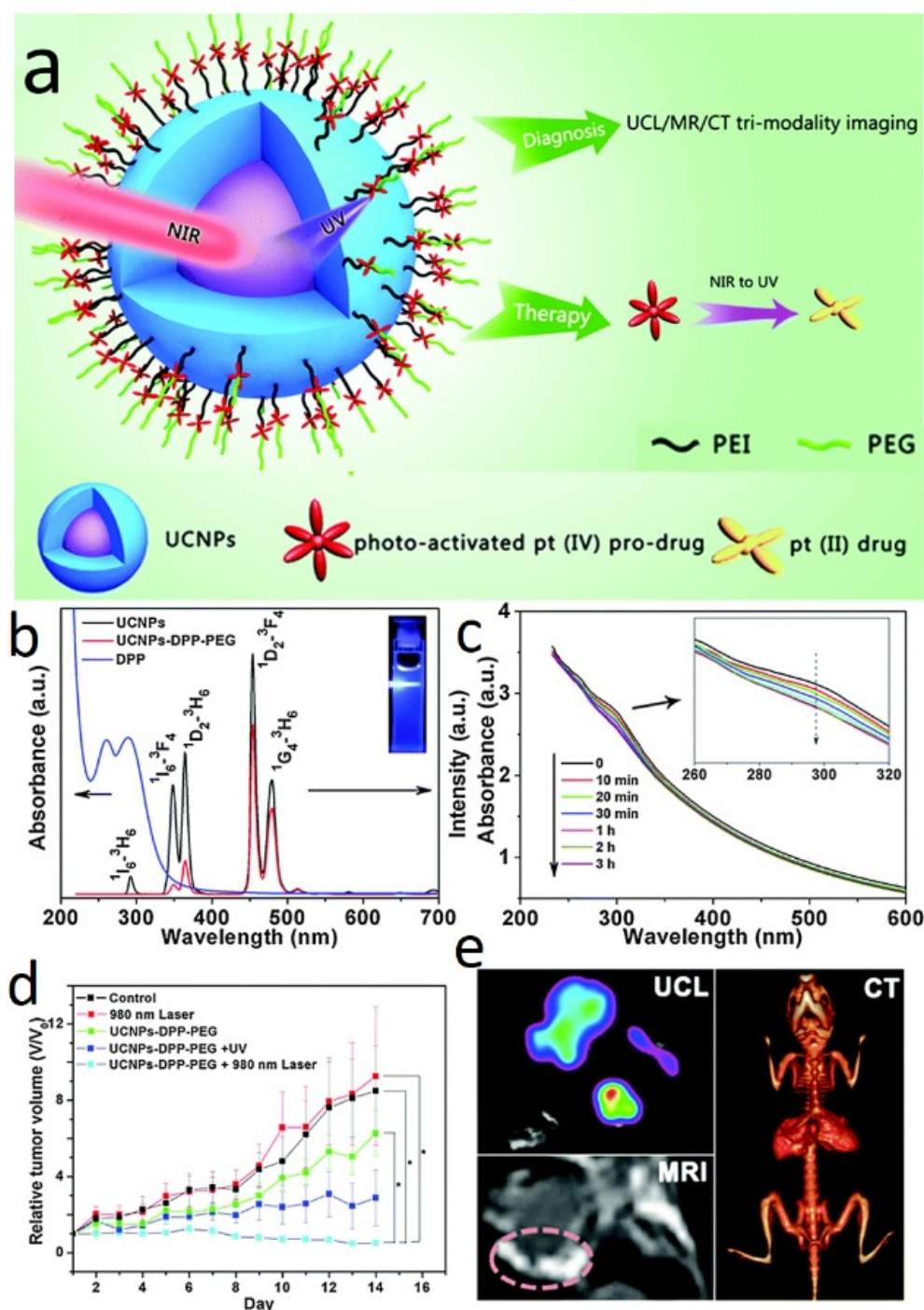


**Figure 3. 19** (a) Schematic illustration of UCNP–DPP–PEG nanocomposites and their application for cancer diagnosis and therapy. (b) The absorption spectrum of DPP overlapping with the upconversion emission spectra of UCNPs and DPP-UCNPs in the blue region. (c) Absorption spectra of UCNP–DPP–PEG as a function of time under NIR irradiation showing the activation of the prodrug. (d) *In vivo* tumour volume of Balb/c mice in different groups after various treatments. (e) *In vivo* UCL/MR/CT trimodal imaging of a tumour-bearing Balb/c mouse after intratumoral injection of the nanocomposites. Reproduced from Ref. [89].

### 3.5.3 Applications of UCNPs in Photodynamic Therapy

Photodynamic therapy is gaining increasing acceptance as a non-invasive treatment option that can be used to for treating early stage cancers or as adjuvant therapy for malignant tumours [90]. The procedure of PDT involves the application of a non-toxic photosensitizer (PS) to a tumour site followed by light irradiation at the drug excitation wavelength [91]. After the absorption of the excitation light, PSs in the ground state makes a transition to the excited state, followed by a decay to a metastable state [91]. In the presence of oxygen, the excited PS can generate cytotoxic reactive oxygen species (such as singlet oxygen) that will lead to tumour destruction via a series of events, such as apoptosis and/or necrosis of cancer cells, shutting down the tumour microvasculature, and stimulating the host immune system [92]. Compared to the other anti-tumour strategies, PDT is superior in the tumour selectivity, high specificity, and non-invasiveness. The irradiation light and PSs used in PDT are individually harmless. The selectivity and specificity of PDT can attribute to the ability to use PSs locally in the diseased sites and the accurate delivery of light to the treated lesions. Moreover, unlike conventional therapies that will suppress the immune system, PDT is able to trigger an immune response of the immune system to recognize, track down and destroy remaining cancer cells after the treatment. However, these advantages are hampered in clinical applications, where PDT is limited to treat superficial tumours due to the short penetration depth of UV and visible light. As a matter of fact, current PDT is only effective in killing tumours at the depth of millimetres.

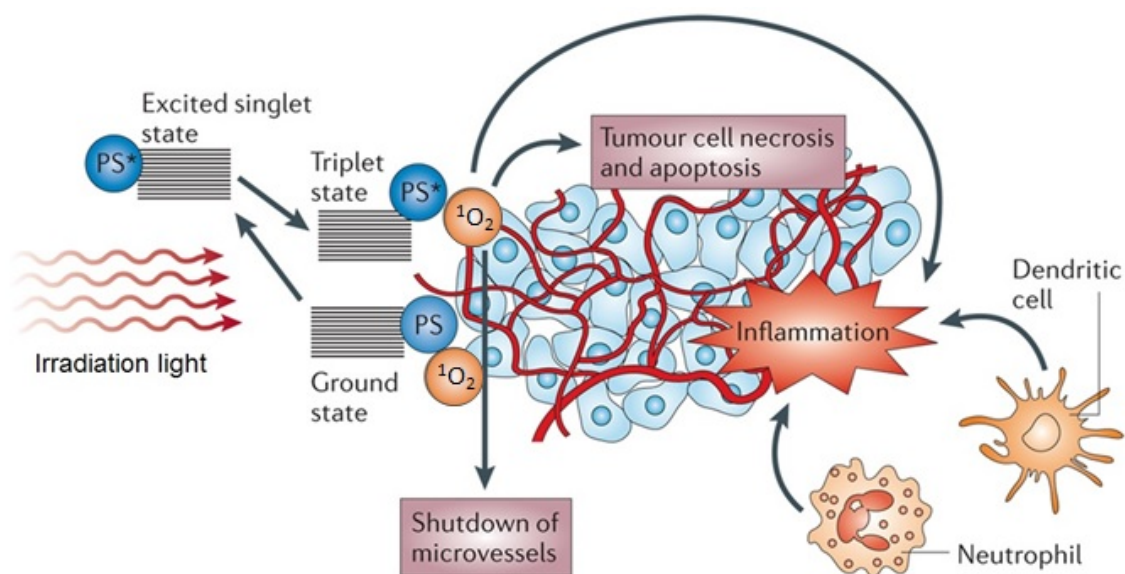


**Figure 3. 20** The mechanism of photodynamic therapy in destroying tumours. Reproduced from Ref. [92].

UCNP harnessing in carrying PSs provides a promising strategy to compensate the disadvantages of the current PDT. In the UCNP-based nanocomposite loaded with PSs, UCNP is capable of converting the deep-penetrating NIR to UV/visible light under the relatively low excitation intensity ( $<1 \text{ W/cm}^2$ ) of the NIR irradiation, thereby initiating the therapeutic effect from the surrounding PSs. NIR irradiation affords the higher accessibility towards the deep tissue, thus providing a possibility of treating deep-seated tumours. The multiple emission and optical tunability of UCNPs provide additional benefits to match absorption of PSs and excite two or more types of PSs in one nanoplatform. In recent years, attempts have been made in the development of the NIR-excited PDT via combination with UCNP and various PSs (summarized in Table 3.1). These studies provide paradigms for a rational design of UCNP-PS nanocomposites.

**Table 3.1** Summary of recent efforts on developing UCNP-based PDT system.

UCNP	PS	Ps activation wavelength (nm)	PS loading method	Targeting agent	PDT experiment	Ref.
NaYF <sub>4</sub> :Yb,Er	MC540	540	Silica encapsulation	antibody	<i>In vitro</i>	[93]
NaYF <sub>4</sub> :Yb,Er	ZnPc	660	Silica encapsulation	–	<i>In vitro</i>	[40]
NaYF <sub>4</sub> :Yb,Er	Ce6	650	Hydrophobic interaction	–	<i>In vivo</i>	[94]
NaYF <sub>4</sub> :Yb,Er	MC540 ZnPc	540 660	Silica encapsulation	FA	<i>In vivo</i>	[77]
NaYF <sub>4</sub> :Yb,Er	pyropheophorbide a	668	Covalent binding	RGD peptide c	<i>In vitro</i>	[95]
NaYF <sub>4</sub> :Yb,Er	RB	550	Covalent binding	FA	<i>In vitro</i>	[62]
NaYF <sub>4</sub> :Yb,Er@NaGdF <sub>4</sub>	Ce6	650	Hydrophobic interaction and covalent binding	–	<i>In vivo</i>	[81]
NaYF <sub>4</sub> :Yb,Er@NaYF <sub>4</sub>	ZnPc	660	Hydrophobic interaction	–	<i>In vitro</i>	[96]
NaYbF <sub>4</sub> :Gd,Tm@NaGdF <sub>4</sub>	Hypocrellin A	475	Hydrophobic interaction	–	<i>In vitro</i>	[97]
NaYF <sub>4</sub> :Yb,Er	ZnPc	660	Hydrophobic interaction	FA	<i>In vivo</i>	[98]

### CHAPTER 3

NaGdF <sub>4</sub> :Yb,Er	RB	550	Hydrophobic interaction	–	<i>In vivo</i>	[99]
NaYF <sub>4</sub> :Yb,Er	MB	650	Physical adsorption	–	<i>In vitro</i>	[100]
NaYF <sub>4</sub> :Yb,Er	ZnPc	660	Covalent binding	–	<i>In vivo</i>	[101]
NaYF <sub>4</sub> :Yb,Gd,Tm	hyaluronated fullerene	475 650	Covalent binding	–	<i>In vitro</i>	[102]
NaYF <sub>4</sub> :Yb,Tm	TiO <sub>2</sub>	348 and 356	Surface coating	–	<i>In vivo</i>	[103]
NaGdF <sub>4</sub> :Yb,Tm	TiO <sub>2</sub>	348 and 356	Physical adsorption	FA	<i>In vivo</i>	[104]
NaYF <sub>4</sub> :Yb,Er@NaYF <sub>4</sub> :Yb,Nd@NaYF <sub>4</sub>	RB	550	Covalent binding	–	<i>In vitro</i>	[105]
NaYF <sub>4</sub> :Yb,Tm	ZnO	330-370	Surface coating	–	<i>In vitro</i>	[106]
NaYF <sub>4</sub> :Yb,Tm	Ce6	650	Covalent binding	–	<i>In vitro</i>	[107]
NaYF <sub>4</sub> :Yb,Er	MB	650	Silica encapsulation	–	<i>In vitro</i>	[108]
NaGdF <sub>4</sub> :Yb,Er,Tm	ZnPc	660	Physical adsorption	–	<i>In vitro</i>	[109]
NaYF <sub>4</sub> :Yb,Er	ZnPc	660	Hydrophobic interaction	c(RGDyK)	<i>In vivo</i>	[110]
NaGdF <sub>4</sub> :Yb,Er@NaGdF <sub>4</sub> :Yb@NaGdF <sub>4</sub> :Yb,Nd	Ce6	650	Covalent binding	Peptide	<i>In vivo</i>	[111]



The pioneering work on UCNP-based PDT has been reported by Zhang and co-workers in which they demonstrated incorporation of MC540 into the dense silica layer of  $\text{NaYF}_4:\text{Yb,Er}@ \text{SiO}_2$  and immobilized the antibodies on the surface of the nanocomposite to achieved targeted therapy [93]. Later on, Liu's group performed an *in vivo* PDT application using UCNP-Ce6 nanocomposite and observed obvious inhibition of the tumour growth after the treatment with NIR irradiation [94]. For the greater therapeutic efficacy, a mesoporous silica layer was coated on UCNPs and used to store the higher payload of PSs. Zhang *et al.* have reported the loading of ZnPc into a mesoporous silica layer of  $\text{NaYF}_4:\text{Yb,Er}@ \text{mSiO}_2$ , and obtained an enhanced cell killing rate [40]. Since upconversion nanoparticles have multicolour emissions, loading two or more photosensitizers that can be activated by individual emission is another strategy to improve the therapy outcome. Following this concept, Zhang and co-workers incorporated two types of PSs (MC540 and ZnPc) into the  $\text{NaYF}_4:\text{Yb,Er}@ \text{mSiO}_2$  nanoplatform, and simultaneously activated MC540 and ZnPc with green and red upconversion emissions from UCNPs, respectively [77]. In comparison with the single-PS nanocomposite, the dual-PSs UCNP system demonstrated the greater PDT efficacy evidenced by the enhanced production of singlet oxygen and reduced cell viability. The pH-responsive technique is also applied to the development of UCNP-based PDT system to enhance the cell internalization of nanoparticles. Lu and co-workers synthesized pH-responsive polymer by co-grafting PAH with PEG and 2,3-dimethylmaleic anhydride (DMMA) and used the yielded co-polymer DMMA-PAH-PEG to cover the Ce6 loaded UCNP, and resulted in a charge-reversible PDT nanocomposite (Figure 3.20a). In the slightly acidic environment in tumour tissues, due to the detachment of DMMA-PAH-PEG, surface charge of the fabricated UCNP-PDT nanocomposites converted from negative into positive (Figure 3.20a). The positive nanocomposites exhibited the higher binding rate towards the cancer cells and thus higher accumulation and retention in tumours as compared to the succinic anhydride coated (SA) negatively-charged particles (UCNP-SA-PEG) (Figure 3.20b-c). Consequently, the *in vivo* PDT effect on delaying tumour growth was significantly improved (Figure 3.20d) [37].

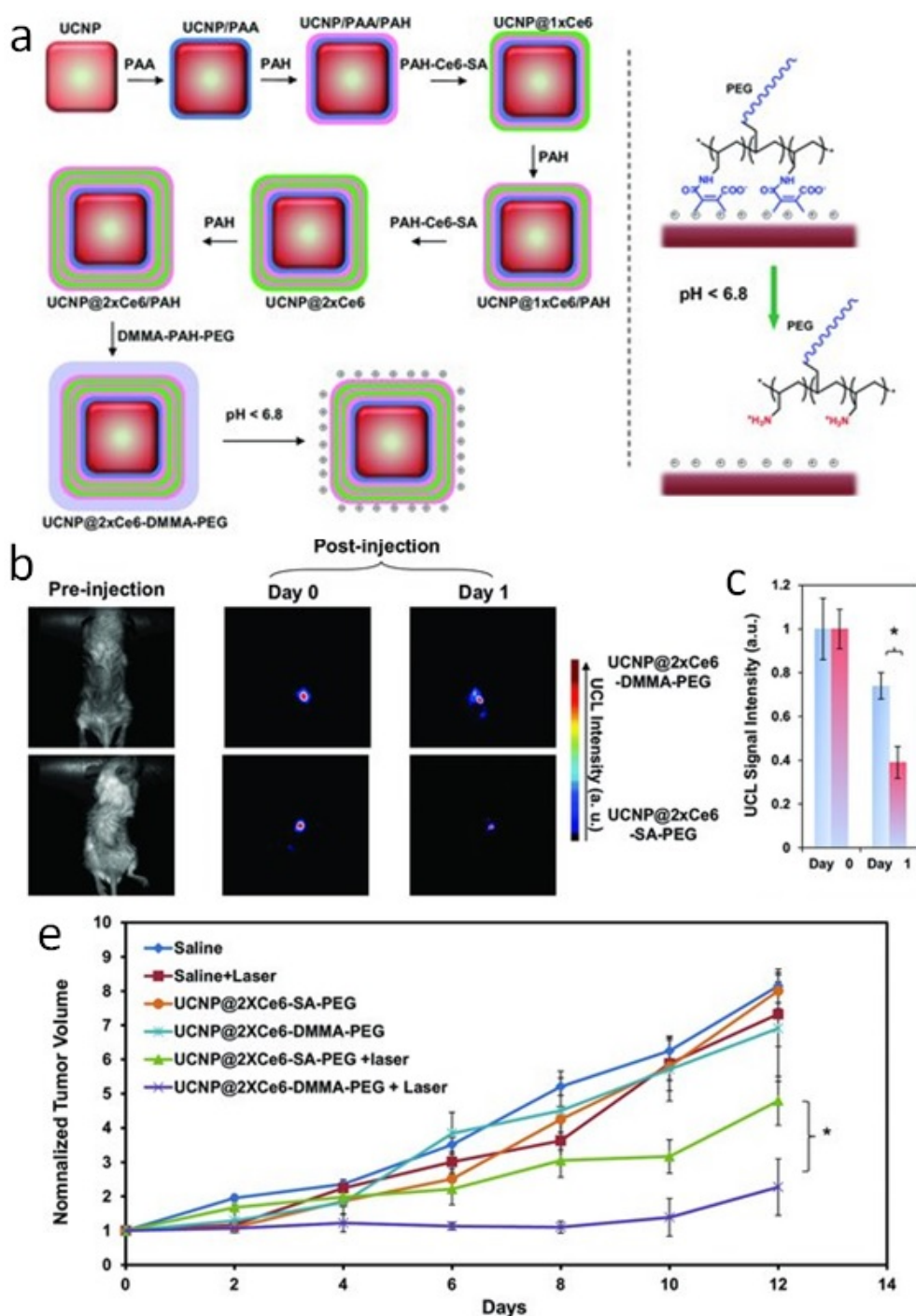


**Figure 3. 21** (a) Schematic illustration of the synthesis of pH-sensitive UCNP-PDT nanocomposites with multi-layers of Ce6 loading. (b) Photoluminescent images of babl/c mice after intratumoral injection of UCNP-DMMA-PEG or UCNP-SA-PEG with the same UCNP dose. (c) Quantification of photoluminescence intensities on images of (b). (d) Normalized tumour volume of different groups of mice after various treatments.

## 3.6 References

1. Zhang, Y.-W., X. Sun, R. Si, L.-P. You, and C.-H. Yan, *Single-crystalline and monodisperse LaF<sub>3</sub> triangular nanoplates from a single-source precursor*. Journal of the American Chemical Society, 2005. **127**(10): p. 3260-3261.
2. Li, Z. and Y. Zhang, *An efficient and user-friendly method for the synthesis of hexagonal-phase NaYF<sub>4</sub>: Yb, Er/Tm nanocrystals with controllable shape and upconversion fluorescence*. Nanotechnology, 2008. **19**(34): p. 345606.
3. Sun, L.-D., H. Dong, P.-Z. Zhang, and C.-H. Yan, *Upconversion of rare earth nanomaterials*. Annual review of physical chemistry, 2015. **66**: p. 619-642.
4. Wang, X., J. Zhuang, Q. Peng, and Y. Li, *A general strategy for nanocrystal synthesis*. Nature, 2005. **437**(7055): p. 121-124.
5. Wang, F., D.K. Chatterjee, Z. Li, Y. Zhang, X. Fan, and M. Wang, *Synthesis of polyethylenimine/NaYF<sub>4</sub> nanoparticles with upconversion fluorescence*. Nanotechnology, 2006. **17**(23): p. 5786.
6. Zhang, F., Y. Wan, T. Yu, F. Zhang, Y. Shi, S. Xie, Y. Li, L. Xu, B. Tu, and D. Zhao, *Uniform Nanostructured Arrays of Sodium Rare - Earth Fluorides for Highly Efficient Multicolor Upconversion Luminescence*. Angewandte Chemie International Edition, 2007. **46**(42): p. 7976-7979.
7. Yi, G., H. Lu, S. Zhao, Y. Ge, W. Yang, D. Chen, and L.-H. Guo, *Synthesis, characterization, and biological application of size-controlled nanocrystalline NaYF<sub>4</sub>: Yb, Er infrared-to-visible up-conversion phosphors*. Nano letters, 2004. **4**(11): p. 2191-2196.
8. Heer, S., K. Kömpe, H.U. Güdel, and M. Haase, *Highly Efficient Multicolour Upconversion Emission in Transparent Colloids of Lanthanide - Doped NaYF<sub>4</sub> Nanocrystals*. Advanced Materials, 2004. **16**(23 - 24): p. 2102-2105.
9. Li, Z. and Y. Zhang, *Monodisperse silica - coated polyvinylpyrrolidone/NaYF<sub>4</sub> nanocrystals with multicolor upconversion fluorescence emission*. Angewandte Chemie, 2006. **118**(46): p. 7896-7899.
10. Yi, G.-S. and G.-M. Chow, *Water-soluble NaYF<sub>4</sub>: Yb, Er (Tm)/NaYF<sub>4</sub>/polymer core/shell/shell nanoparticles with significant enhancement of upconversion fluorescence*. Chemistry of Materials, 2007. **19**(3): p. 341-343.
11. Chen, G., T.Y. Ohulchanskyy, W.C. Law, H. Ågren, and P.N. Prasad, *Monodisperse NaYbF<sub>4</sub>: Tm 3+/NaGdF<sub>4</sub> core/shell nanocrystals with near-infrared to near-infrared upconversion photoluminescence and magnetic resonance properties*. Nanoscale, 2011. **3**(5): p. 2003-2008.
12. Johnson, N.J., A. Korinek, C. Dong, and F.C. van Veggel, *Self-focusing by Ostwald ripening: a strategy for layer-by-layer epitaxial growth on upconverting nanocrystals*. Journal of the American Chemical Society, 2012. **134**(27): p. 11068-11071.
13. Sedlmeier, A. and H.H. Gorris, *Surface modification and characterization of photon-upconverting nanoparticles for bioanalytical applications*. Chemical Society Reviews, 2015. **44**(6): p. 1526-1560.
14. Zhang, T., J. Ge, Y. Hu, and Y. Yin, *A general approach for transferring hydrophobic nanocrystals into water*. Nano letters, 2007. **7**(10): p. 3203-3207.
15. Wong, H.-T., F. Vetrone, R. Naccache, H.L.W. Chan, J. Hao, and J.A. Capobianco, *Water dispersible ultra-small multifunctional KGdF<sub>4</sub>: Tm 3+, Yb 3+ nanoparticles with near-infrared to near-infrared upconversion*. Journal of Materials Chemistry, 2011. **21**(41): p. 16589-16596.
16. Yi, G.S. and G.M. Chow, *Synthesis of Hexagonal - Phase NaYF<sub>4</sub>: Yb, Er and NaYF<sub>4</sub>: Yb, Tm Nanocrystals with Efficient Up - Conversion Fluorescence*. Advanced Functional Materials, 2006. **16**(18): p. 2324-2329.

17. Liu, R., D. Tu, Y. Liu, H. Zhu, R. Li, W. Zheng, E. Ma, and X. Chen, *Controlled synthesis and optical spectroscopy of lanthanide-doped KLaF<sub>4</sub> nanocrystals*. *Nanoscale*, 2012. **4**(15): p. 4485-4491.
18. Bogdan, N., F. Vetrone, R. Roy, and J.A. Capobianco, *Carbohydrate-coated lanthanide-doped upconverting nanoparticles for lectin recognition*. *Journal of Materials Chemistry*, 2010. **20**(35): p. 7543-7550.
19. Yi, G., Y. Peng, and Z. Gao, *Strong red-emitting near-infrared-to-visible upconversion fluorescent nanoparticles*. *Chemistry of Materials*, 2011. **23**(11): p. 2729-2734.
20. Zhang, Q., K. Song, J. Zhao, X. Kong, Y. Sun, X. Liu, Y. Zhang, Q. Zeng, and H. Zhang, *Hexanedioic acid mediated surface-ligand-exchange process for transferring NaYF<sub>4</sub>: Yb/Er (or Yb/Tm) up-converting nanoparticles from hydrophobic to hydrophilic*. *Journal of colloid and interface science*, 2009. **336**(1): p. 171-175.
21. Meiser, F., C. Cortez, and F. Caruso, *Biofunctionalization of Fluorescent Rare - Earth - Doped Lanthanum Phosphate Colloidal Nanoparticles*. *Angewandte Chemie International Edition*, 2004. **43**(44): p. 5954-5957.
22. Kumar, R., M. Nyk, T.Y. Ohulchansky, C.A. Flask, and P.N. Prasad, *Combined optical and MR bioimaging using rare earth ion doped NaYF<sub>4</sub> nanocrystals*. *Advanced Functional Materials*, 2009. **19**(6): p. 853-859.
23. Xiong, L., B. Shen, D. Behera, S.S. Gambhir, F.T. Chin, and J. Rao, *Synthesis of ligand-functionalized water-soluble [18 F] YF<sub>3</sub> nanoparticles for PET imaging*. *Nanoscale*, 2013. **5**(8): p. 3253-3256.
24. Guller, A.E., A.N. Generalova, E.V. Petersen, A.V. Nechaev, I.A. Trusova, N.N. Landyshev, A. Nadort, E.A. Grebenik, S.M. Deyev, and A.B. Shekhter, *Cytotoxicity and non-specific cellular uptake of bare and surface-modified upconversion nanoparticles in human skin cells*. *Nano Research*, 2015. **8**(5): p. 1546-1562.
25. Dong, A., X. Ye, J. Chen, Y. Kang, T. Gordon, J.M. Kikkawa, and C.B. Murray, *A generalized ligand-exchange strategy enabling sequential surface functionalization of colloidal nanocrystals*. *Journal of the American Chemical Society*, 2010. **133**(4): p. 998-1006.
26. Chen, Z., H. Chen, H. Hu, M. Yu, F. Li, Q. Zhang, Z. Zhou, T. Yi, and C. Huang, *Versatile synthesis strategy for carboxylic acid-functionalized upconverting nanophosphors as biological labels*. *Journal of the American Chemical Society*, 2008. **130**(10): p. 3023-3029.
27. Zhou, H.P., C.H. Xu, W. Sun, and C.H. Yan, *Clean and Flexible Modification Strategy for Carboxyl/Aldehyde - Functionalized Upconversion Nanoparticles and Their Optical Applications*. *Advanced Functional Materials*, 2009. **19**(24): p. 3892-3900.
28. Wang, M., J.-L. Liu, Y.-X. Zhang, W. Hou, X.-L. Wu, and S.-K. Xu, *Two-phase solvothermal synthesis of rare-earth doped NaYF<sub>4</sub> upconversion fluorescent nanocrystals*. *Materials Letters*, 2009. **63**(2): p. 325-327.
29. Bogdan, N., F. Vetrone, G.A. Ozin, and J.A. Capobianco, *Synthesis of ligand-free colloidally stable water dispersible brightly luminescent lanthanide-doped upconverting nanoparticles*. *Nano letters*, 2011. **11**(2): p. 835-840.
30. Jiang, G., J. Pichaandi, N.J. Johnson, R.D. Burke, and F.C. van Veggel, *An effective polymer cross-linking strategy to obtain stable dispersions of upconverting NaYF<sub>4</sub> nanoparticles in buffers and biological growth media for biolabeling applications*. *Langmuir*, 2012. **28**(6): p. 3239-3247.
31. Cheng, L., K. Yang, M. Shao, S.-T. Lee, and Z. Liu, *Multicolor in vivo imaging of upconversion nanoparticles with emissions tuned by luminescence resonance energy transfer*. *The Journal of Physical Chemistry C*, 2011. **115**(6): p. 2686-2692.
32. Cheng, L., K. Yang, S. Zhang, M. Shao, S. Lee, and Z. Liu, *Highly-sensitive multiplexed in vivo imaging using PEGylated upconversion nanoparticles*. *Nano research*, 2010. **3**(10): p. 722-732.

33. Budijono, S.J., J. Shan, N. Yao, Y. Miura, T. Hoye, R.H. Austin, Y. Ju, and R.K. Prud'homme, *Synthesis of stable block-copolymer-protected NaYF<sub>4</sub>: Yb<sup>3+</sup>, Er<sup>3+</sup> up-converting phosphor nanoparticles*. Chemistry of Materials, 2009. **22**(2): p. 311-318.
34. Liang, S., X. Zhang, Z. Wu, Y. Liu, H. Zhang, H. Sun, H. Sun, and B. Yang, *Decoration of up-converting NaYF<sub>4</sub>: Yb, Er (Tm) nanoparticles with surfactant bilayer. A versatile strategy to perform oil-to-water phase transfer and subsequently surface silication*. CrystEngComm, 2012. **14**(10): p. 3484-3489.
35. Li, L.L., R. Zhang, L. Yin, K. Zheng, W. Qin, P.R. Selvin, and Y. Lu, *Biomimetic Surface Engineering of Lanthanide - Doped Upconversion Nanoparticles as Versatile Bioprobes*. Angewandte Chemie International Edition, 2012. **51**(25): p. 6121-6125.
36. Wang, L., R. Yan, Z. Huo, L. Wang, J. Zeng, J. Bao, X. Wang, Q. Peng, and Y. Li, *Fluorescence Resonant Energy Transfer Biosensor Based on Upconversion - Luminescent Nanoparticles*. Angewandte Chemie International Edition, 2005. **44**(37): p. 6054-6057.
37. Wang, C., L. Cheng, Y. Liu, X. Wang, X. Ma, Z. Deng, Y. Li, and Z. Liu, *Imaging - Guided pH - Sensitive Photodynamic Therapy Using Charge Reversible Upconversion Nanoparticles under Near - Infrared Light*. Advanced Functional Materials, 2013. **23**(24): p. 3077-3086.
38. Xing, H., W. Bu, S. Zhang, X. Zheng, M. Li, F. Chen, Q. He, L. Zhou, W. Peng, and Y. Hua, *Multifunctional nanoprobes for upconversion fluorescence, MR and CT trimodal imaging*. Biomaterials, 2012. **33**(4): p. 1079-1089.
39. Liu, J.-N., W.-B. Bu, and J.-L. Shi, *Silica Coated Upconversion Nanoparticles: A Versatile Platform for the Development of Efficient Theranostics*. Accounts of Chemical Research, 2015. **48**(7): p. 1797-1805.
40. Qian, H.S., H.C. Guo, P.C.L. Ho, R. Mahendran, and Y. Zhang, *Mesoporous - Silica - coated up - conversion fluorescent nanoparticles for photodynamic therapy*. Small, 2009. **5**(20): p. 2285-2290.
41. Gai, S., P. Yang, C. Li, W. Wang, Y. Dai, N. Niu, and J. Lin, *Synthesis of Magnetic, Up - Conversion Luminescent, and Mesoporous Core-Shell - Structured Nanocomposites as Drug Carriers*. Advanced Functional Materials, 2010. **20**(7): p. 1166-1172.
42. Liu, J., J. Bu, W. Bu, S. Zhang, L. Pan, W. Fan, F. Chen, L. Zhou, W. Peng, and K. Zhao, *Real - Time In Vivo Quantitative Monitoring of Drug Release by Dual - Mode Magnetic Resonance and Upconverted Luminescence Imaging*. Angewandte Chemie International Edition, 2014. **53**(18): p. 4551-4555.
43. Yang, D., Z. Hou, Z. Cheng, C. Li, and J. Lin, *Current advances in lanthanide ion (Ln<sup>3+</sup>)-based upconversion nanomaterials for drug delivery*. Chemical Society Reviews, 2015. **44**(6): p. 1416-1448.
44. Kamimura, M., D. Miyamoto, Y. Saito, K. Soga, and Y. Nagasaki, *Design of poly (ethylene glycol)/streptavidin coimmobilized upconversion nanophosphors and their application to fluorescence biolabeling*. Langmuir, 2008. **24**(16): p. 8864-8870.
45. Liu, Q., Y. Sun, C. Li, J. Zhou, C. Li, T. Yang, X. Zhang, T. Yi, D. Wu, and F. Li, *18F-labeled magnetic-upconversion nanophosphors via rare-earth cation-assisted ligand assembly*. Acs Nano, 2011. **5**(4): p. 3146-3157.
46. Xiong, L., Z. Chen, Q. Tian, T. Cao, C. Xu, and F. Li, *High contrast upconversion luminescence targeted imaging in vivo using peptide-labeled nanophosphors*. Analytical chemistry, 2009. **81**(21): p. 8687-8694.
47. Zhou, J., Y. Sun, X. Du, L. Xiong, H. Hu, and F. Li, *Dual-modality in vivo imaging using rare-earth nanocrystals with near-infrared to near-infrared (NIR-to-NIR) upconversion luminescence and magnetic resonance properties*. Biomaterials, 2010. **31**(12): p. 3287-3295.

48. Cao, T., T. Yang, Y. Gao, Y. Yang, H. Hu, and F. Li, *Water-soluble NaYF<sub>4</sub>: Yb/Er upconversion nanophosphors: Synthesis, characteristics and application in bioimaging*. Inorganic Chemistry Communications, 2010. **13**(3): p. 392-394.
49. Wang, F., Y. Han, C.S. Lim, Y. Lu, J. Wang, J. Xu, H. Chen, C. Zhang, M. Hong, and X. Liu, *Simultaneous phase and size control of upconversion nanocrystals through lanthanide doping*. Nature, 2010. **463**(7284): p. 1061-1065.
50. Dong, B., S. Xu, J. Sun, S. Bi, D. Li, X. Bai, Y. Wang, L. Wang, and H. Song, *Multifunctional NaYF<sub>4</sub>: Yb<sup>3+</sup>, Er<sup>3+</sup>@ Ag core/shell nanocomposites: integration of upconversion imaging and photothermal therapy*. Journal of Materials Chemistry, 2011. **21**(17): p. 6193-6200.
51. Wang, Z.-L., J. Hao, H.L. Chan, G.-L. Law, W.-T. Wong, K.-L. Wong, M.B. Murphy, T. Su, Z. Zhang, and S. Zeng, *Simultaneous synthesis and functionalization of water-soluble up-conversion nanoparticles for in-vitro cell and nude mouse imaging*. Nanoscale, 2011. **3**(5): p. 2175-2181.
52. Nyk, M., R. Kumar, T.Y. Ohulchanskyy, E.J. Bergey, and P.N. Prasad, *High contrast in vitro and in vivo photoluminescence bioimaging using near infrared to near infrared up-conversion in Tm<sup>3+</sup> and Yb<sup>3+</sup> doped fluoride nanophosphors*. Nano letters, 2008. **8**(11): p. 3834-3838.
53. Zhan, Q., J. Qian, H. Liang, G. Somesfalean, D. Wang, S. He, Z. Zhang, and S. Andersson-Engels, *Using 915 nm laser excited Tm<sup>3+</sup>/Er<sup>3+</sup>/Ho<sup>3+</sup>-doped NaYbF<sub>4</sub> upconversion nanoparticles for in vitro and deeper in vivo bioimaging without overheating irradiation*. ACS nano, 2011. **5**(5): p. 3744-3757.
54. Chen, Q., X. Wang, F. Chen, Q. Zhang, B. Dong, H. Yang, G. Liu, and Y. Zhu, *Functionalization of upconverted luminescent NaYF<sub>4</sub>: Yb/Er nanocrystals by folic acid-chitosan conjugates for targeted lung cancer cell imaging*. Journal of Materials Chemistry, 2011. **21**(21): p. 7661-7667.
55. Shen, J., L.-D. Sun, Y.-W. Zhang, and C.-H. Yan, *Superparamagnetic and upconversion emitting Fe<sub>3</sub>O<sub>4</sub>/NaYF<sub>4</sub>: Yb, Er hetero-nanoparticles via a crosslinker anchoring strategy*. Chemical Communications, 2010. **46**(31): p. 5731-5733.
56. Zhou, J., L. Yao, C. Li, and F. Li, *A versatile fabrication of upconversion nanophosphors with functional-surface tunable ligands*. Journal of Materials Chemistry, 2010. **20**(37): p. 8078-8085.
57. Rantanen, T., M.L. Järvenpää, J. Vuojola, K. Kuningas, and T. Soukka, *Fluorescence - Quenching - Based Enzyme - Activity Assay by Using Photon Upconversion*. Angewandte Chemie, 2008. **120**(20): p. 3871-3873.
58. Chatterjee, D.K. and Z. Yong, *Upconverting nanoparticles as nanotransducers for photodynamic therapy in cancer cells*. Nanomedicine, 2008. **3**(1): p. 73-82.
59. Wang, C., L. Cheng, and Z. Liu, *Drug delivery with upconversion nanoparticles for multi-functional targeted cancer cell imaging and therapy*. Biomaterials, 2011. **32**(4): p. 1110-1120.
60. Cheng, L., K. Yang, Y. Li, J. Chen, C. Wang, M. Shao, S.T. Lee, and Z. Liu, *Facile Preparation of Multifunctional Upconversion Nanoprobes for Multimodal Imaging and Dual - Targeted Photothermal Therapy*. Angewandte Chemie, 2011. **123**(32): p. 7523-7528.
61. Wang, L. and Y. Li, *Green upconversion nanocrystals for DNA detection*. Chemical communications, 2006(24): p. 2557-2559.
62. Liu, K., X. Liu, Q. Zeng, Y. Zhang, L. Tu, T. Liu, X. Kong, Y. Wang, F. Cao, and S.A. Lambrechts, *Covalently assembled NIR nanoplatform for simultaneous fluorescence imaging and photodynamic therapy of cancer cells*. ACS Nano, 2012. **6**(5): p. 4054-4062.

63. Li, Z., L. Wang, Z. Wang, X. Liu, and Y. Xiong, *Modification of NaYF<sub>4</sub>: Yb, Er@ SiO<sub>2</sub> nanoparticles with gold nanocrystals for tunable green-to-red upconversion emissions*. The Journal of Physical Chemistry C, 2011. **115**(8): p. 3291-3296.
64. Wang, M., C.-C. Mi, W.-X. Wang, C.-H. Liu, Y.-F. Wu, Z.-R. Xu, C.-B. Mao, and S.-K. Xu, *Immunolabeling and NIR-excited fluorescent imaging of HeLa cells by using NaYF<sub>4</sub>: Yb, Er upconversion nanoparticles*. ACS nano, 2009. **3**(6): p. 1580-1586.
65. Xiong, L.-Q., Z.-G. Chen, M.-X. Yu, F.-Y. Li, C. Liu, and C.-H. Huang, *Synthesis, characterization, and in vivo targeted imaging of amine-functionalized rare-earth up-converting nanophosphors*. Biomaterials, 2009. **30**(29): p. 5592-5600.
66. Zhang, C., Y. Yuan, S. Zhang, Y. Wang, and Z. Liu, *Biosensing platform based on fluorescence resonance energy transfer from upconverting nanocrystals to graphene oxide*. Angewandte Chemie International Edition, 2011. **50**(30): p. 6851-6854.
67. Kumar, M., Y. Guo, and P. Zhang, *Highly sensitive and selective oligonucleotide sensor for sickle cell disease gene using photon upconverting nanoparticles*. Biosensors and bioelectronics, 2009. **24**(5): p. 1522-1526.
68. Lee, J., T.S. Lee, J. Ryu, S. Hong, M. Kang, K. Im, J.H. Kang, S.M. Lim, S. Park, and R. Song, *RGD Peptide-Conjugated Multimodal NaGdF<sub>4</sub>: Yb<sup>3+</sup>/Er<sup>3+</sup> Nanophosphors for Upconversion Luminescence, MR, and PET Imaging of Tumor Angiogenesis*. Journal of Nuclear Medicine, 2013. **54**(1): p. 96-103.
69. Yu, X.-F., Z. Sun, M. Li, Y. Xiang, Q.-Q. Wang, F. Tang, Y. Wu, Z. Cao, and W. Li, *Neurotoxin-conjugated upconversion nanoprobe for direct visualization of tumors under near-infrared irradiation*. Biomaterials, 2010. **31**(33): p. 8724-8731.
70. Lu, H., G. Yi, S. Zhao, D. Chen, L.-H. Guo, and J. Cheng, *Synthesis and characterization of multi-functional nanoparticles possessing magnetic, up-conversion fluorescence and bio-affinity properties*. Journal of Materials Chemistry, 2004. **14**(8): p. 1336-1341.
71. Zhang, X., F. Ai, T. Sun, F. Wang, and G. Zhu, *Multimodal Upconversion Nanoplatform with a Mitochondria-Targeted Property for Improved Photodynamic Therapy of Cancer Cells*. Inorganic chemistry, 2016. **55**(8): p. 3872-3880.
72. Zako, T., H. Nagata, N. Terada, A. Utsumi, M. Sakono, M. Yohda, H. Ueda, K. Soga, and M. Maeda, *Cyclic RGD peptide-labeled upconversion nanophosphors for tumor cell-targeted imaging*. Biochemical and biophysical research communications, 2009. **381**(1): p. 54-58.
73. Ryu, J., H.-Y. Park, K. Kim, H. Kim, J.H. Yoo, M. Kang, K. Im, R. Grailhe, and R. Song, *Facile synthesis of ultrasmall and hexagonal NaGdF<sub>4</sub>: Yb<sup>3+</sup>, Er<sup>3+</sup> nanoparticles with magnetic and upconversion imaging properties*. The Journal of Physical Chemistry C, 2010. **114**(49): p. 21077-21082.
74. Wang, X., K. Liu, G. Yang, L. Cheng, L. He, Y. Liu, Y. Li, L. Guo, and Z. Liu, *Near-infrared light triggered photodynamic therapy in combination with gene therapy using upconversion nanoparticles for effective cancer cell killing*. Nanoscale, 2014. **6**(15): p. 9198-9205.
75. Dai, Y., X. Kang, D. Yang, X. Li, X. Zhang, C. Li, Z. Hou, Z. Cheng, P.a. Ma, and J. Lin, *Platinum (IV) Pro - Drug Conjugated NaYF<sub>4</sub>: Yb<sup>3+</sup>/Er<sup>3+</sup> Nanoparticles for Targeted Drug Delivery and Up - Conversion Cell Imaging*. Advanced healthcare materials, 2013. **2**(4): p. 562-567.
76. Chen, F., S. Zhang, W. Bu, Y. Chen, Q. Xiao, J. Liu, H. Xing, L. Zhou, W. Peng, and J. Shi, *A Uniform Sub - 50 nm - Sized Magnetic/Upconversion Fluorescent Bimodal Imaging Agent Capable of Generating Singlet Oxygen by Using a 980 nm Laser*. Chemistry—A European Journal, 2012. **18**(23): p. 7082-7090.
77. Idris, N.M., M.K. Gnanasammandhan, J. Zhang, P.C. Ho, R. Mahendran, and Y. Zhang, *In vivo photodynamic therapy using upconversion nanoparticles as remote-controlled nanotransducers*. Nature medicine, 2012. **18**(10): p. 1580-1585.

78. He, S., K. Krippes, S. Ritz, Z. Chen, A. Best, H.-J. Butt, V. Mailänder, and S. Wu, *Ultralow-intensity near-infrared light induces drug delivery by upconverting nanoparticles*. Chemical Communications, 2015. **51**(2): p. 431-434.
79. Zhao, L., J. Peng, Q. Huang, C. Li, M. Chen, Y. Sun, Q. Lin, L. Zhu, and F. Li, *Near - Infrared Photoregulated Drug Release in Living Tumor Tissue via Yolk - Shell Upconversion Nanocages*. Advanced Functional Materials, 2014. **24**(3): p. 363-371.
80. Chen, G., J. Shen, T.Y. Ohulchanskyy, N.J. Patel, A. Kutikov, Z. Li, J. Song, R.K. Pandey, H. Ågren, and P.N. Prasad, *( $\alpha$ -NaYbF<sub>4</sub>: Tm<sup>3+</sup>)/CaF<sub>2</sub> core/shell nanoparticles with efficient near-infrared to near-infrared upconversion for high-contrast deep tissue bioimaging*. ACS nano, 2012. **6**(9): p. 8280-8287.
81. Park, Y.I., H.M. Kim, J.H. Kim, K.C. Moon, B. Yoo, K.T. Lee, N. Lee, Y. Choi, W. Park, and D. Ling, *Theranostic Probe Based on Lanthanide - Doped Nanoparticles for Simultaneous In Vivo Dual - Modal Imaging and Photodynamic Therapy*. Advanced Materials, 2012. **24**(42): p. 5755-5761.
82. Xia, A., Y. Gao, J. Zhou, C. Li, T. Yang, D. Wu, L. Wu, and F. Li, *Core-shell NaYF<sub>4</sub>: Yb<sup>3+</sup>, Tm<sup>3+</sup>@ Fe x O y nanocrystals for dual-modality T<sub>2</sub>-enhanced magnetic resonance and NIR-to-NIR upconversion luminescent imaging of small-animal lymphatic node*. Biomaterials, 2011. **32**(29): p. 7200-7208.
83. He, M., P. Huang, C. Zhang, H. Hu, C. Bao, G. Gao, R. He, and D. Cui, *Dual phase - controlled synthesis of uniform lanthanide - doped NaGdF<sub>4</sub> upconversion nanocrystals via an OA/ionic liquid two - phase system for in vivo dual - modality imaging*. Advanced Functional Materials, 2011. **21**(23): p. 4470-4477.
84. Liu, Y., K. Ai, J. Liu, Q. Yuan, Y. He, and L. Lu, *A High - Performance Ytterbium - Based Nanoparticulate Contrast Agent for In Vivo X - Ray Computed Tomography Imaging*. Angewandte Chemie International Edition, 2012. **51**(6): p. 1437-1442.
85. Zhu, X., J. Zhou, M. Chen, M. Shi, W. Feng, and F. Li, *Core-shell Fe<sub>3</sub>O<sub>4</sub>@ NaLuF<sub>4</sub>: Yb, Er/Tm nanostructure for MRI, CT and upconversion luminescence tri-modality imaging*. Biomaterials, 2012. **33**(18): p. 4618-4627.
86. Sun, Y., X. Zhu, J. Peng, and F. Li, *Core-shell lanthanide upconversion nanophosphors as four-modal probes for tumor angiogenesis imaging*. ACS nano, 2013. **7**(12): p. 11290-11300.
87. Garcia, J.V., J. Yang, D. Shen, C. Yao, X. Li, R. Wang, G.D. Stucky, D. Zhao, P.C. Ford, and F. Zhang, *NIR - triggered release of caged nitric oxide using upconverting nanostructured materials*. Small, 2012. **8**(24): p. 3800-3805.
88. Liu, J., W. Bu, L. Pan, and J. Shi, *NIR - Triggered Anticancer Drug Delivery by Upconverting Nanoparticles with Integrated Azobenzene - Modified Mesoporous Silica*. Angewandte Chemie International Edition, 2013. **52**(16): p. 4375-4379.
89. Dai, Y., H. Xiao, J. Liu, Q. Yuan, P.a. Ma, D. Yang, C. Li, Z. Cheng, Z. Hou, and P. Yang, *In vivo multimodality imaging and cancer therapy by near-infrared light-triggered trans-platinum pro-drug-conjugated upconversion nanoparticles*. Journal of the American Chemical Society, 2013. **135**(50): p. 18920-18929.
90. Juarranz, Á., P. Jaén, F. Sanz-Rodríguez, J. Cuevas, and S. González, *Photodynamic therapy of cancer. Basic principles and applications*. Clinical and Translational Oncology, 2008. **10**(3): p. 148-154.
91. Dougherty, T.J., C.J. Gomer, B.W. Henderson, G. Jori, D. Kessel, M. Korbelik, J. Moan, and Q. Peng, *Photodynamic therapy*. Journal of the National Cancer Institute, 1998. **90**(12): p. 889-905.
92. Castano, A.P., P. Mroz, and M.R. Hamblin, *Photodynamic therapy and anti-tumour immunity*. Nature Reviews Cancer, 2006. **6**(7): p. 535-545.



93. Zhang, P., W. Steelant, M. Kumar, and M. Scholfield, *Versatile photosensitizers for photodynamic therapy at infrared excitation*. Journal of the American Chemical Society, 2007. **129**(15): p. 4526-4527.
94. Wang, C., H. Tao, L. Cheng, and Z. Liu, *Near-infrared light induced in vivo photodynamic therapy of cancer based on upconversion nanoparticles*. Biomaterials, 2011. **32**(26): p. 6145-6154.
95. Zhou, A., Y. Wei, B. Wu, Q. Chen, and D. Xing, *Pyropheophorbide A and c (RGDyK) comodified chitosan-wrapped upconversion nanoparticle for targeted near-infrared photodynamic therapy*. Molecular Pharmaceutics, 2012. **9**(6): p. 1580-1589.
96. Wang, Y., H. Wang, D. Liu, S. Song, X. Wang, and H. Zhang, *Graphene oxide covalently grafted upconversion nanoparticles for combined NIR mediated imaging and photothermal/photodynamic cancer therapy*. Biomaterials, 2013. **34**(31): p. 7715-7724.
97. Jin, S., L. Zhou, Z. Gu, G. Tian, L. Yan, W. Ren, W. Yin, X. Liu, X. Zhang, and Z. Hu, *A new near infrared photosensitizing nanoplatfrom containing blue-emitting up-conversion nanoparticles and hypocrellin A for photodynamic therapy of cancer cells*. Nanoscale, 2013. **5**(23): p. 11910-11918.
98. Cui, S., D. Yin, Y. Chen, Y. Di, H. Chen, Y. Ma, S. Achilefu, and Y. Gu, *In vivo targeted deep-tissue photodynamic therapy based on near-infrared light triggered upconversion nanoconstruct*. ACS Nano, 2012. **7**(1): p. 676-688.
99. Chen, Q., C. Wang, L. Cheng, W. He, Z. Cheng, and Z. Liu, *Protein modified upconversion nanoparticles for imaging-guided combined photothermal and photodynamic therapy*. Biomaterials, 2014. **35**(9): p. 2915-2923.
100. Zhou, L., Z. Li, Z. Liu, M. Yin, J. Ren, and X. Qu, *One-step nucleotide-programmed growth of porous upconversion nanoparticles: application to cell labeling and drug delivery*. Nanoscale, 2014. **6**(3): p. 1445-1452.
101. Xia, L., X. Kong, X. Liu, L. Tu, Y. Zhang, Y. Chang, K. Liu, D. Shen, H. Zhao, and H. Zhang, *An upconversion nanoparticle–zinc phthalocyanine based nanophotosensitizer for photodynamic therapy*. Biomaterials, 2014. **35**(13): p. 4146-4156.
102. Wang, X., C.-X. Yang, J.-T. Chen, and X.-P. Yan, *A dual-targeting upconversion nanoplatform for two-color fluorescence imaging-guided photodynamic therapy*. Analytical Chemistry, 2014. **86**(7): p. 3263-3267.
103. Lucky, S.S., N. Muhammad Idris, Z. Li, K. Huang, K.C. Soo, and Y. Zhang, *Titania coated upconversion nanoparticles for near-infrared light triggered photodynamic therapy*. ACS nano, 2015. **9**(1): p. 191-205.
104. Zhang, L.e., L. Zeng, Y. Pan, S. Luo, W. Ren, A. Gong, X. Ma, H. Liang, G. Lu, and A. Wu, *Inorganic photosensitizer coupled Gd-based upconversion luminescent nanocomposites for in vivo magnetic resonance imaging and near-infrared-responsive photodynamic therapy in cancers*. Biomaterials, 2015. **44**: p. 82-90.
105. Lu, F., L. Yang, Y. Ding, and J.J. Zhu, *Highly Emissive Nd<sup>3+</sup> - Sensitized Multilayered Upconversion Nanoparticles for Efficient 795 nm Operated Photodynamic Therapy*. Advanced Functional Materials, 2016.
106. Dou, Q.Q., A. Rengaramchandran, S.T. Selvan, R. Paulmurugan, and Y. Zhang, *Core–shell upconversion nanoparticle–semiconductor heterostructures for photodynamic therapy*. Scientific Reports, 2015. **5**.
107. Dou, Q., C. Teng, E. Ye, and X. Loh, *Effective near-infrared photodynamic therapy assisted by upconversion nanoparticles conjugated with photosensitizers*. Int. J. Nanomed, 2015. **10**: p. 419-432.
108. Wang, H., R.-l. Han, L.-m. Yang, J.-h. Shi, Z.-j. Liu, Y. Hu, Y. Wang, S.-j. Liu, and Y. Gan, *Design and Synthesis of Core–Shell–Shell Upconversion Nanoparticles for NIR-Induced Drug Release, Photodynamic Therapy, and Cell Imaging*. ACS applied materials & interfaces, 2016. **8**(7): p. 4416-4423.

109. Wang, A., W. Jin, E. Chen, J. Zhou, L. Zhou, and S. Wei, *Drug delivery function of carboxymethyl- $\beta$ -cyclodextrin modified upconversion nanoparticles for adamantine phthalocyanine and their NIR-triggered cancer treatment*. Dalton Transactions, 2016. **45**(9): p. 3853-3862.
110. Gao, W., Z. Wang, L. Lv, D. Yin, D. Chen, Z. Han, Y. Ma, M. Zhang, M. Yang, and Y. Gu, *Photodynamic Therapy Induced Enhancement of Tumor Vasculature Permeability Using an Upconversion Nanoconstruct for Improved Intratumoral Nanoparticle Delivery in Deep Tissues*. Theranostics, 2016. **6**(8): p. 1131.
111. Zeng, L., Y. Pan, R. Zou, J. Zhang, Y. Tian, Z. Teng, S. Wang, W. Ren, X. Xiao, and J. Zhang, *808 nm-excited upconversion nanoprobe with low heating effect for targeted magnetic resonance imaging and high-efficacy photodynamic therapy in HER2-overexpressed breast cancer*. Biomaterials, 2016. **103**: p. 116-127.

# 4

## **Deep-Penetrating Photodynamic Therapy with KillerRed Mediated by Upconversion Nanoparticles**

### **4.1 Introduction**

KillerRed is a protein photosensitizer that holds promise as an alternative for the existing hydrophobic photosensitizers that are widely used in clinical photodynamic therapy (PDT) procedures. However, applications of KillerRed to deep-seated tumours are limited by the insufficient penetration depth of the excitation light in highly scattering and absorbing biological tissue. As reviewed in Chapter 3, UCNPs can serve as an efficient means to deliver UV and visible light to centimetre-depth in biological tissue to trigger photobiological processes. In particular, I explored the use of UCNP to transduce deep-penetrating NIR light to green light and induce the phototoxicity of KillerRed in tissue in depth.

This chapter reports the deployment of UCNPs to enhance the treatment depth of KillerRed in PDT. We demonstrated the coupling of KillerRed to UCNPs via covalent conjugation. Colloidal stability and biocompatibility of the assembled nanocomposite KillerRed-UCNP were investigated. The energy transfer between UCNP and KillerRed under NIR irradiation was verified. Furthermore, a deep-seated tumour model was applied to compare the ROS generation level and therapeutic efficiency between NIR-irradiated PDT of KillerRed-UCNP and conventional KillerRed PDT with yellow irradiation. This chapter validated the feasibility of using UCNP to achieve effective treatment of conventional PDT in deep lesions.

### 4.2 Author's Contribution to The Paper

The PhD candidate (Liuen Liang) is the first author of this paper. She carried out most of the wet chemistry experiments in this work, including the synthesis of UCNPs, surface modification of UCNPs, bioconjugation of KillerRed to UCNP, and nanocomposite characterization using TEM, Zetasizer, FTIR, fluorescence spectroscopy, and protein assay. She also performed all the cellular experiments, including imaging of internalized nanocomposites in cells, *in vitro* cytotoxicity study, intracellular ROS generation detection, and PDT efficiency investigation. She then did the majority of data analysis, prepared the figures, and wrote the paper.

Dr. Yiqing Lu set up the irradiation stage, conducted the measurement of nanoparticle luminescence decay, and analysed the corresponding data. Dr. Run Zhang was involved in the project design, interpretation of results, and manuscript revising. Dr. Andrew Care produced the purified KillerRed protein and wrote the corresponding experimental details for the manuscript. Mr. Tiago Ortega built the yellow laser for the sample irradiation. Prof. Sergey Deyev contributed the KillerRed plasmid and developed the protein production procedure. Prof. Yi Qian participated in the manuscript revising. A/Prof. Andrei Zvyagin (the corresponding author) contributed to the main idea of the paper, supervised the project with continuous feedback, and wrote up the paper. All co-authors provided their useful discussion towards the completion of this work.

### 4.3 Full Paper

#### **Deep-penetrating photodynamic therapy with KillerRed mediated by upconversion nanoparticles**

Liuen Liang,<sup>a,b</sup> Yiqing Lu,<sup>a,c</sup> Run Zhang,<sup>a\*</sup> Andrew Care,<sup>a</sup> Tiago A. Ortega,<sup>c</sup> Sergey M. Deyev,<sup>d,e</sup> Yi Qian,<sup>b</sup> and Andrei V. Zvyagin<sup>acfg\*</sup>

<sup>a</sup>ARC Centre of Excellence for Nanoscale BioPhotonics, Macquarie University, North Ryde, Sydney, NSW 2109, Australia

<sup>b</sup>Department of Biomedical Sciences, Macquarie University, North Ryde, Sydney, NSW 2109, Australia

<sup>c</sup>Department of Physics and Astronomy, Macquarie University, North Ryde, Sydney, NSW 2109, Australia

<sup>d</sup>Shemyakin & Ovchinnikov Institute of Bioorganic Chemistry of the Russian Academy of Sciences, Moscow 117997, Russia

<sup>e</sup>National Research Tomsk Polytechnic University, Tomsk 634050, Russia

<sup>f</sup>Laboratory of Optical Theranostics, N. I. Lobachevsky State University of Nizhny Novgorod, Nizhny Novgorod 603950, Russia

<sup>g</sup>Institute for Regenerative Medicine, Sechenov First Moscow State Medical University, Moscow 119991, Russia

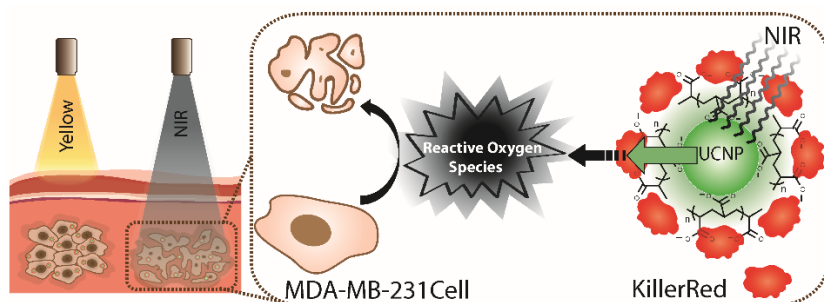
Corresponding authors at: ARC Centre of Excellence for Nanoscale BioPhotonics, Macquarie University, North Ryde, Sydney, NSW 2109, Australia.

E-mail addresses: [run.zhang@mq.edu.au](mailto:run.zhang@mq.edu.au) (R. Zhang), [andrei.zvyagin@mq.edu.au](mailto:andrei.zvyagin@mq.edu.au) (A.V. Zvyagin).

### Abstract

The fluorescent protein KillerRed, a new type of biological photosensitizer, is considered as a promising substitute for current synthetic photosensitizers used in photodynamic therapy (PDT). However, broad application of this photosensitizer in treating deep-seated lesions is challenging due to the limited tissue penetration of the excitation light with the wavelength falling in the visible spectral range. To overcome this challenge, we employ upconversion nanoparticles (UCNPs) that are able to convert deep-penetrating near infrared (NIR) light to green light to excite KillerRed locally, followed by the generation of reactive oxygen species (ROS) to kill tumour cells under centimetre-thick tissue. The photosensitizing bio-nanohybrids, KillerRed-UCNPs, are fabricated through covalent conjugation of KillerRed and UCNPs. The resulting KillerRed-UCNPs exhibit excellent colloidal stability in biological buffers and low cytotoxicity in the dark. Cross-comparison between the conventional KillerRed and UCNP-mediated KillerRed PDT demonstrated superiority of KillerRed-UCNPs photosensitizing by NIR irradiation, manifested by the fact that ~70% PDT efficacy was achieved at 1-cm tissue depth, whereas that of the conventional KillerRed dropped to ~7%.

### Graphical Abstract



**Keywords:** Photodynamic therapy; Photosensitizing protein; Upconversion Nanoparticles; Energy transfer; Reactive oxygen species

## 1. Introduction

Photodynamic therapy (PDT) is an important alternative and supplement for treating cancers and other diseases because of its site specificity, high selectivity, minimal invasiveness, and the capability to stimulate immune response [1-3]. In combatting tumours, PDT relies on photochemical reactions between the excitation light and photosensitizers (PSs) to produce on-demand cytotoxic reactive oxygen species (ROS) in the treated tissue [4, 5]. The existing PSs, including porphyrin and phthalocyanine derivatives, are aromatic and lipophilic, and thus have limited solubility in aqueous solutions as well as low biocompatibility in live organisms [6, 7]. These PSs are prone to aggregation under physiological conditions, leading to poor penetration through the plasma membrane and consequently low therapeutic efficacy [8]. Although the use of amphiphilic delivery systems is helpful to enhance their water-solubility and enable systematic administration, the preparation of pharmaceutical formation is often complicated and poorly reproducible [9].

To overcome this challenge, KillerRed, a genetically encoded red fluorescent protein, has recently been developed as a substitute bio-photosensitizer that offers excellent solubility and biocompatibility in physiological solutions [10]. In view of that, the application of KillerRed as photosensitizer in PDT has attracted considerable attention [10-12]. Under yellow-orange light irradiation (~582 nm), KillerRed demonstrated efficient production of ROS, whose phototoxicity exceeded that of the other fluorescent chromoproteins by at least 1000-fold [10, 13]. This remarkable phototoxicity in addition to its water solubility and biocompatibility has placed KillerRed among the top ideal hydrophilic candidates for PDT, which has been proven in both cell and animal models [14-20].

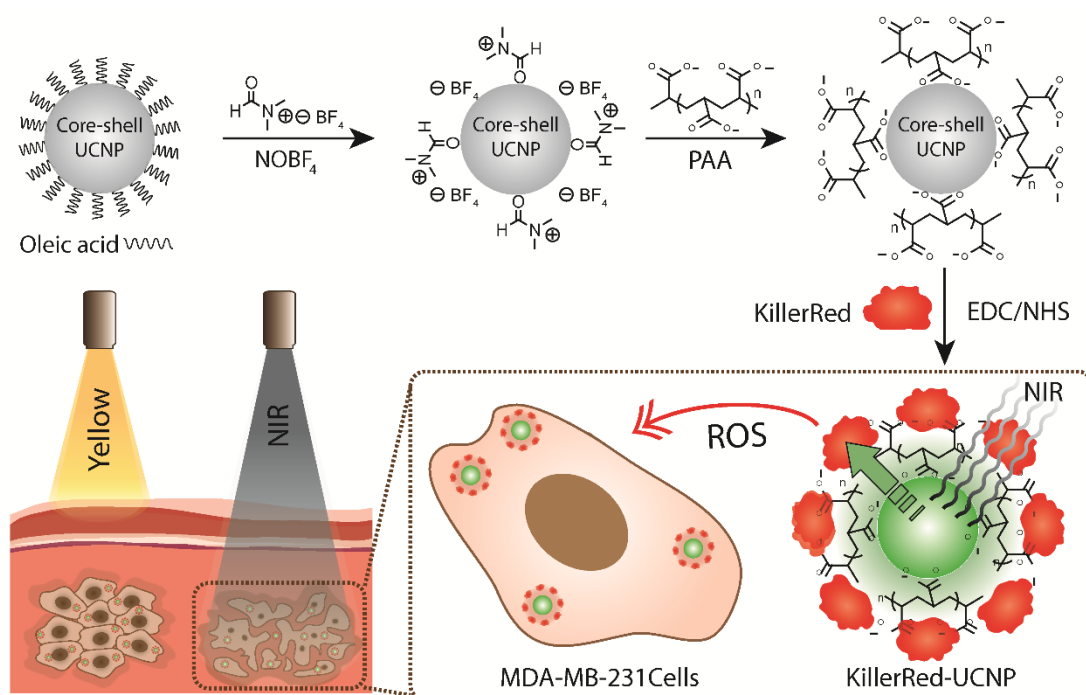
Despite these advantages, the shallow penetration depth of the excitation light (~582 nm) in biological tissues is a major obstacle in the applications of KillerRed, as well as the most state-of-the-art PSs, to deep-seated tumours. This stems from the strong attenuation of the excitation light in highly scattering/absorbing biological tissues in the visible spectral range, and plagues an uptake of PDT in clinical practices [21]. The penetration depth of visible light in living tissue is typically less than 3 mm [22], which hampers the effectiveness of KillerRed-based PDT at the centimetre-depth.

Recently, upconversion nanoparticles (UCNPs) have been introduced to counter this limitation by converting deeply-penetrating near-infrared (NIR) light to visible light and

photoactivating PSs via energy transfer [23-28]. Being inorganic nanocrystals doped with rare-earth ions, UCNPs are capable of being excited at NIR wavelengths (e.g. 980 nm) to radiate anti-Stokes shifted emission at several narrow discrete-bands, which can be selected by controlling the doping elements and concentrations [29, 30]. The use of UCNPs has therefore enabled a lucrative approach to deliver visible or even UV light to deep tissue, and hence photosensitize PDT drugs to treat deep lesions that were not accessible by traditional treatment with visible light [31-34]. Despite that UCNP-mediated PDT has been demonstrated in a number of reports, the deployment of UCNP as energy transfer donor has been mainly reported in the excitation of traditional synthetic PSs [35, 36]. It remains unknown whether KillerRed, a protein photosensitizer, can receive efficient energy transfer for activating PDT after coupling with UCNPs, while retaining its advantages of excellent water solubility and biocompatibility.

In this study, we report covalently-linked assembly of KillerRed and green-emitting UCNP for improving the treatment depth of KillerRed PDT under the NIR excitation. As shown in Scheme 1, oleic acid-capped core-shell UCNPs (hexagonal-phase UCNP core  $\beta$ -NaYF<sub>4</sub>:Yb,Er coated with a shell of NaYF<sub>4</sub>, denoted as  $\beta$ -NaYF<sub>4</sub>:Yb,Er@NaYF<sub>4</sub>) were prepared to convert NIR light to visible light (spectral band, 510–560 nm) for KillerRed activation. Following the modification of the core-shell UCNPs with poly(acrylic acid) (PAA), KillerRed were covalently bound to PAA-UCNPs via EDC/NHS chemistry. The energy transfer process from UCNPs to KillerRed was investigated under the irradiation with 980 nm. The stability, biocompatibility, and capability of intracellular ROS generation of the bio-nanohybrids were examined in detail. Using an *in vitro* deep-seat tumour model, the intracellular ROS generation and anti-cancer effectiveness of KillerRed-UCNPs were compared between visible light and NIR light excitation.





**Scheme 1.** A schematic illustration of KillerRed-UCNP assembly and its application in the centimetre-deep PDT. EDC and NHS refer to *N*-(3-dimethylaminopropyl)-*N'*-ethylcarbodiimide hydrochloride and *N*-hydroxysulfosuccinimide sodium salt, respectively.

## 2. Materials and methods

### 2.1. Materials

Cyclohexane (99.5%), ethanol ( $\geq 99.8\%$ ), nitrosyl tetrafluoroborate ( $\text{NOBF}_4$ , 95%), dichloromethane ( $\geq 99\%$ ), dimethylformamide (DMF), toluene ( $\geq 99.5\%$ ), poly(acrylic acid) (PAA,  $M_n = \sim 130,000$ ), *N*-(3-dimethylaminopropyl)-*N'*-ethylcarbodiimide hydrochloride (EDC·HCl), *N*-hydroxysulfosuccinimide sodium salt (Sulfo-NHS), paraformaldehyde (PFA), thiazolyl blue tetrazolium bromide (MTT), and dimethyl sulfoxide (DMSO), fluorescein isothiocyanate conjugated lectin from triticum vulgaris (wheat) (WGA-FITC), 4'-6-diamidino-2-2phenylindole (DAPI) were obtained from Sigma-Aldrich Chemicals (Sydney, Australia). Image-IT®LIVE green reactive oxygen species detection kit and Thermo-Scientific Pierce Micro BCA protein assay kit were from Thermo Fisher Scientific (USA). All reagents were used as received without further purification.

### 2.2. Production and purification of KillerRed

For the production of His-tagged KillerRed, *E. coli* T7 Express lysY/Iq cells (New England BioLabs) were transformed with the plasmid, pQE30-KillerRed. Cells were

grown in Luria Bertani (LB) medium supplemented with 50 mg/mL carbenicillin and incubated at 37 °C with shaking until the A<sub>600</sub> was within 0.7–1.0. The incubation temperature was then reduced to 27 °C and protein synthesis was induced by the addition of 0.05 mM isopropyl  $\beta$ -D thiogalactoside (IPTG). Cells were harvested 24 h after induction by centrifugation for 20 min at 10,000 g at 4 °C.

His-tagged KillerRed was purified by Ni-NTA affinity chromatography. Briefly, cells were resuspended in ice-cold lysis buffer (50 mM Na-phosphate, pH 7, 300 mM NaCl) supplemented with 1 mg/mL lysozyme and sonicated on ice. Cellular debris was removed by centrifugation for 20 min at 10,000 g at 4 °C. The resulting supernatant was loaded onto a Ni-NTA Agarose column (Qiagen) and washed with lysis buffer. Purified KillerRed was then released from the column with elution buffer (50 mM Na-phosphate, 500 mM Imidazole, pH = 7, 300 mM NaCl) (see Fig. S1), and dialysed (molecular weight cut-off: 10 kDa) against phosphate-buffered saline solution (PBS) of pH 7.4 for 16 h at 4 °C. Protein concentration (mg/mL) was then determined using absorption measurements at a wavelength of 280 nm. KillerRed was aliquoted, snap-frozen, and stored at –80 °C for use in subsequent experiments.

### 2.3. Preparation of PAA modified upconversion nanoparticles

Synthesis of the core-shell NaYF<sub>4</sub>:Yb,Er@NaYF<sub>4</sub> was previously described in detail [37]. To modify UCNPs with PAA, oleic acid (OA) bound to UCNP surface were firstly removed by NOBF<sub>4</sub> followed by replacing NOBF<sub>4</sub> with PAA via a ligand-exchange process [38]. Typically, 5.84 mg of NOBF<sub>4</sub> were dissolved with 5 mL of dichloromethane and mixed with 5 mL of NaYF<sub>4</sub>:Yb,Er@NaYF<sub>4</sub> cyclohexane solution (5 mg/mL). The mixed solution was kept stirring for 10 h in a sealed flask at room temperature (RT). Then, the particles were centrifuged and re-dispersed in DMF. Subsequently, a toluene and cyclohexane mixture (1:1 v/v) was added to flocculate the nanoparticles. After centrifugation, NOBF<sub>4</sub>-capped UCNPs (NOBF<sub>4</sub>-UCNP) were then dispersed with 5 mL of DMF to form a clear solution. Subsequently, 150 mg of PAA was dissolved with 5 mL of DMF and mixed with the DMF dispersion of NOBF<sub>4</sub>-UCNPs. The reaction mixture was heated to 80 °C and kept vigorous stirring in a flask for 3 h. The PAA-coated UCNPs (PAA-UCNPs) were then precipitated with ethanol and washed three times with ethanol and three additional times with water, and finally dispersed in water as the stock solution.

## 2.4. Conjugation of KillerRed to PAA-UCNPs

KillerRed were covalently grafted to PAA-UCNPs using EDC·HCl and Sulfo-NHS as crossing-linking agents. 1 mg of PAA-UCNPs were dispersed with 1 mL of distilled water (pH = 5.5). Then, 0.4 mg of EDC·HCl and 1.1 mg of Sulfo-NHS were added to the PAA-UCNP solution to activate the carboxyl groups of PAA on UCNP surface. The mixture was sonicated for 30 min at RT. After activation, PAA-UCNPs were centrifuged and washed with distilled water for three times. The particles were re-dispersed with 100  $\mu$ L of PBS (pH = 7.4) via sonication in cold condition. Then, the activated nanoparticles were added into a 200  $\mu$ L of PBS containing 50  $\mu$ g of KillerRed. The mixture was sonicated for 30s followed by incubation with tilt rotation at 4 °C for 24 h. The unbound KillerRed molecules were removed by washing the particles with PBS for three times. The KillerRed-PAA-UCNPs (referred to as KillerRed-UCNPs) product was finally re-dispersed in 1 mL PBS and stored at 4 °C for subsequent experiments. The KillerRed content in KillerRed-UCNPs suspension was estimated by the micro bicinchoninic acid (BCA) assay.

## 2.5. Characterization

The morphology and size of nanoparticles were characterized using a Philips CM10 transmission electron microscope (TEM) operated at 100 kV accelerating voltage. Size distribution of nanoparticles was analysed using ImageJ software. The  $\zeta$ -potential and dynamic light scattering (DLS) measurements were carried out using a Malvern Nano ZS90 Zetasizer. Emission and excitation spectra were acquired using a Fluorolog-Tau-3 spectrofluorometer from Jobin Yvon-Horiba equipped with a 450 W Xe lamp and an external 978-nm continuous-wave diode laser with maximum achievable power of  $\sim$ 1.2 W. Fourier transform infrared (FTIR) spectra of surface modified nanoparticles were recorded using a Nicolet iS10 spectrophotometer from Thermo Scientific. Luminescence decays were collected by a home-built setup employing a pulsed 978-nm diode laser as the excitation source and an electronically gateable photomultiplier tube (PMT) as the detector arranged in orthogonal optical paths and synchronised in antiphase. Optical filters were inserted before the PMT to select the emission peaks of either UCNP or KillerRed. The data curves were fitted to exponential functions to obtain the lifetime values using the Origin software.

### 2.6. Imaging of internalized KillerRed-UCNPs in cells

MDA-MB-231 human breast cancer cells were cultured in Dulbecco's modified Eagle's medium (DMEM) supplemented with 10% fetal bovine serum (FBS) and 1% penicillin–streptomycin (P/S) at 37 °C in a 5% CO<sub>2</sub>-containing humidified incubator. Cells were seeded onto cover slips in a 24-well plate at the density of  $2.5 \times 10^4$  cells per well. After 24 h, the original cell culture medium was replaced with fresh culture medium containing KillerRed-UCNPs (100 µg/mL) and incubated for another 12 h. Afterward, cells were washed three times with PBS to remove the free KillerRed-UCNPs and fixed with 4% PFA solution for 15 min at RT. After rinsing with PBS for three times, cell membrane and nuclei were stained with WGA-FITC and DAPI, respectively in a PBS staining solution for 15 min at RT. After washing with PBS for three times, the cells were imaged by an inverted Zeiss LSM 880 laser scanning confocal microscope using a  $\times 40$  oil-immersion objective. The microscope is equipped with a fiber-coupled diode 978 nm laser to illuminate the UCNPs.

### 2.7. Detection of intracellular ROS generation

Intracellular level of ROS production was detected using 2',7'-dichlorodihydrofluorescein diacetate (DCFH-DA) as a fluorescence ROS probe. MDA-MB2-231 cells were seeded into 96-well plates with four parallel wells for each sample and left to grow for 24 h. 200 µg/mL of KillerRed-UCNPs and PAA-UCNPs were incubated with the cells respectively for 12 h. After removing the culture media, 25 µM DCFH-DA solution was applied to the cells and incubated in darkness for 30 min. Cells were then gently rinsed twice with sterile  $1 \times$  Hank's balanced salt solution (HBSS) and exposed to 586 nm ( $0.2 \text{ W/cm}^2$ ) and 980 nm ( $0.5 \text{ W/cm}^2$ ) irradiation respectively for 30 min. Immediately after washing the cells twice with  $1 \times$  HBSS buffer, fluorescence intensity derived from DCFH-DA were measured with a PHERAstar microplate reader at the excitation of 485 nm and emission of 520 nm. Cells were treated with increasing concentrations of *tert*-butylhydro peroxide (TBHP) for 1.5 h as the positive control. To compare the ROS generation from KillerRed-UCNPs induced by yellow and NIR irradiation, pork tissues of 5 mm and 10 mm were placed on top of the cells to simulate the deep-seated tumour conditions *in vitro*. The 586 nm yellow laser used to irradiate cells is a home-built continuous-wave diode Raman laser with a maximum achievable output of 1 W. The NIR laser is a pulsed 980 nm fiber-coupled diode laser with maximum output power of 5 W.

To visualize the ROS generation by imaging, MDA-MB-231 cells were seeded into confocal dishes at a density of  $3 \times 10^5$  cells per dish until adherent and incubated with 200  $\mu\text{g/mL}$  of KillerRed-UCNPs for 12 h. After similar treatment, the fluorescent signal from oxidized product DCF was observed under an Olympus FV1200 confocal laser scanning microscope under 473 nm laser excitation and the emission was collected in the range of 490–590 nm.

### **2.8. In vitro cytotoxicity**

Cytotoxicity of nanoparticles was evaluated by MTT assay. MDA-MB-231 cells were seeded in a 96-well culture plate at a density of 5000 cells per well for 12 h. The cells were treated respectively with PAA-UCNPs and KillerRed-UCNPs at various concentrations of 0, 12.5, 25, 50, 75, 100, 200 and 400  $\mu\text{g/mL}$ , and KillerRed at the concentrations of 0, 0.97, 1.94, 3.88, 5.82, 7.76, 15.52  $\mu\text{g/mL}$ . After 24 h of incubation in the dark, 100  $\mu\text{L}$  of 0.5 mg/mL MTT solution in PBS was added to each well, and the cells were incubated for another 4 h. The excess MTT solution was then carefully removed from each well, and the formed formazan was dissolved in 100  $\mu\text{L}$  of DMSO (dimethyl sulfoxide). Absorbance of the MTT product was acquired at 520 nm using the PHERAstar microplate reader. Cell viability for each concentration were assessed in quintuplicate and was determined as relative to untreated control cells. The following formula was used to calculate the viability of cell growth:

Viability (%) = (mean of absorbance value of treatment group – blank)/(mean absorbance value of control – blank)  $\times$  100 %.

### **2.9. Photodynamic therapy treatment on viability of cancer cells**

Concentration and irradiation dose dependant PDT effect of KillerRed-UCNPs on cell viability was investigated. MDA-MB-231 cells were incubated with different concentrations of KillerRed-UCNPs (0, 100 and 200  $\mu\text{g/mL}$ ) in a 96-well plate, cultured for 24 h at 37 °C in the dark. Subsequently, cells were washed three times with PBS to remove the excess nanoparticles and subject to NIR irradiation for 0, 5, 10 and 15 min. PAA-UCNPs with same loading concentration and NIR exposure duration were used as controls. Finally, after another 12 h of incubation in the dark, cell viability was determined via MTT colorimetric assay. To compare the laser-induced therapeutic efficacy between yellow and NIR irradiation on deep-seat cancer cells, pork tissues of varying thickness (0,

5, and 10 mm) were placed between lasers and cells loaded with KillerRed-UCNPs (200  $\mu\text{g/mL}$ ) during the 30 min of laser exposure.

## 2.10. Statistical analysis

Data are presented as mean  $\pm$  standard deviation. Statistical analysis was performed by one-tailed paired Student's *t*-test. Statistical significance was designated with \* $P < 0.05$ , \*\* $P < 0.01$  and \*\*\* $P < 0.001$ .

## 3. Results and discussion

### 3.1. Synthesis and characterization of KillerRed-UCNPs

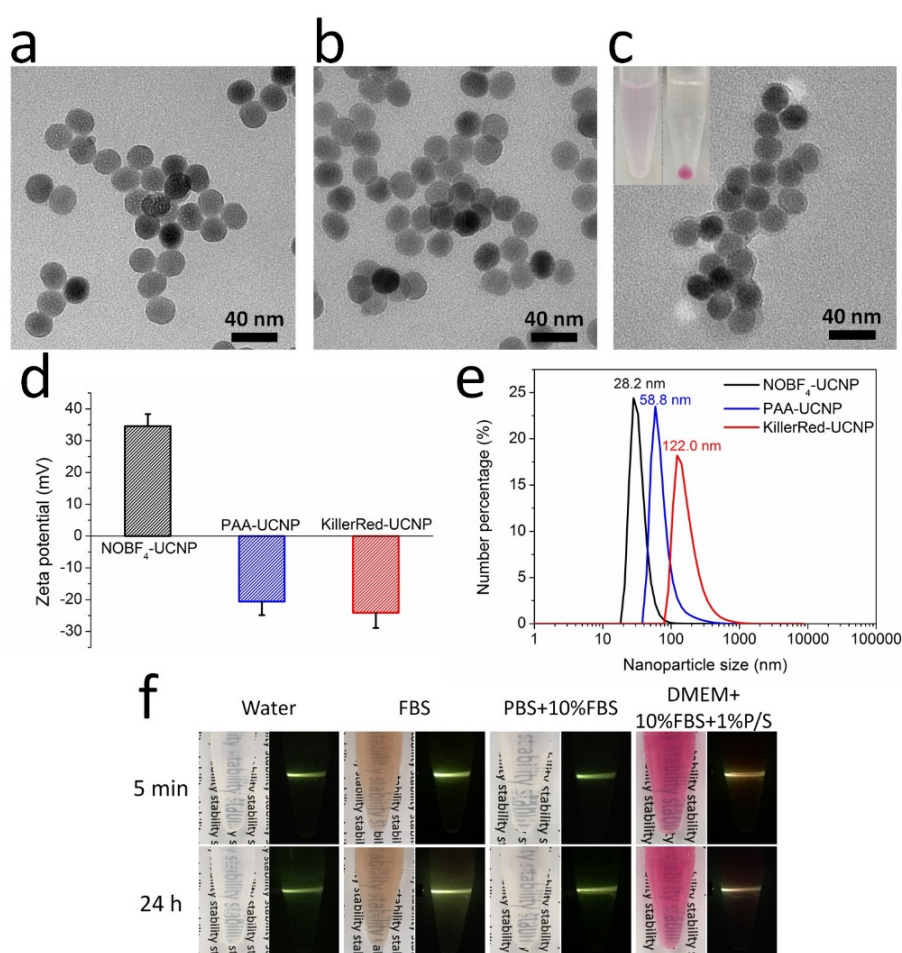


**Fig. 1.** TEM images of (a) NOBF<sub>4</sub>-UCNPs, (b) PAA-UCNPs and (c) KillerRed-UCNPs. Inset in (c), photographs of 3-mg KillerRed-UCNPs dispersed in water (left) and pelleted after centrifugation at 10,000 g for 10 min.  $\zeta$ -potential (d) and DLS size distribution (e) of NOBF<sub>4</sub>-UCNPs, PAA-UCNPs and KillerRed-UCNPs. (f) Photographs of 1-mg KillerRed-UCNPs dispersed in water, FBS, PBS with 10 % FBS, and DMEM cell culture medium supplemented with 10% FBS and 1% P/S, for 5 min and 24 h. The dispersions were illuminated with a 980 nm laser beam.

Core-shell  $\beta$ -NaYF<sub>4</sub>:Yb(18%),Er(2%)@NaYF<sub>4</sub> were fabricated by a two-step crystallisation process.  $\beta$ -NaYF<sub>4</sub>:Yb,Er core particles were firstly synthesized using a solvothermal decomposition method, and Ostwald ripening method was subsequently adopted to grow NaYF<sub>4</sub> shell [39, 40]. Monodispersed core-shell UCNP were formed with the average diameter of  $23.8 \pm 0.8$  nm, as shown in TEM images (Fig. S2a-d). A thin ( $\sim 1$  nm) layer of NaYF<sub>4</sub> deprived of sensitizer/activator ions served to avoid the surface quenching of sensitizer/activator ions in the core. As a result, the upconverted emission was enhanced by 1.4-fold compared to the bare  $\beta$ -NaYF<sub>4</sub>:Yb,Er particles, as illustrated in Fig. S2e. The as-prepared UCNP were hydrophobic due to their hydrophobic oleic acid surface ligand. The core-shell UCNP were rendered hydrophilic via a ligand exchange process with NOBF<sub>4</sub>, followed by replacement of NOBF<sub>4</sub> with PAA (Fig. 1a and b) [38, 41]. Decoration of the nanoparticle surface with PAA not only rendered them water dispersible facilitating conjugation, but also provided abundant carboxylic groups that enabled covalent KillerRed binding to the surface by forming strong amide bonds.

The surface modification of UCNP with PAA were characterized by measuring and analyzing the resultant hydrodynamic diameter,  $\zeta$ -potential and surface moieties by means of DLS and FTIR spectroscopy. As it is shown in Fig. 1d,  $\zeta$ -potential of the sample changed from  $+34.6 \pm 3.8$  mV for NOBF<sub>4</sub>-UCNP to  $-20.6 \pm 4.3$  mV for PAA-UCNP, where the dramatic surface charge downshift was explained by the formation of abundant carboxylic groups on the surface of PAA-UCNP. Moreover, the hydrodynamic size of PAA-UCNP was increased in comparison with that of NOBF<sub>4</sub>-UCNP aqueous colloid, as determined by DLS (Fig. 1e). The size increase was ascribed to the long molecule structure of PAA that swelled in the solution and formed a hydrated PAA layer around UCNP. The successful modification of UCNP with PAA was also confirmed by carrying out FTIR spectral analysis of PAA-UCNP surface groups (see Fig. S3).

Next, we carried out coupling of KillerRed to UCNP and explored two approaches: physical adsorption and covalent conjugation. The results showed that covalent conjugation provided better binding efficiency as detailed in Fig. S4. After conjugating KillerRed to UCNP, the resultant KillerRed-UCNP aqueous colloid turned pink (Fig. 1c inset), with no signs of KillerRed shedding off in the solution (Fig. 1c inset). TEM images of KillerRed-UCNP showed a gelatinous layer ( $\sim 2$  nm) enclosing each particle, which could be interpreted as protein KillerRed coating [42]. The fabricated KillerRed-

UCNPs exhibited identical excitation and emission spectra with those of unbound KillerRed in PBS, displaying the characteristic excitation and emission bands centred at 582 and 606 nm, respectively (Fig. S5). In addition, lyophilized KillerRed-UCNPs were further characterized by FTIR, with the results presented to confirm the KillerRed attachment (Fig. S3).

$\zeta$ -potential value of KillerRed-UCNPs in water ( $-24.1 \pm 4.80$  mV) was more negative than that of PAA-UCNPs due to the KillerRed layer, which carried an overall negative charge on their surface. The hydrodynamic diameter of as-synthesized KillerRed-UCNPs peaked at  $\sim 122$  nm, as it was evident from the DLS analysis (Fig. 1e). The size increase from that of PAA-UCNPs to KillerRed-UCNPs is attributed to the immobilization of KillerRed molecules, and partial aggregation that was noted considering the size distribution broadening. The concentration of KillerRed in the nanoparticle suspension of 200  $\mu\text{g/mL}$  was identified as  $0.52 \pm 0.03$   $\mu\text{M}$  based on the micro BCA assay (Fig. S6) and the purity of KillerRed (Fig. S1). This concentration was slightly higher than that reported  $\text{IC}_{50}$  of KillerRed, which exerted the phototoxic effect on cancer cells [43].

To evaluate the colloidal stability of KillerRed-UCNPs, photographs of KillerRed-UCNP aqueous colloids were taken 5 min and 24 h after dispersion in various physiological solutions. 10% of FBS was used as the representative supplement concentration in cell culture in biological studies. Colloidal samples of KillerRed-UCNP showed no signs of a turbidity increase or precipitation at the bottom of the tested vials. No obvious decrease of the photoluminescence was observed along the trajectory of a narrow 980-nm laser beam passing through the upper half of the vial after 24-h incubation (Fig. 1f). Therefore, the nanocomposites demonstrated excellent physiological stability for 24 h, which represented a time interval sufficient for cellular binding and internalization of nanocomposites.



### 3.2. Energy transfer between KillerRed and UCNP

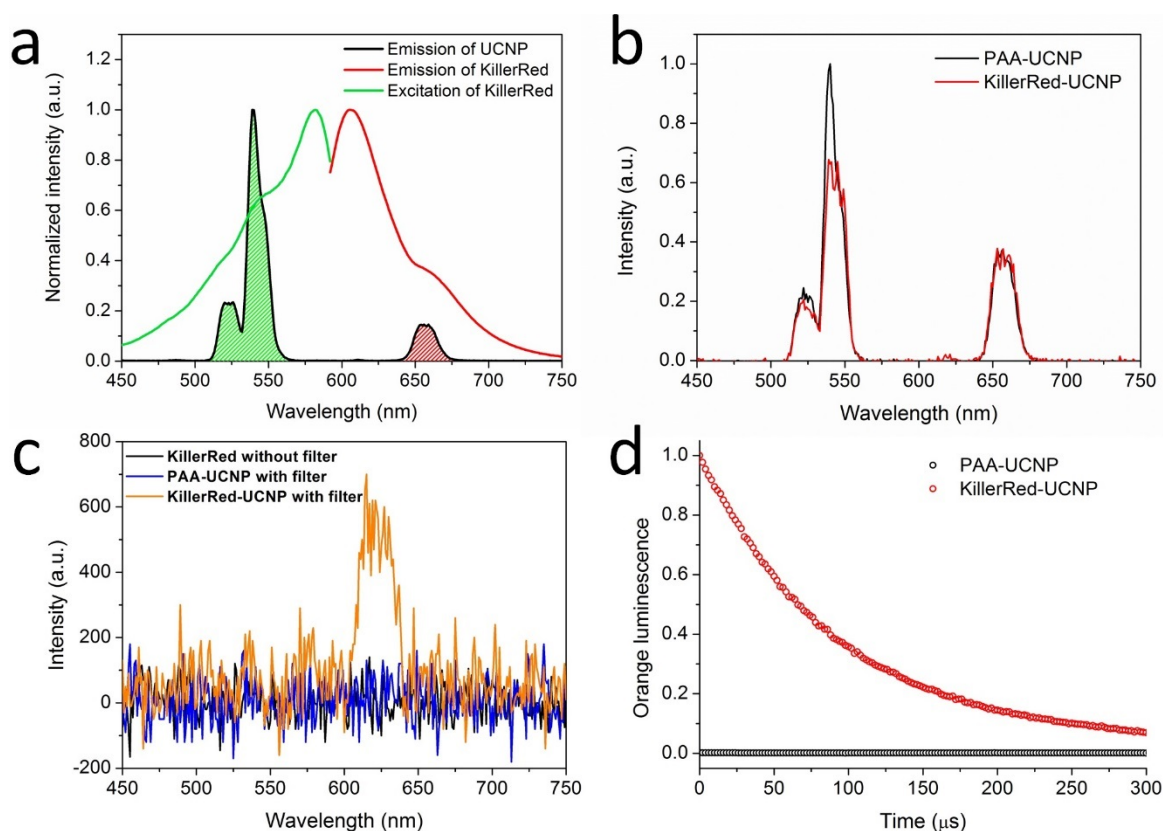


**Fig. 2.** (a) Normalized excitation (green line) and emission (red line) spectra of KillerRed, and emission spectrum of UCNP (black line) under 980-nm excitation. (b) Emission spectra of PAA-UCNPs (black line) and KillerRed-UCNPs (red line) under 980-nm excitation. (c) Emission spectra of KillerRed (black line), PAA-UCNP (blue line) and KillerRed-UCNP (orange line) under 980-nm excitation. The emission spectra of PAA-UCNP and KillerRed-UCNP were collected using a bandpass filter (model 5914-B from New Focus,  $\sim 600$ – $642$  nm). (d) Photoluminescence signal trajectory versus time for PAA-UCNPs (black line) and KillerRed-UCNP (red line) at  $\sim 607$  nm under 980-nm excitation.

The excitation spectrum of KillerRed overlaps with the emission spectrum of UCNP at  $\sim 545$  nm (Fig. 2a), which dictated the use of UCNP green emission band for the photoactivation of KillerRed. In order to confirm the energy transfer process, a comparison of the upconversion photoluminescence (UCL) spectra of KillerRed-UCNPs and unconjugated UCNP was conducted, with the result shown in Fig. 2b. While the red emission of UCNP was almost unaffected by the conjugation, the green emission was notably decreased due to the energy transfer from UCNP to KillerRed (Fig. 2b). The expected characteristic emission of KillerRed in UCL spectrum was difficult to observe because of the high-intensity eclipsing green and red emission of UCNP under 980-nm excitation. The use of a bandpass interference filter ( $\sim 600$ – $642$  nm) allowed to suppress

UCNP emission and enabled detection of the characteristic orange emission peak of KillerRed (cf. Fig. 2a) under 980-nm excitation, as it is shown in Fig. 2c. The detected signal of KillerRed at ~620 nm displayed a small spectral cut-out (600 to 642 nm) of the KillerRed broad emission from 592 to 750 nm, which was reasonably expected when 88% energy transfer efficiency was observed (Fig. S7) Additionally, UCL decay with the lifetime of 104  $\mu$ s was detected at ~607 nm in KillerRed-UCNP sample (Fig. 2d), corroborating the detected energy transfer from UCNPs to KillerRed.

### 3.3. Cellular internalization of KillerRed-UCNPs

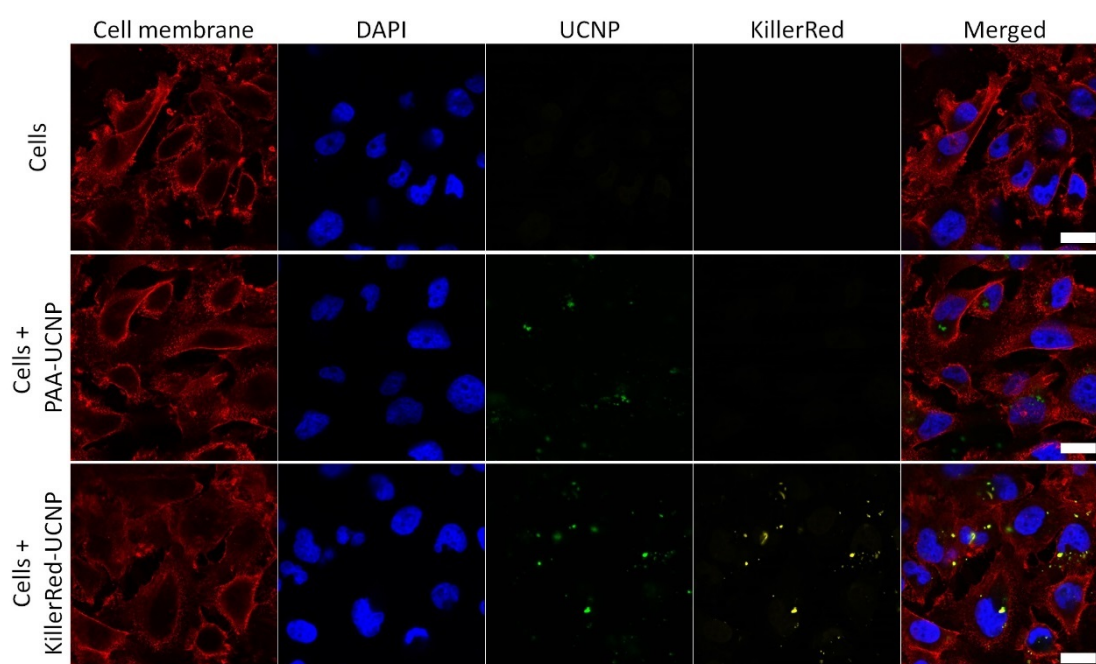


**Fig. 3.** Confocal laser-scanning microscopy images of MDA-MB-231 cells incubated without nanoparticles (top panel), with PAA-UCNPs (middle panel) and KillerRed-UCNPs (bottom panel) for 12 h. The cell membrane, nuclei, UCNPs and KillerRed are pseudocolored in red, blue, green and yellow, respectively. Scale bars, 20  $\mu$ m.

The cell uptake of KillerRed-UCNPs was visualized by confocal microscopy coupled with a 980-nm laser for UCNPs excitation. Human breast cancer cells MDA-MB-231 were incubated with KillerRed-UCNPs for 12 h to allow sufficient time for internalization. After washing off unbound nanoparticles, cells were fixed, followed by membrane staining with WGA-FITC and nuclei staining with DAPI. The cellular uptake was evident from green color of UCNPs emitted in the cell cytoplasm, when excited with 980 nm (Fig. 3). The internalization of nanocomposites was also confirmed in the cross-sectional images of MDA-MB-231 cells after the incubation with KillerRed-UCNPs (Fig. S8). At

the same time, the emission from KillerRed was also clearly observed upon 561-nm excitation, displaying considerable colocalisation with the UCNP photoluminescence in an overlaid image (Fig. 3). Considering the close proximity ( $<10$  nm) between UCNPs and KillerRed was crucial for the efficient energy transfer, these results suggested that KillerRed were bound to UCNPs even after the cellular uptake, which was desirable to induce NIR-triggered production of ROS.

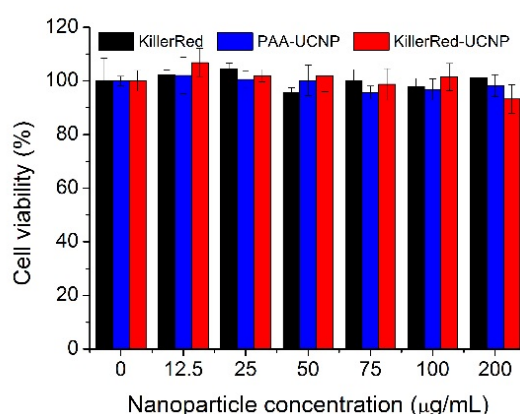


**Fig. 4.** Viability of MDA-MB-231 cells treated with KillerRed, PAA-UCNPs and KillerRed-UCNPs at various concentrations for 24 h in the dark. The KillerRed dosage is in line with the protein content in the corresponding concentration of KillerRed-UCNPs. The data represents means  $\pm$  standard deviation of five replicates.

In order to ensure minimum side-effect of our introduced potential PDT agent, we investigated dark cytotoxicity of KillerRed, PAA-UCNPs and the synthesized nanocomposite KillerRed-UCNPs *in vitro* by using MTT assay. MDA-MB-231 cells were treated with these three agents at the concentrations of 0–200  $\mu\text{g/mL}$  for one day in the dark. The cell viability was evaluated by making use of the absorbance of MTT-formazan product at 520 nm, with the results presented in Fig. 4. It is noted that the concentrations of KillerRed were equivalent to the corresponding protein concentrations in KillerRed-UCNPs, as determined by BCA assay. Upon the addition of the nanoparticles up to 200  $\mu\text{g/mL}$ , the cell viability rates remained higher than 90% for all of the tested samples (Fig. 4). This result demonstrated that no cytotoxic effect of the synthesized KillerRed-UCNPs was found, with no exposure to the excitation light.

## 3.4. Detection of NIR-induced ROS generation in deep-seated tumour cells

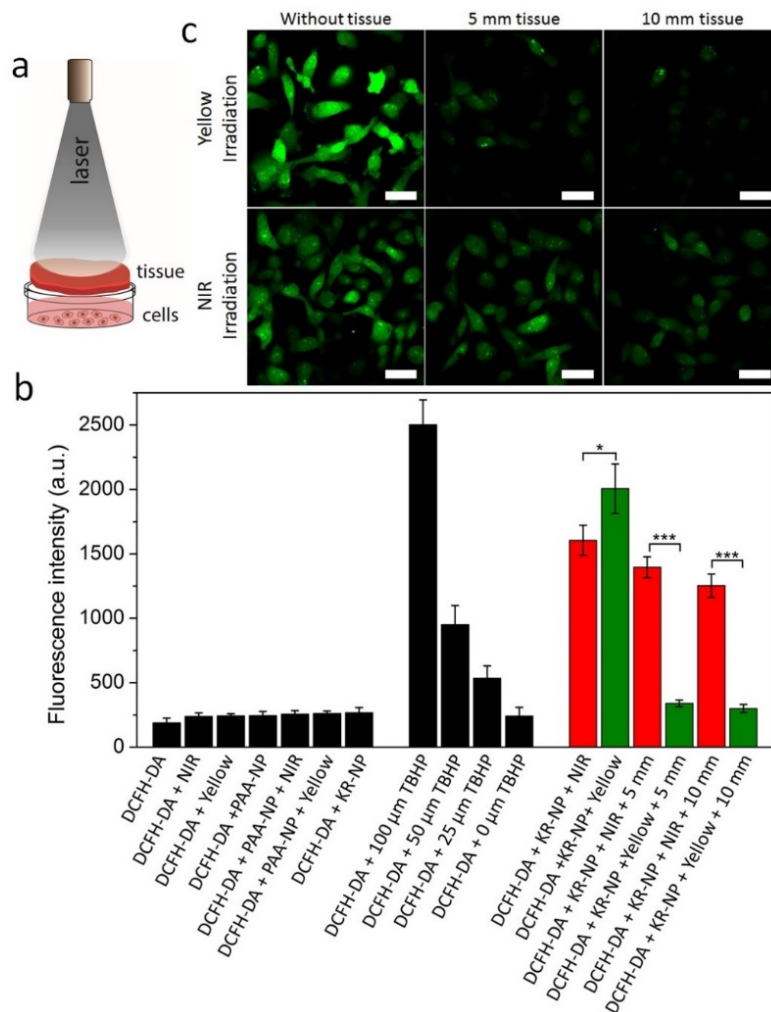


**Fig. 5.** (a) Illustration of an *in vitro* deep-seated tumour model. (b) A histogram of the ROS production level in MDA-MB-231 cells quantified by the fluorescent intensity of DCF at 520 nm. Cells were incubated with DCFH-DA and treated with various combinations of NIR irradiation, yellow irradiation, PAA-UCNPs (PAA-NP) incubation, KillerRed-UCNPs (KR-NP) incubation, and covering cells with tissue of thickness 5 or 10-mm. Cells treated with different concentrations of TBHP served as positive control group. (c) Confocal laser scanning microscopy images of DCF in MDA-MB-231 cells, treated with KillerRed-UCNPs and exposed to yellow (left column) and NIR irradiation (right column) in the presence or absence of tissue coverage. Scale bars, 40  $\mu$ m.

KillerRed has been proven to have high yield of ROS of radicals and hydrogen peroxides upon yellow-red light excitation [44]. The generation of ROS by internalized KillerRed-UCNPs were investigated in live cell by using commercial oxidant-sensing probe DCFH-DA. After entering cells, DCFH-DA is immediately hydrolyzed into non-fluorescent DCFH, and oxidized to fluorescent DCF, when its interaction with ROS takes place.

Therefore, the level of ROS generation is reported in terms of DCF fluorescent intensity. In order to compare the ROS generation in deep-seat tumour cells excited by a yellow laser (586 nm) and NIR laser (980 nm), a piece of pork tissue (0, 5, 10 mm) was placed atop of the cell chamber and laser-illuminated from the above, as schematically shown in Fig. 5a. The excitation intensities of the yellow and NIR beams were set at  $0.2 \text{ W/cm}^2$  and  $0.5 \text{ W/cm}^2$ , respectively, to avoid heating of cells mediated by water molecules (Fig. S9). It is noted that the chosen intensities are widely used to excite KillerRed and UCNPs respectively [28, 43], and the power densities are below the maximum permissible exposure limits for biological systems ( $0.726 \text{ W/cm}^2$  at 980 nm, and  $0.2 \text{ W/cm}^2$  in the range of 400–700 nm) [45]. The recorded fluorescence signals in live cells were shown in Fig. 5b. Negligible fluorescence was detected in all negative control groups together with the significant level of fluorescence detected in the TBHP positive groups, confirming the high level of the ROS production was exclusively resulted from KillerRed-UCNPs under the excitation with the yellow or NIR lasers (Fig. 5b).

When the cells were exposed directly to the laser sources, the fluorescence intensity was higher for the yellow-treated group compared with the NIR group (Fig. 5a). At the same time, covering the cell chamber with pork tissues led to a dramatic decrease ( $>80\%$ ) in the yellow-excited ROS generation, whereas the ROS rate reduced by only  $\sim 13\%$  and  $\sim 21\%$  when NIR light passed through the 5-mm and 10-mm tissue layer, respectively (Fig. 5b), which is comparable to that of the cells subjected to 50–100  $\mu\text{M}$  TBHP treatment. Similar results were obtained when the DCF staining was visualized using the confocal microscopy. As shown in Fig. 5c, MDA-MB-231 cells incubated with KillerRed-UCNPs displayed the stronger green signal beneath the pork tissues, when irradiated with the NIR laser compared to that with yellow irradiation. These results validated the deep-penetration capability of the NIR laser as a photoactivation source and demonstrated the effective production of ROS by KillerRed-UCNPs under NIR irradiation.

## 3.5. Deep-penetrating photodynamic effect of KillerRed-UCNPs

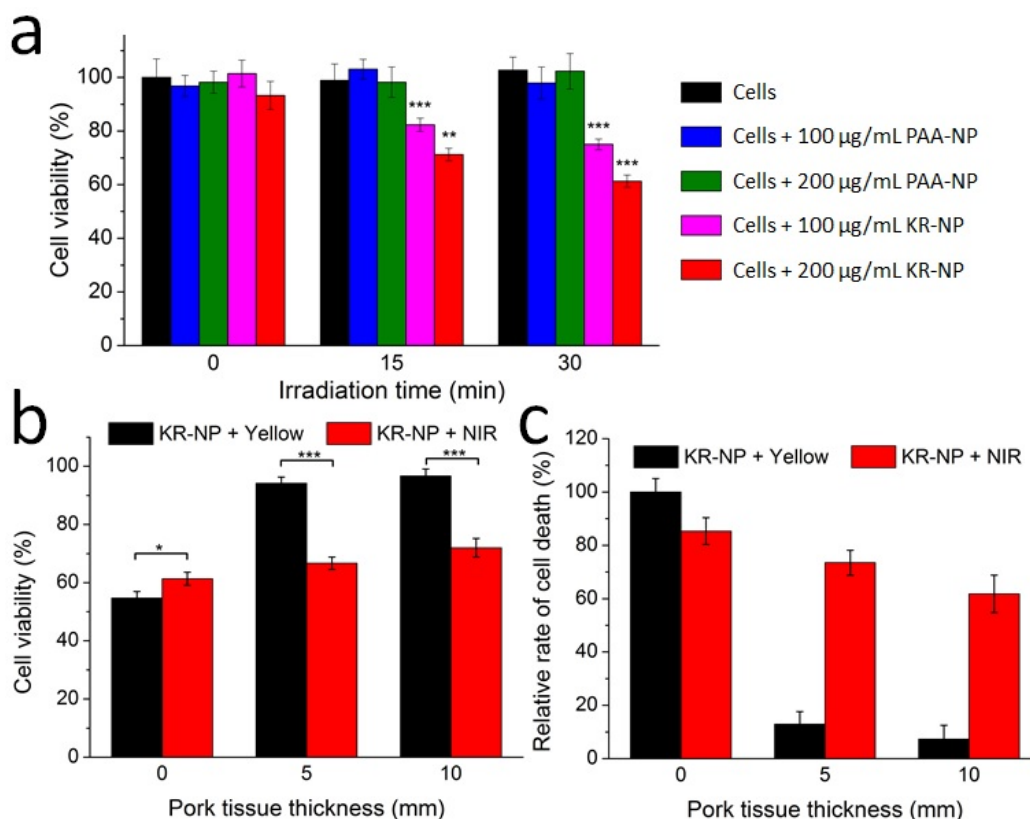


**Fig. 6.** (a) Viability of MDA-MB-231 cells treated with various concentrations (0, 100, and 200  $\mu\text{g/mL}$ ) of PAA-UCNPs, KillerRed-UCNPs and irradiated with the NIR laser at the intensity of 0.5  $\text{W/cm}^2$  for different durations (0, 15, and 30 min). Values are means  $\pm$  standard deviation of five replicates (*t*-test comparing to the control cells without treatment). (b) Cell viability of MDA-MB-231 cells treated with KillerRed-UCNPs (200  $\mu\text{g/mL}$ ) and irradiated with the NIR laser (0.5  $\text{W/cm}^2$ ) and yellow laser (0.2  $\text{W/cm}^2$ ) for 30 min with different thickness (0, 5, and 10 mm) of pork tissue placed on the top of the cell chamber. (c) Cell death rate of MDA-MB-231 cells after PDT treatment as relative to yellow irradiation (0.2  $\text{W/cm}^2$ , 30 min) without tissue blocking. KR and NP stand for KillerRed and UCNPs. Values are means  $\pm$  standard deviation of five replicates.

The cell viability versus the laser intensity was firstly examined by exposing cells to the yellow and NIR irradiation for 30 min. The laser irradiation alone induced neither overheating nor cytotoxicity at the tested intensity level (Fig. S9, S10). The anti-cancer efficacy of KillerRed-UCNPs was assessed by incubating MDA-MB-231 cells with different concentrations of nanoparticles (0, 100, 200  $\mu\text{g/mL}$ ), followed by the NIR exposure for three time intervals: 0, 15 and 30 min. As indicated by the cell viability results, PAA-UCNPs did not cause adverse effects on the cell growth (Fig. 6a). In contrast, KillerRed-UCNPs demonstrated concentration- and light dosage- dependant

phototoxicity on cancer cells (Fig. 6a), where the survival rate of cells was reduced by approximately 40% with the particle concentration of 200  $\mu\text{g/mL}$ , with 30-min light treatment (Fig. 6a).

To investigate the deep tissue PDT, a side-by-side comparison of the phototoxicity of KillerRed-UCNPs between yellow and NIR excitations was carried out. MDA-MB-231 cells were incubated with 200- $\mu\text{g/mL}$  KillerRed-UCNPs and covered with pork tissue of thickness 0, 5 and 10 mm, which was irradiated by the laser sources mounted above (Fig. 5c). Without the tissue coverage, i.e. under direct exposure to the laser light, the phototoxicity was the greatest, with the yellow irradiation marginally more efficient than the NIR, as induced by the corresponding cell death of  $\sim 45\%$  and  $\sim 40\%$ . However, the yellow laser induced insignificant cell death level ( $<6\%$ ), when the tested cells were covered with pork tissue (Fig. 6b), suggesting considerable extinction of the excitation light caused by the tissue absorption and scattering. At the same time, the NIR laser light exposure was much less affected by the overlaying tissue, inducing only marginally lower phototoxicity (measured by the cell death rate decrease as small as  $\sim 10\%$  under the 10-mm tissue). The therapeutic effect of KillerRed-UCNPs triggered by the yellow laser was no longer attainable, when the cell killing rate dropped to 13% under the 5-mm tissue blocking and further to 7% in case of 10-mm tissue. However, more than 60% therapeutic efficacy of KillerRed-UCNPs was maintained under the 10-mm tissues using the NIR excitation source (Fig. 6c). It is noted that the therapeutic outcome of the prepared nanocomposites is remained to be improved for clinical tumour destruction. Nonetheless, the above results have demonstrated promise of UCNPs to enhance the treatment depth of KillerRed, thus pushing the application boundaries of PDT.

#### 4. Conclusions

In this work, we demonstrated the design and application of a new-class hybrid protein-nanoparticle photosensitizer suitable for the extended depth photodynamic treatment (PDT). This photosensitizer was structured as a core-shell upconversion nanoparticle (UCNP) bioconjugated to fluorescent proteins KillerRed. The covalent coupling of UCNPs to KillerRed appeared to be the core design parameter ensuring the stability of the nanoparticle-protein complex from the synthesis to translocation to the cell cytoplasm. UCNPs functioned as a transducer of deeply-penetrating near-infrared light to visible green light, which photosensitized KillerRed producing cytotoxic reactive oxygen species



and killing targeted cells. The resultant nanocomplex exhibited excellent stability in biological solutions and cells and low cytotoxicity in the dark. We demonstrated the KillerRed-UCNP superiority over unbound KillerRed in a proof-of-principle *in vitro* PDT model of cancer cells buried under ~1-cm pork tissue and illuminated with a 980-nm laser of the intensity and dosage acceptable in PDT practices. The successful demonstration of the extended-depth PDT treatment using our hybrid protein-nanoparticle photosensitizer, open several interesting opportunities. Among these, the introduced UCNP-based platform prompts investigation of phototoxic potential of endogenous and exogenous proteins in the visible and even ultraviolet spectral ranges towards their potential utilisation in PDT.

### 5. Conflicts of interest

The authors confirm that there is no conflict of interest.

### Acknowledgements

This work was supported by the Grant to the Government of the Russian Federation (Megagrant), grant number 14.Z50.31.0022 in the part of the optical imaging, and by the RSF grant No. 14-24-00106 in the part of protein engineering and purification, and the Macquarie University Postgraduate Research Funding. Transmission electron microscopy characterization was performed in Macquarie Microscopy Unit under the supervision of Dr Nicole Vella. We also would like to thank Prof Roger Chung from Department of Biomedical Sciences in Macquarie University for access to their confocal laser scanning microscope.

### Appendix A. Supplementary data

Supplementary data associated with this article can be found, in the online version.

### References

- [1] S.B. Brown, E.A. Brown, I. Walker, The present and future role of photodynamic therapy in cancer treatment, *The lancet oncology* 5(8) (2004) 497-508.
- [2] C. Hopper, Photodynamic therapy: a clinical reality in the treatment of cancer, *The lancet oncology* 1(4) (2000) 212-219.
- [3] F.H. van Duijnhoven, R.I. Aalbers, J.P. Rovers, O.T. Terpstra, P.J. Kuppen, The immunological consequences of photodynamic treatment of cancer, a literature review, *Immunobiology* 207(2) (2003) 105-113.
- [4] D.E. Dolmans, D. Fukumura, R.K. Jain, Photodynamic therapy for cancer, *Nat. Rev. Cancer* 3(5) (2003) 380-387.
- [5] B.W. Henderson, T.J. Dougherty, How does photodynamic therapy work?, *Photochem. Photobiol.* 55(1) (1992) 145-157.



- [6] L.B. Josefsen, R.W. Boyle, Unique diagnostic and therapeutic roles of porphyrins and phthalocyanines in photodynamic therapy, imaging and theranostics, *Theranostics* 2(9) (2012) 916-966.
- [7] A. Roby, S. Erdogan, V.P. Torchilin, Solubilization of poorly soluble PDT agent, meso-tetraphenylporphyrin, in plain or immunotargeted PEG-PE micelles results in dramatically improved cancer cell killing in vitro, *Eur. J. Pharm. Biopharm.* 62(3) (2006) 235-240.
- [8] D. Bechet, P. Couleaud, C. Frochot, M.-L. Viriot, F. Guillemain, M. Barberi-Heyob, Nanoparticles as vehicles for delivery of photodynamic therapy agents, *Trends Biotechnol.* 26(11) (2008) 612-621.
- [9] Y.N. Konan, R. Gurny, E. Allémann, State of the art in the delivery of photosensitizers for photodynamic therapy, *J. Photochem. Photobiol. B: Biol.* 66(2) (2002) 89-106.
- [10] M.E. Bulina, D.M. Chudakov, O.V. Britanova, Y.G. Yanushevich, D.B. Staroverov, T.V. Chepurnykh, E.M. Merzlyak, M.A. Shkrob, S. Lukyanov, K.A. Lukyanov, A genetically encoded photosensitizer, *Nat. Biotechnol.* 24(1) (2006) 95-99.
- [11] M. Muthiah, S.-H. Park, M. Nurunnabi, J. Lee, Y.-k. Lee, H. Park, B.-I. Lee, J.-J. Min, I.-K. Park, Intracellular delivery and activation of the genetically encoded photosensitizer Killer Red by quantum dots encapsulated in polymeric micelles, *Colloids Surf. B. Biointerfaces* 116 (2014) 284-294.
- [12] D.S. Kuznetsova, M.V. Shirmanova, V.V. Dudenkova, P.V. Subochev, I.V. Turchin, E.V. Zagaynova, S.A. Lukyanov, B.E. Shakhov, V.A. Kamensky, Photobleaching and phototoxicity of KillerRed in tumor spheroids induced by continuous wave and pulsed laser illumination, *J. Biophotonics* 8(11-12) (2015) 952-960.
- [13] M.E. Bulina, K.A. Lukyanov, O.V. Britanova, D. Onichtchouk, S. Lukyanov, D.M. Chudakov, Chromophore-assisted light inactivation (CALI) using the phototoxic fluorescent protein KillerRed, *Nat. Protoc.* 1(2) (2006) 947-953.
- [14] M.V. Shirmanova, E.O. Serebrovskaya, K.A. Lukyanov, L.B. Snopova, M.A. Sirotkina, N.N. Prodanetz, M.L. Bugrova, E.A. Minakova, I.V. Turchin, V.A. Kamensky, Phototoxic effects of fluorescent protein KillerRed on tumor cells in mice, *J. Biophotonics* 6(3) (2013) 283-290.
- [15] Z.-X. Liao, Y.-C. Li, H.-M. Lu, H.-W. Sung, A genetically-encoded KillerRed protein as an intrinsically generated photosensitizer for photodynamic therapy, *Biomaterials* 35(1) (2014) 500-508.
- [16] T. Shibuya, Y. Tsujimoto, Deleterious effects of mitochondrial ROS generated by KillerRed photodynamic action in human cell lines and *C. elegans*, *J. Photochem. Photobiol. B: Biol.* 117 (2012) 1-12.
- [17] S.-J. Tseng, Z.-X. Liao, S.-H. Kao, Y.-F. Zeng, K.-Y. Huang, H.-J. Li, C.-L. Yang, Y.-F. Deng, C.-F. Huang, S.-C. Yang, Highly specific in vivo gene delivery for p53-mediated apoptosis and genetic photodynamic therapies of tumour, *Nat. Commun.* 6 (2015).
- [18] E.O. Serebrovskaya, A.P. Ryumina, M.E. Boulina, M.V. Shirmanova, E.V. Zagaynova, E.A. Bogdanova, S.A. Lukyanov, K.A. Lukyanov, Phototoxic effects of lysosome-associated genetically encoded photosensitizer KillerRed, *J. Biomed. Opt.* 19(7) (2014) 071403-071403.
- [19] D.C. Williams, R. El Bejjani, P.M. Ramirez, S. Coakley, S.A. Kim, H. Lee, Q. Wen, A. Samuel, H. Lu, M.A. Hilliard, Rapid and permanent neuronal inactivation in

- vivo via subcellular generation of reactive oxygen with the use of KillerRed, *Cell Rep.* 5(2) (2013) 553-563.
- [20] E.O. Serebrovskaya, T.V. Gorodnicheva, G.V. Ermakova, E.A. Solovieva, G.V. Sharonov, E.V. Zagaynova, D.M. Chudakov, S. Lukyanov, A.G. Zaisky, K.A. Lukyanov, Light-induced blockage of cell division with a chromatin-targeted phototoxic fluorescent protein, *Biochem. J.* 435(1) (2011) 65-71.
- [21] J.V. Frangioni, In vivo near-infrared fluorescence imaging, *Curr. Opin. Chem. Biol.* 7(5) (2003) 626-634.
- [22] K.R. Byrnes, R.W. Waynant, I.K. Ilev, X. Wu, L. Barna, K. Smith, R. Heckert, H. Gerst, J.J. Anders, Light promotes regeneration and functional recovery and alters the immune response after spinal cord injury, *Lasers Surg. Med.* 36(3) (2005) 171-185.
- [23] J. Hu, Y.a. Tang, A.H. Elmenoufy, H. Xu, Z. Cheng, X. Yang, Nanocomposite - Based Photodynamic Therapy Strategies for Deep Tumor Treatment, *Small* 11(44) (2015) 5860-5887.
- [24] N.M. Idris, M.K.G. Jayakumar, A. Bansal, Y. Zhang, Upconversion nanoparticles as versatile light nanotransducers for photoactivation applications, *Chem. Soc. Rev.* 44(6) (2015) 1449-1478.
- [25] N.M. Idris, M.K. Gnanasammandhan, J. Zhang, P.C. Ho, R. Mahendran, Y. Zhang, In vivo photodynamic therapy using upconversion nanoparticles as remote-controlled nanotransducers, *Nature Medicine* 18(10) (2012) 1580-1585.
- [26] S. Cui, D. Yin, Y. Chen, Y. Di, H. Chen, Y. Ma, S. Achilefu, Y. Gu, In vivo targeted deep-tissue photodynamic therapy based on near-infrared light triggered upconversion nanoconstruct, *ACS Nano* 7(1) (2012) 676-688.
- [27] W. Gao, Z. Wang, L. Lv, D. Yin, D. Chen, Z. Han, Y. Ma, M. Zhang, M. Yang, Y. Gu, Photodynamic Therapy Induced Enhancement of Tumor Vasculature Permeability Using an Upconversion Nanoconstruct for Improved Intratumoral Nanoparticle Delivery in Deep Tissues, *Theranostics* 6(8) (2016) 1131.
- [28] A. Punjabi, X. Wu, A. Tokatli-Apollon, M. El-Rifai, H. Lee, Y. Zhang, C. Wang, Z. Liu, E.M. Chan, C. Duan, Amplifying the red-emission of upconverting nanoparticles for biocompatible clinically used prodrug-induced photodynamic therapy, *ACS Nano* 8(10) (2014) 10621-10630.
- [29] X. Li, F. Zhang, D. Zhao, Lab on upconversion nanoparticles: optical properties and applications engineering via designed nanostructure, *Chem. Soc. Rev.* 44(6) (2015) 1346-1378.
- [30] A. Nadort, J. Zhao, E.M. Goldys, Lanthanide upconversion luminescence at the nanoscale: fundamentals and optical properties, *Nanoscale* (2016).
- [31] S. Wu, H.J. Butt, Near - Infrared - Sensitive Materials Based on Upconverting Nanoparticles, *Adv. Mater.* 28(6) (2016) 1208-1226.
- [32] M.K. Gnanasammandhan, N.M. Idris, A. Bansal, K. Huang, Y. Zhang, Near-IR photoactivation using mesoporous silica-coated NaYF<sub>4</sub>: Yb, Er/Tm upconversion nanoparticles, *Nat. Protoc.* 11(4) (2016) 688-713.
- [33] C. Wang, H. Tao, L. Cheng, Z. Liu, Near-infrared light induced in vivo photodynamic therapy of cancer based on upconversion nanoparticles, *Biomaterials* 32(26) (2011) 6145-6154.
- [34] E. Khaydukov, K. Mironova, V. Semchishen, A. Generalova, A. Nechaev, D. Khochenkov, E. Stepanova, O. Lebedev, A. Zvyagin, S. Deyev, Riboflavin photoactivation by upconversion nanoparticles for cancer treatment, *Sci. Rep.* 6 (2016).

- [35] Z. Gu, L. Yan, G. Tian, S. Li, Z. Chai, Y. Zhao, Recent advances in design and fabrication of upconversion nanoparticles and their safe theranostic applications, *Adv. Mater.* 25(28) (2013) 3758-3779.
- [36] C. Wang, L. Cheng, Z. Liu, Upconversion nanoparticles for photodynamic therapy and other cancer therapeutics, *Theranostics* 3(5) (2013) 317-330.
- [37] L. Liang, A. Care, R. Zhang, Y. Lu, N.H. Packer, A. Sunna, Y. Qian, A.V. Zvyagin, Facile Assembly of Functional Upconversion Nanoparticles for Targeted Cancer Imaging and Photodynamic Therapy, *ACS Appl. Mater. Interfaces* (2016).
- [38] A. Dong, X. Ye, J. Chen, Y. Kang, T. Gordon, J.M. Kikkawa, C.B. Murray, A generalized ligand-exchange strategy enabling sequential surface functionalization of colloidal nanocrystals, *J. Am. Chem. Soc.* 133(4) (2010) 998-1006.
- [39] F. Wang, Y. Han, C.S. Lim, Y. Lu, J. Wang, J. Xu, H. Chen, C. Zhang, M. Hong, X. Liu, Simultaneous phase and size control of upconversion nanocrystals through lanthanide doping, *Nature* 463(7284) (2010) 1061-1065.
- [40] N.J. Johnson, A. Korinek, C. Dong, F.C. van Veggel, Self-focusing by Ostwald ripening: a strategy for layer-by-layer epitaxial growth on upconverting nanocrystals, *J. Am. Chem. Soc.* 134(27) (2012) 11068-11071.
- [41] L. Zhao, A. Kutikov, J. Shen, C. Duan, J. Song, G. Han, Stem cell labeling using polyethylenimine conjugated ( $\alpha$ -NaYbF<sub>4</sub>: Tm<sup>3+</sup>)/CaF<sub>2</sub> upconversion nanoparticles, *Theranostics* 3(4) (2013) 249-257.
- [42] Q. Chen, C. Wang, L. Cheng, W. He, Z. Cheng, Z. Liu, Protein modified upconversion nanoparticles for imaging-guided combined photothermal and photodynamic therapy, *Biomaterials* 35(9) (2014) 2915-2923.
- [43] E.O. Serebrovskaya, E.F. Edelweiss, O.A. Stremovskiy, K.A. Lukyanov, D.M. Chudakov, S.M. Deyev, Targeting cancer cells by using an antireceptor antibody-photosensitizer fusion protein, *Proc. Natl. Acad. Sci. U. S. A.* 106(23) (2009) 9221-9225.
- [44] L. Bernard, Reactive oxygen species in photochemistry of the red fluorescent protein "Killer Red", *Chem. Commun.* 47(17) (2011) 4887-4889.
- [45] American National Standard for Safe Use of Lasers, Laser Institute of America, Orlando, FL 2000.

### Supporting Information

#### Deep-penetrating photodynamic therapy with KillerRed mediated by upconversion nanoparticles

Luen Liang, Yiqing Lu, Run Zhang,\* Andrew Care, Tiago A. Ortega, Sergey M. Deyev, Yi Qian, and Andrei V. Zvyagin\*

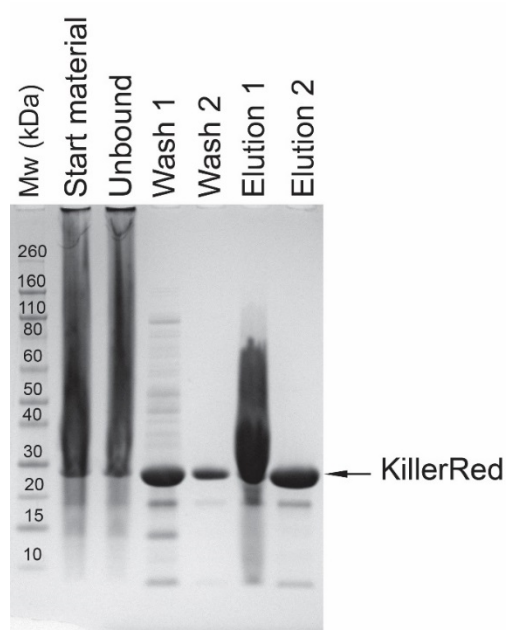


**Fig. S1.** SDS-PAGE analysis of Ni-NTA affinity purification of His-tagged KillerRed.

The purity of KillerRed in the Elution 2 fraction (used in all subsequent experiments) was estimated to be ~90%. Purity was determined by analyzing the intensity of protein bands on SDS-PAGE digital image using ImageJ software.

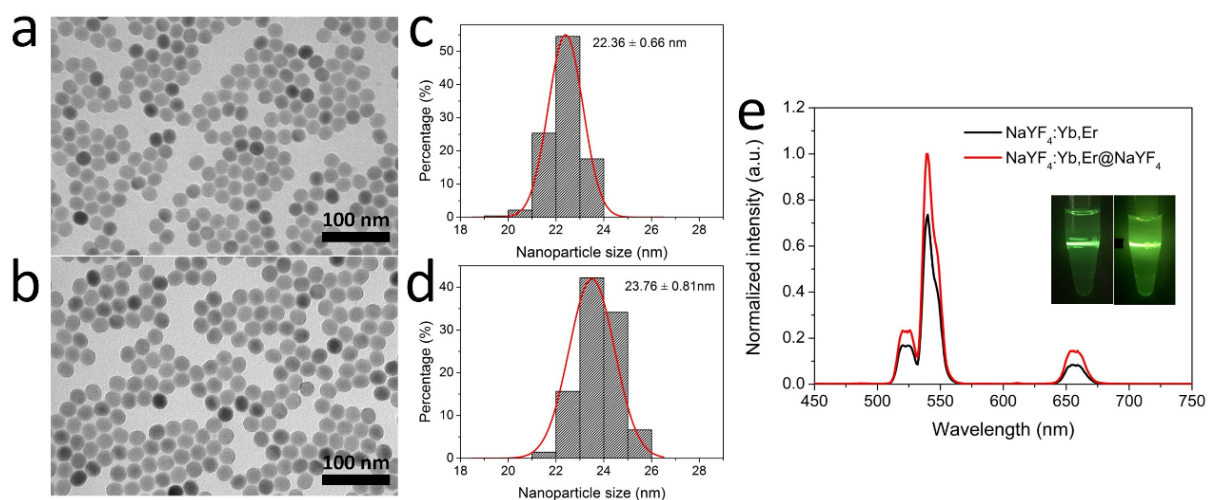


**Fig. S2.** TEM images of (a) core UCNPs (NaYF<sub>4</sub>:Yb,Er) and (b) core-shell UCNPs (NaYF<sub>4</sub>:Yb,Er@NaYF<sub>4</sub>) and their corresponding size distributions histograms (c) and (d). (e) Upconversion luminescence spectra of core and core-shell UCNPs under the excitation of 980 nm. The insets are photographs of core (left) and core-shell (right) UCNPs dispersed in cyclohexane and illuminated with a 980 nm laser beam.

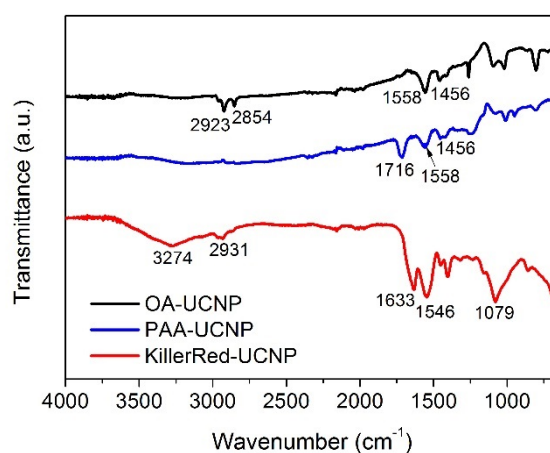


**Fig. S3.** FTIR spectra of oleic acid capped UCNP (OA-UCNP), PAA modified UCNP (PAA-UCNP) and KillerRed conjugated UCNP (KillerRed-UCNP).

As shown in Fig. S2, two peaks at 2923 and 2854 cm<sup>-1</sup> attributed to the C-H stretching vibration of OA were found in the spectrum of OA-UCNP, but were not obviously observed in the spectrum of PAA-UCNP. Additionally, the band at 1716 cm<sup>-1</sup> associated with the C=O stretching vibration of the -COOH group were found in spectrum of PAA-UCNPs. KillerRed was also evidenced in the FTIR spectrum of lyophilized KillerRed-UCNPs by the N-H stretching vibration (3200–3400 cm<sup>-1</sup>), the amino I band (1633 cm<sup>-1</sup>), and amide II peak band at 1546 cm<sup>-1</sup>.

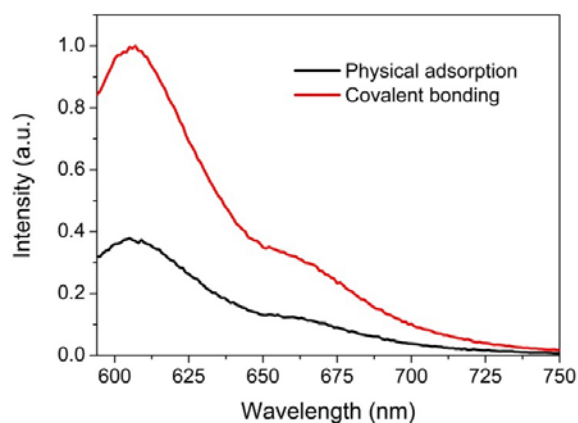


**Fig. S4.** Emission spectra of KillerRed-UCNP prepared by physical adsorption and covalent conjugation.

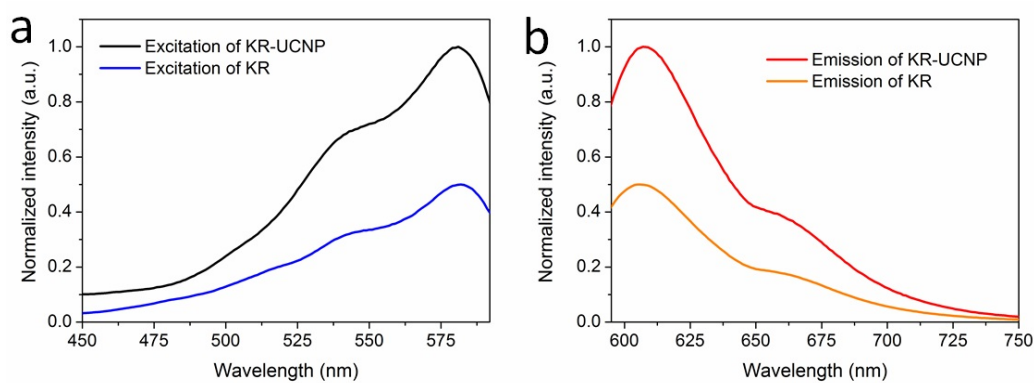


**Fig. S5.** (a) Excitation and (b) emission spectra of KillerRed-UCNP (KR-UCNP) and KillerRed (KR).

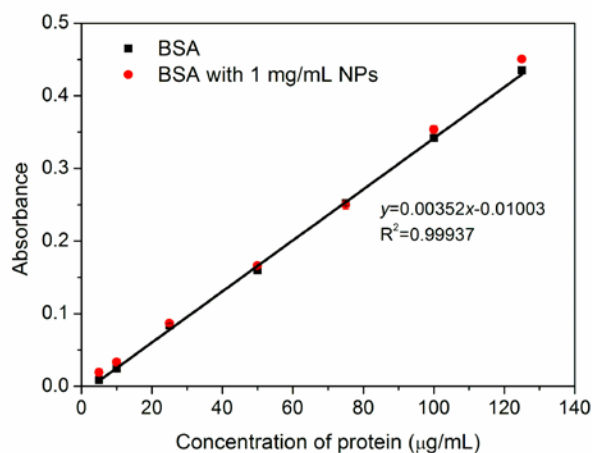


**Fig. S6.** Standard curve for protein quantification using the micro BCA assay kit.

The micro BCA assay is a biochemical assay for the colorimetric detection and quantification of total protein. In an alkaline environment, protein will reduce  $\text{Cu}^{2+}$  to cuprous cation  $\text{Cu}^{1+}$ , which will form a purple-blue chelate complex with two molecules of BCA. This water-soluble complex exhibits absorbance at 562 nm that increases linearly with increasing protein concentrations, thus providing a basis to quantify the amount of proteins in a sample.

**S7.** Calculation of resonance energy transfer (RET) efficiency ( $\eta_{RET}$ )

$$\eta_{RET} = \frac{A_{o,KR-UCNP}}{A_{o,KR-UCNP}^*} \times 100\% \quad (1)$$

$$A_{o,KR-UCNP}^* = (A_{g,PAA-UCNP} - A_{g,KR-UCNP}) \times \eta_{QY,KR} \times \frac{A_{o,KR}}{A_{KR}} \quad (2)$$

Where,  $A_{o,KR-UCNP}$  is the detected orange fluorescence signal from KR-UCNP integrated over the spectral range of 600–642 nm, corresponding to the bandpass filter.

$A_{o,KR-UCNP}^*$  is the upper limit of the orange fluorescence signal from KR-UCNP integrated over the spectral range of 600–642 nm.

$\eta_{QY,KR}$  is the quantum yield of KillerRed ( $\eta_{QY,KR} = 0.25$ ) [1].

$A_{g,PAA-UCNP}$  and  $A_{g,KR-UCNP}$  represent the NIR-excited photoluminescence intensity integrated over the green emission band (500–575 nm) of PAA-UCNP and KR-UCNP, respectively.

$A_{o,KR}$  and  $A_{KR}$  represent the relative photoluminescence intensity of KR (excited at 582 nm) integrated over the spectral range of 600–642 nm and 592–750 nm, respectively.

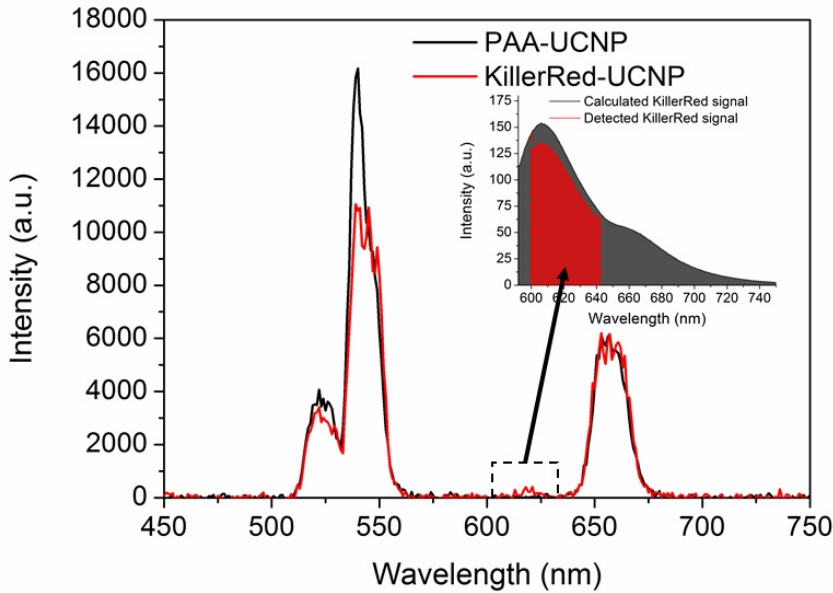


**Fig. S7.** Emission spectra of PAA-UCNPs (black line) and KillerRed-UCNPs (red line) under 980-nm excitation. The inset is the reconstructed KillerRed-UCNP emission spectrum based on the calculation of the depleted green energy from UCNP (black area), and the reconstructed KillerRed-UCNP emission at 600–642 nm (red area) based on the integrated signal from the detected emission of KillerRed-UCNP at 600–642 nm.



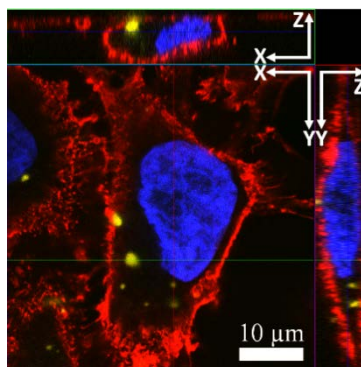


**Fig. S8.** Orthogonal images of KillerRed-UCNPs uptaken by MDA-MB-231 cells. The images are constructed from z-step images, and presented as viewed in the x-z (top) and y-z (right) planes.

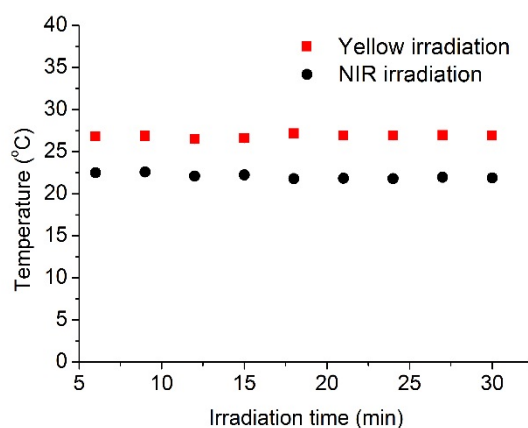


**Fig. S9.** Temperature profile of MDA-MB-231 cells seeded in cell culture dishes as a function of exposure time under yellow laser ( $0.2 \text{ W/cm}^2$ ) and NIR nm laser irradiation ( $0.5 \text{ W/cm}^2$ ). The temperature was measured with the U5855A TrueIR Thermal Imager camera.

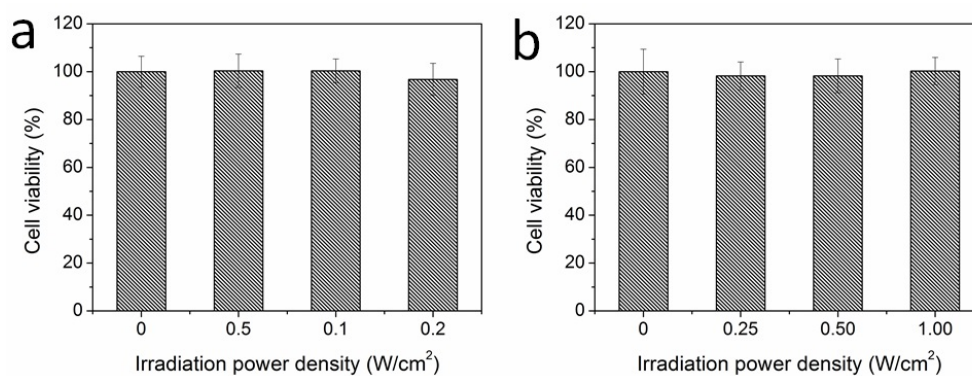


**Fig. S10.** Cell viability of MDA-MB-231 cells irradiated with different power densities of yellow laser (0, 0.05, 0.1 and  $0.2 \text{ W/cm}^2$ ) and NIR laser (0, 0.25, 0.5, and  $1.00 \text{ W/cm}^2$ ).

## CHAPTER 4

---

Cell death rate is determined by  $(100\% - \text{cell viability})$ .

### Reference

[1] M.E. Bulina, D.M. Chudakov, O.V. Britanova, Y.G. Yanushevich, D.B. Staroverov, T.V. Chepurnykh, E.M. Merzlyak, M.A. Shkrob, S. Lukyanov, K.A. Lukyanov, A genetically encoded photosensitizer, *Nat. Biotechnol.* 24(1) (2006) 95-99.

# 5

## **Facile Assembly of Functional Upconversion Nanoparticles for Targeted Cancer Imaging and Photodynamic Therapy**

### **5.1 Introduction**

UCNP-based theranostics has been demonstrated to be promising to improve the therapeutic efficacy and minimize side-effects of anti-cancer drugs. UCNPs are often employed in nanocomposites coupled with a targeting capability usually implemented by coupling to cancer-specific antibodies. As reviewed in Chapter 3, an amine-reactive cross-linking method is most commonly used to anchor antibodies to UCNPs. However, this conventional technique suffers from several drawbacks, such as the lack of sufficient control over the functional display of immobilized antibodies, and the propensity of the nanocomposite aggregation.

In this chapter, we report a facile and robust approach to assemble UCNPs, PDT agents, and targeting antibodies by the use of peptide-linker technology to enable targeted recognition and ligand-guided treatment of cancer. We firstly encapsulated the photosensitizer, Rose Bengal, in the silica-coated UCNPs, and functionalized them with the targeting antibodies, anti-EpCAM. Then we explored the targeting ability and photodynamic effect of the UCNPs biohybrid towards cancer cells HT-29 *in vitro*. The detailed evaluation and experimental results for this work were reported in a peer-reviewed paper “Facile Assembly of Functional Upconversion Nanoparticles for Targeted Cancer Imaging and Photodynamic Therapy”, which forms the content of this chapter.

### 5.2 Author's Contribution to The Paper

The PhD candidate (Liu Liang) is the first author of this paper. She performed the synthesis, surface modification, and material characterizations of the UCNPs. She also conducted the experiments associated with cells, including cell culture, nanoparticle incubation with cells, intracellular ROS detection, *in vitro* cytotoxicity investigation, and evaluation of therapeutic efficiency of the nanocomposites. In addition, she prepared the samples and carried out the optical imaging of nanoparticles labelling cells. Finally, she collected and analysed the data, constructed the figures, interpreted the results, and wrote the manuscript.

The other authors have all made significant scientific contributions to this paper. Dr. Andrew Care designed the bioconjugation procedures and partly participated in the optical imaging experiments. Dr. Run Zhang was involved in most stages of this work on experiment design, result discussion, and data analysis. Dr. Yiqing Lu built the irradiation setup and provided the instrumental support on imaging nanoparticles. Dr. Anwar Sunna devised the technology of solid peptide linker that we used to bind the antibodies to silica-coated UCNPs. Prof. Packer and Prof. Qian provided the essential resources for the preparation of nanoparticles and peptide linkers, and the facilities for the material characterizations. A/Prof. Zvyagin (the corresponding author), planned this work, coordinated the project, and finalized the manuscript. All authors were involved in the revising of the manuscript.

# Facile Assembly of Functional Upconversion Nanoparticles for Targeted Cancer Imaging and Photodynamic Therapy

Liuven Liang,<sup>†,‡</sup> Andrew Care,<sup>‡,§</sup> Run Zhang,<sup>‡,§</sup> Yiqing Lu,<sup>‡</sup> Nicolle H. Packer,<sup>‡,§</sup> Anwar Sunna,<sup>‡,§</sup> Yi Qian,<sup>†</sup> and Andrei V. Zvyagin<sup>\*,‡,‡,‡</sup>

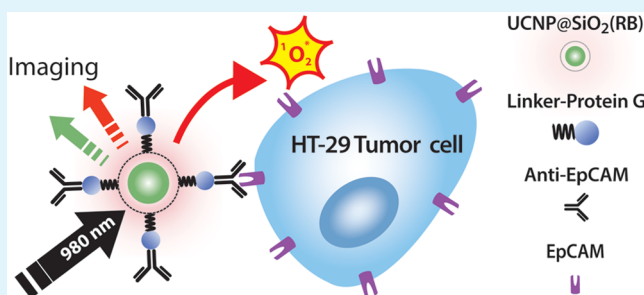
<sup>†</sup>Department of Biomedical Sciences, <sup>§</sup>Department of Chemistry and Biomolecular Sciences, and <sup>‡</sup>ARC Centre of Excellence for Nanoscale BioPhotonics, Macquarie University, North Ryde, New South Wales 2109, Australia

<sup>‡</sup>Laboratory of Optical Theranostics, N. I. Lobachevsky State University of Nizhny Novgorod, Nizhny Novgorod 603950, Russia

## Supporting Information

**ABSTRACT:** The treatment depth of existing photodynamic therapy (PDT) is limited because of the absorption of visible excitation light in biological tissue. It can be augmented by means of upconversion nanoparticles (UCNPs) transforming deep-penetrating near-infrared (NIR) light to visible light, exciting PDT drugs. We report here a facile strategy to assemble such PDT nanocomposites functionalized for cancer targeting, based on coating of the UCNPs with a silica layer encapsulating the Rose Bengal photosensitizer and bioconjugation to antibodies through a bifunctional fusion protein consisting of a solid-binding peptide linker genetically fused to *Streptococcus* Protein G'. The fusion protein (Linker-Protein G) mediates the functionalization of silica-coated UCNPs with cancer cell antibodies, allowing for specific target recognition and delivery. The resulting nanocomposites were shown to target cancer cells specifically, generate intracellular reactive oxygen species under 980 nm excitation, and induce NIR-triggered phototoxicity to suppress cancer cell growth in vitro.

**KEYWORDS:** photodynamic therapy, upconversion nanoparticles, targeted imaging, luminescence resonance energy transfer, solid-binding peptides



## INTRODUCTION

Existing cancer treatments, including chemotherapy and radiotherapy, suffer from concomitant side effects. Clinically accepted light-based photodynamic therapy (PDT) offers a unique localized treatment with mild side effects and can supplement the other regimens. PDT stands out because of its reduced invasiveness, high sensitivity, site specificity,<sup>1,2</sup> and immunogenicity capable of driving antitumor immunity,<sup>3</sup> in contrast with the immunosuppressive effects of chemotherapy and radiotherapy. PDT is based on the photochemical reactions of photosensitizers (PSs) to generate cytotoxic reactive oxygen species (ROS) toward cancer cells.<sup>4</sup> The majority of PSs currently used in PDT are excited by light in the ultraviolet (UV) or visible range, where the treatment penetration depth in biological tissues ranges from 60  $\mu\text{m}$  (at 340 nm) to several millimeters at the far-red wavelength band.<sup>5</sup> This limitation largely precludes PDT treatment of tumors with sizes of more than 1 cm.<sup>6</sup>

In contrast to UV and visible light, light of the near-IR (NIR) wavelength from 650 to 1350 nm has a larger penetration depth in biological tissues,<sup>7,8</sup> providing a promising approach to improving the treatment depth for PDT.<sup>9</sup> In particular, increasing attention has been paid to the lanthanide-doped upconversion nanoparticles (UCNPs) that are capable of

converting NIR excitation to visible/UV emission, as light transducers to activate clinically approved PSs.<sup>10–12</sup> Depending on PS absorption, UCNPs can be engineered to have optimized emission overlapping with the absorption band of the PS, which facilitates the process of energy transfer and makes such NIR-mediated PDT highly efficient.<sup>13–16</sup> Additionally, UCNPs offer exceptional photostability and background-free imaging capability, which is ideal for high-contrast biomedical imaging.<sup>17–21</sup> Therefore, a hybrid nanocomposite combining UCNPs and PSs holds great promise for image-guided diagnosis and PDT.

To enable targeted PDT treatment with minimum side effects as well as direct visualization of the tumor, UCNP nanocomposites are required to bioconjugate to active tumor-targeting moieties such as folic acid,<sup>22–24</sup> peptides,<sup>25</sup> and antibodies.<sup>26</sup> Unfortunately, the conventional bioconjugation techniques (e.g., amine-reactive cross-linking) used in these reports often lack sufficient control over the functional display of the immobilized targeting moiety, which may prevent selective molecular recognition between the targeting moiety and its receptor/molecular partner. In addition, these biohybrid nano-

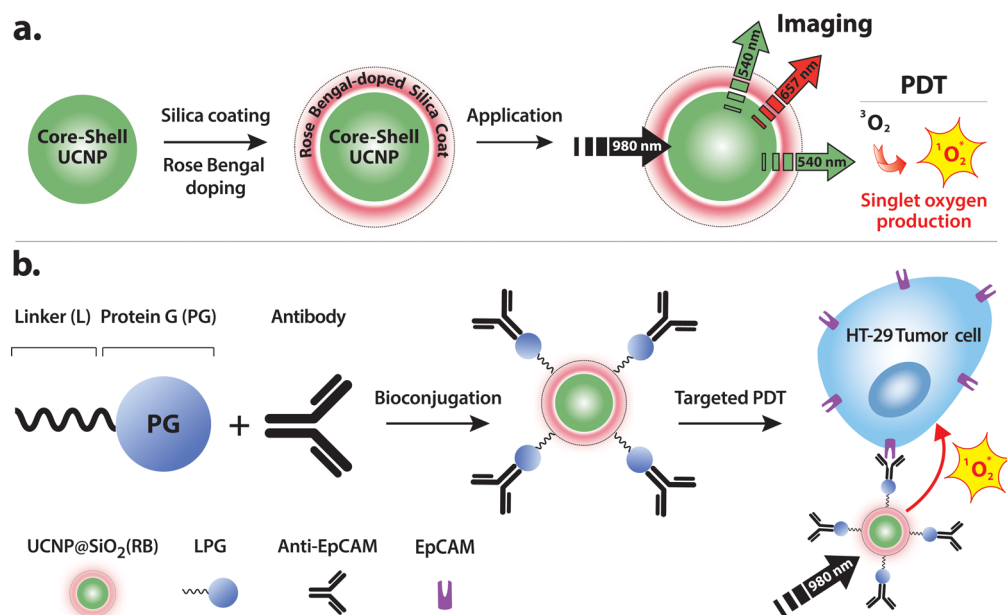
Received: January 19, 2016

Accepted: April 27, 2016

Published: April 27, 2016



**Scheme 1. Schematic Illustration of (a) the Fabrication of UCNP@SiO<sub>2</sub>(RB) and Its Functionality and (b) LPG-Mediated Bioconjugation of UCNP@SiO<sub>2</sub>(RB) with Antibodies and Their Application in Targeted PDT**



complexes are assembled via a chemical reaction between targeting molecules and nanoparticles, where an antibody can bind to more than one nanoparticle, leading to particle aggregation. Therefore, new strategies of assembling UCNPs with PSs and targeting moieties while maintaining their functionality and selectivity are highly desirable.

In this work, we explore a facile strategy to assemble targeting UCNP–PS nanocomposites. As illustrated in Scheme 1, first, the green-emitting Yb<sup>3+</sup>/Er<sup>3+</sup>-codoped UCNPs are coated with a silica layer that encapsulates a common PS, Rose Bengal (RB), for PDT. Upon 980 nm irradiation, energy is transferred from the UCNPs to the neighboring RB molecules to activate the generation of singlet oxygen. Then, a bifunctional fusion protein, consisting of a silica-specific solid-binding peptide (referred to as the Linker, L) genetically fused to the N-terminus of *Streptococcus* Protein G' (PG, an antibody-binding protein), is applied to facilitate oriented and sterically accessible immobilization of tumor-targeting antibodies onto the surfaces of the silica-coated nanocomposites. The Linker domain of Linker–Protein G (LPG) exhibits high binding affinity toward the silica surface, and the IgG-binding protein (PG) binds to the Fc fragment of IgG antibodies, thereby ensuring the functional display of conjugated antibodies and avoiding concurrent reactions between one antibody and different nanoparticles in cross-linking methods. Finally, these functionalized nanocomposites are validated for targeted imaging and selective killing of human colorectal adenocarcinoma HT-29 cells in vitro.

## EXPERIMENTAL SECTION

**Reagents and Chemicals.** All reagents were of analytical grade and were used as received without further purification. Yttrium(III) chloride hexahydrate (YCl<sub>3</sub>·6H<sub>2</sub>O; 99.999%), ytterbium(III) chloride hexahydrate (YbCl<sub>3</sub>·6H<sub>2</sub>O; 99.9%), erbium(III) chloride hexahydrate (ErCl<sub>3</sub>·6H<sub>2</sub>O; 99.9%), sodium hydroxide (NaOH; ≥97.0%), ammonium fluoride (NH<sub>4</sub>F; ≥98.0%), oleic acid (OA; 90%), oleylamine (OM; ≥98.0%), 1-octadecene (ODE; 90%), cyclohexane (99.5%), tetraethyl orthosilicate (TEOS), Igpal CO-520, ammonium hydroxide solution (NH<sub>4</sub>OH; 30%), 1,3-diphenylisobenzofuran (DPBF), thiazolyl blue tetrazolium bromide (MTT), dimethyl sulfoxide (DMSO), 4,6-

diamidino-2-phenylindole dihydrochloride (DAPI), and paraformaldehyde (PFA) were obtained from Sigma-Aldrich Chemicals (Sydney, Australia). Rose Bengal (RB) was purchased from Alfa Aesar (China). Purified mouse antihuman CD326 (EpCAM; clone HEA-125) was purchased from Miltenyi Biotec (Sydney, Australia). Recombinant LPG was produced in *Escherichia coli* and purified by ion-exchange chromatography as described previously.<sup>27</sup>

**Characterization Instruments.** The absorbance spectra of RB were obtained using a UV/vis spectrophotometer (Cary 5000, Varian). Transmission electron microscopy (TEM) measurements were performed with a Philips CM10 transmission electron microscope operating at 100 kV. The size distribution of UCNPs was analyzed using *ImageJ*. The high-resolution TEM (HRTEM) image was recorded using a JEM-3000F transmission electron microscope operating at 300 kV. Emission and excitation spectra were acquired using a Fluorolog-Tau3 spectrofluorometer (Jobin Yvon-Horiba) equipped with an external 978 nm continuous-wave diode laser with maximum achievable power of ~1.2 W. The ζ-potential and dynamic light scattering measurements were carried out using a Zetasizer Nano ZS90 (Malvern Instruments Ltd.).

**Synthesis of Core–Shell (NaYF<sub>4</sub>:Yb,Er@NaGdF<sub>4</sub>) Nanoparticles.** Core β-NaYF<sub>4</sub>:Yb,Er nanoparticles were synthesized following a protocol developed previously.<sup>28</sup> Typically, for the synthesis of NaYF<sub>4</sub>:Yb(18%),Er(2%) nanoparticles, 0.8 mmol of YCl<sub>3</sub> was mixed with 0.18 mmol of YbCl<sub>3</sub> and 0.02 mmol of ErCl<sub>3</sub> with 6 mL of OA and 15 mL of ODE in a 100 mL three-neck round-bottomed reaction flask. The mixture was heated to 160 °C for 30 min under an argon flow. The resulting mixture formed a light-yellow solution and was cooled to room temperature (RT). Afterward, a methanol solution containing NH<sub>4</sub>F (0.148 g) and NaOH (0.1 g) was added, and the resulting solution was stirred for 30 min. The solution then was heated slowly to 110 °C under an argon flow for 30 min to completely remove methanol along with some water. After this step, the reaction mixture was heated to 310 °C for 1 h with constant stirring. Finally, nanoparticles were precipitated with ethanol and washed several times with ethanol/methanol (1:1, v/v) and the resulting core UCNPs were redispersed in cyclohexane.

The synthesis of NaYF<sub>4</sub>:Yb,Er@NaGdF<sub>4</sub> nanoparticles was based on the Ostwald ripening-mediated method with some modification.<sup>29</sup> First, cubic NaGdF<sub>4</sub> nanocrystals were prepared as follows: 1 mmol of YCl<sub>3</sub>, 6 mL of OA, and 10 mL of ODE were mixed in a 50 mL reaction flask, and the resulting mixture was heated to 150 °C under an argon flow with constant stirring for 30 min to form a light-yellow solution that was



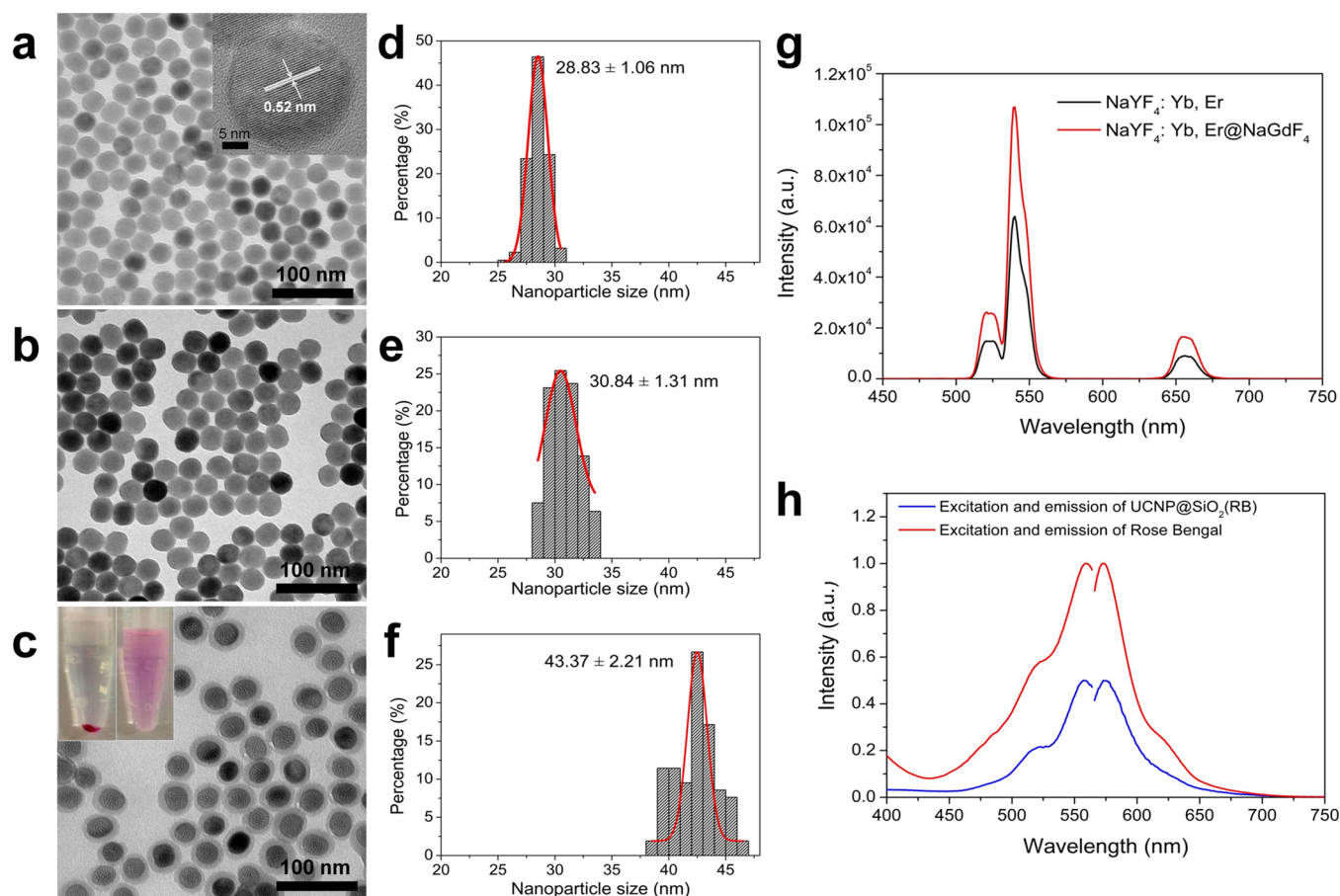


**Figure 1.** TEM images of (a) core UCNPs (NaYF<sub>4</sub>:Yb,Er; the inset is the HRTEM image of a single core nanoparticle) and (b) core-shell UCNPs (NaYF<sub>4</sub>:Yb,Er@NaGdF<sub>4</sub>). (c) Core-shell UCNPs with UCNP@SiO<sub>2</sub>(RB). The insets are photographs of UCNP@SiO<sub>2</sub>(RB) pelleted (left) and dispersed (right) in water. (d–f) Size distributions of the corresponding nanoparticles. (g) Upconversion luminescence spectra of core and core-shell UCNPs under 980 nm excitation. (h) Normalized excitation and emission spectra of UCNP@SiO<sub>2</sub>(RB) and free RB.

cooled to RT. Second, 10 mL of a methanol solution containing 1.6 mmol of NH<sub>4</sub>F and 1 mmol of NaOH was added, and the solution was stirred for 30 min. After heating to remove methanol, the solution was cooled, and 3 mL of OM was added. The solution was heated to 290 °C under an argon flow with vigorous stirring for 45 min and then cooled to RT. The NaGdF<sub>4</sub> particles obtained were collected and resuspended in a mixture of 5 mL of OA, 8 mL of ODE, and 1 mL of OM and used as sacrificial nanoparticles. A total of 0.2 mmol of core UCNPs in 15 mL of cyclohexane was added to a 100 mL reaction flask and mixed with 10 mL of OA, 16 mL of ODE, and 2 mL of OM. After heating slowly to 110 °C for 30 min to remove cyclohexane, the solution was heated to 305 °C, and 300, 200, and 100  $\mu$ L sacrificial nanoparticles were injected stepwise into the reaction with 10 min reaction ripening after each injection. The resulting core-shell NaYF<sub>4</sub>:Yb,Er@NaGdF<sub>4</sub> nanoparticles were collected and washed with centrifugation and dispersed in cyclohexane for further silica coating.

**Synthesis of RB-Loaded Silica-Coated UCNP [UCNP@SiO<sub>2</sub>(RB)].** A modified water-in-oil microemulsion method<sup>30</sup> was used to prepare UCNP@SiO<sub>2</sub>(RB). In a typical procedure, 0.5 mL of Igepal CO-520 was dispersed in 5 mL of cyclohexane, followed by injection of a 0.1 mmol of core-shell UCNPs in 5 mL of cyclohexane solution into the mixture. After stirring for 3 h, 1 mg of RB was added to the mixture, and stirring was continued for another 2 h. A total of 500  $\mu$ L of ammonia (30%) was then added, followed by slowly injection of 35  $\mu$ L of TEOS (2  $\mu$ L/min). The mixture was sealed and kept stirring for 24 h. The product was then precipitated and washed three times with ethanol, followed by washing with water three times and finally storage in water.

**LPG-Mediated Functionalization of UCNPs.** UCNP@SiO<sub>2</sub> (with and without RB) was functionalized with antibodies via LPG as follows. Nanoparticles (1 mg) were sonicated before use and then rinsed three

times with a 100 mM Tris-HCl buffer, pH 7.5. The washed particles were resuspended by sonication in the same buffer containing 30  $\mu$ g of purified LPG and incubated with rotation at RT for 15 min. Particles were collected by centrifugation, and the unbound LPG was removed, after which the particles were washed two times. The LPG-coated particles were then incubated with 20  $\mu$ g of antibody (referred to as Ab) with rotation at RT for 15 min. Particles were collected by centrifugation, and the unbound Ab was removed, followed by two additional washing steps. The resulting Ab-functionalized UCNPs finally were dispersed in 200  $\mu$ L of phosphate-buffered saline (PBS) for use in subsequent experiments.

**Cell Imaging.** Human colon adenocarcinoma HT-29 cells and murine microglial BV2 cells were cultured with Dulbecco's modified Eagle's medium (DMEM) supplemented with 10% fetal bovine serum (FBS) and 1% penicillin-streptomycin under 5% CO<sub>2</sub> at 37 °C in a humidified incubator.

For the EpCAM-targeted imaging, 2.5  $\times$  10<sup>4</sup> cells/well of HT-29 (high EpCAM expression) and BV2 (low EpCAM expression) cells were seeded into 24-well plates with a coverslip placed at the bottom of each well. After incubation for 24 h, both of the plates of cells were washed three times with PBS and fixed with a 4% PFA solution for 15 min at RT before washing again three times with PBS. The cells were incubated with a 25  $\mu$ g/mL UCNP@SiO<sub>2</sub>(RB)-LPG-Ab PBS suspension at RT for 1 h, followed by DAPI nuclei staining for 10 min. Afterward, PBS was used to rinse the cells five times to wash away the unlabeled nanoparticles and DAPI. Finally, the coverslips were then mounted on glass slides and sealed with nail polish. Upconversion fluorescence imaging was performed with our in-house-built epiluminescence microscope equipped with a fiber-coupled 978 nm diode laser and a 405 nm laser to illuminate the UCNPs and DAPI. The filters used

in the microscopes include a high-pass absorbance filter (850 nm) placed in the excitation beam path, a dichroic beam splitter (511 nm), and an additional short-pass filter (842 nm) in the detection beam path. The overall emission of the nanocomposite in the range of 511–842 nm was detected by the camera and represents photoluminescence from UCNP.

**Detection of Singlet Oxygen in Solution.** Singlet oxygen generation was evaluated in a solution of UCNP@SiO<sub>2</sub>(RB)-LPG-Ab using DPBF as a <sup>1</sup>O<sub>2</sub> detection probe. Typically, 10  $\mu$ L of a 10 mM DPBF ethanol solution was mixed with 1 mL of a 1 mg/mL UCNP@SiO<sub>2</sub>(RB)-LPG-Ab aqueous suspension. The solution then was placed in a cuvette and irradiated with a 980 nm NIR laser at 1.5 W/cm<sup>2</sup> for 30 min. The absorption of DPBF was collected every 5 min using a NanoDrop 2000c UV–vis spectrophotometer. For comparison, the same amounts of DPBF mixed with UCNP@SiO<sub>2</sub>(RB)-LPG-Ab in the dark and UCNP@SiO<sub>2</sub>-LPG-Ab with NIR treatment were measured as controls.

**Intracellular ROS Generation Detection.** Intracellular singlet oxygen generation was detected with an Image-iT LIVE Green Reactive Oxygen Species Kit (Molecular Probes). HT-29 cells were seeded into coverglass–bottom confocal dishes at a density of  $3 \times 10^5$  cells/dish and left to grow for 1 day at 37 °C in an incubator. Then the HT-29 cells were loaded with 100  $\mu$ g/mL UCNP@SiO<sub>2</sub>(RB)-LPG-Ab and UCNP@SiO<sub>2</sub>-LPG-Ab for 12 h. 2',7'-Dichlorodihydrofluorescein diacetate (DCFH-DA; 25  $\mu$ M) was loaded into the cells, which were incubated in darkness for 30 min. The cells then were washed twice with 1×HBSS and subjected to NIR irradiation for 5 min (with intermittent 1 min breaks after each 1 min of irradiation to prevent overheating) at a power density of 1.5 W/cm<sup>2</sup>. The cells were washed twice and incubated with 1×HBSS buffer. The production of singlet oxygen was visualized by an Olympus Fluoview FV1200 confocal microscope. Oxidized 2',7'-dichlorofluorescein (DCF) was excited with a 473 nm laser, and the emission was collected through a 490–590 nm filter.

The intracellular ROS level was analyzed via the fluorescent intensity from DCF. HT-29 cells were seeded into 96-well plates until adherent and then incubated with 100  $\mu$ g/mL UCNP@SiO<sub>2</sub>(RB)-LPG-Ab and UCNP@SiO<sub>2</sub>-LPG-Ab for 12 h. After treatment similar to that mentioned above, the fluorescent intensity of the cells in different treatments was recorded with excitation at 485 nm and emission at 520 nm using a PHERAstar microplate reader.

**In Vitro Cytotoxicity Study.** HT-29 cells were seeded in a 96-well culture plate at a density of 5000 cells/well for in vitro cytotoxicity assays. After being incubated for 12 h, the cells were loaded with UCNP@SiO<sub>2</sub>, UCNP@SiO<sub>2</sub>(RB), UCNP@SiO<sub>2</sub>(RB)-LPG, and UCNP@SiO<sub>2</sub>(RB)-LPG-Ab at serial concentrations of 0, 12.5, 25, 50, 100, and 200  $\mu$ g/mL with five parallel wells for each concentration. Treated cells were kept incubated in the dark for another 24 h. The standard MTT assay was carried out to determine the cell viabilities relative to untreated cells.

**Photodynamic Effect of UCNP@SiO<sub>2</sub>(RB)-LPG-Ab on Cancer Cells.** HT-29 cells were incubated with different concentrations of UCNP@SiO<sub>2</sub>(RB)-LPG-Ab (0, 100, and 200  $\mu$ g/mL) in a 96-well plate for 24 h at 37 °C in the dark to assay the EpCAM-targeted PDT effect. After removal of the medium containing noninternalized nanoparticles, the cells were washed three times with PBS and then irradiated with NIR light (1.5 W/cm<sup>2</sup>; 1 min interval breaks to avoid overheating) in fresh culture media for 0, 5, 10, and 15 min. After NIR treatment, the cells were incubated for a further 12 h in the dark before viability evaluation with MTT assay.

## RESULTS AND DISCUSSION

**Synthesis and Characterization of UCNP@SiO<sub>2</sub>(RB).** NaYF<sub>4</sub>:Yb,Er UCNP were synthesized using a solvothermal decomposition method. The TEM image (Figure 1a) indicates that these nanoparticles were monodispersed with a narrow size distribution (mean diameter of  $29 \pm 1$  nm; Figure 1d). The interplanar spacing of the nanoparticle was measured to be 0.52 nm according to HRTEM (Figure 1a, inset), which was in good agreement with the *d* spacing of the {111} plane in hexagonal  $\beta$ -

phase NaYF<sub>4</sub>. To suppress surface-related quenching of the upconversion emission, an inert shell of NaGdF<sub>4</sub> ( $\sim 1$  nm thickness) was further deposited onto the core UCNP. The core–shell UCNP (NaYF<sub>4</sub>:Yb,Er@NaGdF<sub>4</sub>) retained their morphology and dispersion (Figure 1b) and had an average diameter of  $31 \pm 1$  nm (Figure 1e). Compared to the core UCNP, the core–shell UCNP exhibited 1.7-fold enhanced upconversion photoluminescence under continuous-wave 980 nm excitation (Figure 1g).

Silica coating is commonly applied to UCNP to improve their aqueous solubility and stability in physiological environments. It can also serve as reservoirs for storing substantial quantities of therapeutic drugs, including PSs.<sup>31–34</sup> A thin layer of silica (SiO<sub>2</sub>) was coated onto the core–shell UCNP using a water-in-oil microemulsion method. The RB molecules were loaded into the silica layer simultaneously during the coating process. The resulting UCNP@SiO<sub>2</sub>(RB) particles were spherical in shape, with a mean diameter of  $43 \pm 2$  nm (Figure 1c,f). The core–shell UCNP were individually enclosed by a uniform layer of silica, with a thickness of approximately 6 nm as measured by TEM. This was within the critical distance required for efficient luminescence resonance energy transfer (<10 nm) between the UCNP and RB molecules encapsulated within the silica layer.<sup>35,36</sup> Because the silica-coated UCNP can be easily centrifuged and redispersed in water, successful encapsulation of the RB was directly confirmed by its red color, and no release of RB was observed in the solution when the nanoparticles were centrifuged to the bottom of the tube (Figure 1c, inset). Additionally, RB carried an overall negative charge, which resulted in the  $\zeta$ -potential values for UCNP@SiO<sub>2</sub>(RB) dispersed in water being significantly lower (−36.5 mV) than those for UCNP@SiO<sub>2</sub> (without RB, −25.3 mV; see Table 1).

**Table 1.**  $\zeta$ -Potential of Unconjugated and Conjugated UCNP

particle type	$\zeta$ -potential (mV)
UCNP@SiO <sub>2</sub>	−25 $\pm$ 6
UCNP@SiO <sub>2</sub> (RB)	−36.5 $\pm$ 8
UCNP@SiO <sub>2</sub> (RB)-LPG	−25.5 $\pm$ 7
UCNP@SiO <sub>2</sub> (RB)-LPG-Ab	−31 $\pm$ 7

UCNP@SiO<sub>2</sub>(RB) was further examined by fluorescence spectroscopy and exhibited excitation and emission maxima at 546 and 570 nm, respectively (Figure 1h), identical with those from free RB in water.

### LPG-Mediated Self-Assembly of Functional UCNP.

Bioconjugation of the as-prepared UCNP@SiO<sub>2</sub>(RB) to cancer antibodies is based on a bifunctional fusion protein (LPG) consisting of two distinct functional domains: a solid-binding peptide linker (L) and Protein G' (PG). Solid-binding peptides are short amino acid sequences that selectively bind to their corresponding solid surfaces with high affinity through a combination of multiple noncovalent interactions (e.g., van der Waals forces, electrostatic, hydrophobic, and  $\pi$  effects).<sup>37–39</sup> The solid-binding peptide linker used here [with a sequence of (VKQTATSREEPPRLPSKHPG)<sub>4</sub>VKTQTAS] is capable of mediating the specific binding of the LPG to silica-coated nanoparticles across a wide pH range (5–9).<sup>27,37,40</sup> The linker region contains a high number of basic lysine (*K* = 8) and arginine (*R* = 12) residues and thus carries a high net positive charge.<sup>41</sup> Also, almost 80% of the residues within the linker sequence promote a less stable peptide structure. This intrinsic structural disorder imparts flexibility and plasticity to the linker,



allowing it to undergo conformational changes that maximize the electrostatic interactions between its positively charged residues and the negatively charged silica surfaces. The Protein G' domain binds to the Fc region of the antibodies with nanomolar disassociation constants ( $K_D$ ), which provides another level of orientation and prevents interference with the antigen-binding sites of the antibodies.<sup>40,42</sup> Thus, LPG can act as an anchorage point for the attachment of targeting antibodies onto silica-coated UCNP via simple mixing and washing steps.

To validate LPG-mediated bioconjugation, UCNP@SiO<sub>2</sub>(RB) was incubated with an antibody-conjugated fluorescein isothiocyanate (Ab-FITC) in the presence/absence of LPG. The emission spectra of both samples dispersed in water were measured by fluorescence spectrometry under excitation at 488 nm. As shown in Figure 2, a significant intensity was

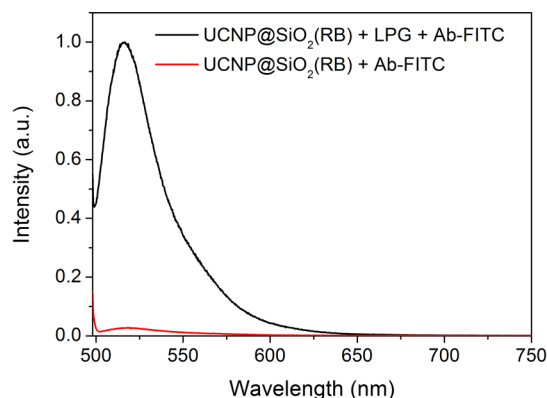


**Figure 2.** Fluorescent emission from FITC-conjugated antibodies immobilized on UCNP with (black) and without (red) LPG under 488 nm excitation.

observed in the green band (500–550 nm) for the LPG-mediated sample, indicating the effective conjugation of Ab-FITC onto the nanoparticles. In contrast, only negligible green emission resulting from nonspecific physical adsorption was detected from the control sample without LPG. This proves that LPG enables efficient and rapid bioconjugation of antibodies to the silica surface of UCNP@SiO<sub>2</sub>(RB). It was further confirmed that LPG technology permitted control over the concentration of conjugated antibodies by varying the amount of LPG during the incubation process (see Figure S2).

**Targeted Imaging of Cancer Cells Using UCNP@SiO<sub>2</sub>(RB)-LPG-Ab.** LPG was applied to mediate conjugation of UCNP@SiO<sub>2</sub>(RB) with the monoclonal antibody for epithelial cell adhesion molecules (EpCAM; also known as CD326). EpCAM is a transmembrane glycoprotein that is expressed at low levels in normal epithelia but overexpressed in epithelial cancers (i.e., carcinomas) and is a recognized target for immunotherapy.<sup>43</sup> Successful functionalization of UCNP@SiO<sub>2</sub>(RB) with anti-EpCAM (Ab for short hereafter) was indicated by measuring the  $\zeta$ -potential values. As shown in Table 1, the strong negative charge from UCNP@SiO<sub>2</sub>(RB) (−36.5 mV) was reduced after incubation with LPG (−25.5 mV) because of the positive charge of the linker region containing a high number of basic lysine ( $K = 8$ ) and arginine ( $R = 12$ ) residues. Conjugation of Ab to the LPG-attached UCNP@SiO<sub>2</sub>(RB) was confirmed by a negative shift observed from −25.5 to −31 mV. Additionally, the increase in the hydrodynamic diameter from UCNP@SiO<sub>2</sub> to UCNP@SiO<sub>2</sub>(RB)-LPG-Ab also suggested the successful binding of antibodies on UCNP

(Figure S3). The developed nanocomposites also demonstrated good dispersibility and colloidal stability in water, PBS, and FBS (Figure S4), which is regarded as beneficial for cellular binding and internalization.

The in vitro binding ability and specificity of the functionalized UCNP@SiO<sub>2</sub>(RB)-LPG-Ab nanocomposites were examined using HT-29, an EpCAM-overexpressing human colon adenocarcinoma cell line, and BV2, an EpCAM-negative murine microglia cell line. Each cell line was incubated with 25  $\mu$ g/mL nanoparticles for 1 h and washed five times before fluorescence imaging. As shown in Figure 3 (top and second rows), the UCNP nanocomposites selectively labeled the membrane of the EpCAM-positive HT-29 cells, with their green emission outlining the membrane surface. In contrast, negligible UCNP nanocomposites were observed with the EpCAM-negative BV2 cells.

Additionally, two control experiments were conducted by incubating HT-29 cells with unconjugated UCNP@SiO<sub>2</sub>(RB)-LPG and UCNP@SiO<sub>2</sub>(RB)-LPG conjugated to a control antibody CRY104, where CRY104 is a murine monoclonal antibody and has no specific interaction with EpCAM. The conjugation of CRY104 (FITC-labeled) to UCNP@SiO<sub>2</sub>(RB) was confirmed in fluorescent emission spectra (Figure S6). As seen from Figure 3 (third and fourth rows), both of the control samples showed insignificant green emission after proper washing. Note that the pseudogreen color in the images represents the integrated green and red emissions from UCNP. These results confirm that the LPG-mediated bioconjugation approach allows anti-EpCAM to maintain good targeting capability when conjugated onto the UCNP nanocomposites, which behave very much like the antibodies conjugated to a fluorescent dye, such as FITC (Figure S7).

**Photoinduced Production of ROS.** The anticancer effect of PDT is determined by generation of ROS to induce cell apoptosis and/or necrosis. RB is a broadly used type II PS that is capable of producing highly reactive singlet oxygen (<sup>1</sup>O<sub>2</sub>) from triplet molecular oxygen (<sup>3</sup>O<sub>2</sub>) under green-light excitation.<sup>44</sup> RB has an absorption spectrum overlapping precisely with the green emission (~545 nm) of the Yb<sup>3+</sup>/Er<sup>3+</sup>-codoped UCNP (Figure 4a), and energy transfer between the UCNP and RB was confirmed by comparing the steady-state upconversion photoluminescence spectra of nanocomposites with and without RB. The UCNP@SiO<sub>2</sub>(RB)-LPG-Ab nanocomposites demonstrated a ~20% decrease in the green emission (500–550 nm) compared to those of UCNP@SiO<sub>2</sub>-LPG-Ab (Figure 4b). The consumed green emission was expected to be used by the RB encapsulated in the silica layer for production of <sup>1</sup>O<sub>2</sub>.

The rate of <sup>1</sup>O<sub>2</sub> generated by NIR-excited UCNP@SiO<sub>2</sub>(RB)-LPG-Ab in solution was detected by an absorption bleaching method using 1,3-diphenylisobenzofuran (DPBF). DPBF can rapidly and irreversibly react with <sup>1</sup>O<sub>2</sub>, leading to reduced intensity in its absorption spectrum. When mixed with UCNP@SiO<sub>2</sub>(RB)-LPG-Ab, the absorption intensity of DPBF dropped progressively as a function of time under NIR irradiation for 30 min (Figure 5a), confirming the steady production of <sup>1</sup>O<sub>2</sub>. Notably, ~30% of DPBF was consumed after 30 min of irradiation (Figure 5b), demonstrating similar <sup>1</sup>O<sub>2</sub> production that is consistent with previous reports of UCNP-based PDT.<sup>11,31,45</sup> By contrast, UCNP@SiO<sub>2</sub>-LPG-Ab did not exert any effect on the DPBF absorption intensity upon NIR irradiation nor did UCNP@SiO<sub>2</sub>(RB)-LPG-Ab without NIR irradiation (Figure 5b), indicating that no singlet oxygen was generated in both cases (Figure 5b). These results demonstrated

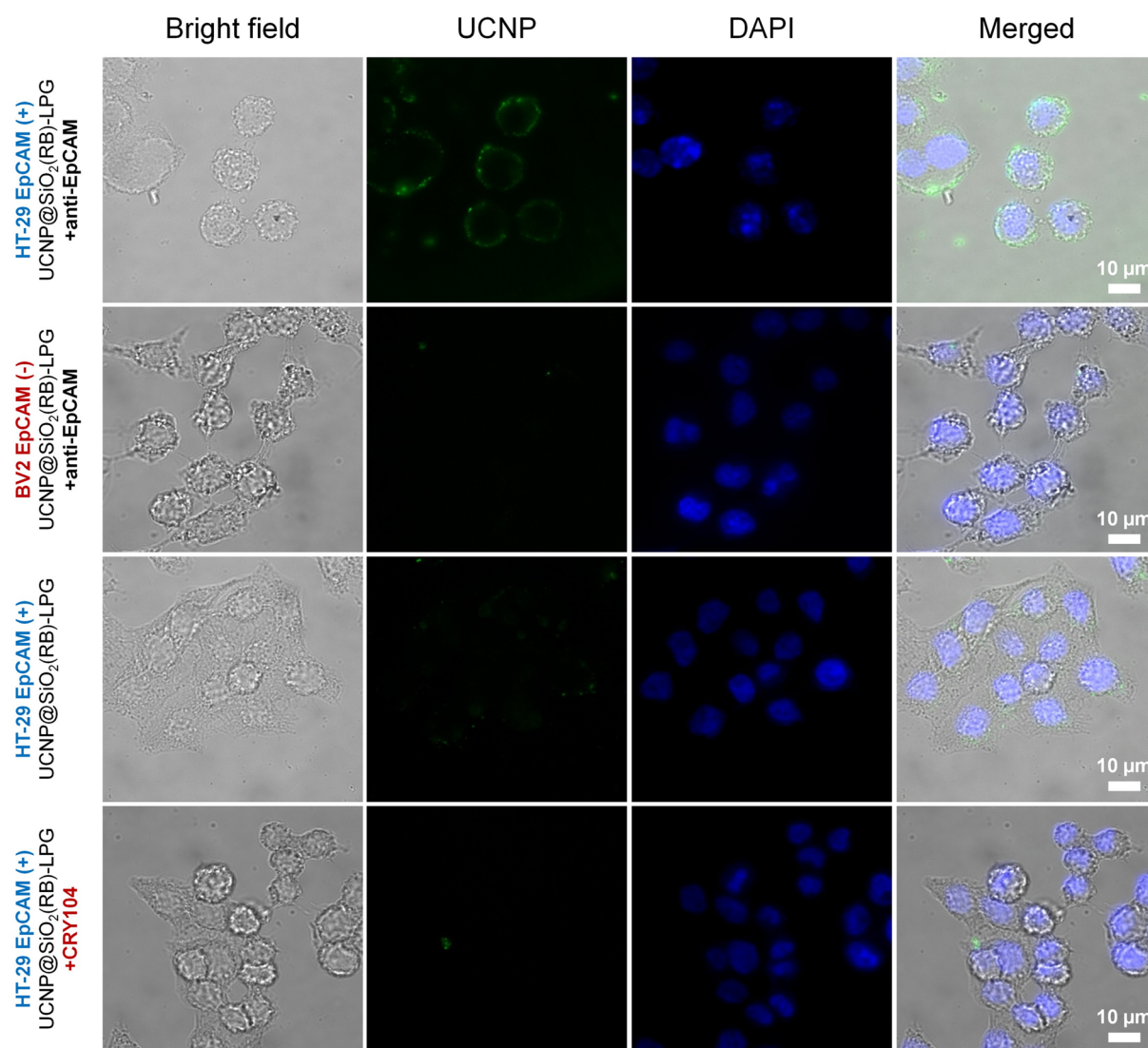


**Figure 3.** Fluorescent images of HT-29 (first row) and control BV2 cells (second row) after incubation with UCNP@SiO<sub>2</sub>(RB)-LPG-anti-EpCAM and HT-29 cells after incubation with UCNP@SiO<sub>2</sub>(RB)-LPG (third row) and UCNP@SiO<sub>2</sub>(RB)-LPG-CRY104 (fourth row).

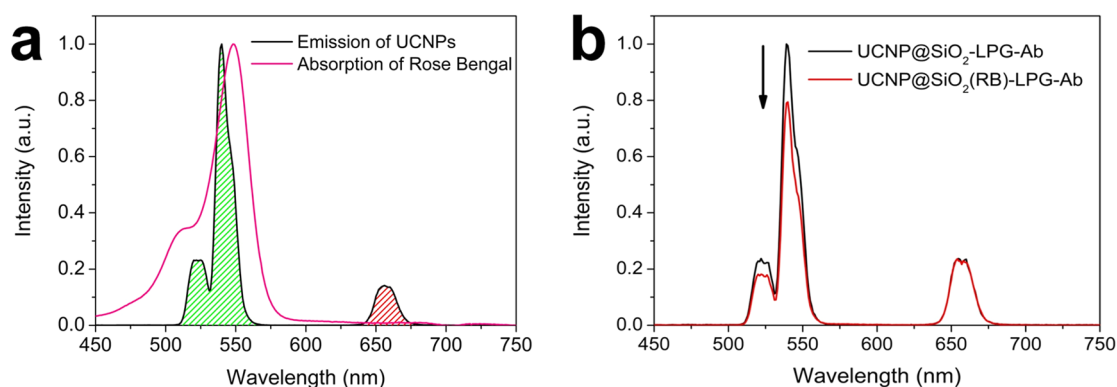


**Figure 4.** (a) Normalized absorption spectrum of RB (red line) and fluorescent emission spectrum of UCNPs (black line, area-hatched) under 980 nm excitation. (b) Upconversion luminescence spectra of UCNP@SiO<sub>2</sub>-LPG-Ab (black) and UCNP@SiO<sub>2</sub>(RB)-LPG-Ab (red) under 980 nm excitation, normalized at the red emission peak.

that <sup>1</sup>O<sub>2</sub> could be generated by efficient energy transfer between the NIR-excited UCNP and RB molecules in the silica shell.

We further investigated the production of ROS by the internalized UCNP@SiO<sub>2</sub>(RB)-LPG-Ab inside live cells (including the <sup>1</sup>O<sub>2</sub> produced by RB as well as other ROS derived

from <sup>1</sup>O<sub>2</sub>), which induce phototoxicity by direct oxidation of intracellular components such as DNA, mitochondria, and membranes. This was evaluated using a cell-permeable oxidant-sensing probe (DCFH-DA). Once diffused into cells, DCFH-DA is converted into DCFH and then transformed into green

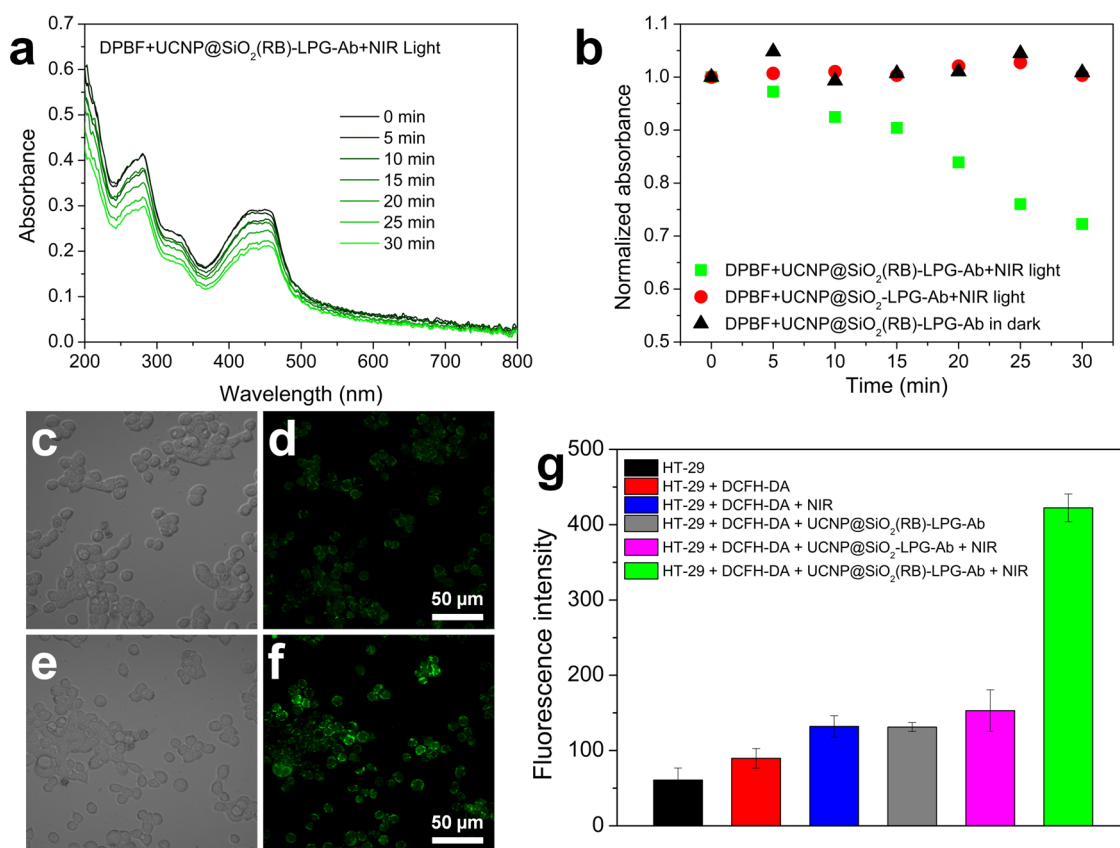


**Figure 5.** (a) Absorption spectra of a DPBF solution containing UCNP@SiO<sub>2</sub>(RB)-LPG-Ab after different times of irradiation with a 980 nm laser. (b) Comparison of DPBF consumption under NIR irradiation over 30 min. Intracellular ROS generated in HT-29 cells treated with antibody-conjugated UCNP@SiO<sub>2</sub> (c and d) and UCNP@SiO<sub>2</sub>(RB) (e and f) and then exposed to a 980 nm laser at 1.5 W/cm<sup>2</sup> for 5 min. Confocal images showing green fluorescence indicate positive staining of the marker DCFH-DA. (g) Production of intracellular ROS measured by the fluorescence intensity of DCF. HT-29 cells were treated with or without UCNP@SiO<sub>2</sub>-LPG-Ab and UCNP@SiO<sub>2</sub>(RB)-LPG-Ab, then labeled with 25  $\mu$ M DCFH-DA, and exposed to a NIR laser (1.5 W/cm<sup>2</sup>) for 5 min. Each value represents the mean  $\pm$  standard deviation of five replicates.

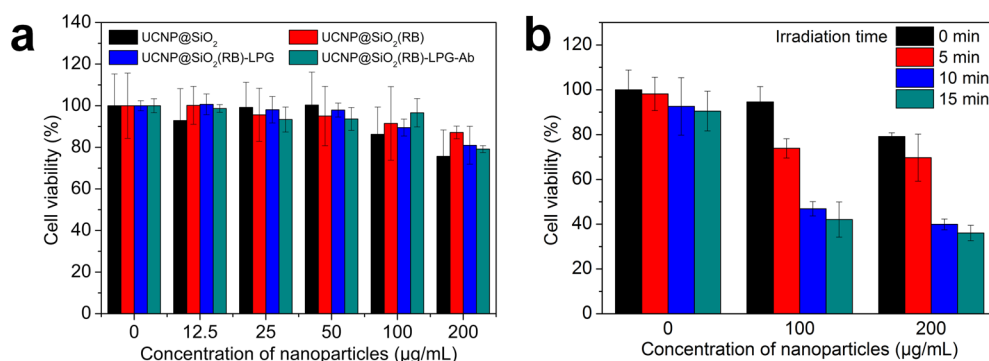


**Figure 6.** (a) Cell viability of HT-29 cells treated with UCNP@SiO<sub>2</sub>, UCNP@SiO<sub>2</sub>(RB), UCNP@SiO<sub>2</sub>(RB)-LPG, or UCNP@SiO<sub>2</sub>(RB)-LPG-Ab at various concentrations for 24 h in the dark. (b) Cell viability of HT-29 cells treated with various concentrations (0, 100, and 200  $\mu$ g/mL) of UCNP@SiO<sub>2</sub>(RB)-LPG-Ab and then exposed to 980 nm laser irradiation (1.5 W/cm<sup>2</sup>) for different durations (0, 5, 10, and 15 min). The cell viability was quantified by standard MTT assay. Each value represents the mean  $\pm$  standard deviation of five replicates.

fluorescent DCF in the presence of ROS. As shown in Figure 5d,f, after irradiation with 980 nm NIR light of identical conditions, live HT-29 cells incubated with UCNP@SiO<sub>2</sub>(RB)-LPG-Ab displayed green fluorescence significantly stronger than the same batch of cells incubated with UCNP@SiO<sub>2</sub>-LPG-Ab. The production of ROS was quantified by measuring the intensity of DCF fluorescence, showing that cells loaded with UCNP@SiO<sub>2</sub>(RB)-LPG-Ab and irradiated with NIR light had  $\sim$ 3-fold more intracellular ROS generated than any other control

samples (Figure 5g). These results illustrate that the UCNP@SiO<sub>2</sub>(RB)-LPG-Ab nanocomposite is capable of intracellular production of cytotoxic <sup>1</sup>O<sub>2</sub>, which was essential for operative PDT under selective NIR excitation.

**In Vitro Cytotoxicity and PDT.** The biocompatibility of the UCNP@SiO<sub>2</sub>(RB)-LPG-Ab nanocomposite was evaluated in vitro alongside the intermediate products [i.e., UCNP@SiO<sub>2</sub>, UCNP@SiO<sub>2</sub>(RB), and UCNP@SiO<sub>2</sub>(RB)-LPG]. HT-29 cells were incubated with each of the products at various



concentrations for 24 h in the dark condition, and then the cellular viability was tested using standard MTT assay. More than 80% of the cells were viable for all of the tested samples, even at the highest concentration of 200  $\mu\text{g/mL}$  (Figure 6a). This demonstrates the low cytotoxicity of the UCNP@SiO<sub>2</sub>(RB)-LPG-Ab nanocomposites when not being photoactivated, minimizing the off-target side effect for safe PDT in practice.

The effect of NIR exposure on live cells was first assessed using HT-29 cells in the absence of any nanoparticles. A power density of up to 1.5 W/cm<sup>2</sup> for 5 min was shown to not affect the cell growth afterward (Figure S9). This power density was therefore used for photoactivation in this study (although higher values have been applied in previous reports<sup>11,22,46,47</sup>). The NIR-induced cancer-targeting PDT was evaluated in vitro by incubating the HT-29 cells with UCNP@SiO<sub>2</sub>(RB)-LPG-Ab of different concentrations (0, 100, and 200  $\mu\text{g/mL}$ ) for 24 h. Noninternalized nanoparticles were removed by washing three times with PBS, and a fresh culture medium (DMEM) was added to the cells. A 980 nm NIR irradiation with a power density of 1.5 W/cm<sup>2</sup> was then applied for different exposure times (0, 5, 10, and 15 min), followed by incubation for another 12 h. The viability of the HT-29 cells was eventually determined using MTT assay. As seen from Figure 6b, the results showed that NIR irradiation itself (without the nanocomposites) had a limited effect on the cells, whereas the viability of the cells dropped significantly when treated with both the nanocomposites and NIR irradiation. For example, the viability of the HT-29 cells cultured with 100  $\mu\text{g/mL}$  UCNP@SiO<sub>2</sub>(RB)-LPG-Ab was reduced by  $\sim 20\%$  after 5 min of NIR irradiation and further reduced by  $\sim 40\%$  after 10 min of irradiation. As expected, the greatest effect was achieved with the highest concentrations of nanocomposites and longest irradiation time. For example, the cell viability decreased markedly to below 50% when the irradiation time was increased beyond 10 min, suggesting a therapeutic threshold of cytotoxic <sup>1</sup>O<sub>2</sub>. This confirms the PDT effect of the nanocomposite.

## CONCLUSIONS

In summary, we developed a facile strategy to synthesize targeted PDT nanocomposites combining PS molecules with upconversion nanoparticles and tumor-targeting antibodies (UCNP@SiO<sub>2</sub>(RB)-LPG-Ab). This is based on encapsulation of the PSs in a silica coating of the UCNPs and the use of LPG to directly conjugate antibodies onto the silica surface. The prepared nanocomposites were shown to specifically target tumor cells overexpressing cancer-characteristic antigens and generate singlet oxygen extracellularly and intracellularly upon NIR irradiation via energy transfer. The in vitro viability of cells after NIR irradiation demonstrates the feasibility of using these engineered nanocomposites for cancer-targeted PDT. Our study exemplified the first-time use of peptide-linker technology to assemble a biohybrid UCNP complex. The introduced biohybrid assembly provides a diverse selection of silica-coated nanoparticles, including UCNPs, PSs, and a virtually unlimited line of IgG antibodies to target specific cancer cells, endorsing the broad applicability of this platform technology for potential antibody–UCNPs coupling in different biomedical applications.

## ASSOCIATED CONTENT

### Supporting Information

The Supporting Information is available free of charge on the ACS Publications website at DOI: 10.1021/acsami.6b00713.

546 nm excited emission spectrum of 1 mg/mL UCNP@SiO<sub>2</sub>(RB), calibration curve of RB, fluorescent imaging for Ab-FITC labeling of HT-29 cells, and NIR exposure effect on the cell viability (PDF)

## AUTHOR INFORMATION

### Corresponding Author

\*Phone: +61 2 9850 7760. Fax: +61 2 9850 8115. E-mail: andrei.zvyagin@mq.edu.au.

### Notes

The authors declare no competing financial interest.

## ACKNOWLEDGMENTS

The authors acknowledge the Federal Targeted Program of the Russian Federation (Grant RFMEFI57814X0030). We thank Dr. Annemarie Nadort and Anna Guller for the discussion of ROS detection and quantitative analysis of the fluorescent intensity on imaging figures. We acknowledge also the facilities and scientific and technical assistance of the Australian Microscopy & Microanalysis Research Facility at the Australian Centre for Microscopy & Microanalysis at the University of Sydney.

## REFERENCES

- (1) Castano, A. P.; Mroz, P.; Hamblin, M. R. Photodynamic Therapy and Anti-Tumour Immunity. *Nat. Rev. Cancer* **2006**, 6 (7), 535–545.
- (2) Dolmans, D. E.; Fukumura, D.; Jain, R. K. Photodynamic Therapy for Cancer. *Nat. Rev. Cancer* **2003**, 3 (5), 380–387.
- (3) Garg, A. D.; Nowis, D.; Golab, J.; Vandenabeele, P.; Krysko, D. V.; Agostinis, P. Immunogenic Cell Death, Damps and Anticancer Therapeutics: An Emerging Amalgamation. *Biochim. Biophys. Acta, Rev. Cancer* **2010**, 1805 (1), 53–71.
- (4) Castano, A. P.; Demidova, T. N.; Hamblin, M. R. Mechanisms in Photodynamic Therapy: Part One—Photosensitizers, Photochemistry and Cellular Localization. *Photodiagn. Photodyn. Ther.* **2004**, 1 (4), 279–293.
- (5) Meinhardt, M.; Krebs, R.; Anders, A.; Heinrich, U.; Tronnier, H. Wavelength-Dependent Penetration Depths of Ultraviolet Radiation in Human Skin. *J. Biomed. Opt.* **2008**, 13 (4), 044030–044030–5.
- (6) Guiot, C.; Degiorgis, P. G.; Delsanto, P. P.; Gabriele, P.; Deisboeck, T. S. Does Tumor Growth Follow a "Universal Law"? *J. Theor. Biol.* **2003**, 225 (2), 147–151.
- (7) Smith, A. M.; Mancini, M. C.; Nie, S. Bioimaging: Second Window for in Vivo Imaging. *Nat. Nanotechnol.* **2009**, 4 (11), 710–711.
- (8) Weissleder, R. A Clearer Vision for in Vivo Imaging. *Nat. Biotechnol.* **2001**, 19 (4), 316–317.
- (9) Dai, Y.; Xiao, H.; Liu, J.; Yuan, Q.; Ma, P. a.; Yang, D.; Li, C.; Cheng, Z.; Hou, Z.; Yang, P.; Lin, J. In Vivo Multimodality Imaging and Cancer Therapy by near-Infrared Light-Triggered Trans-Platinum Pro-Drug-Conjugated Upconversion Nanoparticles. *J. Am. Chem. Soc.* **2013**, 135 (50), 18920–18929.
- (10) Idris, N. M.; Jayakumar, M. K. G.; Bansal, A.; Zhang, Y. Upconversion Nanoparticles as Versatile Light Nanotransducers for Photoactivation Applications. *Chem. Soc. Rev.* **2015**, 44 (6), 1449–1478.
- (11) Wang, H.; Liu, Z.; Wang, S.; Dong, C.; Gong, X.; Zhao, P.; Chang, J. Mc540 and Upconverting Nanocrystal Coloaded Polymeric Liposome for near-Infrared Light-Triggered Photodynamic Therapy and Cell Fluorescent Imaging. *ACS Appl. Mater. Interfaces* **2014**, 6 (5), 3219–3225.
- (12) Lucky, S. S.; Muhammad Idris, N.; Li, Z.; Huang, K.; Soo, K. C.; Zhang, Y. Titania Coated Upconversion Nanoparticles for near-Infrared Light Triggered Photodynamic Therapy. *ACS Nano* **2015**, 9 (1), 191–205.
- (13) Wang, F.; Liu, X. Upconversion Multicolor Fine-Tuning: Visible to near-Infrared Emission from Lanthanide-Doped NaYF<sub>4</sub> Nanoparticles. *J. Am. Chem. Soc.* **2008**, 130 (17), 5642–5643.

- (14) Wang, M.; Mi, C.; Zhang, Y.; Liu, J.; Li, F.; Mao, C.; Xu, S. NIR-Responsive Silica-Coated Naybf<sub>4</sub>: Er/Tm/Ho Upconversion Fluorescent Nanoparticles with Tunable Emission Colors and Their Applications in Immunolabeling and Fluorescent Imaging of Cancer Cells. *J. Phys. Chem. C* **2009**, *113* (44), 19021–19027.
- (15) Hou, Z.; Zhang, Y.; Deng, K.; Chen, Y.; Li, X.; Deng, X.; Cheng, Z.; Lian, H.; Li, C.; Lin, J. Uv-Emitting Upconversion-Based Tio<sub>2</sub> Photosensitizing Nanoplatfrom: Near-Infrared Light Mediated in Vivo Photodynamic Therapy Via Mitochondria-Involved Apoptosis Pathway. *ACS Nano* **2015**, *9* (3), 2584–2599.
- (16) Punjabi, A.; Wu, X.; Tokatli-Apollon, A.; El-Rifai, M.; Lee, H.; Zhang, Y.; Wang, C.; Liu, Z.; Chan, E. M.; Duan, C.; Han, G. Amplifying the Red-Emission of Upconverting Nanoparticles for Biocompatible Clinically Used Prodrug-Induced Photodynamic Therapy. *ACS Nano* **2014**, *8* (10), 10621–10630.
- (17) Wei, Y.; Chen, Q.; Wu, B.; Zhou, A.; Xing, D. High-Sensitivity in Vivo Imaging for Tumors Using a Spectral up-Conversion Nanoparticle Nayf<sub>4</sub>: Yb 3+, Er 3+ in Cooperation with a Microtubulin Inhibitor. *Nanoscale* **2012**, *4* (13), 3901–3909.
- (18) Song, Z.; Anissimov, Y. G.; Zhao, J.; Nechaev, A. V.; Nadort, A.; Jin, D.; Prow, T. W.; Roberts, M. S.; Zvyagin, A. V. Background Free Imaging of Upconversion Nanoparticle Distribution in Human Skin. *J. Biomed. Opt.* **2013**, *18* (6), 061215.
- (19) Nadort, A.; Sreenivasan, V. K.; Song, Z.; Grebenik, E. A.; Nechaev, A. V.; Semchishen, V. A.; Panchenko, V. Y.; Zvyagin, A. V. Quantitative Imaging of Single Upconversion Nanoparticles in Biological Tissue. *PLoS One* **2013**, *8* (5), e63292.
- (20) Gai, S.; Li, C.; Yang, P.; Lin, J. Recent Progress in Rare Earth Micro/Nanocrystals: Soft Chemical Synthesis, Luminescent Properties, and Biomedical Applications. *Chem. Rev.* **2014**, *114* (4), 2343–2389.
- (21) Zhou, J.; Liu, Z.; Li, F. Upconversion Nanophosphors for Small-Animal Imaging. *Chem. Soc. Rev.* **2012**, *41* (3), 1323–1349.
- (22) Idris, N. M.; Gnanasamandhan, M. K.; Zhang, J.; Ho, P. C.; Mahendran, R.; Zhang, Y. In Vivo Photodynamic Therapy Using Upconversion Nanoparticles as Remote-Controlled Nanotransducers. *Nat. Med.* **2012**, *18* (10), 1580–1585.
- (23) Cui, S.; Yin, D.; Chen, Y.; Di, Y.; Chen, H.; Ma, Y.; Achilefu, S.; Gu, Y. In Vivo Targeted Deep-Tissue Photodynamic Therapy Based on near-Infrared Light Triggered Upconversion Nanoconstruct. *ACS Nano* **2013**, *7* (1), 676–688.
- (24) Liu, K.; Liu, X.; Zeng, Q.; Zhang, Y.; Tu, L.; Liu, T.; Kong, X.; Wang, Y.; Cao, F.; Lambrechts, S. A.; Aalders, M. C. G.; Zhang, H. Covalently Assembled Nir Nanoplatfrom for Simultaneous Fluorescence Imaging and Photodynamic Therapy of Cancer Cells. *ACS Nano* **2012**, *6* (5), 4054–4062.
- (25) Zhou, A.; Wei, Y.; Wu, B.; Chen, Q.; Xing, D. Pyropheophorbide a and C (Rgdyk) Comodified Chitosan-Wrapped Upconversion Nanoparticle for Targeted near-Infrared Photodynamic Therapy. *Mol. Pharmaceutics* **2012**, *9* (6), 1580–1589.
- (26) Zhang, P.; Steelant, W.; Kumar, M.; Scholfield, M. Versatile Photosensitizers for Photodynamic Therapy at Infrared Excitation. *J. Am. Chem. Soc.* **2007**, *129* (15), 4526–4527.
- (27) Sunna, A.; Chi, F.; Bergquist, P. L. A Linker Peptide with High Affinity Towards Silica-Containing Materials. *New Biotechnol.* **2013**, *30* (5), 485–492.
- (28) Li, Z.; Zhang, Y.; Jiang, S. Multicolor Core/Shell-Structured Upconversion Fluorescent Nanoparticles. *Adv. Mater.* **2008**, *20* (24), 4765–4769.
- (29) Johnson, N. J.; Korinek, A.; Dong, C.; van Veggel, F. C. Self-Focusing by Ostwald Ripening: A Strategy for Layer-by-Layer Epitaxial Growth on Upconverting Nanocrystals. *J. Am. Chem. Soc.* **2012**, *134* (27), 11068–11071.
- (30) Xing, H.; Bu, W.; Zhang, S.; Zheng, X.; Li, M.; Chen, F.; He, Q.; Zhou, L.; Peng, W.; Hua, Y.; Shi, J. Multifunctional Nanoprobes for Upconversion Fluorescence, Mr and Ct Trimodal Imaging. *Biomaterials* **2012**, *33* (4), 1079–1089.
- (31) Fan, W.; Shen, B.; Bu, W.; Chen, F.; He, Q.; Zhao, K.; Zhang, S.; Zhou, L.; Peng, W.; Xiao, Q.; Ni, D.; Liu, J.; Shi, J. A Smart Upconversion-Based Mesoporous Silica Nanotheranostic System for Synergetic Chemo-/Radio-/Photodynamic Therapy and Simultaneous Mr/Ucl Imaging. *Biomaterials* **2014**, *35* (32), 8992–9002.
- (32) Qiao, X.-F.; Zhou, J.-C.; Xiao, J.-W.; Wang, Y.-F.; Sun, L.-D.; Yan, C.-H. Triple-Functional Core–Shell Structured Upconversion Luminescent Nanoparticles Covalently Grafted with Photosensitizer for Luminescent, Magnetic Resonance Imaging and Photodynamic Therapy in Vitro. *Nanoscale* **2012**, *4* (15), 4611–4623.
- (33) Liu, J.-N.; Bu, W.-B.; Shi, J.-L. Silica Coated Upconversion Nanoparticles: A Versatile Platform for the Development of Efficient Theranostics. *Acc. Chem. Res.* **2015**, *48* (7), 1797–1805.
- (34) Yang, D.; Ma, P.; Hou, Z.; Cheng, Z.; Li, C.; Lin, J. Current Advances in Lanthanide Ion (Ln 3+)-Based Upconversion Nanomaterials for Drug Delivery. *Chem. Soc. Rev.* **2015**, *44* (6), 1416–1448.
- (35) Wuister, S. F.; de Mello Donegá, C.; Meijerink, A. Efficient Energy Transfer between Nanocrystalline Yag: Ce and Tritc. *Phys. Chem. Chem. Phys.* **2004**, *6* (8), 1633–1636.
- (36) Wang, Y.; Liu, K.; Liu, X.; Dohnalová, K.; Gregorkiewicz, T.; Kong, X.; Aalders, M. C.; Buma, W. J.; Zhang, H. Critical Shell Thickness of Core/Shell Upconversion Luminescence Nanoplatfrom for Fret Application. *J. Phys. Chem. Lett.* **2011**, *2* (17), 2083–2088.
- (37) Care, A.; Bergquist, P. L.; Sunna, A. Solid-Binding Peptides: Smart Tools for Nanobiotechnology. *Trends Biotechnol.* **2015**, *33* (5), 259–268.
- (38) Sarikaya, M.; Tamerler, C.; Jen, A. K.-Y.; Schulten, K.; Baneyx, F. Molecular Biomimetics: Nanotechnology through Biology. *Nat. Mater.* **2003**, *2* (9), 577–585.
- (39) Tang, Z.; Palafox-Hernandez, J. P.; Law, W.-C.; Hughes, Z. E.; Swihart, M. T.; Prasad, P. N.; Knecht, M. R.; Walsh, T. R. Biomolecular Recognition Principles for Bionanocombinatorics: An Integrated Approach to Elucidate Enthalpic and Entropic Factors. *ACS Nano* **2013**, *7* (11), 9632–9646.
- (40) Care, A.; Chi, F.; Bergquist, P. L.; Sunna, A. Biofunctionalization of Silica-Coated Magnetic Particles Mediated by a Peptide. *J. Nanopart. Res.* **2014**, *16* (8), 1–9.
- (41) Coyle, B. L.; Baneyx, F. A Cleavable Silica-Binding Affinity Tag for Rapid and Inexpensive Protein Purification. *Biotechnol. Bioeng.* **2014**, *111* (10), 2019–2026.
- (42) Nahshol, O.; Bronner, V.; Notcovich, A.; Rubrecht, L.; Laune, D.; Bravman, T. Parallel Kinetic Analysis and Affinity Determination of Hundreds of Monoclonal Antibodies Using the Proteon Xpr36. *Anal. Biochem.* **2008**, *383* (1), 52–60.
- (43) Patriarca, C.; Macchi, R. M.; Marschner, A. K.; Mellstedt, H. Epithelial Cell Adhesion Molecule Expression (Cd326) in Cancer: A Short Review. *Cancer Treat. Rev.* **2012**, *38* (1), 68–75.
- (44) Paczkowski, J.; Lamberts, J.; Paczkowska, B.; Neckers, D. Photophysical Properties of Rose Bengal and Its Derivatives (Xii). *J. Free Radicals Biol. Med.* **1985**, *1* (5), 341–351.
- (45) Zhao, Z.; Han, Y.; Lin, C.; Hu, D.; Wang, F.; Chen, X.; Chen, Z.; Zheng, N. Multifunctional Core-Shell Upconverting Nanoparticles for Imaging and Photodynamic Therapy of Liver Cancer Cells. *Chem. - Asian J.* **2012**, *7* (4), 830–837.
- (46) Wang, Y.; Wang, H.; Liu, D.; Song, S.; Wang, X.; Zhang, H. Graphene Oxide Covalently Grafted Upconversion Nanoparticles for Combined Nir Mediated Imaging and Photothermal/Photodynamic Cancer Therapy. *Biomaterials* **2013**, *34* (31), 7715–7724.
- (47) Shan, J.; Budijono, S. J.; Hu, G.; Yao, N.; Kang, Y.; Ju, Y.; Prud'homme, R. K. Pegylated Composite Nanoparticles Containing Upconverting Phosphors and Meso-Tetraphenyl Porphine (Tpp) for Photodynamic Therapy. *Adv. Funct. Mater.* **2011**, *21* (13), 2488–2495.

### Supporting Information

#### Facile Assembly of Functional Upconversion Nanoparticles for Targeted Cancer Imaging and Photodynamic Therapy

*Liuen Liang,<sup>†,⊥</sup> Andrew Care,<sup>‡,⊥</sup> Run Zhang,<sup>‡,⊥</sup> Yiqing Lu,<sup>⊥</sup> Nicolle H. Packer,<sup>‡,⊥</sup>*

*Anwar Sunna,<sup>‡,⊥</sup> Yi Qian,<sup>†</sup> and Andrei V. Zvyagin<sup>\*,⊥,§</sup>*

<sup>†</sup> Department of Biomedical Sciences, Macquarie University, North Ryde, NSW 2109, Australia

<sup>‡</sup> Department of Chemistry and Biomolecular Sciences, Macquarie University, North Ryde, NSW 2109, Australia

<sup>⊥</sup> ARC Centre of Excellence for Nanoscale BioPhotonics, Macquarie University, North Ryde, NSW 2109, Australia

<sup>§</sup> Laboratory of Optical Theranostics, N. I. Lobachevsky Nizhny Novgorod State University, Nizhny Novgorod 603950, Russia

\* Corresponding authors      Andrei V. Zvyagin

Department of Physics and Astronomy

Macquarie University

North Ryde, Sydney, NSW 2109

Australia

Phone: +61 2 9850 7760

Fax: +61 2 9850 8115

Email: andrei.zvyagin@mq.edu.au

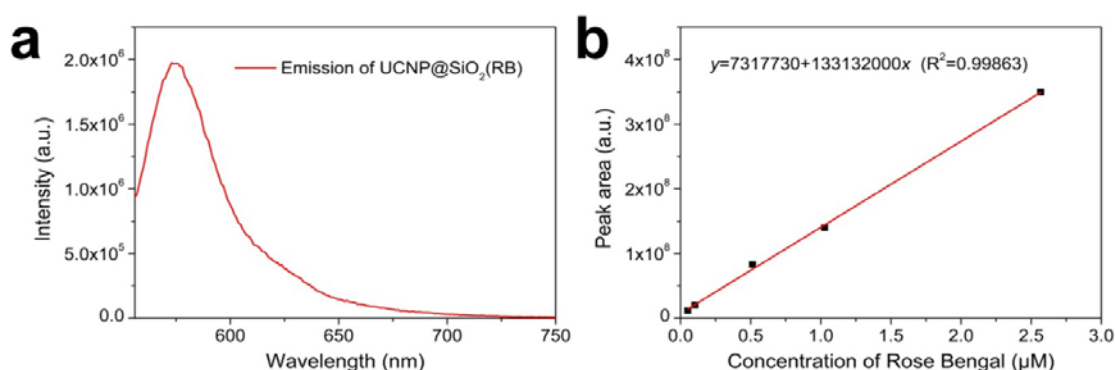


**Figure S1.** (a) Emission spectrum of 1 mg/mL UCNP@SiO<sub>2</sub>(RB) excited at 546 nm. (b) Calibration curve for RB fluorescence emission.

The calibration curve of RB was prepared by a series of known concentrations of RB solutions that were excited at 546 nm and the fluorescent emission spectra recorded between 556 nm and 750 nm using a Fluorolog-Tau3 spectrofluorometer (Jobin Yvon-Horiba) in a quartz cuvette at room temperature using xenon lamp as an excitation source. The areas of each fluorescent emission spectra were correlated with the RB concentration (μM) to obtain the standard curve. The estimated area of UCNP@SiO<sub>2</sub>(RB) emission spectrum (Fig. 1a) is  $9.2 \times 10^7$ ; therefore, the calculated concentration of RB is 0.64 μM. The loading efficiency (loading efficiency = RB loaded × 100% / RB added) is determined as  $1.7 \pm 0.2\%$ . The relative concentration of RB in our UCNP treatment dose (100 μg/mL) is calculated to be 64 nM, which is higher than the reported level of nanoparticle bound RB (50 nM) exerting phototoxic effect to cancer cells.<sup>1</sup>

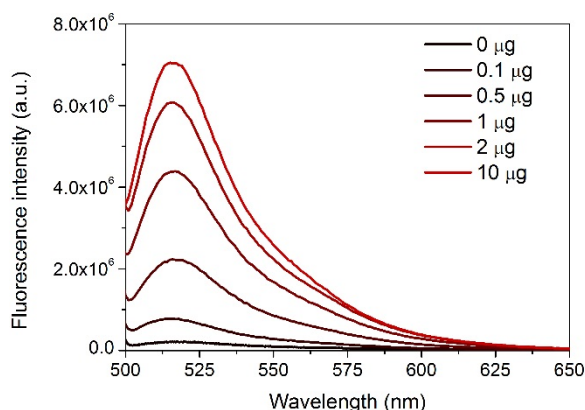


**Figure S2.** Fluorescent emission spectra of FITC-labelled antibodies conjugated to UCNP@SiO<sub>2</sub>(RB) versus LPG amount under 488-nm excitation.

Various amounts of LPG (0, 0.1, 0.5, 1, 2, 10 μg) were firstly conjugated to UCNP@SiO<sub>2</sub>(RB) (1 mg/mL), followed by addition of 10-μg FITC-labelled antibodies. After removal of the unconjugated antibodies, the emission spectra of FITC-antibodies from the nanocomposites were recorded under 488-nm light excitation. The result showed that the average number of bound antibodies was increased versus the amount of LPG mediator.

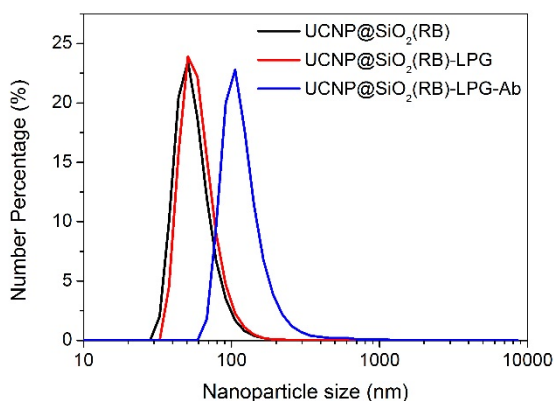


**Figure S3.** Size distribution of UCNP@SiO<sub>2</sub>(RB), UCNP@SiO<sub>2</sub>(RB)-LPG and UCNP@SiO<sub>2</sub>(RB)-LPG-Ab, determined by DLS.

DLS measurement was performed to characterise the size distribution of nanocomposites



in water. It was shown that LPG binding resulted in a slight increase of nanoparticle hydrodynamic mean diameter, but had little effect on the distribution and stability. The antibodies conjugation to LPG-bound nanoparticles resulted in an overall hydrodynamic diameter increase of ~45 nm, indicating the successful attachment of antibodies to the nanocomposite surface. This apparent hydrodynamic diameter increase can be attributed to the attachment of antibodies sized approximately 10 nm,<sup>2</sup> accounting for the hydrodynamic diameter increase of ~20 nm; and also partial aggregation of the nanocomposites whose negative surface charges were shielded by antibody macromolecules.

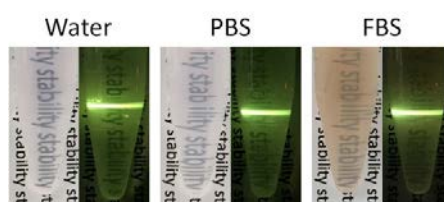


**Figure S4.** Photographs of UCNP@SiO<sub>2</sub>(RB)-LPG-Ab dispersed in water, PBS, and FBS for 4 h, and illuminated with the 980 nm laser beam.

Colloidal stability of the nanocomposite was examined by dispersing the nanoparticles in water, PBS, and FBS. No observable aggregation of nanocomposites was found in all suspensions after 4 h incubation, which ensured ample time duration for their uptake in cells.

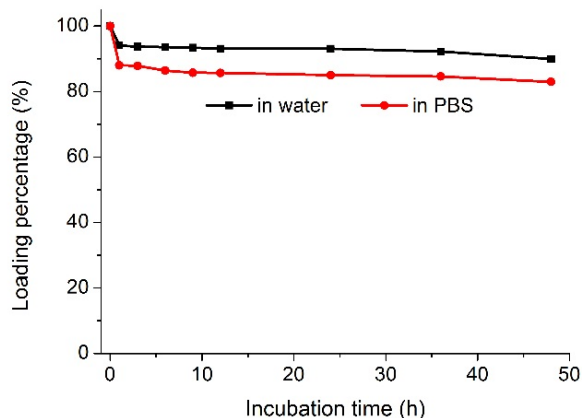


**Figure S5.** Release curve for RB entrapped in UCNP@SiO<sub>2</sub>(RB)-LPG-Ab in water and PBS (pH=7.4).

The release of RB in UCNP@SiO<sub>2</sub>(RB)-LPG-Ab was monitored for a period of 48 h in water and pH 7.4 PBS, respectively. The nanoparticles suspension was kept shaking continuously at room temperature. At certain time intervals, nanoparticles were spined down by centrifugation and the emission from released RB in the supernatants was detected under the excitation at 546 nm. The release percentage was calculated relative to the loading concentration of RB by by integrating the RB emission in the spectral interval of 565–750 nm. Minor release of RB (< 20%) was observed in both water and PBS after shaking for 48 h. The results suggest stable encapsulation of RB molecules inside the dense silica layer of the nanocomposites.

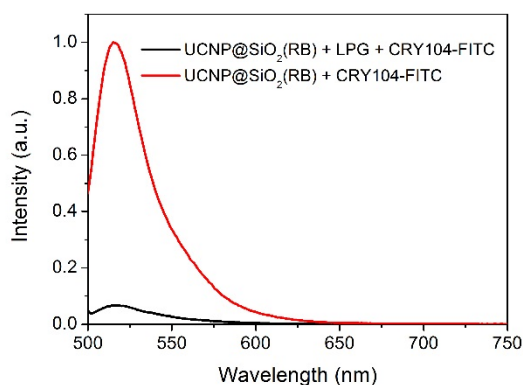


**Figure S6.** Normalized fluorescent emission from FITC-conjugated CRY104 immobilized on UCNPs with (red) and without (black) LPG under 488 nm excitation.

To confirm the conjugation of CRY104 to UCNP@SiO<sub>2</sub>(RB), 20 µg FITC-labelled CRY104 was incubated with 1 mg nanoparticles in the presence and absence of 30 µg LPG in 100 mM Tris-HCl buffer. Experimental details are given in experiment section “LPG-mediated Functionalization of UCNPs”. After washing the unbound antibodies, emission from CRY104-FITC immobilized on nanoparticles was measured by fluorescence spectrofluorometer under 488 nm excitation. Significant green emission was observed when LPG was added in the incubation, confirming the LPG-mediated conjugation of CRY104 to UCNP@SiO<sub>2</sub>(RB).

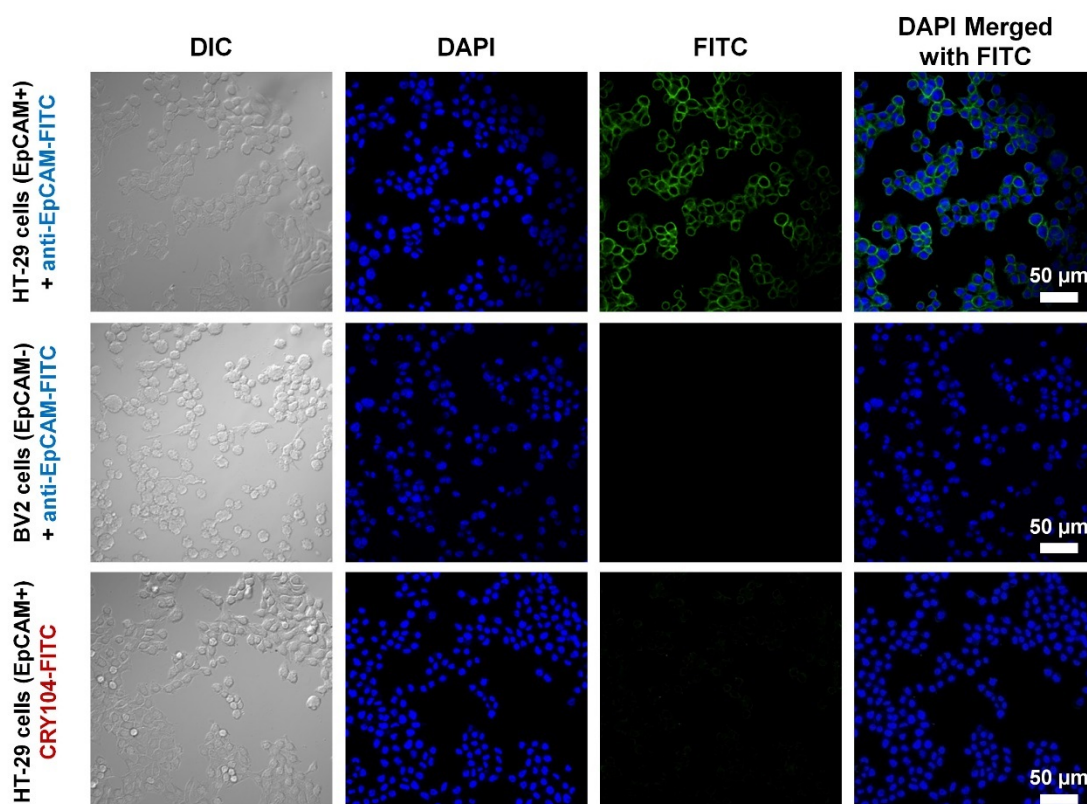


**Figure S7.** Fluorescence imaging of HT-29 (top row), control BV2 cells (middle row) after incubation with anti-EpCAM-FITC and HT-29 (bottom row) after incubation with CRY104-FITC. DIC refers to differential interference contrast.

Fluorescent imaging for anti-EpCAM-FITC showed a strong green signal in HT-29 cells (top row) with EpCAM expression and no signal in EpCAM-negative BV2 cells (middle row). The negative control CRY104-FITC showed no signal for the HT-29 cells. These results confirmed the specific targeting ability of anti-EpCAM towards HT-29 cells. FITC was visualized using an Olympus Fluoview FV1200 confocal microscope excited with a 473 nm laser and emission was filtered and collected through 490–590 nm.

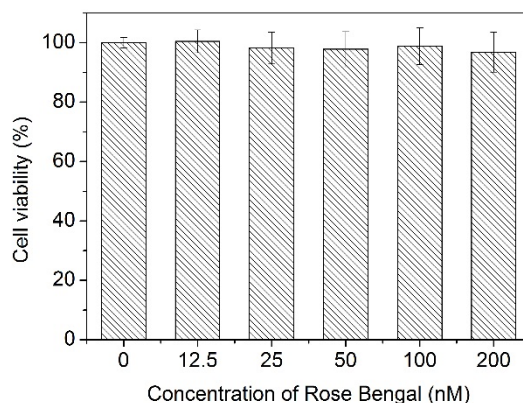


**Figure S8.** Cell viability of HT-29 cells treated with different concentrations of RB for 24 h in dark, and determined by MTT assay.

To assess the cytotoxicity of RB on HT-29 cells, cells were seeded at a density of 5000 cells per well onto a 96-well plate and allowed to grow for 12 h, followed by incubation with various concentration of RB in the dark for another 24 h. The impact of RB on HT-29 cell viability was determined by MTT assay. No toxicity of RB to cells was observed.

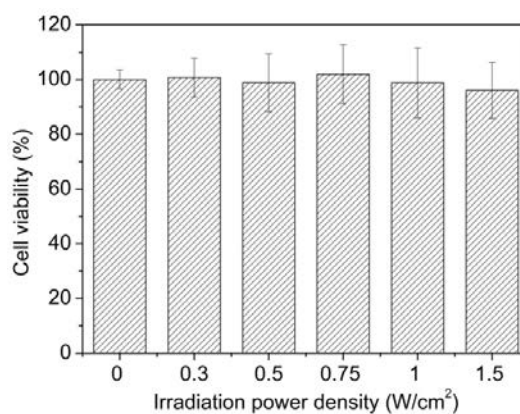


**Figure S9.** Viability of HT-29 cells irradiated with a 980 nm laser at different power densities (0, 0.3, 0.5, 0.75, 1 and 1.5 W/cm<sup>2</sup>).

To assess NIR exposure effect on cells viability, HT-29 cells were grown in a 96-well plate at the density of 5000 cells/well and incubated for 24 h at 37 °C under 5% CO<sub>2</sub>. A power-adjustable 980 nm CW diode laser with a maximum power output of 10 W was

used as the excitation source. After 5 min of 980 nm irradiation at different power densities (0, 0.3, 0.5, 0.75, 1 and 1.5 W/cm<sup>2</sup>), the cells were incubated for an additional 12 h. The cell viability was measured with the MTT assay.

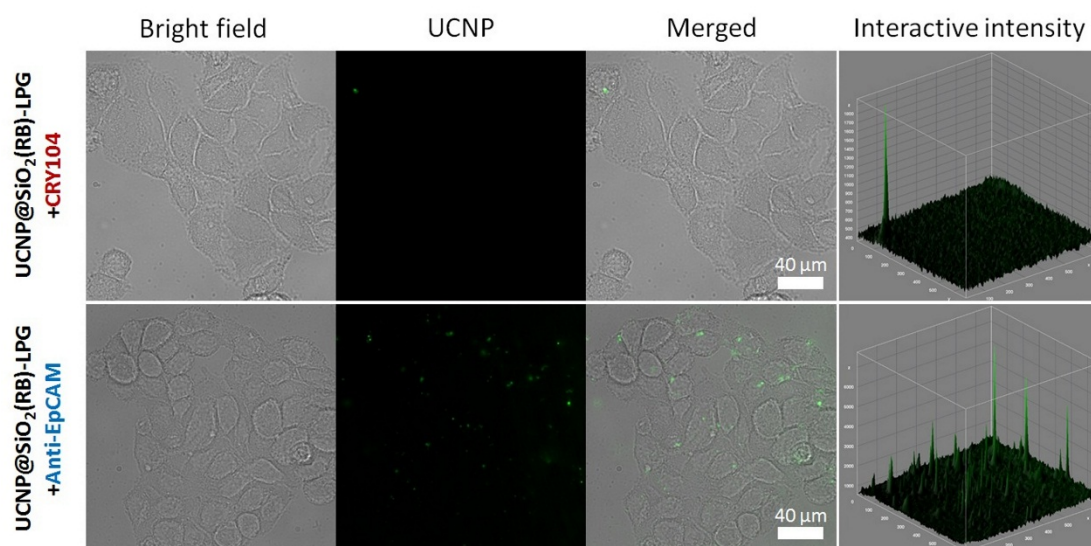


**Figure S10.** Upconversion luminescence imaging of HT-29 cells incubated with 100 μg/mL of non-specific antibodies coated UCNP (UCNP@SiO<sub>2</sub>(RB)-LPG-CRY104, upper panel) and specific antibodies coated UCNP (UCNP@SiO<sub>2</sub>(RB)-LPG- anti-EpCAM, lower panel) for 12 h at 37 °C. The 3D interactive intensity of the luminescence images was analysed using ImageJ.

The cellular binding was investigated by incubating HT-29 cells with nanoparticles functionalised with non-specific-binding antibodies (CRY104) and targeting antibodies (anti-EpCAM). Cells were cooled to 4 °C for 20 min before the addition of nanoparticles to avoid non-specific internalisation. Nanoparticles conjugated with different antibodies were incubated with the cells at 4 °C. After 10 min of incubation, cells were rinsed twice with fresh cell culture media followed by incubation for 12 h at 37 °C. The internalised nanoparticles were then observed by fluorescence imaging (see experiment section Cell Imaging for instrument description). As shown in Figure S10, negligible UCNP nanocomposites were found in cells incubated with UCNP@SiO<sub>2</sub>(RB)-LPG-CRY104. By contrast, significant amount of UCNP@SiO<sub>2</sub>(RB)-LPG-anti-EpCAM were observed

in cells after proper washing.

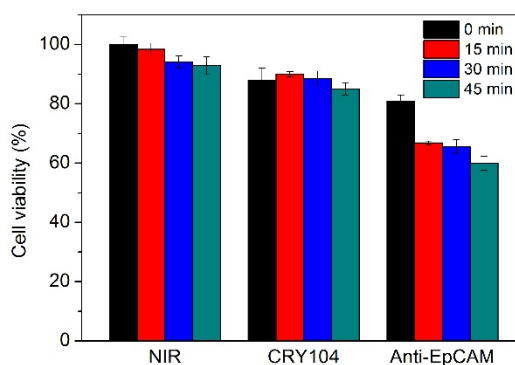


**Figure S11.** Cell viability of HT-29 cells treated without nanoparticles (NIR), with 100  $\mu\text{g/mL}$  of non-specific antibodies coated UCNP (UCNP@SiO<sub>2</sub>(RB)-LPG-CRY104) and 100  $\mu\text{g/mL}$  of specific antibodies coated UCNP (UCNP@SiO<sub>2</sub>(RB)-LPG-anti-EpCAM), followed by 980 nm laser irradiation (0.5 W/cm<sup>2</sup>) for different durations (0, 15, 30, 45 min).

In order to test whether the nanocomposites exert therapeutic effect on cancer cells under the lower irradiation power density, NIR irradiation of the nanocomposites was performed using the power density of 0.5 W/cm<sup>2</sup>. HT-29 cells were incubated with 100  $\mu\text{g/mL}$  non-specific and specific nanocomposites at 4 °C for 10 min, respectively. Unbound nanoparticles were removed by rinsing the cells twice with fresh cell culture media. Cells were then cultured for another 12 h before NIR irradiation for different time (0, 15, 30 and 45 min). As a result, the comparison between cells loaded without nanoparticles, treated with CRY104 functionalized nanoparticles and with anti-EpCAM functionalized nanoparticles showed a borderline significant effect, where the cell viability below 70% was observable in the group that was incubated with the targeting nanocomposites. Although the higher power density of 1.5 W/cm<sup>2</sup> is preferred, the efficacy of NIR PDT photosensitized by targeting UCNP@SiO<sub>2</sub>(RB)-LPG-anti-EpCAM nanocomposites was confirmed using the lower power density of 0.5 W/cm<sup>2</sup>.

### References

- (1) Wang, B.; Wang, J.-H.; Liu, Q.; Huang, H.; Chen, M.; Li, K.; Li, C.; Yu, X.-F.; Chu, P. K., Rose-Bengal-Conjugated Gold Nanorods for in Vivo Photodynamic and Photothermal Oral Cancer Therapies. *Biomaterials* **2014**, *35* (6), 1954-1966.
- (2) Reth, M., Matching Cellular Dimensions with Molecular Sizes. *Nat. Immunol.* **2013**, *14* (8), 765-767.



# 6

## **The Effect of Surface Characteristics of Upconversion Nanoparticle on Corona Formation and Cell Interaction**

### **6.1 Introduction**

In a protein-abundant biological medium, nanoparticles (NPs) have propensity to interact with proteins due to their nanometre size and large surface-to-volume ratio. The adsorption of proteins results in formation of a dynamic protein corona on the nanoparticle surface, which is profoundly affected by the protein properties, as well as the physiochemical characteristics of NPs. Recent studies have demonstrated that a protein corona layer would give a biological identity to NPs and thereby influenced their cellular uptake, cytotoxicity, targeting ability, and biodistribution. Hence, a careful understanding of the corona composition and its effect on the biological behaviour of NPs is of great importance for applications of NPs in biomedicine. In view of that, the corona formation has been characterized for a variety of nanoparticles in physiological fluids, including silica, silver, gold, polystyrene, carbon nanotubes, and iron oxide nanoparticles. Interestingly, no detailed studies have been conducted for the interaction of serum proteins with UCNPs. Hence, there is an urgent need to investigate the corona formation on UCNPs and its effects on UCNP-cell interactions.

The evaluation of UCNPs for biomedical applications is generally performed in an *in vitro* cell culture system, which typically contains 10% FBS as serum supplement. FBS is a complex mixture of different types of proteins mixed at various concentrations. Therefore, thorough analysis of the FBS proteins binding on UCNP surface is essential to further elucidate the cellular implications of corona. In this chapter, we aim to identify and characterize the amount and composition of FBS proteins firmly bound onto charged

UCNPs, using BCA protein assay and mass spectrometry. Moreover, the presence of a protein corona on UCNPs was further investigated to understand its effect on the cytotoxicity, cell binding, and cell uptake of UCNPs on cancer cells MDA-MB-231. The findings of this work will enhance the existing knowledge on UCNPs protein adsorption and provide useful information for correlating the UCNPs-cell interaction to their surface corona proteins in the *in vitro* studies.

### 6.2 Author's Contribution to The Paper

The PhD candidate (Liu Liang) is the first author of this paper. She contributed to the preparation, surface modifications, and characterizations of UCNPs. She also performed the coating of hard corona on UCNPs and conducted the BCA assay. She set up the cellular experiments and collected the data. She did the majority of data analysis, figure preparation, and manuscript writing.

Dr. Arun Everest-Dass provided an important contribution on the proteomic analysis of the UCNPs corona by preparing the samples for mass spectrometry, constructing the corresponding figures, and interpreting the results. Dr. Run Zhang contributed the helpful discussion about the experiment planning. Prof. Yi Qian gave advice and provided lab facilities for cell experiments. Prof. Nicolle Packer provided the instrumental and financial support for the protein mass spectrum measurement. A/Prof. Andrei Zvyagin coordinated this work, designed the project, provided continuous feedback, and finalized the manuscript writing. All authors gave their feedback on this manuscript.

### 6.3 Full Paper

#### The Effect of Surface Characteristics of Upconversion Nanoparticles on Corona Formation and Cell Interaction

*Liuen Liang,<sup>a,b</sup> Arun V. Everest-Dass,<sup>a</sup> Run Zhang,<sup>a,c</sup> Yi Qian,<sup>b</sup> Nicolle H. Packer,<sup>a</sup> Andrei V. Zvyagin,<sup>a,d,\*</sup>*

a-ARC Centre of Excellence for Nanoscale BioPhotonics (CNBP), Macquarie University, Sydney, NSW 2109, Australia

b-Department of Biomedical Sciences, Macquarie University, Sydney, NSW 2109, Australia

c-Australian Institute for Bioengineering and Nanotechnology, The University of Queensland, Brisbane, QLD 4072, Australia

d-Laboratory of Optical Theranostics, N. I. Lobachevsky State University of Nizhny, Novgorod, Nizhny Novgorod 603950, Russia

\* Corresponding author      Andrei V. Zvyagin  
Department of Physics and Astronomy  
Macquarie University  
North Ryde, Sydney, NSW 2109  
Australia

Phone:                              +61 2 9850 7760

Fax:                                 +61 2 9850 8115

Email:                              andrei.zvyagin@mq.edu.au

### Abstract

Most applications of nanoparticles in the life sciences require control over their properties in the protein-abundant biological fluids, where the nanoparticle surface is quickly redressed with physisorbed proteins, forming a “protein corona”. Owing to the unique optical properties, emerging photophotoluminescent upconversion nanoparticles (UCNPs) provide a particularly attractive test for investigation of the protein corona formation. For the first time, we present a systematic study of the protein corona formation in complete cell culture medium on three most representative surface-modified UCNP coated with positively-charged (+) polyethylenimine (PEI), (–) negatively-charged poly(acrylic acid) (PAA), and neutral (0) poly(ethylene glycol) (PEG). Our quantitative assay revealed ~4-times greater protein content on (+) PEI-UCNP in comparison with that of (–) PAA- and (0) PEG- UCNP samples. This was corroborated by the mass spectrometry based proteomic analysis, showing distinct protein abundance on (+) PEI-UCNP. The presence of a protein corona (♣) on UCNPs was found to inhibit the binding and cellular uptake of PAA- and PEG- UCNPs, while enhancing the binding and uptake of PEI-UCNP by MDA-MB-231 cells. The cytotoxicity of UCNP-corona composites (♣UCNPs) was found slightly reduced for all surface coatings. Our findings point to the surface coating charge as the key determinant for the formation of protein corona on UCNP, which then mediates the nanoparticle interactions with cells.

### Keywords

Upconversion nanoparticles, protein corona, nanoparticle toxicity, protein adsorption, nanoparticle uptake

## 1. Introduction

Design, production and applications of biofunctional nanoparticles (NPs) are at the heart of the field of nanomedicine, which is paving a way for modern personalized medicine.<sup>1-</sup>

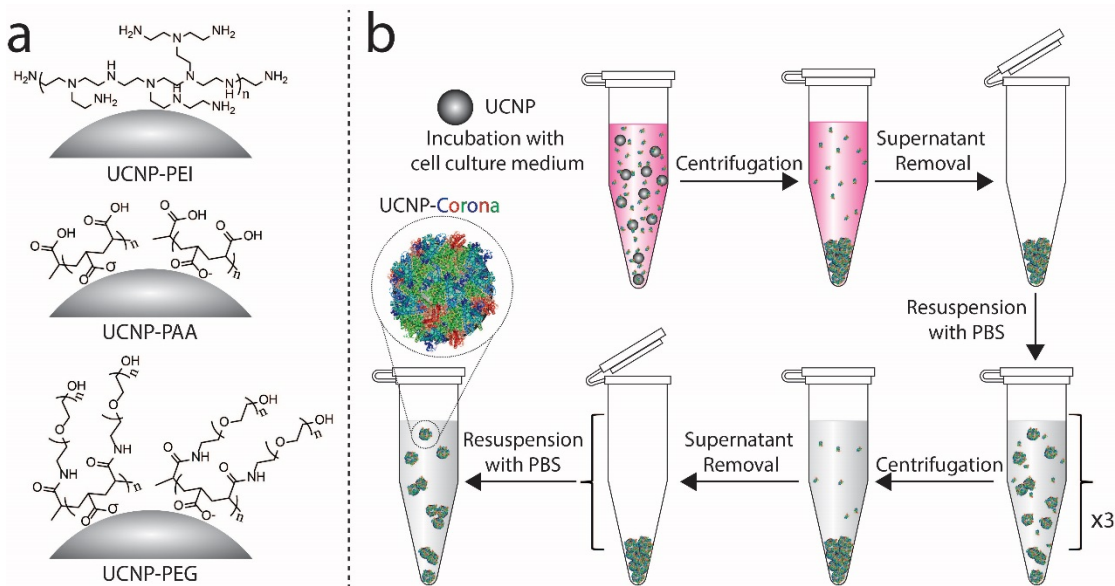
<sup>4</sup> Compared with bulk materials, nanoparticles possess a number of unique characteristics, such as controllable nanometre size and shape, large surface area-to-volume ratio, and adjustable surface chemistry, allowing to assemble cargo-loading vectors for theranostics applications.<sup>5</sup> Besides, the surface of nanoparticles can be functionalized with targeting molecules to enable navigation in complex *in vivo* environment and specific binding to cells.<sup>6</sup> The state-of-the-art theranostics nanocomplexes makes use excellent contrast properties of quantum dots, gold and iron oxide nanocrystals.<sup>3, 7</sup> These prominent characteristics of nanoparticles have provided promising opportunities in the diagnosis and treatment of disease at the early stage.

Among a variety of nanoparticles useful for theranostics applications, lanthanide-doped upconversion nanoparticles (UCNPs) have gained considerable attention over the last two decades due to their unique optical properties.<sup>8, 9</sup> Unlike the existing fluorescence contrast agents (organic dyes and quantum dots), UCNPs are photoluminescent nanomaterials that are capable of absorbing several near-infrared (NIR) low-energy photons to emit the higher-energy (anti-Stokes) photons.<sup>10</sup> This upconversion excitation-emission process endows UCNPs with significant advantages in biomedical imaging, including exceptional blinking-free photostability,<sup>11</sup> superior contrast with suppressed background,<sup>12</sup> deep-tissue imaging capability,<sup>13</sup> wavelength-controllable narrow spectral bands, enabling multiplexed imaging,<sup>14</sup> and long lifetime (100–1000  $\mu$ s) allowing time-gated imaging with zero background.<sup>15</sup> Moreover, tuneable UCNP emission over a broad range of wavelengths can be dialled at the synthesis stage. This allows UCNPs to be used as a versatile energy transducer in converting near-infrared (NIR) light to ultraviolet (UV), visible or NIR light to trigger photoreactions of interest.<sup>10</sup> In addition, UCNPs exhibit low intrinsic cytotoxicity and several reports suggest the biocompatibility of UCNPs on the whole organism level.<sup>16, 17</sup> The demonstrated application scope of UCNP is broad, including multi-model cell and animal imaging,<sup>18</sup> biosensing,<sup>19</sup> drug/gene delivery,<sup>20</sup> photodynamic therapy,<sup>21</sup> and photothermal therapy.<sup>22</sup>

Harnessing UCNP interactions with cells provides a gateway to these applications, where the surface characteristics of UCNPs were generally consented to play the key role.<sup>23, 24</sup>

However, the realistic cellular context, such as complete culture medium, adds an extra dimension to the interaction picture by way of nonspecific binding of proteins to UCNPs in the first place, before encountering cells. It has been recently recognised that a nanoparticle is quickly covered by biomolecules (*e.g.* plasma proteins) to form a layer of a protein corona upon entering into the biological systems.<sup>25</sup> This process is ubiquitous and occurs regardless of the particle material.<sup>26</sup> As a result, the physicochemical properties of the nanoparticles such as size, shape, surface characteristics, and aggregation state are altered dramatically.<sup>27, 28</sup> Accordingly, the biological properties of the nanoparticles in terms of toxicity,<sup>29</sup> cellular recognition,<sup>30</sup> cellular uptake,<sup>31</sup> blood circulation lifetime,<sup>32</sup> tumour accumulation,<sup>33</sup> and bio-distribution<sup>34</sup> are also affected. For example, the protein corona on nanoparticles was shown to reduce the nanoparticle adhesion to the cell membrane and mitigate the disruptive effect of bare nanoparticles to the cell membrane.<sup>31</sup> Pre-coating of nanoparticles with albumin was demonstrated to inhibit their plasma protein adsorption, decrease the complement activation, prolong the blood circulation time, and reduce their toxicity.<sup>35</sup> On the other hand, the protein corona can screen targeting molecules on the surface of nanoparticles, leading to the loss or reduction of their specificity to target cells.<sup>36</sup> Although understanding the nanoparticle corona and its influence on biological functions of nanoparticles is under research highlight, the corona formation on UCNPs in cell culture medium or in body fluids has not been addressed.

In this work, we aim to address the corona formation on UCNPs in cell culture environment and its influence on the interaction between UCNPs and cells. A comparative study was performed to evaluate the surface charge effect of UCNPs on the adsorption of serum proteins in complete cell culture medium. To this end, UCNPs were functionalized with polyethylenimine (PEI), polyacrylic acid (PAA), and polyethylene glycol (PEG) to yield particles with positive (+), negative (−) and neutral surface (0) charges (Scheme 1a). UCNPs were then incubated with complete cell culture medium to form a hard protein corona, a protein layer that was consisting of the serum proteins remaining tightly binding after a few washing steps (Scheme 1b).<sup>37</sup> The amount of adsorbed proteins on these three types of UCNPs were quantitatively analysed. Using high performance liquid chromatography and electrospray ionisation mass spectrometry (LC-ESI-MS), a comprehensive proteomics workflow for the identification and



purchased from Lyasan Bio (USA). Phosphate buffered saline (PBS, pH = 7.4) and Penicillin-Streptomycin (10000 U/mL) were purchased from Life Technologies (Australia). Thermo-Scientific Pierce Micro bicinchoninic acid (BCA) protein assay kit was purchased from Thermo Fisher Scientific (Australia). All reagents were used as received without further purification.

### Characterization

Transmission electron microscopy (TEM) images were obtained using a Philips CM10 transmission electron microscope at 100 kV. For negative staining, nanoparticles on formvar-coated copper grids were incubated with 5  $\mu$ L of 2% PTA aqueous solution (pH = 7.0) for 30 seconds at room temperature. The excess staining solution was drained off, and the samples were dried and observed under TEM. Upconversion photoluminescence spectra were recorded at a Fluorolog-Tau3 spectrofluorometer (Jobin Yvon-Horiba). Dynamic Light Scattering (DLS) and  $\zeta$ -potential were determined with a Nano ZS90 Zetasizer (Malvern). The nanoparticles were diluted with distilled water for the Zetasizer measurement. Fourier transform infrared (FTIR) spectra were acquired using a Nicolet iS10 FTIR spectrometer (Thermo Fisher Scientific). Thermal gravimetric analysis (TGA) was performed on a TGA/DSC 1 STARe System (Mettler Toledo).

### Preparation of PEI-, PAA-, and PEG- UCNPs

Hexagonal-phase UCNPs (NaYF<sub>4</sub>:18%Yb,2%Er) were prepared via the solvothermal decomposition method as described in our previous report.<sup>41</sup> The nanoparticles prepared from different batches were mixed together to obtain ~2 g of homogenized oleate-capped UCNPs (UCNP-OA) for subsequent surface modification with polymers. To modify UCNPs with PEI, PAA and PEG, oleate ligands on UCNP surface were firstly removed with NOBF<sub>4</sub>.<sup>42</sup> Typically, 10 mL of UCNP-OA cyclohexane suspension (5 mg/mL) was mixed with 10 mL of NOBF<sub>4</sub> (11.68 mg) dichloromethane solution in a sealed flask, and kept vigorous stirring at room temperature overnight. The resulting NOBF<sub>4</sub>-capped UCNPs (UCNP-NOBF<sub>4</sub>) were pelleted by centrifugation and the supernatant was discarded. The precipitated nanoparticles were re-dispersed in DMF, flocculated with the mixture of toluene and cyclohexane. After centrifugation, 5 mL of DMF was added again to disperse the nanoparticles. For the synthesis of UCNP-PAA, 5 mL of PAA DMF solution (30 mg/mL) was added to the UCNP-NOBF<sub>4</sub> suspension. The mixture was heated to 80 °C under stirring for 3 h in a sealed flask. The UCNP-PAA nanoparticles



were then collected with centrifugation and washed three times with ethanol and three times with water. The final product was dispersed in water for storage. UCNP-PEI nanoparticles were prepared using the same protocol except the addition of 25 mL of PEI ethanol solution (4 mg/mL) instead of PAA. The PEI ligand exchange reaction was conducted at room temperature for 24 h. PEG-NH<sub>2</sub> was grafted to UCNP-PAA to obtain UCNP-PEG via chemical bonding. 1 mg of UCNP-PAA were dispersed with 1-mL distilled water (pH = 5.5) and the carboxylic groups of PAA were activated by 0.4 mg of EDC·HCl and 1.1-mg sulfo-NHS. After 30 min of incubation at room temperature, nanoparticles were centrifuged and washed with distilled water for three times and dispersed with 200  $\mu$ L of PBS (pH = 7.4) via sonication in cold condition. 200  $\mu$ L of PBS containing 1.5 mg of PEG-NH<sub>2</sub> was added in followed by incubation on a rotary shaker at 4 °C overnight. The unreacted PEG-NH<sub>2</sub> was removed by centrifugation and the UCNP-PEG particles were purified by three times washing with distilled water.

#### **Formation of a hard corona on UCNPs**

Before incubating with nanoparticles, the complete cell culture medium (DMEM supplemented with 10% FBS and 1% P/S) was filtered through a 0.22- $\mu$ m membrane filter to remove clustered proteins. To form a hard corona on UCNPs, 1-mg UCNPs were dispersed with 1 mL complete cell culture medium. The suspension was sonicated under cold condition for 30 s, and then shaken in a rocking incubator at 37 °C for different time intervals. The UCNP-corona colloids were centrifuged at 10000 g for 7 min and re-dispersed with PBS. The suspension was transferred to a new vial. The same washing steps with centrifugation were repeated for three times to remove the unbound or loosely bound proteins. Finally, the nanocomposites were dispersed with 1-mL PBS. Prior to all characterization and testing, ♣UCNPs were freshly prepared. For subsequent cellular assays, UCNP-corona samples were prepared by incubating polymer-modified nanoparticles with complete cell culture medium for 24 h.

#### **Quantification of protein adsorbed on UCNPs**

The temporal formation of a hard corona on UCNPs were quantified by micro BCA assay according to the manufacturer's protocol. UCNP-corona was formed by incubating nanoparticles with complete cell culture medium for different times (10 min, 30 min, 1h, 2h, 4h, and 24 h), followed by three cycles of centrifugation and re-dispersion as previously described. 25  $\mu$ L of UCNP-corona suspensions (1 mg/mL) was pipetted into

five replicate wells of a 96-well plate. Then, 200  $\mu$ L of BCA working reagent was added in each well. The mixture was shaken on a rocking platform for 5 min and then incubated at 60 °C for 60 min in dark conditions. After cooling to room temperature, the absorbance of the samples was measured at 562 nm using a PHERAstar plate reader with the background absorbance subtracted. Same measurements were carried out on a series of bovine serum albumin solution with increasing concentrations (0–125  $\mu$ g/mL) to plot the standard curve. Samples of UCNP-PAA in PBS and UCNP-PAA in BSA standard solutions were used as controls. The total protein concentration was calculated relative to the BSA standard.

### **Proteomics of protein adsorbed on UCNPs**

The hard corona formed on the differently modified UCNPs were identified using a nanoLC-ESI MS approach. Samples of the PEG-, PEI- and PAA- modified UCNPs (50  $\mu$ L; 1mg/ml) in triplicates were denatured (95 °C for 5 min) and reduced (60 °C for 1 h) in 10-mM DTT. Samples were then alkylated with 25-mM IAA (30 min in dark) and digested with trypsin overnight (1  $\mu$ g). The samples were centrifuged for 5 min at 14,100 g. The supernatant containing the digested peptides were transferred into new tubes and dried. Samples were reconstituted in 40- $\mu$ L 0.1% formic acid prior to nanoLC-ESI-MS analysis.

A Triple TOF 6600 (AB Sciex) mass spectrometer connected to Eksigent Ultra nanoLC system (Eksigent) was used for the analysis. The digested peptide samples were chromatographically separated using a Halo C18, 160Å, 2.7 $\mu$ m, 150  $\mu$ m  $\times$  10 cm analytical column. The digested sample (10  $\mu$ L) was injected onto a peptide trap (Michrome peptide Captrap) for pre-concentration and desalted with 0.1% formic acid, 2% ACN, at 10  $\mu$ L/min for 5 min. The peptide trap was then switched into line with the analytical column. Peptides were eluted from the column using a linear solvent gradient, with steps, from H<sub>2</sub>O:CH<sub>3</sub>CN (95:5; + 0.1% formic acid) to H<sub>2</sub>O:CH<sub>3</sub>CN (5:95; + 0.1% formic acid) with a constant flow rate (600 nL/min) over an 80 min gradient. The LC eluent was subject to positive ion nanoflow electrospray MS analysis in an information dependent acquisition mode (IDA). In the IDA mode, a TOFMS survey scan was acquired (m/z 350-1500, 0.25 s), with twenty largest multiply charged ions (counts >200) in the survey scan sequentially subjected to MS/MS analysis. The tandem MS/MS spectra were accumulated for 200 milli-seconds (m/z 100–1500) with rolling collision energy.

The generated raw data files (.wiff) were converted to mascot generic files (.mgf) using AB SCIEX CommandDriver software and submitted to Mascot (Matrix Science, UK) and searched against SwissProt other mammalian database.

Protein abundance data were calculated using Normalized Spectral Abundance Factors (NSAF),<sup>43</sup> with an addition of a spectral fraction of 0.5 to all spectral counts to compensate for null values and enable log transformation for subsequent statistical analyses. Summed NSAF values were used as a measure of the relative protein abundance. To identify difference in protein abundance, the natural log NSAF values were analyzed using a series of *t*-tests and the significance level was set at  $P < 0.05$  for all comparisons. An analysis of variance (ANOVA) was also performed to identify proteins changing in abundance among those proteins present reproducibly in the three UCNP surface modifications conditions. Data processing was carried out using Scrappy package.<sup>43</sup>

### **Cell Culture**

MDA-MB-231 human breast cancer cells were cultured in complete cell culture medium, containing DMEM medium, 10% (v/v) FBS, and 1% (v/v) P/S, and maintained at 37 °C in a humidified incubator with 5% CO<sub>2</sub>.

### **Cytotoxicity study**

The cytotoxicity of nanoparticles for MDA-MB-231 cells were evaluated by MTT assay. MDA-MB-231 cells were plated in 96-well plates at the density of 5000 cells/well. After incubation overnight, the cells were washed three times with PBS to remove the residual FBS. Nanoparticles coated with or without a hard corona were dispersed with DMEM to obtain suspensions with different concentrations (0, 12.5, 25, 50, 100 and 200 µg/mL). Cells were then incubated with the nanoparticle suspensions for 24 h. MTT assays were conducted to determine the cell viability with respect to the control well without nanoparticle treatment.

### **Measurement of UCNPs binding to the cells**

The amount of UCNPs adhering to cells was quantified using inductively coupled plasma mass spectrometry (ICP-MS). MDA-MB-231 cells were seeded into 12-well plates at the density of  $1 \times 10^5$  cells/well and allowed to grow until 80% confluency. Before adding nanoparticles, the cells were pre-incubated at 4 °C for 20 min to deplete their energy and inhibit nanoparticle uptake. After washing the cells three times with cold PBS, 1 mL of

nanoparticle suspension (25 µg/mL) in DMEM was added into each well and incubated for 10 min at 4 °C. Cells in DMEM without nanoparticle treatment were used as the control. Under the cold condition, the nanoparticle suspension was removed; the cells were rinsed three times with PBS to remove unbound nanoparticles, harvested with trypsin for cell counting and centrifuged at 1000 g for 5 min to separate from growth medium. To dehydrate, the cells were placed in an oven at 60 °C for 24 h. Samples were then digested with 500 µL of concentrated nitric acid (70%) for 4 h and diluted with 9.5 mL of distilled water. The yttrium content in each sample was analysed by ICP-MS. The results from ICP-MS represented an average of triplicate samples and error bars represented the standard deviation.

### **Measurement of internalized amount of UCNPs**

MDA-MB-231 cells were seeded into 12-well plates at the density of  $1 \times 10^5$  cells/well and allowed to adhere for one day. After washing three times with DMEM, 1 mL of nanoparticle suspension (25 µg/mL) in DMEM was added into each well. Control experiments were performed by adding DMEM without nanoparticles. After the incubation over 24 h, non-internalized nanoparticles were washed three times with PBS by shaking on a rocking platform for 5 min. The cells were then trypsinized, centrifuged, dried in oven, digested with nitric acid, and finally analysed with ICP-MS. The sample preparation procedures for ICP-MS measurement were the same, as described above.

### 3. Results and discussion

#### Synthesis and characterization of PEI-, PAA-, and PEG- UCNP

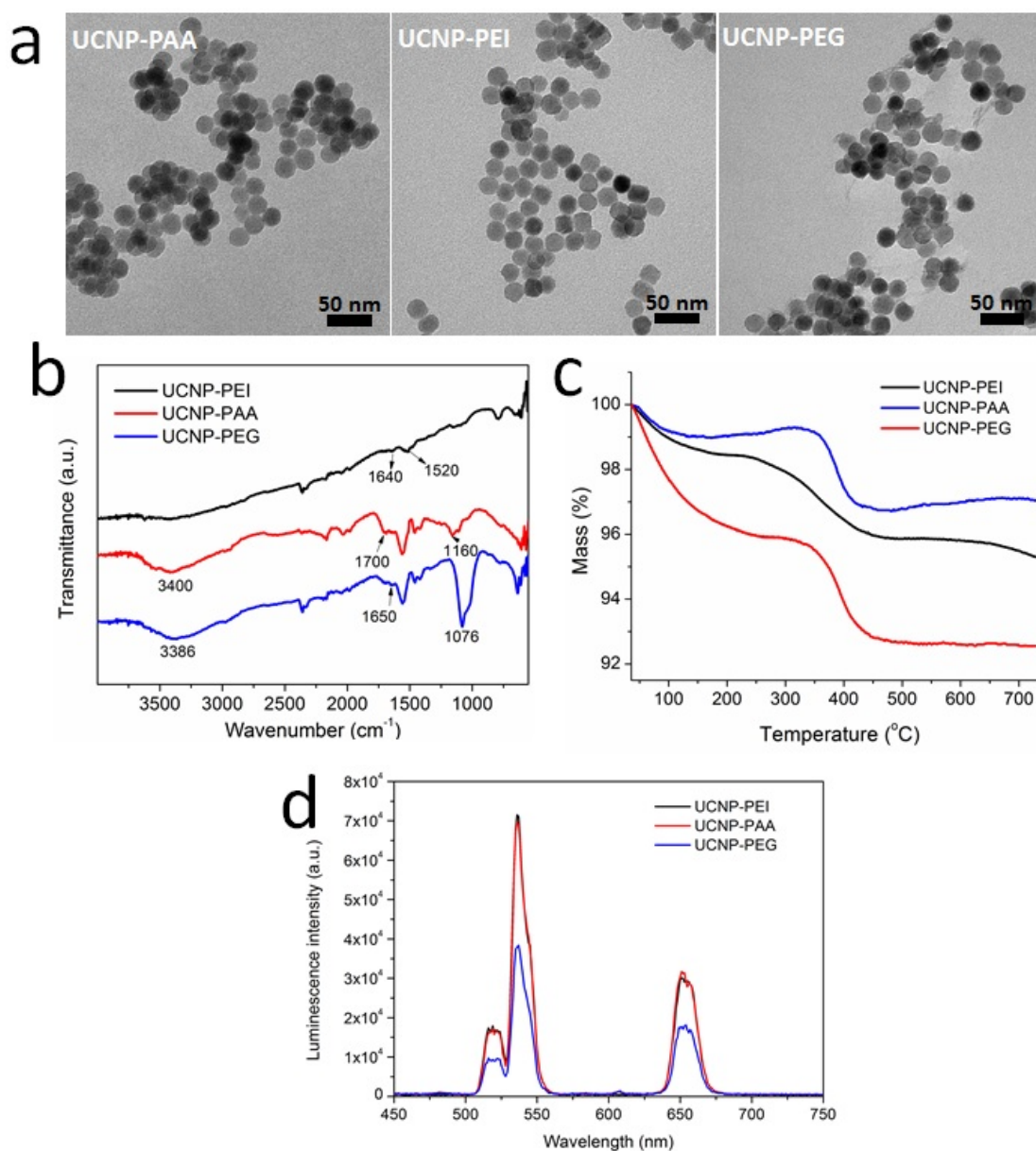


Fig. 1 (a) TEM images, (b) FTIR spectra and (c) TG analyses of UCNP-PEI, PAA-UCNP, and PEG-UCNP, respectively. (d) Upconversion photoluminescence spectra of UCNP-PEI, UCNP-PAA and UCNP-PEG dispersed in distilled water at the concentration of 1 mg/mL.

UCNPs were synthesized as described previously by using a one-pot solvothermal decomposition method<sup>41</sup> and were subsequently coated with PEI or PAA to yield positively (UCNP-PEI) and negatively (UCNP-PAA) charged surfaces. The neutrally charged UCNPs were prepared by further coating as-prepared UCNP-PAA with PEG-

NH<sub>2</sub> by means of the EDC/NHS activation, whereby amine groups of PEG-NH<sub>2</sub> were covalently conjugated to carboxylic groups of PAA on UCNP surface. TEM images of as-produced samples showed that nanoparticles were monodispersed with the average size of  $22.8 \pm 1.8$  nm (Fig. 1a). The morphology and physical diameter of NPs were not affected by the surface modifications (Fig. 1a). The binding of polymers to the surface of UCNPs was validated by FTIR spectroscopy. As shown in Fig. 1b, the absorption at 1640 and 1520 cm<sup>-1</sup> in UCNP-PEI spectrum corresponded to the stretching vibrations of N-H and C-N in PEI, respectively. In the spectrum of UCNP-PAA, the peaks at 1700 and 1160 cm<sup>-1</sup> were attributed to the C=O and C-O stretching vibrations in the carboxylic groups, indicating the presence of PAA on UCNPs. The absorption peak at 1650 cm<sup>-1</sup> was characteristic of the C=O in amide groups, the strong stretching vibration bands at 1076 cm<sup>-1</sup> and 3386 cm<sup>-1</sup> resulted from the vibration of C-O and O-H in -CH<sub>2</sub>-OH groups of PEG chain. The significant difference between the spectra and characteristic absorptions of the functional groups confirmed the successful surface modifications of UCNPs by PEI, PAA and PEG, respectively. The TGA curve of UCNP-PEI showed a total weight loss of ~3% from 36°C to 700 °C when the absorbed water and organic groups of the sample were completely combusted (Fig. 1c). Meanwhile, the higher weight loss (~8%) was observed in the sample of UCNP-PEG than UCNP-PAA (~5%) (Fig. 1c), the additional weight loss of ~3% further demonstrated the presence of PEG layer on UCNP-PEG nanoparticles. Furthermore, effect of the polymer coatings on the upconversion photoluminescent (UCL) properties of UCNP-PEI, UCNP-PAA and UCNP-PEG were investigated, with the results shown in Fig. 1d. Three UCNP aqueous suspensions exhibited similar UCL spectra under NIR excitation at 980 nm. Three dominant peaks at 525, 540 and 655 nm (Fig. 1d) were observed, corresponding to the <sup>2</sup>H<sub>11/2</sub>→<sup>4</sup>I<sub>15/2</sub>, <sup>4</sup>S<sub>3/2</sub>→<sup>4</sup>I<sub>15/2</sub>, and <sup>4</sup>F<sub>9/2</sub>→<sup>4</sup>I<sub>15/2</sub> transitions of Er<sup>3+</sup> ions. Negligible difference was detected in the emission intensity between UCNP-PEI and UCNP-PAA samples (Fig. 1d), indicating similar effect of the polymer coatings on the photoluminescence efficiency of UCNPs. However, the emission intensity of UCNP-PEG was significantly lower in both green and red emission bands than that of UCNP-PEI and UCNP-PAA (Fig.1d). The reduction in the emission intensity can be attributed to the greater quenching effect of the additional PEG layer grafted on PAA-UCNP, since PEG has abundant quenching groups (C-H and O-H), as reported in literature.<sup>44, 45</sup>

### Temporal formation of protein corona

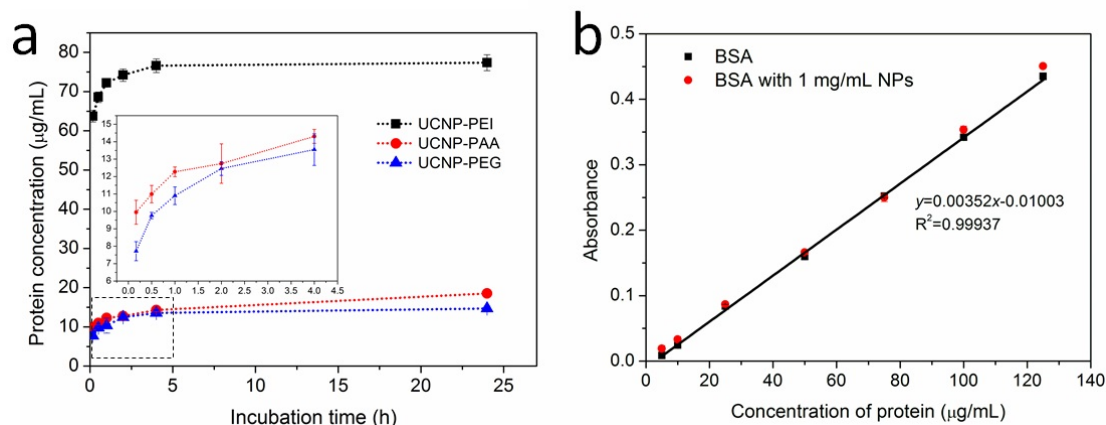


Fig. 2 (a) The amount of hard protein adsorbed on UCNP-PEI, UCNP-PAA and UCNP-PEG after incubation with complete cell culture medium for different times (10 min, 30 min, 1 h, 2 h, 4 h and 24 h). Each value represents the mean  $\pm$  standard deviation of five replicates. (b) Standard curve of BSA in the presence and absence of 1mg/mL UCNP-PAA particles.

The formation of a hard protein corona on UCNPs, as a function of the polymer coatings and incubation time was evaluated by a standard BCA assay. The hard corona was formed by incubating UCNPs with complete cell culture medium for several time intervals. The complete cell culture medium used in this study consisting of DMEM, 10% FBS and 1% antibiotics were a typical combination of culture medium for *in vitro* pharmacological studies. After three times of PBS washes, a hard corona remaining on the NPs surface reacted with BCA reagent to produce a purple product featuring a strong absorbance at 562 nm. Based on the absorbance intensity of the BCA product, the protein concentrations were determined by benchmarking against the BSA calibration curve (Fig. 2b).

As shown in Fig. 2a, all three types of NPs were observed to acquire a measurable hard corona, following 10-min incubation. Overall, the corona protein content increased rapidly during the first 3 h of incubation, exhibiting an onset of the saturation after 4-h incubation (Fig. 2a). PEI-UCNPs exhibited the greatest protein adsorption among the three tested UCNP surface coatings at all time points and showed approximately 4-fold more protein adhesion (77.4 μg/mL) after 24 h-incubation in comparison with that of UCNP-PAA (18.5 μg/mL) and UCNP-PEG (14.7 μg/mL). Electrostatic interaction plays an important role in the adsorption of proteins at charged surfaces.<sup>46, 47</sup> As it was reported in literature, negatively charged proteins, *e.g.* albumin, and positively charged proteins, *e.g.* immunoglobulin G, exhibited propensity to bind to correspondingly positively and

negatively charged nanoparticles.<sup>48</sup> The complete cell culture medium is enriched with serum proteins with isoelectric points (pI) below the pH (7.4) of the cell culture medium (Tab. S1). Thus, the abundant serum proteins generally possess a net negative charge, thereby leading to the tendency of more proteins adsorb to positively charged surfaces. UCNP-PEI, having a large number of positively charged amine groups in the branched structure of PEI, are thus more likely to attract more negative serum proteins via electrostatic interaction compared with negatively charged PAA and neutrally charged PEG. Our result is consistent with the findings in previous work on PEI- and PAA-functionalized magnetite nanoparticles, which demonstrated much higher amount of FBS protein formed on NPs with PEI coating.<sup>49</sup> Although a PEG layer is regarded as excellent protein repellent, we observed protein adsorption on UCNP-PEG. At the same time, the adsorbed protein amount on UCNP-PAA was statistically higher ( $P < 0.05$ ) than that of UCNP-PEG, which was attributed to the stronger binding affinity of proteins on PAA-modified UCNPs. Similar results were obtained in previous studies, which showed the higher initial protein adsorption on neutral than negatively charged NPs, yet most of proteins bound on neutral surface were washed away in the PBS step and ultimately exhibited lower content in the hard corona.<sup>50</sup> Taken together, our results showed that UCNP surface charge determined predominantly the amount of adsorbed proteins by the selective adhesion of serum proteins. As such, the adsorbed content of the hard corona was largely related to the charge of the surface polymers as well as the binding affinity of the proteins.



## Effect of the protein adsorption on the physicochemical characteristics of UCNPs

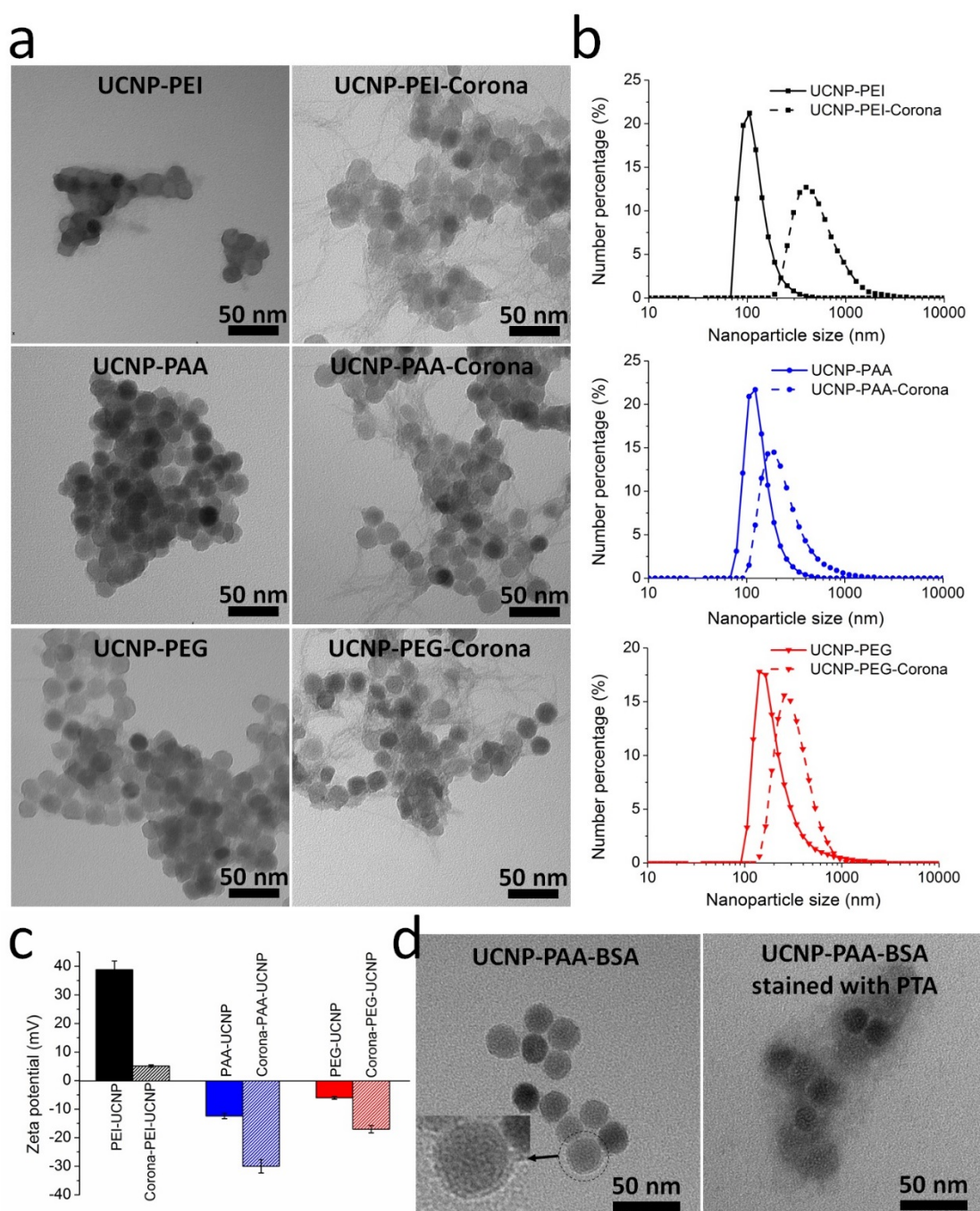


Fig. 3 (a) TEM images of UCNPs (UCNP-PEI, UCNP-PAA, and UCNP-PEG) and  $\clubsuit$ UCNPs (UCNP-PEI-corona, UCNP-PAA-corona, and UCNP-PEG-corona) after the negative staining with 2% PTA. (b) DLS size distribution and (c)  $\zeta$ -potential measurement of polymer-coated UCNPs and  $\clubsuit$ UCNPs. (d) TEM images of UCNP-PAA-BSA nanoparticles (left) and UCNP-PAA-BSA composites after the negative staining with 2% PTA.

The presence of corona on nanoparticles was verified by TEM using PTA negative staining. Compared with the untreated UCNPs, hard coronas were visualized on ♣UCNPs as a disordered protein network (Fig. 3a). This protein network was observed on all the polymer-coated UCNPs irrespective of their surface charge (Fig. 3a). However, a further investigation of UCNPs-PAA incubated with 10% BSA revealed a uniform layer of protein surrounding UCNPs (Fig. 3d), which were mostly observed on TEM images of nanoparticles conjugated with a single type of protein.<sup>51-53</sup> The convoluted corona patterns can be resulted from the unstable and reversible processes of the corona formation in FBS.<sup>54, 55</sup> The diversity of FBS proteins further contributed to the complexity of the protein adhesion. Heterogeneous charged and hydrophobic domains of FBS proteins governed the observed convoluted self-assembly in TEM images.

The DLS and  $\zeta$ -potential of UCNPs before and after corona formation were also characterized. As shown in Fig. 3b-c, an obvious size increase was observed in all three types of UCNPs after incubating with complete cell culture medium. The size distribution of three samples was also broadened due to the protein adsorption. As the hydrodynamic diameter of proteins in the cell culture medium was ~6.5 nm (Fig. S1), the obtained size increase and broader size distribution suggested the aggregation of nanoparticles during corona formation. This diameter increase was notably greatest in PEI-modified UCNPs compared with PEI- and PAA- UCNPs, indicative of the highest amount of the protein adsorption. The DLS size measurement was in good agreement with the BCA assay results. In addition, the surface charge of the tested nanoparticles became more negative after the corona formation, with values changing from  $38.8 \pm 3.0$  mV to  $5.1 \pm 0.4$  mV for UCNPs-PEI,  $-12.4 \pm 1.0$  mV to  $-30.0 \pm 2.4$  mV for UCNPs-PAA and  $-6.0 \pm 0.5$  mV to  $-17.0 \pm 1.3$  mV for UCNPs-PEG.

### **Proteomic analysis of the protein coronas**

In order to identify and quantify the composition of the hard protein corona formed on the surface-modified UCNPs, the purified ♣UCNPs samples underwent denaturation with reducing agents, followed by enzymatic trypsin digestion to release proteins bound to the UCNPs. The mass spectrometry based characterisation of the hard protein corona from three surface-modified UCNPs identified 68 unique proteins, among these 57 were found common between the tested samples. 20 most-abundant corona proteins from three samples are illustrated in Fig. 4. The resultant overall protein abundance was consistent

with the previously reported abundance of serum proteins.<sup>29</sup> The hard protein corona of UCNP-PEI was markedly different from those observed in UCNP-PAA and UCNP-PEG. For example, although Alpha 2-HS glycoprotein was found to be the most abundant protein among the tested samples, its abundance in UCNP-PEI corona was significantly lower than that of PAA- and PEG- coronae. Similarly, Apolipoprotein A-I and Apolipoprotein A-II were more abundant in UCNP-PEI corona compared with UCNP-PAA and UCNP-PEG.

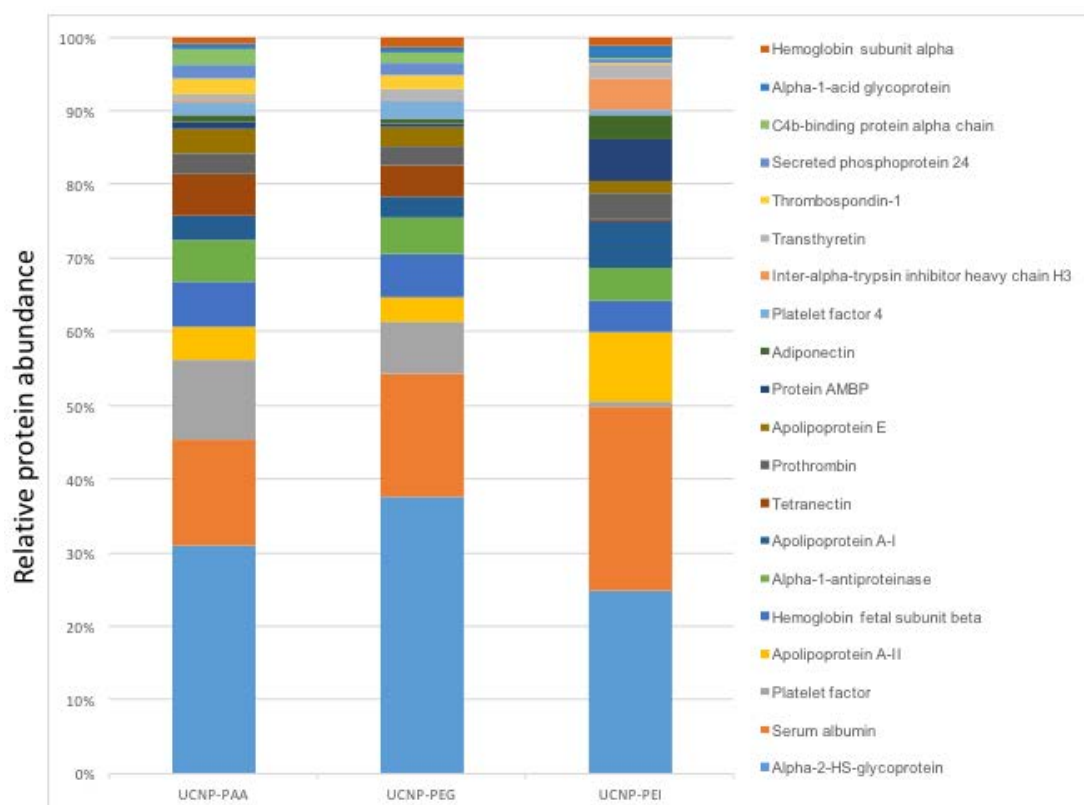


Fig. 4. A bar chart of the relative abundance of twenty most abundant proteins in UCNP-PAA, UCNP-PEG and UCNP-PEI hard protein coronae, as assayed by nanoLC-ESI-MS mass spectrometry.

Multivariate statistical analysis using heat-map and hierarchical clustering highlights the different corona protein content in UCNP-PEI, as shown in Fig. 5. The heat-map delineates 18 proteins abundant in UCNP-PEI corona from the other abundant proteins detected in PAA-, PEG- UCNP coronae. The relative abundance among the different samples and within the three replicates can be easily visualised. The heat-map showed good reproducibility of the hard corona bound to the three different types of UCNPs. The cluster analysis showed that abundant proteins falling into 2 clusters (the upper cluster

and the lower cluster). In the upper cluster, proteins were hardly found in UCNP-PEI-corona, whereas the lower cluster were enriched in the corona extracted from UCNP-PAA-corona and UCNP-PEG-corona. Fig. 6 illustrates the normalised spectral abundance of eight most significantly observed protein identified from the hierarchical clustering. Thrombospondin-1, heat shock protein HSP90-alpha, C4b-binding protein alpha chain were more abundant in UCNP-PEG and UCNP-PAA coronae, while Inter alpha trypsin inhibitor heavy chain H2, adiponectin, alpha-2 microglobulin, complement c3 and apolipoprotein A-I were of the higher abundance in UCNP-PEI corona.

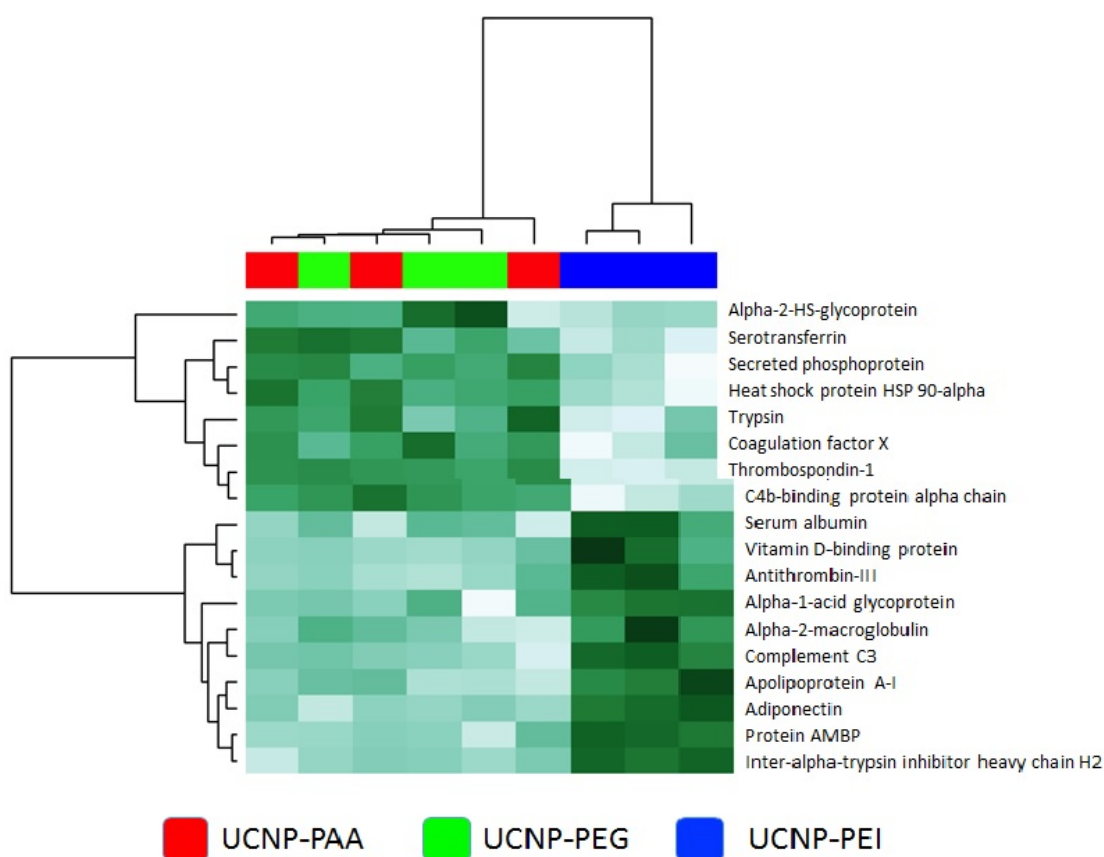


Fig. 5. Heat map and hierarchical clustering of the protein abundances of UCNP-PAA, UCNP-PEG, UCNP-PEI coronae.

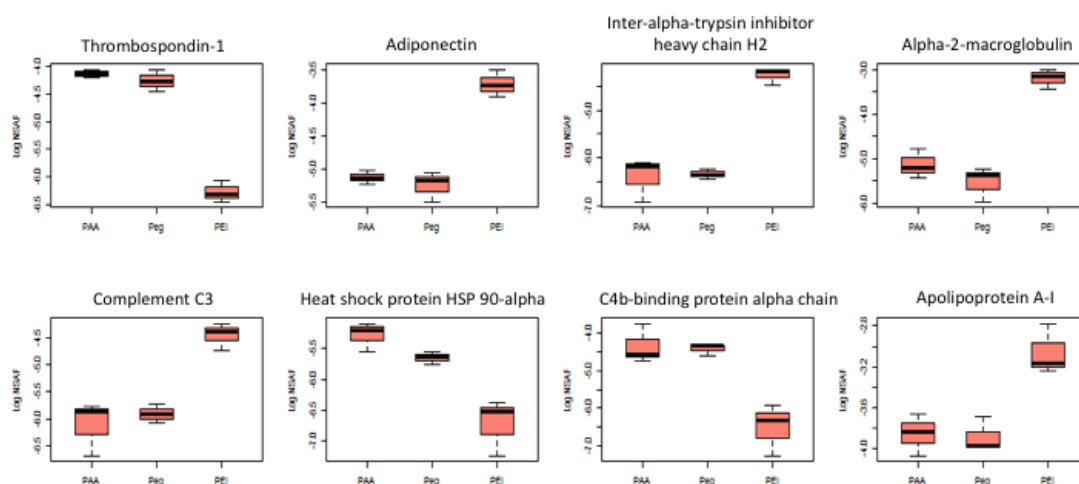


Fig. 6. Box and whisker plots of eight most abundant proteins between the coronae of the tested UCNP samples. The statistical significance was estimated by using a student *t*-test on the log-transformed NSAF values from the original biological triplicates ( $P < 0.05$ ).

The proteomic analysis of the surface-modified UCNPs revealed distinct hard corona abundances. Interestingly, the hard corona profiles of UCNP-PAA and UCNP-PEG were quite comparable, while the corona of UCNP-PEI was significantly altered with different protein concentrations, even among the most abundant plasma proteins. We explain the observed specificity of the protein abundances of PEI-UCNP corona by the positive surface charge of PEI-UCNP, which predominantly governed the adsorption of the majority of negatively charged serum proteins.

## Effect of the protein adsorption on the cytotoxicity of UCNPs

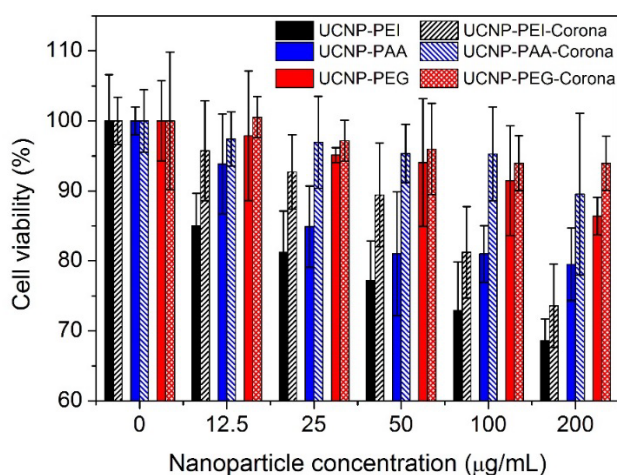


Fig. 7 Cell viability of MDA-MB-231 after treating with tested polymer-coated UCNPs and  $\clubsuit$ UCNPs at the concentrations ranging from 0 to 200  $\mu\text{g/mL}$  for 24 h. The presented values were mean  $\pm$  standard deviation.

The effect of the corona on the cytotoxicity of nanoparticles was investigated using MDA-MB-231 cells. This cell line was chosen aiming prospective application of UCNPs in the cancer theranostics. Cells at the stage of exponential growth phase were incubated with serum-free DMEM in the presence of bare UCNPs or  $\clubsuit$ UCNPs, and then the cellular viability was evaluated using a colorimetric MTT assay. The absence of FBS in cell culture was firstly examined and showed no influence on the cell growth rate and cell morphology (Fig. S2). The cytotoxicity of UCNPs was known to depend on their surface modifications.<sup>17, 23</sup> In our experiments, UCNP-PAA and UCNP-PEG showed negligible influence on the cell viability of MDA-MB-231 cells at the incubated concentrations from 0 to 200  $\mu\text{g/mL}$  (Fig. 7). In all investigated nanoparticle concentrations, UCNP-PEG were slightly more biocompatible compared to the equal amount of UCNP-PAA, while UCNP-PEI are more toxic than that of UCNP-PAA and UCNP-PEG (Fig. 7). UCNP-PEI of the low concentrations had no effect on the cell viability, while the high concentration dosages (100 and 200  $\mu\text{g/mL}$ ) showed pronounced cytotoxicity, as displayed by the lower survival rates ( $< 80\%$ ) (Fig. 7). The cytotoxicity of UCNP-PEI was expected to originate from the severe cytotoxicity of PEI,<sup>17, 23, 56</sup> which was moderated with an ad-layer of a hard corona in our study. Generally,  $\clubsuit$ UCNPs were less toxic compared to the polymer-coated UCNPs. The mitigation effect of the protein corona on the cell cytotoxicity were also observed in the reported studies of the other of nanoparticle types.<sup>57, 58</sup> Therefore, the



cytotoxicity of UCNPs can be mediated by pre-coating the nanoparticles with serum proteins to enable their safer applications in living systems.

### Effect of protein adsorption on cell binding

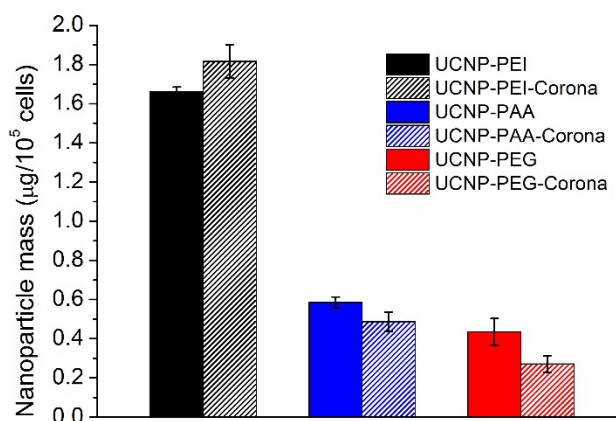


Fig. 8. Average weight of UCNPs and ♣UCNPs binding to MDA-MB-231 cells ( $\mu\text{g}/10^5$  cells). Each value represents a mean of triplicate experiments  $\pm$  standard deviation.

The use of UCNPs for cellular theranostics applications often requires nanoparticle binding to the cell surface and subsequent internalization. Previous studies have shown that the nanoparticle binding was a crucial phase of their interactions with living cells.<sup>59</sup> The binding ability of nanoparticles was demonstrated to depend strongly on the surface charges of the nanoparticles.<sup>60, 61</sup> However, once dispersed in cell culture medium, UCNP surface was rapidly covered by protein molecules, and they become a new determinant of the particle binding to the cells. In order to investigate the effect of a corona layer on the binding of UCNPs to cells, we pre-coated three types of UCNPs with a hard corona after 24-h incubation in complete cell culture medium. To prevent the cellular uptake, UCNPs and ♣UCNPs were incubated with MDA-MB-231 cells at 4 °C. The binding degree of nanoparticles was determined by ICP-MS analysis based on the trace amount of  $\text{Y}^{3+}$ . As shown in Fig. 8, the order of UCNP binding can be described as  $\text{UCNP-PEI} > \text{UCNP-PAA} > \text{UCNP-PEG}$ . The same binding order was observed for ♣UCNPs. Since the cell plasma membrane was negatively charged, the distinct binding results was interpreted in terms of the higher membrane attraction for positively charged UCNP-PEI and UCNP-PEI-corona, and the lower membrane attraction for negatively charged UCNP-PAA and neutral UCNP-PEG and their corresponding corona composites. The preformed corona was shown to inhibit the binding of UCNP-PAA and UCNP-PEG to

the cell membrane. On the contrary, the presence of a hard corona increased the binding level of UCNP-PEI (Fig. 8). This result was confirmed by the similar observation in the previous study.<sup>49</sup> Proteins on UCNPs could mediate their adhesion to cells via specific and non-specific binding. From the non-specific binding perspective, the lower surface energy of the corona-coated UCNPs might be the reason for the weaker binding of UCNP-PAA-corona and UCNP-PEG-corona to the cell membrane.<sup>59</sup> However, since the greatest extent of the protein adsorption was observed for UCNP-PEI, multiple serum proteins on UCNP-PEI might confer specific binding to the cell membrane with stronger affinity and thus account for higher binding ability of UCNP-PEI-corona. For example, Apolipoprotein A-I proteins found abundant in UCNP-PEI corona were suggested to interact specifically with the negatively charged phospholipids on cell membrane.<sup>62</sup> We therefore concluded that the surface charge of nanoparticles as well as the content and composition of proteins attached to the nanoparticle surface were the important factors that determine the nanoparticle binding to cells. A further investigation will have to be conducted to correlate the relative abundance of the identified proteins with the enhanced or decreased cellular binding of nanoparticles towards cells.

#### Effect of protein adsorption on cellular uptake

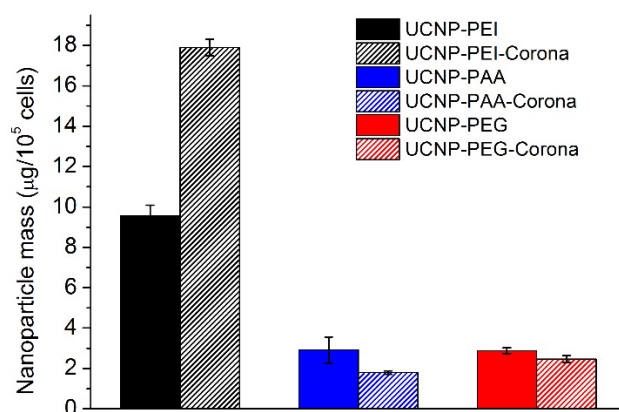


Fig. 9. Average weight of UCNPs and UCNPs internalized in MDA-MB-231 cells ( $\mu\text{g}/10^5\text{cells}$ ). Each value represents a mean of triplicate experiments  $\pm$  standard deviation.

The uptake of UCNPs by MDA-MB-231 cells in the presence and absence of corona was further investigated and quantified by ICP-MS. UCNPs were incubated with cells for 24 h to ensure their internalization in cells. Before measurements, a vigorous washing step with 5 min of sample rocking was performed for three times to remove non-internalized nanoparticles. As illustrated in Fig. 6, the presence of hard corona significantly enhanced



the cellular uptake of UCNP-PEI. However, the uptake amount observed for UCNP-PAA and UCNP-PEG were both reduced due to the hard corona. The uptake rate of UCNP-PAA-corona by cells was decreased by 38%, and that of UCNP-PEG-corona was decreased by 14%. Thus, the extent of the corona inhibition effect was more pronounced for UCNP-PAA than for UCNP-PEG. This observation was consistent with a previous study, showing the higher cellular uptake for neutral UCNPs than that of positively charged UCNPs.<sup>23</sup> In general, these results correlated well with the above findings on the binding degree of UCNPs. Since the cellular uptake prefaced by the initial adsorption of nanoparticles to the cell membrane and subsequent cellular internalization, the adhesion capacity of nanoparticles is thus considered as the principal determinant of their uptake efficacy by cells. Our results suggested that the presence of a corona favoured the binding and therefore the uptake of positive UCNP-PEI, whereas inhibited the adhesion and consequently decreased the uptake efficiency of negative UCNP-PAA and neutral UCNP-PEG. The different roles of the preferentially attached proteins might be responsible for the different effects on UCNPs binding and internalization during their interaction with cells. Additionally, the observed cytotoxicity of UCNPs and ♣UCNPs are also shown to be related to the level of binding and cellular uptake of the nanocomposites (Fig. 7, Fig. 8, and Fig. 9). In general, positively charged UCNP-PEI and UCNP-PEI-corona exhibited higher toxicity than negatively charged UCNP-PAA, UCNP-PEG, and their corona composites. Therefore, the stronger the interaction of cells with nanoparticles may be the reason for higher cytotoxicity of positively charged nanocomposites (Fig. 7).

#### 4. Conclusions

In summary, we report on investigation of the hard corona formation on positively (polyethylenimine, PEI), negatively (polyacrylic acid, PAA) and neutrally (polyethylene glycol, PEG) charged upconversion nanoparticles (UCNPs) and the mediating effect of the corona on UCNP-cell interactions. As-produced surface-modified UCNPs were swiftly coated with serum proteins when exposed to FBS-containing cell culture medium. For all types of the surface-modified UCNPs, the hard corona formation resulted in the surface charge decrease, increase of their hydrodynamic diameters (especially pronounced in case of PEI-UCNP) accompanied by aggregation, and mitigation of the cytotoxicity. At the same time, PEI-UCNP differed markedly from both UCNP-PAA and

UCNP-PEG in terms of its hard corona acquisition capacity (4-fold) and its protein composition, featuring the prevalence of lipoproteins and albumins, in comparison with the prevalence of glycoproteins and platelet factors in UCNP-PAA and UCNP-PEG coronae. As a result, PEI-UCNP- corona exhibited the strongest degree of binding and internalisation in MDA-MB-231 cells. Taken together, our results portray the following picture. In protein-abundant biological fluids, nanoparticles swiftly acquire a protein corona, which then presents a new biological identity to cells. The protein corona thickness, content and biological identify of positively charged nanoparticles display a profound difference to that of the more common negatively charged and neutral nanoparticles.

### 5. Conflict of interest

The authors declare no conflict of interest.

### Acknowledgements

This research was supported by the Grant to the Government of Russian Federation, grant number 14.z50.31.0022. The authors would like to thank Australian National Measurement Institute for the samples measurement on inductively coupled plasma mass spectrometry. We also wish to thank Dr Tao Kan for his help in thermal gravimetric measurement. The use of the Microscopy Unit at Macquarie University is also acknowledged.

### References

1. E. Blanco, H. Shen and M. Ferrari, *Nat. Biotechnol.*, 2015, **33**, 941-951.
2. L. Zhang, F. Gu, J. Chan, A. Wang, R. Langer and O. Farokhzad, *Clinical pharmacology and therapeutics*, 2008, **83**, 761-769.
3. G. Chen, I. Roy, C. Yang and P. N. Prasad, *Chem. Rev.*, 2016, **116**, 2826-2885.
4. Y. Min, J. M. Caster, M. J. Eblan and A. Z. Wang, *Chem. Rev.*, 2015, **115**, 11147-11190.
5. O. C. Farokhzad and R. Langer, *ACS Nano*, 2009, **3**, 16-20.
6. A. Chrastina, K. A. Massey and J. E. Schnitzer, *Wiley Interdisciplinary Reviews: Nanomedicine and Nanobiotechnology*, 2011, **3**, 421-437.
7. P. Zhang, C. Hu, W. Ran, J. Meng, Q. Yin and Y. Li, *Theranostics*, 2016, **6**, 948.
8. G. Chen, H. Qiu, P. N. Prasad and X. Chen, *Chem. Rev.*, 2014, **114**, 5161-5214.
9. W. Fan, W. Bu and J. Shi, *Adv. Mater.*, 2016, **28**, 3987-4011.

10. X. Li, F. Zhang and D. Zhao, *Chem. Soc. Rev.*, 2015, **44**, 1346-1378.
11. S. Wu, G. Han, D. J. Milliron, S. Aloni, V. Altoe, D. V. Talapin, B. E. Cohen and P. J. Schuck, *Proceedings of the National Academy of Sciences*, 2009, **106**, 10917-10921.
12. Z. Song, Y. G. Anissimov, J. Zhao, A. V. Nechaev, A. Nadort, D. Jin, T. W. Prow, M. S. Roberts and A. V. Zvyagin, *J. Biomed. Opt.*, 2013, **18**, 061215.
13. D. K. Chatterjee, A. J. Rufaihah and Y. Zhang, *Biomaterials*, 2008, **29**, 937-943.
14. L. Cheng, K. Yang, S. Zhang, M. Shao, S. Lee and Z. Liu, *Nano research*, 2010, **3**, 722-732.
15. X. Zheng, X. Zhu, Y. Lu, J. Zhao, W. Feng, G. Jia, F. Wang, F. Li and D. Jin, *Anal. Chem.*, 2016, **88**, 3449-3454.
16. L. Xiong, T. Yang, Y. Yang, C. Xu and F. Li, *Biomaterials*, 2010, **31**, 7078-7085.
17. A. E. Guller, A. N. Generalova, E. V. Petersen, A. V. Nechaev, I. A. Trusova, N. N. Landyshev, A. Nadort, E. A. Grebenik, S. M. Deyev and A. B. Shekhter, *Nano Research*, 2015, **8**, 1546-1562.
18. J. Zhou, Z. Liu and F. Li, *Chem. Soc. Rev.*, 2012, **41**, 1323-1349.
19. L. Wang, R. Yan, Z. Huo, L. Wang, J. Zeng, J. Bao, X. Wang, Q. Peng and Y. Li, *Angew. Chem. Int. Ed.*, 2005, **44**, 6054-6057.
20. D. Yang, Z. Hou, Z. Cheng, C. Li and J. Lin, *Chem. Soc. Rev.*, 2015, **44**, 1416-1448.
21. C. Wang, L. Cheng and Z. Liu, *Theranostics*, 2013, **3**, 317-330.
22. L. Cheng, K. Yang, Y. Li, J. Chen, C. Wang, M. Shao, S. T. Lee and Z. Liu, *Angew. Chem.*, 2011, **123**, 7523-7528.
23. J. Jin, Y.-J. Gu, C. W.-Y. Man, J. Cheng, Z. Xu, Y. Zhang, H. Wang, V. H.-Y. Lee, S. H. Cheng and W.-T. Wong, *ACS Nano*, 2011, **5**, 7838-7847.
24. S. S. Lucky, N. M. Idris, Z. Li, K. Huang, K. C. Soo and Y. Zhang, *ACS Nano*, 2015, **9**, 191-205.
25. M. Lundqvist, *Nat. Nanotechnol.*, 2013, **8**, 701-702.
26. J. Sund, H. Alenius, M. Vippola, K. Savolainen and A. Puustinen, *ACS Nano*, 2011, **5**, 4300-4309.
27. A. E. Nel, L. Mädler, D. Velegol, T. Xia, E. M. Hoek, P. Somasundaran, F. Klaessig, V. Castranova and M. Thompson, *Nat. Mater.*, 2009, **8**, 543-557.
28. S. Dominguez-Medina, L. Kisley, L. J. Tauzin, A. Hoggard, B. Shuang, A. S. DS Indrasekara, S. Chen, L.-Y. Wang, P. J. Derry and A. Liopo, *ACS Nano*, 2016, **10**, 2103-2112.
29. S. Tenzer, D. Docter, J. Kuharev, A. Musyanovych, V. Fetz, R. Hecht, F. Schlenk, D. Fischer, K. Kiouptsi and C. Reinhardt, *Nat. Nanotechnol.*, 2013, **8**, 772-781.
30. I. Lynch, A. Salvati and K. A. Dawson, *Nat. Nanotechnol.*, 2009, **4**, 546-547.
31. A. Lesniak, F. Fenaroli, M. P. Monopoli, C. Åberg, K. A. Dawson and A. Salvati, *ACS Nano*, 2012, **6**, 5845-5857.
32. C. Sacchetti, K. Motamedchaboki, A. Magrini, G. Palmieri, M. Mattei, S. Bernardini, N. Rosato, N. Bottini and M. Bottini, *ACS Nano*, 2013, **7**, 1974-1989.
33. J. Lazarovits, Y. Y. Chen, E. A. Sykes and W. C. Chan, *Chem. Commun.*, 2015, **51**, 2756-2767.
34. C. Gunawan, M. Lim, C. P. Marquis and R. Amal, *J. Mater. Chem. B*, 2014, **2**, 2060-2083.
35. Q. Peng, S. Zhang, Q. Yang, T. Zhang, X.-Q. Wei, L. Jiang, C.-L. Zhang, Q.-M. Chen, Z.-R. Zhang and Y.-F. Lin, *Biomaterials*, 2013, **34**, 8521-8530.
36. A. Salvati, A. S. Pitek, M. P. Monopoli, K. Prapainop, F. B. Bombelli, D. R. Hristov, P. M. Kelly, C. Åberg, E. Mahon and K. A. Dawson, *Nat. Nanotechnol.*, 2013, **8**, 137-143.
37. C. D. Walkey and W. C. Chan, *Chem. Soc. Rev.*, 2012, **41**, 2780-2799.
38. D. Docter, U. Distler, W. Storck, J. Kuharev, D. Wünsch, A. Hahlbrock, S. K. Knauer, S. Tenzer and R. H. Stauber, *Nature protocols*, 2014, **9**, 2030-2044.
39. N. Fernández-Iglesias and J. Bettmer, *Nanoscale*, 2015, **7**, 14324-14331.

40. D. Pozzi, G. Caracciolo, A. L. Capriotti, C. Cavaliere, S. Piovesana, V. Colapicchioni, S. Palchetti, A. Riccioli and A. Laganà, *Molecular BioSystems*, 2014, **10**, 2815-2819.
41. L. Liang, A. Care, R. Zhang, Y. Lu, N. H. Packer, A. Sunna, Y. Qian and A. V. Zvyagin, *ACS Appl. Mater. Interfaces*, 2016.
42. A. Dong, X. Ye, J. Chen, Y. Kang, T. Gordon, J. M. Kikkawa and C. B. Murray, *J. Am. Chem. Soc.*, 2010, **133**, 998-1006.
43. K. A. Neilson, T. Keighley, D. Pascovici, B. Cooke and P. A. Haynes, *Proteomics for Biomarker Discovery*, 2013, 205-222.
44. Y. Wang, L. Tu, J. Zhao, Y. Sun, X. Kong and H. Zhang, *J. Phys. Chem. C*, 2009, **113**, 7164-7169.
45. G.-S. Yi and G.-M. Chow, *Chem. Mater.*, 2007, **19**, 341-343.
46. H. Larsericsdotter, S. Oscarsson and J. Buijs, *J. Colloid Interface Sci.*, 2001, **237**, 98-103.
47. M. van der Veen, W. Norde and M. C. Stuart, *Colloids Surf. B. Biointerfaces*, 2004, **35**, 33-40.
48. P. Aggarwal, J. B. Hall, C. B. McLeland, M. A. Dobrovolskaia and S. E. McNeil, *Adv. Drug Del. Rev.*, 2009, **61**, 428-437.
49. M. P. Calatayud, B. Sanz, V. Raffa, C. Riggio, M. R. Ibarra and G. F. Goya, *Biomaterials*, 2014, **35**, 6389-6399.
50. U. Sakulkhu, M. Mahmoudi, L. Maurizi, J. Salaklang and H. Hofmann, *Scientific Reports*, 2014, **4**, 5020.
51. M. Schäffler, M. Semmler-Behnke, H. Sarioglu, S. Takenaka, A. Wenk, C. Schleh, S. M. Hauck, B. D. Johnston and W. G. Kreyling, *Nanotechnology*, 2013, **24**, 265103.
52. I. Radauer-Preiml, A. Andosch, T. Hawranek, U. Luetz-Meindl, M. Wiederstein, J. Horejs-Hoeck, M. Himly, M. Boyles and A. Duschl, *Particle and fibre toxicology*, 2016, **13**, 1.
53. J. H. Shannahan, R. Podila, A. A. Aldossari, H. Emerson, B. A. Powell, P. C. Ke, A. M. Rao and J. M. Brown, *Toxicol. Sci.*, 2014, kfu217.
54. S. Milani, F. Baldelli Bombelli, A. S. Pitek, K. A. Dawson and J. Rädler, *ACS Nano*, 2012, **6**, 2532-2541.
55. W. Liu, J. Rose, S. Plantevin, M. Auffan, J.-Y. Bottero and C. VIDAUD, *Nanoscale*, 2013, **5**, 1658-1668.
56. O. Boussif, F. Lezoualc'h, M. A. Zanta, M. D. Mergny, D. Scherman, B. Demeneix and J.-P. Behr, *Proceedings of the National Academy of Sciences*, 1995, **92**, 7297-7301.
57. W. Hu, C. Peng, M. Lv, X. Li, Y. Zhang, N. Chen, C. Fan and Q. Huang, *ACS Nano*, 2011, **5**, 3693-3700.
58. C. Ge, J. Du, L. Zhao, L. Wang, Y. Liu, D. Li, Y. Yang, R. Zhou, Y. Zhao and Z. Chai, *Proceedings of the National Academy of Sciences*, 2011, **108**, 16968-16973.
59. A. Lesniak, A. Salvati, M. J. Santos-Martinez, M. W. Radomski, K. A. Dawson and C. Åberg, *J. Am. Chem. Soc.*, 2013, **135**, 1438-1444.
60. E. Fröhlich, *Int J Nanomedicine*, 2012, **7**, 5577-5591.
61. A. Verma and F. Stellacci, *Small*, 2010, **6**, 12-21.
62. S. Ritz, S. Schöttler, N. Kotman, G. Baier, A. Musyanovych, J. r. Kuharev, K. Landfester, H. r. Schild, O. Jahn and S. Tenzer, *Biomacromolecules*, 2015, **16**, 1311-1321.

## Supporting Information

### The Effect of Surface Characteristics of Upconversion Nanoparticles on Corona Formation and Cell Interaction

Tab. S1 List of the 20 most abundant proteins detected in the  $\clubsuit$ UCNP by nanoLC-ESI-MS mass spectrometry. The isoelectric points were calculated using the protein analysis tool Compute pI/Mw on the ExPASy server (<http://web.expasy.org/>).

No.	Protein	Isoelectric point (pI)	Molecular weight (Da)
1	Alpha-2-HS-glycoprotein	5.26	38394
2	Serum albumin	5.82	69248
3	Platelet factor	6.11	9517
4	Apolipoprotein A-II	7.80	11195
5	Hemoglobin fetal subunit beta	6.51	15849
6	Alpha-1-antiproteinase	6.05	46075
7	Apolipoprotein A-I	5.71	30258
8	Tetranectin	5.47	22130
9	Prothrombin	5.97	70461
10	Apolipoprotein E	5.67	36003
11	Protein AMBP	7.81	39209
12	Adiponectin	5.44	26117
13	Platelet factor 4	8.46	9124
14	Inter-alpha-trypsin inhibitor heavy chain H3	5.59	99489
15	Transthyretin	5.90	15717
16	Thrombospondin-1	4.74	129451
17	Secreted phosphoprotein 24	8.30	23119
18	C4b-binding protein alpha chain	5.98	68841
19	Alpha-1-acid glycoprotein	5.62	23168
20	Hemoglobin subunit alpha	7.94	15528

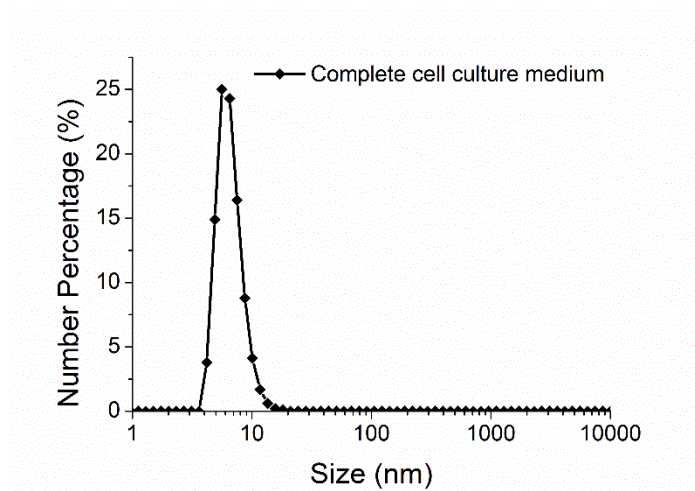


Fig. S1 DLS measurement of proteins in complete cell culture medium.

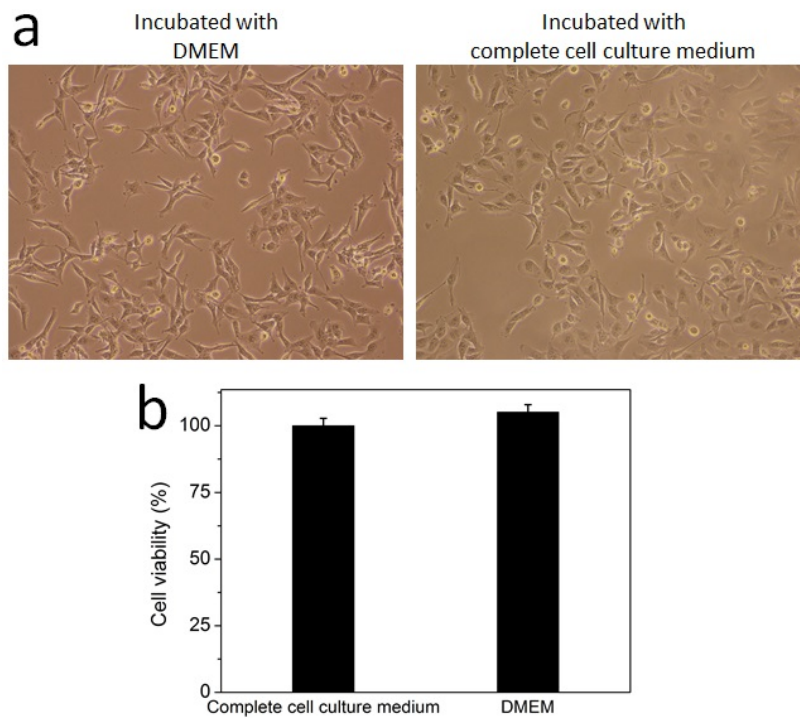


Fig. S2 (a) Phase-contrast images of MDA-MB-231 cells growing in serum-free DMEM and complete cell culture medium. (b) Cell viability of MDA-MB-231 cells after incubated with complete cell culture medium and serum-free DMEM for 24 h.

## **Systematic Assessment of Blood Circulation Time of Functionalized Upconversion Nanoparticles in the Chick Embryo**

### **7.1 Introduction**

UCNP-based theranostics systems have potential to advance the cancer imaging and treatment techniques because of their advantageous optical properties. The diagnostic and therapeutical efficacy of these UCNP nanocomposites correlates strongly with their blood circulation time. Generally, the longer blood residence time will increase propensity of nanoparticles to extravagate through the leaky vasculature and accumulate in tumour sites, thereby enhancing the therapeutic efficiency. Therefore, understanding the blood circulation time of UCNPs is of great importance for their translation to clinical applications.

Surface chemistry of nanoparticles is a crucial design feature that controls their blood circulation time and tumour accumulation. Following the *in vitro* studies in the last few chapters, this chapter reports on *in vivo* investigations of the blood circulation time of UCNPs functionalized with different surface groups. To this end, UCNPs were coated with a silica layer and further functionalized with -COOH, -NH<sub>2</sub>, and -PEG groups. A versatile animal model, chick embryo, was developed to facilitate the evaluation of UCNPs *in vivo*. After an intravenous injection of NPs, blood was collected from the chorioallantoic membrane of a chick embryo at different time points to determine remaining UCNPs in the blood. The deployment of a chick embryo model for simple blood circulation study and quantification of UCNPs in the blood smear by microscope

was demonstrated for the first time in this work. The obtained results provided further insights into the effect of the surface chemistry on *in vivo* behaviour of UCNPs.

### 7.2 Author's Contribution to The Paper

The PhD candidate (Liu Liang) is the second author of this paper. Her contribution to this paper was the nanoparticle-related chemistry work, including preparation of UCNPs, coating UCNPs with silica layer, surface modification of nanoparticles with different functional groups, and the nanomaterial characterization using TEM. She also drew the schematic figures of UCNPs and analysed the size distribution of nanoparticles using ImageJ. Together with the authors, Dr. Annemarie Nadort and Ms Anna Guller, she took part in development of the chick embryo, injection of nanoparticles, and blood smear preparation. The first author, Dr. Annemarie Nadort carried out the imaging of UCNPs in the blood smear, analysed the obtained results, designed figures, and wrote the manuscript. Dr. Ekaterina Grebenik was involved at the initial stage of developing the chick embryo models. Ms Anna Guller contributed to the results interpretation. Dr. Yiqing Lu participated in the development of the UCNP imaging system. Prof. Yi Qian and Prof Ewa Goldys provided the comments on the paper. A/Prof. Andrei Zvyagin conceived of the idea, participated in the data analysis, and supervised the research.



## 7.3 Full Paper

## Systematic assessment of blood circulation time of functionalized upconversion nanoparticles in the chick embryo

Annemarie Nadort<sup>a,\*</sup>, Liuen Liang<sup>a,b</sup>, Ekaterina Grebenik<sup>a</sup>, Anna Guller<sup>a</sup>, Yiqing Lu<sup>a</sup>, Yi Qian<sup>b</sup>, Ewa Goldys<sup>a</sup> and Andrei Zvyagin<sup>a</sup>

<sup>a</sup>ARC Centre of Excellence for Nanoscale BioPhotonics, MQ Photonics, Macquarie University, NSW 2109, Australia

<sup>b</sup>Faculty of Medicine and Health Science, Macquarie University, NSW 2109, Australia

### ABSTRACT

Nanoparticle-based delivery of drugs and contrast agents holds great promise in cancer research, because of the increased delivery efficiency compared to ‘free’ drugs and dyes. A versatile platform to investigate nanotechnology is the chick embryo chorioallantoic membrane tumour model, due to its availability (easy, cheap) and accessibility (interventions, imaging). In our group, we developed this model using several tumour cell lines (e.g. breast cancer, colon cancer). In addition, we have synthesized in-house silica coated photoluminescent upconversion nanoparticles with several functional groups (COOH, NH<sub>2</sub>, PEG). In this work we will present the systematic assessment of their *in vivo* blood circulation times. To this end, we injected chick embryos grown *ex ovo* with the functionalized UCNPs and obtained a small amount of blood at several time points after injection to create blood smears. The UCNP signal from the blood smears was quantified using a modified inverted microscope imaging set-up. The results of this systematic study are valuable to optimize biochemistry protocols and guide nanomedicine advancement in the versatile chick embryo tumour model.

**Keywords:** upconversion nanoparticle, chick embryo chorioallantoic membrane, drug delivery, blood circulation time

### 1. INTRODUCTION

Upconversion photoluminescence is a nonlinear optical process where two or more near infrared excitation photons are converted to higher energy emission photons. Unlike other multiphoton processes (2-photon fluorescence, second harmonic generation), in the upconverting system real intermediate excited states are involved, usually within the f-electrons of lanthanide ions, which enables the process to happen at moderate excitation density ( $1 - 10^2 \text{ W/cm}^2$ )<sup>1</sup>. The synthesis of nanoscale upconverting materials consisting of an inorganic crystalline host matrix doped with lanthanide-ions<sup>2,3</sup>, increased the interest for biomedical applications<sup>4</sup>.

Upconversion nanoparticles (UCNPs) have several optical advantages for biomedical imaging, such as background-free imaging capability<sup>5</sup>, excitation and emission within the tissue optical transparency window<sup>6</sup> and long emission lifetimes allowing time-gated detection. For effective *in vivo* application, UCNPs should not only exhibit advantageous optical properties but also excellent biochemical properties. The evaluation of UCNP properties in the context of *in vivo* situations is crucial for the translation of UCNPs from the lab to clinical applications.

An identified purpose is the delivery of UCNPs through the leaky tumour vasculature for enhanced detection and/or tumour therapy<sup>7</sup>. In view of this, a versatile model is the chick embryo chorioallantoic membrane (CAM), an extra-embryonic vascularised membrane responsible for the gas exchange of the developing chick embryo. The development of protocols

\*annemarie.nadort@mq.edu.au

describing *ex ovo* culturing of chick embryos by transferring the embryo into a sterile container, enabled exposure of the CAM and easy access for intervention and imaging<sup>8, 9</sup>. Since the embryos are immune-deficient (up to embryonic development day 14) foreign cancer cells can be introduced without rejection. Grafting tumour cells on the CAM results in their adoption by the CAM and subsequent tumour-induced angiogenesis enables their growth into proliferating, vascularized tumours<sup>10, 11</sup>. The CAM-based tumour development and their microvascular environment can be studied in detail<sup>12, 13</sup>, including the delivery of photoluminescent macromolecules like fluorescent dextran<sup>14</sup> and virus-derived fluorescently labelled nanoparticles<sup>15</sup> to the tumour sites. The presence of nearly all relevant stroma factors e.g. immune cells (at a later stage), extracellular matrix components, blood and lymphatic vessels make the CAM model highly suited for studying tumour-stroma interactions, tumour metastasis, and therapy-induced changes in tumour development, implying the upcoming role of the CAM model in cancer research<sup>16</sup>.

For *in vivo* use, UCNPs should exhibit surface properties that offer a good dispersability in buffers and ensure biocompatible interaction with tissues. Unfortunately, inorganic nanoparticles are naturally colloiddally instable, and prone to aggregation due to the vanderWaals attractive forces between them<sup>17</sup>. In biological media UCNPs can bind to proteins, or other molecules, which can influence their photochemical and biochemical properties, and the biological response and distribution *in vivo*. Several strategies in surface chemistry have been developed to repel the UCNPs from each other, for example by adding surface charge to induce electrostatic repulsion or molecular spacers for steric repulsion. Since UCNPs are generally hydrophobic after preparation by the solvothermal decomposition method, UCNPs firstly need to be transferred into the aqueous phase. Silanization and water-dispersible polymer functionalization are commonly used methods. Among them, silica coating with functional groups (-NH<sub>2</sub>, -COOH, -SH) and PAA, PMAO, PEG wrapping are popular surface modifications for UCNPs *in vitro* and *in vivo* studies<sup>18-20</sup>. In addition, the functional groups provide opportunity for the binding of molecules (e.g. antibodies) with tumour-specific targeting properties. Biocompatible surface properties prevent or delay the uptake by the immune system thereby increasing the nanoparticle circulation times<sup>21</sup>. Long circulation times enhance the probability that the particles will end up in the tumour and facilitate enhanced tumour visibility or induce therapy. Feedback on the UCNP chick embryo circulation time is thus meaningful for UCNP design. In this proceeding we report our first preliminary *in vivo* results on the blood circulation time of silica coated UCNPs, further functionalized with -NH<sub>2</sub>, -COOH, and -PEG surface groups in the chick embryo vasculature.

## 2. METHODS

### 2.1. Synthesis and characterization of UCNPs

The UCNPs were synthesized and coated in house. Core  $\beta$ -NaYF<sub>4</sub>:Yb,Er nanoparticles were synthesized following a protocol developed previously<sup>22</sup>. To prepare UCNP@SiO<sub>2</sub> a modified water-in-oil microemulsion method was used<sup>23</sup>. Silica coated UCNPs were further conjugated with APTES, APTES plus succinic anhydride and MPEG-silane, to obtain NH<sub>2</sub>, COOH and PEG surface functional groups, respectively<sup>24, 25</sup>. The resulting particles were mono-disperse, with an average size of  $28 \pm 1.5$  nm after silica-coating. TEM images, size distribution and emission spectrum of the particles, are shown in Fig. 1.

### 2.2. Chick embryo *ex ovo* culturing

Fertile eggs were purchased and the embryos were incubated *in ovo* for 3 days while being rotated every 180 min, at 37.5°C and 70% humidity. At embryonic development day (EDD) 3 the eggs were carefully opened and the contents transferred to sterile plastic weighing boats, perforated for oxygen transfer and covered with sterile plastic wrapping. The embryos were returned to the incubator with the same temperature and humidity settings. At EDD 15 the embryos were removed from the incubator and carefully injected with 50  $\mu$ l 0.5mg/mL UCNP@SiO<sub>2</sub>-COOH, UCNP@SiO<sub>2</sub>-NH<sub>2</sub> or UCNP@SiO<sub>2</sub>-PEG respectively, using micrometer-sized glass needles under stereomicroscopic viewing. At several time points after injection a small amount of blood (5  $\mu$ l) was drawn from the chick embryo, away from the site of injection. A maximum of 6 time points per chick embryo was chosen to reduce physiological impact. To cover a wide range of time points [2 - 720 min] and increase the accuracy of the results given unavoidable biological variations we included a total of 22 chick

embryos in the experiment. The average number of chick embryos per time point per coating was 2.8 with a minimum of 2. The protocol has been evaluated and approved by the Animal Ethics Committee.

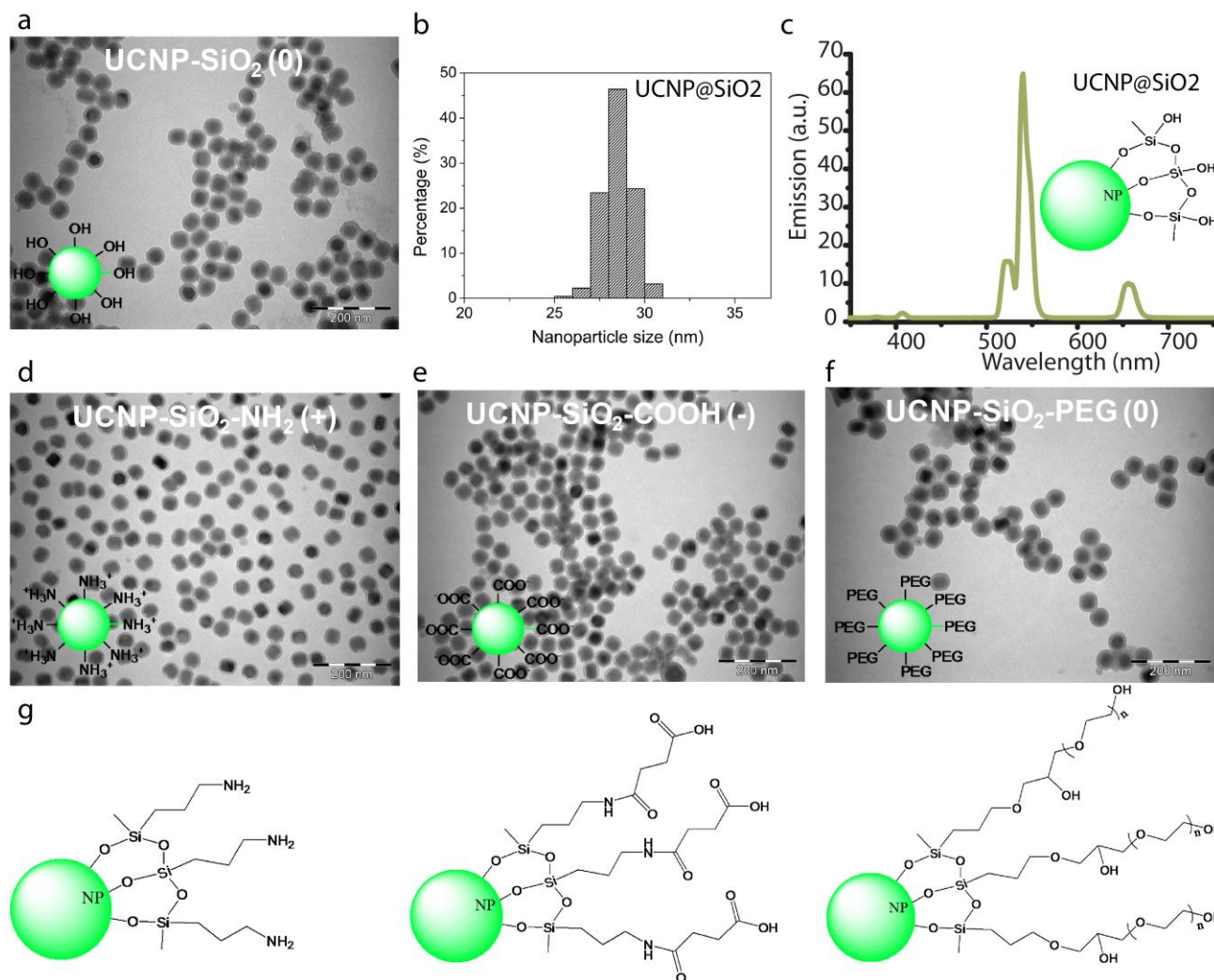


Fig. 1. Geometrical and optical characterization of in-house synthesized UCNPs. (a) – (c) TEM images, size distribution and emission spectrum of UCNPs@SiO<sub>2</sub>. (d) – (g) TEM images and schematic drawing of UCNPs@SiO<sub>2</sub>-COOH/NH<sub>2</sub>/PEG coatings.

### 2.3. Blood smear preparation

Immediately after drawing the blood samples were prepared as blood smears on microscope objectives, resulting in a monolayer of red blood cells (RBCs) on each slide. The circulating UCNPs present in the blood samples would thus be deposited on the slides as well and could be quantified using upconversion microscopy. No anticoagulants were used in this procedure. We fixed the slides using 100% methanol.

### 2.4. Upconversion microscopy

The slides were imaged with a wide-field inverted epi-luminescence microscope (Olympus IX70, with objective 40×, NA 1.15) modified to allow external laser illumination at the sample plane (fiber-coupled diode laser at wavelength 980 nm,

Shenzhen LEO Photoelectric Co. Ltd). The excitation laser was directed to the focal plane using a modified Köhler illumination scheme and adjustable iris diaphragm to achieve uniform and controlled excitation power density and spot size at the sample plane. A detailed description of the imaging system is provided in ref <sup>26</sup>. During the whole experiment the excitation density was kept at  $440\pm10$  W/cm<sup>2</sup> ( $720\pm20$  mW on a circular spot of 230  $\mu$ m in diameter). An EMCCD camera (Andor iXon DU-885) was mounted to the microscope detection port. We used a high-pass absorbance filter as emission filter (cut-off 850 nm, Edmund Optics); a dichroic beam-splitter (cut-off, 511 nm, Semrock) for the reflection of 980 nm toward the sample and passing the visible emitted light to the detection path; and two additional filters (short pass interference filter, cut-off 842 nm, Semrock and band pass filter, KG-5 coloured glass, Thorlabs) as emission filters. The combination of a high-performance interference filter and coloured glass band pass filter was needed to adequately reject the high excitation power scattered by the cells.

2.5 Image acquisition

Each blood smear slide corresponded to a specific time point after injection, UCNP-coating group and chick embryo. A total of 100 slides were collected. We installed an automated X,Y scanner at the sample plane, however, re-focusing after spatial translation was needed so that the process was only semi-automatic. As the slide covers an area of several cm<sup>2</sup>, imaging the whole slide was too time-consuming. As the UCNP-signal decreased with time we recorded more images per slide for the longer time points. A minimum of 20 regions per slide was recorded, corresponding to an area of minimally 0.5 mm<sup>2</sup>. Each UCNP-image was recorded 3 times, and the average image was saved. The exposure time and EMgain were fixed at 0.5s and x100 respectively during the whole experiment. In addition, due to an inhomogeneous distribution of RBCs over the microscope slides we took bright field and UCNP-images of the same area to correct for the number of RBCs (and thus correct for sampled blood volume).

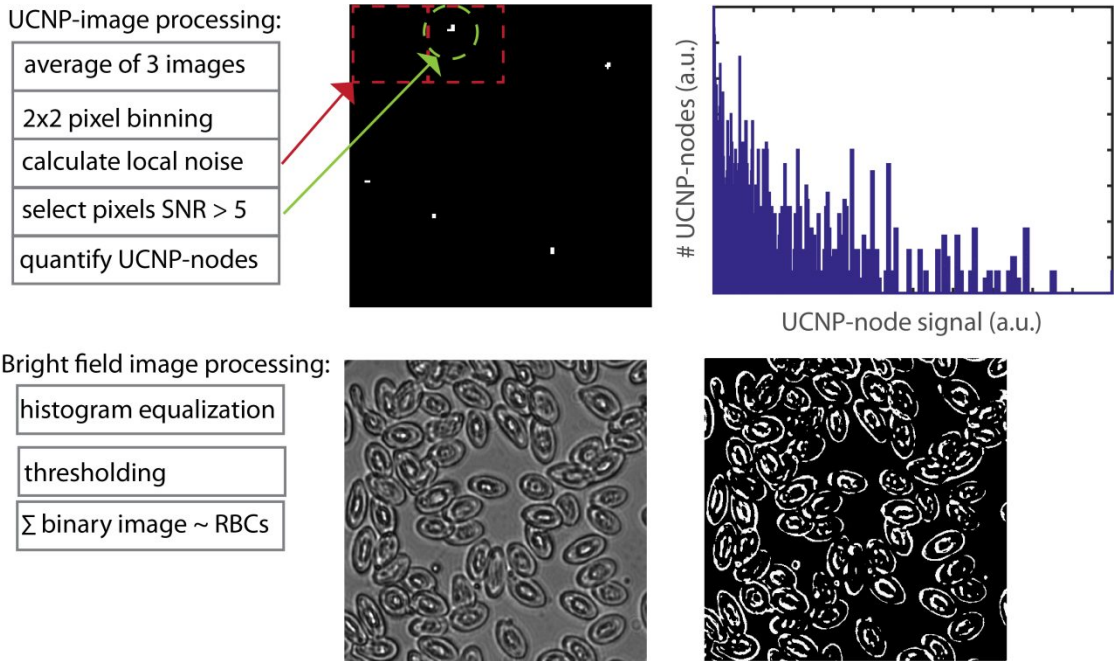


Fig. 2. Overview of quantitative image analysis steps

2.6. Image analysis

The fast amount of images (~8000) required an automated analysis. The UCNP-images were 2x2 pixel binned to reduce the read noise. A positive UCNP signal was defined as an SNR of 5 or higher, (the *Rose criterion* states that an SNR of at

least 5 is needed to be able to distinguish image features at 100% certainty<sup>27</sup>). The background noise contained a slight gradient, however, as the UCNP signal was sparsely distributed over the images, it was possible to estimate the local noise level as the mean of a 30x30 pixel area around a central pixel. If the central pixel value (signal) was 5 times higher than the local noise, the pixel was designated UCNP signal. In addition to simply 'adding' the entire UCNP signal per blood smear we also quantified the distribution of UCNP signal by grouping adjacent signal pixels together that belong to one UCNP-node. This way we obtained information on the size distribution of the UCNP nodes in the blood smears. Finally, the bright field images were used to correct for the blood sample volume related to the UCNP signal. The bright field images were histogram equalized to get consistent results, subsequently binarized by thresholding to obtain the total area as a measure for number of RBCs. The process is schematically drawn in Fig. 2.

### 3. RESULTS

The quantified UCNP-signal in the blood smear images as a function of time after injection is shown in Fig. 3. All data points are averaged over all images and chicken embryos, and corrected for RBC area in the bright field images. As can be seen, the -PEG and -NH<sub>2</sub> coated UCNP@SiO<sub>2</sub> don't decrease much in the first  $\pm 20$  minutes, however they rapidly decrease in the following period. We can estimate the blood circulation half-time at  $\tau_{1/2, \text{PEG}} = 25 \pm 10$  minutes, and  $\tau_{1/2, \text{NH}_2} = 20 \pm 10$  minutes. On the other hand, COOH coated UCNP@SiO<sub>2</sub> already show a reduced signal in the beginning, which does not decrease much with time. No reliable estimate of  $\tau_{1/2, \text{COOH}}$  can be made. A further analysis of the images showed that the size distribution of the detected UCNP nodes in the blood smears is quite different for the -COOH group as compared with the -PEG and -NH<sub>2</sub> groups. This is shown in the bar plots in Fig. 4 where the contribution of small, medium and large UCNP nodes ('clusters') to the total signal is calculated, for three different coatings and three different time ranges (short, medium and long). Clearly, the -COOH group is much more influenced by large UCNP-nodes as compared with the NH<sub>2</sub> and PEG groups. This early and substantial clustering of the particles in blood is subject of further study, but should be taken into account when interpreting the data points in Fig. 3.

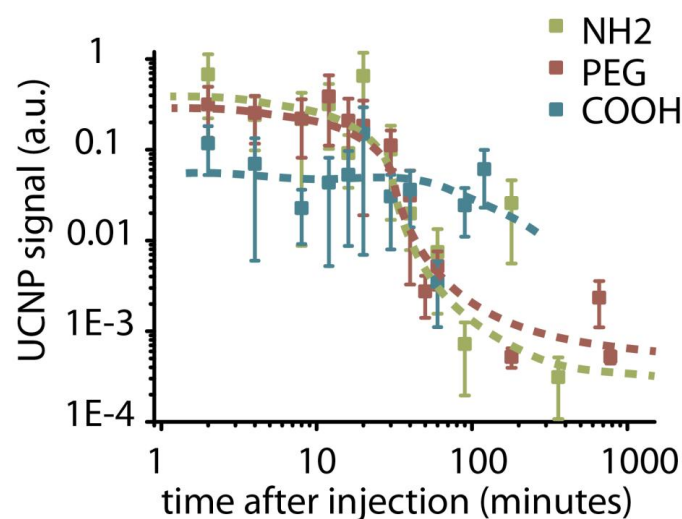


Fig. 3. Blood circulation behavior of UCNP@SiO<sub>2</sub> functionalized with 3 different surface groups: NH<sub>2</sub>, COOH and PEG, in chick embryo circulation. The UCNP-signal as a function of time after injection is quantified from blood smear microscopic images, as described in the text.

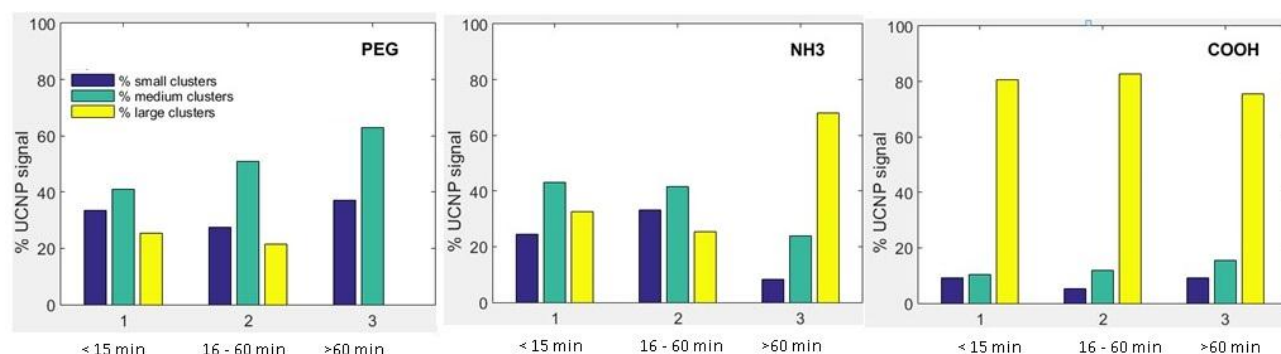


Fig. 4 The quantified UCNP signal from blood smears further analyzed as a dependency on size of UCNP clusters and their contribution to the total UCNP signal, for three different time ranges (short, < 15 minutes, medium, 16 – 60 minutes, long, > 60 minutes)

#### 4. CONCLUSION

We have shown our first, preliminary results of the blood circulation time of UCNP@SiO<sub>2</sub> coated with different functional surface groups. The results show that a blood circulation half time of around 20 – 25 minutes can be expected for UCNPs in the chick embryo *ex ovo* model. Up to several hours after injection particles could still be detected in the blood smear samples. Future investigations on the colloidal behavior of the particles are necessary to draw further conclusions on the blood circulation time of COOH-coated particles. Our practical investigation gives important feedback on the behavior of nanoparticles in the blood stream and is an essential step towards nanoparticle-based drug delivery for oncological purposes.

#### ACKNOWLEDGMENTS

This work was partially funded by the Australian Research Council, DP140104458 to E.G. We thank Dr. Varun Sreenivasan for his support with epi-fluorescence microscopy.

#### REFERENCES

- [1] F. Auzel, "Upconversion and Anti-Stokes Processes With f and d Ions in Solids," *Chemical Reviews*, 104(1), 139-174 (2004).
- [2] S. Heer, K. Kömpe, H. U. Güdel *et al.*, "Highly Efficient Multicolour Upconversion Emission in Transparent Colloids of Lanthanide-Doped NaYF<sub>4</sub> Nanocrystals," *Advanced Materials*, 16(23-24), 2102-2105 (2004).
- [3] G. Yi, H. Lu, S. Zhao *et al.*, "Synthesis, Characterization, and Biological Application of Size-controlled Nanocrystalline NaYF<sub>4</sub>: Yb, Er Infrared-to-Visible Up-Conversion Phosphors," *Nano letters*, 4(11), 2191-2196 (2004).
- [4] H. S. Mader, P. Kele, S. M. Saleh *et al.*, "Upconverting luminescent nanoparticles for use in bioconjugation and bioimaging," *Current opinion in chemical biology*, 14(5), 582-596 (2010).
- [5] Z. Song, Y. G. Anissimov, J. Zhao *et al.*, "Background free imaging of upconversion nanoparticle distribution in human skin," *Journal of Biomedical Optics*, 18(6), 061215-061215 (2013).
- [6] S. A. Hilderbrand, and R. Weissleder, "Near-Infrared Fluorescence: Application to In Vivo Molecular Imaging," *Current Opinion in Chemical Biology*, 14(1), 9-71 (2009).



- [7] H. Maeda, J. Wu, T. Sawa *et al.*, "Tumor vascular permeability and the EPR effect in macromolecular therapeutics: a review," *Journal of controlled release*, 65(1), 271-284 (2000).
- [8] D. S. Dohle, S. D. Pasa, S. Gustmann *et al.*, "Chick ex ovo culture and ex ovo CAM assay: how it really works," *Journal of visualized experiments: JoVE*(33), (2009).
- [9] H. C. Yalcin, A. Shekhar, A. A. Rane *et al.*, "An ex-ovo chicken embryo culture system suitable for imaging and microsurgery applications," *Journal of visualized experiments: JoVE*(44), (2010).
- [10] H. Sun, J. Jia, X. Wang *et al.*, "CD44+/CD24- breast cancer cells isolated from MCF-7 cultures exhibit enhanced angiogenic properties," *Clinical and Translational Oncology*, 15(1), 46-54 (2013).
- [11] D. Ribatti, B. Nico, A. Vacca *et al.*, "Chorioallantoic membrane capillary bed: A useful target for studying angiogenesis and anti-angiogenesis in vivo," *The Anatomical Record*, 264(4), 317-324 (2001).
- [12] E. I. Deryugina, and J. P. Quigley, "Chick embryo chorioallantoic membrane model systems to study and visualize human tumor cell metastasis," *Histochemistry and cell biology*, 130(6), 1119-1130 (2008).
- [13] A. Zijlstra, J. Lewis, B. DeGryse *et al.*, "The inhibition of tumor cell intravasation and subsequent metastasis via regulation of in vivo tumor cell motility by the tetraspanin CD151," *Cancer cell*, 13(3), 221-234 (2008).
- [14] D. B. Pink, W. Schulte, M. H. Parseghian *et al.*, "Real-time visualization and quantitation of vascular permeability in vivo: implications for drug delivery," *PloS one*, 7(3), e33760 (2012).
- [15] C. Choi-Fong, A. Amber, L. Hon-Sing *et al.*, "Evaluation of nanoparticle uptake in tumors in real time using intravital imaging," *Journal of Visualized Experiments*(52), (2011).
- [16] M. Klingenberg, J. Becker, S. Eberth *et al.*, "The chick chorioallantoic membrane as an in vivo xenograft model for Burkitt lymphoma," *BMC cancer*, 14(1), 339 (2014).
- [17] R.-A. Sperling, and W. Parak, "Surface modification, functionalization and bioconjugation of colloidal inorganic nanoparticles," *Philosophical Transactions of the Royal Society of London A: Mathematical, Physical and Engineering Sciences*, 368(1915), 1333-1383 (2010).
- [18] E. A. Grebenik, A. Nadort, A. N. Generalova *et al.*, "Feasibility study of the optical imaging of a breast cancer lesion labeled with upconversion nanoparticle biocomplexes," *Journal of Biomedical Optics*, 18(7), 076004-076004 (2013).
- [19] A. E. Guller, A. N. Generalova, E. V. Petersen *et al.*, "Cytotoxicity and non-specific cellular uptake of bare and surface-modified upconversion nanoparticles in human skin cells," *Nano Research*, 8(5), 1546-1562.
- [20] R. Naccache, F. Vetrone, V. Mahalingam *et al.*, "Controlled synthesis and water dispersibility of hexagonal phase NaGdF<sub>4</sub>: Ho<sup>3+</sup>/Yb<sup>3+</sup> nanoparticles," *Chemistry of Materials*, 21(4), 717-723 (2009).
- [21] J.-W. Yoo, E. Chambers, and S. Mitragotri, "Factors that control the circulation time of nanoparticles in blood: challenges, solutions and future prospects," *Current pharmaceutical design*, 16(21), 2298-2307 (2010).
- [22] Z. Li, Y. Zhang, and S. Jiang, "Multicolor core/shell-structured upconversion fluorescent nanoparticles," *Advanced Materials*, 20(24), 4765-4769 (2008).
- [23] H. Xing, W. Bu, S. Zhang *et al.*, "Multifunctional nanoprobes for upconversion fluorescence, MR and CT trimodal imaging," *Biomaterials*, 33(4), 1079-1089 (2012).
- [24] S. Kralj, M. Drogenik, and D. Makovec, "Controlled surface functionalization of silica-coated magnetic nanoparticles with terminal amino and carboxyl groups," *Journal of Nanoparticle Research*, 13(7), 2829-2841 (2011).
- [25] G. T. Hermanson, [Bioconjugate techniques] Academic press, (2013).
- [26] A. Nadort, V. K. Sreenivasan, Z. Song *et al.*, "Quantitative imaging of single upconversion nanoparticles in biological tissue," *PloS one*, 8(5), e63292 (2013).
- [27] A. E. Burgess, "The Rose model, revisited," *JOSA A*, 16(3), 633-646 (1999).

# 8

## Summary and Future Scope

### 8.1 Summary

Research exploring photoluminescent nanoparticles for cancer theranostics is driven by the increasing demands for high-contrast imaging and deep-tissue therapy. The state-of-the-art photoluminescent nanoparticles used in theranostics research are generally limited by the short-wavelength excitation using ultraviolet (UV) or visible light. The emerging photoluminescent material, upconversion nanoparticles (UCNPs) provide critical solutions for theranostics applications in virtue of its deeply-penetrating near infrared (NIR). UCNPs demonstrate remarkable optical properties, including an unusually large anti-Stokes shift (measured in hundreds nanometres), narrow emission bands, tunable emission spectrum, excellent photostability, and exceptionally long ( $100\ \mu\text{s}$  –  $1\ \text{ms}$ ) photoluminescence lifetime. These properties enable background-free deep tissue imaging of sites of interest labelled with UCNP. Benefiting from these merits along with the flexible surface chemistry, UCNPs are envisioned to fulfil the demanding needs in cancer diagnosis and treatment. This thesis focuses on design, production, and applications of biofunctional UCNPs for targeted labelling and photodynamic therapy of cancer cells. The key research outcomes achieved are summarized below.

The feasibility of using UCNPs to enhance the treatment depth of a fluorescent photosensitising protein KillerRed by converting the excitation NIR light to green emission for photoactivation of KillerRed was explored. To this aim, KillerRed was covalently conjugated to UCNPs to produce a unique protein-UCNP biohybrid (KillerRed-UCNP). The resultant nanocomposites demonstrated excellent colloidal stability in buffers and low dark toxicity to cells. In addition, the energy transfer between



UCNPs and KillerRed under the irradiation at 980 nm was verified using fluorescence spectroscopy and lifetime measurements. The photodynamic therapy outcome was tested *in vitro* in terms of ROS generation and its therapeutic potential was evaluated using biological tissue model of pork meat of different thickness (0 mm, 5 mm, and 10 mm). My collaborators and I found that in comparison with the yellow light optical for the KillerRed excitation, NIR excitation produced by far greater amount of ROS, which resulted in much greater tumouricidal effect on the tested cancer cells in this deep tumour model. This work demonstrated clear potential of UCNPs as the NIR-to-visible light converter to overcome the light penetration limit that has plagued PDT application for many years.

The second major outcome of my work is the demonstration of the use of peptide linker (LPG) technology to assemble UCNP, photosensitizer (Rose Bengal, referred as RB) and targeting antibodies (Ab) for development of targeting and therapeutic UCNP-based nanocomposites (UCNP@SiO<sub>2</sub>(RB)-LPG-Ab). The proposed facile method was proved to be superior over the conventional bioconjugation approaches in providing excellent control over the functional display of conjugated antibodies and alleviating the aggregation problem. As a result, tri-modal capabilities of UCNP-based nanocomposites i.e. optical imaging, targeting, and cancer treatment were developed and demonstrated in *in vitro* assays. This functionality lends itself straightforward generalisation and extension to other targeting or therapeutic agents, and as such address a broad scope of diseases. The applicability of the presented approach was recognised by a prestigious journal ACS Applied Materials and Interfaces, where this work has been published.

A systematic investigation of profound influence of serum proteins on the target-delivery and therapeutic efficacy of biofunctional nanocomposites, in particular, UCNP composites, represents an extension and the third main outcome of my work. In collaboration with my colleagues, I demonstrated that polymer-coated UCNPs acquired protein layer (termed “corona”) swiftly once dispersed in complete cell culture medium. The surface charge of UCNP was found to be the key determinant of the composition and content of this protein corona. In particular, positively charged polymer-coated UCNPs (polyethyleneimine, PEI-UCNP) exhibited 4-fold higher protein adsorption than that of negatively charged (polyacrylic acid, PAA-UCNP) and neutral (polyethylene glycol, PEG-UCNP) nanoparticles. It was found that *e.g.* lipoproteins tend to bind to PEI-UCNPs,

whereas platelet proteins had affinity to PAA- and PEG-UCNPs. The cellular binding and uptake of UCNP-corona complexes formed from PAA-UCNP and PEG-UCNP were inhibited, whereas the binding and uptake of UCNP-corona complexes formed from positively charged PEI-UCNP were enhanced. In all cases, the protein corona was demonstrated to improve the cell compliance with UCNPs. These findings will provide important insight into the nanoparticle interactions with biological systems and useful guidance in designs of biofunctional complexes of UCNPs and other nanoparticles.

For the first time, investigation of the impact of three types (PEG, NH<sub>2</sub>- and COOH-) surface functionalities on the blood circulation time of UCNPs was addressed in my project and represents the fourth outcome of my work. My colleagues and I aimed to engineer a long-circulating UCNPs nanocomposite to achieve the higher yield of target-delivered nano-cargo to tumours by relying on the so-called enhanced permeability and retention effect (EPR). A chick embryo *ex ovo* model was developed to test the blood circulation time of nanoparticles and UCNPs in blood smear by imaging and analysis of UCNPs content in the smear samples from which their circulation lifetime in the blood stream was determined. Our results revealed that the PEG-functionalized UCNPs displayed the longest blood residence time in comparison with that of UCNPs displaying NH<sub>2</sub>- and COOH- surface moieties. In addition, PEG-UCNPs resulted in minimum aggregation, following the intravenous injection of colloidal samples. These findings are believed to provide a useful guidance for prospective *in vivo* applications of UCNPs.

### 8.2 Future Scope

I believe this work has provided a solid foundation for design, production and applications of UCNPs-based nanocomposite for diagnosis and treatment of cancer, as exemplified by the successful applications of KillerRed-UCNPs and UCNPs@SiO<sub>2</sub>(RB)-LPG-Ab in photodynamic therapy and optical imaging. The analysis of UCNPs in this study have been mostly performed in *in vitro* settings. To validate these findings with respect to targeted delivery, it would be desirable to use animal tumour models to explore *in vivo* distributions and targeting ability of antibody-conjugated UCNPs. Since UCNPs are capable to suppress optical background in the whole-animal imaging scenario, *in vivo* optical imaging of UCNPs will provide a useful approach to monitor tumour labelling.

Moreover, the animal tumour model is also applicable to evaluate and optimise therapeutic efficiency of the drug loaded UCNPs nanocomposites.

The chick embryo represents a particularly well-suited model for the *in vivo* analyses of UCNPs delivery because it supports the growth of human tumours, is relatively inexpensive and does not require anesthetization or surgery [1]. To this end, the next step can be development of vascularised tumours in a chick embryo model by placing tumour spheroids [2] or tumour cells enriched matrigels [3] or gelatine-sponges [4] to the chick chorioallantoic membrane (CAM). Considering the accessibility of *ex ovo* CAM tumours by optical microscopes, observing time-dependent tumour accumulation of UCNPs via EPR effect stands as a cutting-edge application in the life sciences [5].

Improving therapeutic outcomes of the developed UCNPs-PDT agents is another direction for future work. In this regard, efforts can be made to couple the drug-loaded UCNPs with antibodies to achieve tumour-targeted therapy, increase the drug payload, and load two or more photosensitizers that absorb different upconversion emissions. For example, mesoporous or hollow mesoporous silica layer can be coated on UCNPs to allow for the higher drug loading in the designed UCNPs@SiO<sub>2</sub>(RB)-LPG-Ab nanoplateform. Additionally, photosensitizers (*e.g.* zinc phthalocyanine, Chlorin e6, and methylene blue) that are excitable with red light can be co-loaded with Rose Bengal to green- and red-emitting NaYF<sub>4</sub>:Yb,Er nanoparticles. In the context of *in vivo* applications, surface modification of UCNPs with PEG and its derivatives is promising to avoid reticuloendothelial system entrapment and enhance the nanoparticle uptake level in tumours [6].

In this project, important preliminary results on the formation and composition of FBS-corona on UCNPs were obtained. This study lends itself a straightforward extension to investigation of the protein corona formation in more representative biological fluids (*e.g.* rodent plasma and human blood). Due to their unique optical properties, upconversion nanoparticles provide a particularly attractive platform to investigate the protein corona formation process *in situ*, which will give an access to real-time pharmacokinetics studies of nanoparticles in blood and blood plasma. Identification and characterization of the proteins adsorbed on UCNPs surface and subsequent analysis of their secondary structures will be necessary to yield more detailed insights into binding mechanism of

proteins and the possible extrapolations of UCNP behaviour *in vitro* and *in vivo* [7]. Circular dichroism (CD) spectroscopy can be exploited to elucidate the protein structures during their interaction with UCNP [8]. In the end, I envisage a rational design of nanoparticle nanocomposites that acquire a protein corona of the composition desired for *in vivo* applications. Evading the immune system of a live organism is a grant goal in theranostics, and it can be addressed by controlling assembly of a protein corona on the rationally designed nanoparticles.

### 8.3 References

1. Liu, K., J.A. Holz, Y. Ding, X. Liu, Y. Zhang, L. Tu, X. Kong, B. Priem, A. Nadort, and S.A. Lambrechts, *Targeted labeling of an early-stage tumor spheroid in a chorioallantoic membrane model with upconversion nanoparticles*. *Nanoscale*, 2015. **7**(5): p. 1596-1600.
2. De Magalhaes, N., L.-H.L. Liaw, and M. Berns, *An instruction on the in vivo shell-less chorioallantoic membrane 3-dimensional tumor spheroid model*. *Cytotechnology*, 2010. **62**(3): p. 279-283.
3. Lokman, N.A., A.S. Elder, C. Ricciardelli, and M.K. Oehler, *Chick chorioallantoic membrane (CAM) assay as an in vivo model to study the effect of newly identified molecules on ovarian cancer invasion and metastasis*. *International journal of molecular sciences*, 2012. **13**(8): p. 9959-9970.
4. Ribatti, D., B. Nico, A. Vacca, and M. Presta, *The gelatin sponge–chorioallantoic membrane assay*. *NATURE PROTOCOLS-ELECTRONIC EDITION-*, 2006. **1**(1): p. 85.
5. Cho, C.-F., A. Ablack, H.-S. Leong, A. Zijlstra, and J. Lewis, *Evaluation of nanoparticle uptake in tumors in real time using intravital imaging*. *JoVE (Journal of Visualized Experiments)*, 2011(52): p. e2808-e2808.
6. Cao, T., T. Yang, Y. Gao, Y. Yang, H. Hu, and F. Li, *Water-soluble NaYF<sub>4</sub>: Yb/Er upconversion nanophosphors: Synthesis, characteristics and application in bioimaging*. *Inorganic Chemistry Communications*, 2010. **13**(3): p. 392-394.
7. Fleischer, C.C. and C.K. Payne, *Nanoparticle–cell interactions: molecular structure of the protein corona and cellular outcomes*. *Accounts of Chemical Research*, 2014. **47**(8): p. 2651-2659.
8. Fleischer, C.C. and C.K. Payne, *Secondary structure of corona proteins determines the cell surface receptors used by nanoparticles*. *The Journal of Physical Chemistry B*, 2014. **118**(49): p. 14017-14026.

## List of Abbreviations

Ab	antibody
APTES	(3-aminopropyl) triethoxysilane
BCA	bicinchoninic acid
CAM	chorioallantoic membrane
Ce6	chlorin e6
CNT	carbon nanotube
CT	computed tomography
CTAB	cetyltrimethylammonium bromide
DAPI	4',6-diamidino-2-phenylindole
DCF	2',7'-dichlorofluorescein
DCFH	2',7'-dichlorodihydrofluorescein
DCFH-DA	2',7'-dichlorodihydrofluorescein diacetate
DLS	dynamic light scattering
DMEM	Dulbecco's modified Eagle's medium
DMF	dimethylformamide
DMSO	dimethyl sulfoxide
DOX	doxorubicin
DPBF	1,3-diphenylisobenzofuran
dSiO <sub>2</sub>	dense silica
EDC	1-ethyl-3-(3-dimethylaminopropyl) carbodiimide hydrochloride
EDC·HCl	<i>N</i> -(3-dimethylaminopropyl)- <i>N'</i> -ethylcarbodiimide hydrochloride
EDD	embryonic development day
EDTA	ethylenediaminetetraacetic acid
EPR	enhanced permeability and retention
FA	folic acid
FBS	fetal bovine serum
FITC	fluorescein isothiocyanate
FTIR	Fourier transform infrared
H&E	Hematoxylin and eosin
HBSS	Hank's balanced salt solution

## LIST OF ABBREVIATIONS

---

hmSiO <sub>2</sub>	hollow mesoporous silica
HRTEM	high-resolution transmission electron microscope
IPTG	isopropyl $\beta$ -D thiogalactoside
KR	KilleRed
L	peptide linker
LB	Luria Bertani
LPG	Linker-Protein G
MB	methylene blue
MC540	merocyanine 540
MRI	magnetic resonance imaging
mSiO <sub>2</sub>	mesoporous silica
MTS	3-(4,5-dimethylthiazol-2-yl)-5-(3-carboxymethoxyphenyl)-2-(4-sulfophenyl)-2H-tetrazolium
MTT	thiazolyl blue tetrazolium bromide
NHS	<i>N</i> -hydroxysuccinimide
NIR	near-infrared
NOBF <sub>4</sub>	nitrosonium tetrafluoroborate
NP	nanoparticle
OA	oleic acid
ODE	1-octadecane
OM	oleylamine
P/S	penicillin–streptomycin
PAA	poly(acrylic acid)
PBS	phosphate-buffered saline
PDT	photodynamic therapy
PEG	poly(ethylene glycol)
PEG-NH <sub>2</sub>	methoxy-poly(ethylene-glycol)-amine
PEI	polyethylenimine
PET	positron emission tomography
PFA	paraformaldehyde
PG	Streptococcus Protein G'
PL	photoluminescence
PMAO	poly(maleic anhydride- <i>alt</i> -1-octadecene)
PMT	photomultiplier tube

## LIST OF ABBREVIATIONS

---

PS	photosensitizer
PTA	tungstophosphoric acid
PVP	polyvinylpyrrolidone
QD	quantum dot
RB	Rose Bengal
RBC	red blood cell
ROS	reactive oxygen species
RT	room temperature
SNR	signal to noise ratio
SPECT	single-photon emission computed tomography
Sulfo-NHS	<i>N</i> -hydroxysulfosuccinimide sodium salt
TEM	transmission electron microscope
TEOS	tetraethyl orthosilicate
TGA	thermal gravimetric analysis
UCL	Upconversion photoluminescence
UCNP	upconversion nanoparticle
UCNP@SiO <sub>2</sub>	silica-coated UCNP
UV	ultraviolet
WGA	lectin from triticum vulgaris (wheat)
ZnPc	zinc phthalocyanine

# ANIMAL RESEARCH AUTHORITY (ARA)

AEC Reference No.: 2013/007-4

Date of Expiry: 31 March 2016**Full Approval Duration:** 1 April 2013 to 31 March 2016 (24 Months+12 months)

This ARA remains in force until the Date of Expiry (unless suspended, cancelled or surrendered) and will only be renewed upon receipt of a satisfactory Progress Report before expiry (see Approval email for submission details).

**Principal Investigator:**

Dr Andrei Zvyagin  
Physics and Astronomy  
Macquarie University, NSW 2109  
andrei.zvyagin@mq.edu.au  
0451 925 116

**Associate Investigators:**

Mark Connor	0413 202 762
Annemarie Nadort	0405 036 690
Liuen Liang	0451 976 934
Anna Guller	0450 124 218

**In case of emergency, please contact:**  
the Principal Investigator / Associate Investigator named above  
**Animal Welfare Officer - 9850 7758 / 0439 497 383,**

The above-named are authorised by MACQUARIE UNIVERSITY ANIMAL ETHICS COMMITTEE to conduct the following research:

**Title of the project:** High-sensitivity targeted imaging of tumours on the chick embryo chorio-allantoic membrane**Purpose:** 4 - Research: Human or Animal Biology

**Aims:**

1. To assess methods to detect tumours, based on labeling tumours with luminescent nanoparticle-antibody complexes that adhere to the tumour;
2. To graft small tumours on the chick embryo chorio-allantoic membrane
3. To develop nanoparticles that can attach to tumours and also have therapeutic effects

**Surgical Procedures category:** 3 - Minor Conscious Intervention**All procedures must be performed as per the AEC-approved protocol, unless stated otherwise by the AEC and/or AWO.****Maximum numbers approved (for the Full Approval Duration):**

Species	Strain	Age/Sex/Weight	Total	Supplier/Source
13	-	Day 11-17	100+160	Country Cacklers
		<b>TOTAL</b>	<b>260</b>	

**Location of research:**

Location	Full street address
MQ	Macquarie University, Building E7B, PC1 lab 109, NSW 2109
ASAM	Level 1, F10A, 2 Technology Place, Macquarie University, NSW 2109

**Amendments approved by the AEC since initial approval:**

1. Experimental design, technique or procedure, number of animals and extension of approval duration (Approved 20 March 2014).
2. Amendment # 2 - Removal of Ekaterina A Ivukina as Associate Investigator (Approved AEC 17 July 2014).
3. Amendment # 3 - Addition of Liuen Liang as Associate Investigator (Exec approved 25 June 2014, ratified at AEC 17 July 2014).
4. Amendment #4 - Addition of Anna Guller as Associate Investigator - (Exec approved & ratified by AEC 16 April 2015)
5. Amendment #5 - Request of extension of 12 months (approved by AEC 16 April 2015)

**Conditions of Approval:** N/A

Being animal research carried out in accordance with the Code of Practice for a recognised research purpose and in connection with animals (other than exempt animals) that have been obtained from the holder of an animal suppliers licence.



**Dr Simon McMullan** (Acting Chair, Animal Ethics Committee)

**Approval Date:** 16 April 2015